Controllable Synthesis of Nanoparticles in Continuous Flow Microreactors

Lina Yang

University of Leeds

School of Chemical and Process Engineering

Submitted in accordance with the requirements for the degree of Doctor of Philosophy

31 March 2024

The candidate affirms that the work submitted is her own, with the exception of work which has formed part of jointly authored publications has been included. The contribution of the candidate and other authors to this work has been explicitly indicated below.

The content of **Chapter 3** of this thesis has been published in the following journal:

Mei Yang, Lina Yang, Jia Zheng, Nicole Hondow, Richard A. Bourne, Tom Bailey, George Irons, Elliot Sutherland, Daniela Lavric, Ke-Jun Wu, 'Mixing performance and continuous production of nanomaterials in an advanced-flow reactor', Chemical Engineering Journal, 2021, volume 412, https://doi.org/10.1016/j.cej.2021.128565

The candidate carried out all experimental work with Mei Yang, George Irons. Data analysis was carried out by the candidate and Mei Yang. The computational fluid dynamics simulation by Jia Zheng. Elliot Sutherland generated the geometry of this Corning Lab AFR using the drawing software, AutoCAD. The manuscript was written by Mei Yang and the candidate with the help of Nicole Hondow, Richard A. Bourne, Tom Bailey, Daniela Lavric, and Ke-Jun Wu.

Acknowledgements

Firstly, I would like to thank Dr Nicole Hondow and Dr Ke-Jun Wu for their excellent guidance, huge help, enthusiasm and technical assistance during my PhD. Nicole's approachability and encouragement have bolstered my confidence both in my research and further career path.

Many thanks to Mei Yang for the collaboration in the work presented in Chapter 3, I spent an unforgettable wonderful time with her. Many thanks to Sang T. Pham, Matt Jellicoe on the data analysis of cuprous oxide in Chapter 5. I also acknowledge and thank XiaoLong Ma for the photocatalytic test of tin dioxide in Chapter 4. Thanks for my dear colleagues, Tom Bailey, Martha Alice IIett, always nice, helpful and reliable. Thanks for all the LEMAS staff, Ben Douglas, Mohammed Javed for the support of test.

I cherish the wonderful time shared with Shuadan, Niannian, Patrice, Mary, Yue, The Pham, Chao, Sue, Lynn, Peter, Christ, Bob, Judy, Andria, Matt, Helen, Pingping, Jihong, Alex in Leeds. Finally, so many thanks to my beloved parents, parents in-law, husband, daughter, brother for their selfless love and support to me.

I would also appreciate the financial support from Leeds-CSC scholarship, and Corning European Technology Centre providing the Corning AFR for my research study.

Abstract

The accurate control of nanoparticle (NP) morphology, particle size and particle size distribution (PSD) is essential to achieve their accurate size/morphology-dependent properties. Continuous microflow reactors offer potential advantages over traditional batch processing in producing micro- and nanoparticles with excellent controllability, reproducibility with merit of superior mixing and mass/heat transfer performance. This thesis focuses on the synthesis of silver NPs (Ag NPs), tin dioxide NPs (SnO_2 NPs), gold@tin dioxide NPs (Au@SnO_2 NPs), and cuprous oxide NPs (Cu_2O NPs) within continuous microfluidic systems, aiming to achieve controllable particle size, PSD and morphology.

While successful cases of micro- and milli-reactors for nanomaterials production have been reported in a lab scale, scaling up these home-made micro-channel / micro-tubular reactors with non-standardized components such as tubing, connectors, adaptors, etc. poses challenges for the large-scale production. One of the commercial examples of continuous flow reactors, Corning Advanced-Flow Reactor (AFR) has demonstrated success in homogeneous and heterogenous organic synthesis process. For the large-scale requirement, the Corning AFR provide a wide range of throughput by increasing the channel size and/or number of the reactor units, while retaining mixing, mass/heat transfer performance, which could helpful to achieve the seamless transition from laboratory-optimized process to industrial- scale production. However, limited studies have been reported on the nanomaterials production using Corning AFR. To evaluate the performance of the Corning AFR (Lab Reactor Module) for the nanomaterials production, the mixing characteristic (on the micro-, meso- and macroscale) at different flow rate and flow rate ratio were evaluated. A case study of colloidal Ag NPs was introduced to examine how flow dynamics and multiscale mixing performance inside the Corning AFR affect average particle size and PSD. It will pave the way for large scale production of size-tunable colloidal nanoparticles in the future work.

Furthermore, plasmonic metal@semiconductor (Au@SnO_2) binary nanomaterials were synthesized in a simple capillary milli/micro-tube reactor. SnO_2, a n-type semiconductor with a direct wide band gap (3.64 eV at 300 K), mainly absorb the UV light (< 5% in solar light). To enhance visible-light

absorption, noble metal NPs are commonly used to improve solar-energy-conversion efficiency in composite photocatalysts through the surface plasmon resonance (SPR) effect and also prevent the hole-electron recombination by charge transfer. The solar energy conversion efficiency of this binary composite photocatalysts is determined by the type, material features, geometric arrangement of the building blocks. In conventional synthetic strategies, semiconductor and metal NPs were synthesised separately, and following sol-immobilisation, impregnation and co-precipitation are commonly used to combine this binary composite. These semi-continuous synthesis methods are challenging to scale up with precise nanostructures control. To address this, the study explores the synthesis of SnO_2 NPs at atmospheric pressure, room temperature to make high-volume production more feasible. Herein, the study introduces a microfluidic way for the continuous synthesis of Au@SnO_2 in a micro-capillary reactor. This study provides a versatile strategy with an economic way to continuously synthesis plasmonic metal/semiconductor with narrow size-distribution on a large scale.

Moreover, as a visible light-driven p-type semiconductor with a narrow bandgap of 1.9-2.2 eV, cuprous oxide (Cu_2O) shows promising potential in photocatalytic applications due to its suitable electronic band structure, earth abundance and nontoxicity. With a face-centered cubic crystal structure ($Pn\bar{3}m$), Cu_2O polyhedron exhibit low-index and/or high-index facets. Achieving controllable crystal facets as well as narrow particle size distribution is vital for Cu_2O NPs synthesis. While wet chemical reduction approaches are the cheapest and simplest methods to manipulate the morphology of Cu_2O NPs in the liquid phase, however, the reported methods are mainly based on the batch-reactor systems in the laboratory settings. To bridge the gap between the academic research and engineering production process, in this study, we present a facile and continuous synthesis method for Cu_2O NPs using a lab-made capillary reactor. The morphological evolution of Cu_2O NPs from cubic to rhombic dodecahedra and from cubic to octahedra was first reported in a single system.

Overall, the results show continuous microfluidic reactor provide a facile method for synthesising nanoparticles with precise control over particle size, PSD and morphology.

Table of Contents

List of Figures

List of Tables

Chapter 1. Introduction

1.1 Motivation and objectives

Nanoparticles, by definition, possess at least one dimension in the nanoscale range from 1 to 100 nm. They show unique physicochemical properties compared to their bulk counterparts due to the elevated surface area-to-volume ratios and the influence of quantum effects. [1] [2] Nanomaterials exhibit a considerable surface area relative their volume, resulting in a significant proportion of their atoms being located on the surface. As a result, their properties are intricately related to factors, e.g. particle size, particle size distribution, composition, crystal structure, and morphologies, etc. [3] Hence, there is great importance in the development of reliable synthesis methods to achieve tightly specified nanostructures. Within the last few decades, wet chemical methods in the liquid phase have commonly been the most efficient bottom-up approach for achieving precise control over nanoparticles. [4] In this method, molecular precursors undergo decomposition or reduction to generate monomers that then nucleate and grow into monodispersed colloids. [5] Batch reactors, often regarded as the most straightforward approach, are commonly used in the synthesis of nanoparticles. Unfortunately, the inferior mass/heat transfer properties within the batch reactor lead to spatial and temporal variations in temperature and concentration, adversely affecting the reproducibility, selectivity, and scalability. [6] Consequently, enlarging the batch reactor for scale-up proves impractical due to poor batch-to-batch reproducibility and scale-up effects, hindering the attainment of high yields from lab-scale to industrial-scale. [7]

Compared to the conventional batch reactor, the reduced reaction volume within microchannels helps to form a more uniform reaction environment, enhanced by better heat and mass transfer and mixing performance. These factors contribute to the production of nanoparticles with greater uniformity. [8] [9] Microfluidic processes for the synthesis of nanoparticles have been extensively explored over recent years, with numerous continuous strategies have been reported through home-made microreactors in lab scale. [10] Therefore, based on the actual production requirements, there is an urgent demand to develop a superior, robust way to synthesis metal nanomaterials while maintaining a uniform product in large scale. [11] [12] Corning Advanced-Flow™ Reactor (Corning AFR), one of

the commercial examples of continuous flow reactor, and has been used industrially for some organic synthesis processes [13] [14] [15]. However, there are few studies on nanomaterials production. In this work, the performance of Corning AFR (Lab Reactor module) on the metal nanoparticles synthesis was evaluated, taking Ag NPs as a case study. An optimised continuous synthetic protocol was proposed.

The application of specific nanoparticles is influenced by the surface atomic arrangements, which are determined by their particle size and morphology. [16] [17] Metal oxide NPs find application as semiconductors with the common synthesis methods in the liquid phase involving sol-gel, precipitation, liquid deposition, and hydrothermal/solvothermal methods. However, these methods usually demand high temperature/pressure of the reactor or heat-treated post-process to get uniform NPs. [18] [19] Using a wide-band gap semiconductor (SnO_2 NPs) and a narrow-band gap semiconductor (Cu_2O NPs) as examples, a facile, continuous, and robust microfluidic method with controllable parameters is developed in this work.

1.2 Chapter overview

- Chapter 2 contains an overview of metal and semiconductor NPs (specifically SnO_2 NPs and Cu_2O NPs), along with an exploration of the various methods employed for their synthesis. It concerns the advantages and potential future direction on scale-up production of microfluidic colloidal nanoparticles synthesis. This chapter also introduces several ways to improve the photocatalytic property of semiconductors, including utilising the plasmonic metal nanoparticles to create the metal/semiconductor hybrid nanostructure. Traditional synthesis ways for achieving the metal/semiconductor hybrid nanostructures, including the metal/SnO_2 NPs as well as the Cu_2O NPs with controlled morphologies, are also discussed.
- Chapter 3 contains the details of the multiscale mixing performance (meso- and macroscales) of Corning AFR (Lab Reactor Module) in a single-phase flow at different flow rates and flow rate ratios. Taking Ag NPs as a case study, the chapter assesses the effects of multiscale mixing on nanoparticle synthesis, focusing on particle size and particle size distribution.

- Chapter 4 introduces the first reported microfluidic synthesis of pristine SnO_2 and Au@SnO_2 nanomaterials. To identify the most effective structure with superior photocatalytic properties, three different structures were explored to incorporate Au NPs with SnO_2: (1) Au NPs coated on the SnO_2 matrixes, (2) Au NPs surrounded by SnO_2 matrixes, and (3) Au NPs embedded with SnO_2 matrixes.
- Chapter 5 introduces a novel study which presents a facile and continuous synthesis method for Cu_2O NPs using a lab-made capillary reactor. The evolution of Cu_2O nanostructures from cubic to rhombic dodecahedra and from cubic to octahedra was first reported in a single system. This chapter also attempts to discuss the influence of mixing performance inside the reactor on morphology and particle size of Cu_2O NPs, considering both thermodynamic and kinetic perspectives.
- Chapter 6 summarizes conclusions drawn from the work presented along with possible future directions.

Chapter 2. Literature review

This chapter will provide an overview of metal and semiconductor nanoparticles, along with an exploration of the various methods employed for their synthesis. The limitations associated with conventional batch synthesis techniques for nanoparticles will be discussed and contrasted to the utilisation of microfluidic reactors as an alternative approach for nanoparticle synthesis. This method offers the advantages of precise control over particle size, distribution, and morphology. Moreover, the limitations inherent to this innovative technique will also be discussed.

2.1 Metal nanoparticles

Nanoparticles (NPs) are defined as materials which have at least one dimension in the range of 1-100 nm. Reducing particle size to the nano-scale results in a higher surface-to-volume ratio, demonstrating the unique extrinsic 'quantum size effect' and surface activity when compared to bulk material. [4] Beyond dimensionality, their size, shape and crystal morphology also play crucial roles in determining their properties. [2] [20] These unique physical and chemical features make them exhibit fantastic physicochemical characteristics in the fields of energy, catalytic chemistry, electromagnetism, etc. surpassing their bulk counterparts. [21] In order to optimise their quality, it is important to develop a way to synthesise them in the actual production process in a controllable manner. [22]

For metal nanoparticles (NPs), the quantum confinement and unique surface plasmon effects make them widely applicable in biomedicine, catalysis, optoelectronics, etc. [23] The properties of metal colloidal nanoparticles, such as gold, [24] silver, [25] and copper, [26] mainly depend on factors including size, morphology and crystal structure. In aqueous suspension, spherical Au NPs exhibit a spectrum of colours from brown, orange, red to purple as the core size increases from 1 to 100 nm, simultaneously exhibiting plasmonic absorption peaks between 500 to 550 nm. Additionally, Au NPs with various shapes, including quasi-spheres, nanorods, nanodumbbells, nanostars, *etc.* have been successfully synthesized. [27] Similarly, the shape-dependent catalytic oxidation properties of Ag NPs greatly depend on the nature of the exposed crystallographic plane. Xu *et al.* [28] found that the rate of reaction over the Ag nanocubes (purely {100} facets) was more than 14 times higher than Ag nanoplates (purely {111} facets) and four times higher than Ag nanospheres (displaying {100} and {111} facets). Muller *et al.*[29] predicted the influence of particle shapes and surface coverage of the relevant facets of Cu NPs (low index of (100), (110), (111) and stepped-edge high index of (211)) on CO_2 hydrogenation via a combination of density functional theory investigations and atomistic thermodynamics.

2.2 Semiconductor nanoparticles

In semiconductors, the activation of electrons from the valence band (VB) to the conduction band (CB) facilitates the conversion of solar energy into chemical energy. Over the past decades, the substantial demand for traditional fossil fuels to meet societal development has resulted in serious environmental pollution. Therefore, the requirement of pollution treatment technology and the utilisation of clean energy have become urgent tasks. [30] Solar energy is cheap and green, and its utilisation will be a key approach for the development of a sustainable society. Photocatalytic research has received worldwide attention since the pioneering work to split water using TiO_2 semiconductor by Fujishima *et al.* in 1972. [31]

In the photocatalytic process, incident light with photon energy equal to or greater than the semiconductor's band gap activates electrons in the VB to transition to the CB (step (i) in Figure 2.1). Subsequently, the generated electrons on the CB and the left holes on the VB migrate to the surface-active sites (usually at picosecond scale 10^{-12} s). Subsequently, the active holes and electrons can react with surface absorbed CO_2, H_2O, N_2, O_2 resulting in the formation of CH_4, CH_3OH, O_2, NH_3, reactive oxygen species (ROS). These photocatalytic processes open up a range of applications in carbon dioxide reduction, [32] pollutant degradation, [33] nitrogen fixation, [34]water splitting, [35] organic chemical synthesis, [36] *etc.* At the same time, random-walk-like electrons and holes tend to recombine because of the confinement of coulomb force, which is unfavourable for the overall efficiency (step (iii) in Fig. 2). [37] This is particularly true when the size of the semiconductor nanoparticle is much larger than the minority diffusion length. [38] In particular, the effective separation of photogenerated electron-hole pairs is very important because charge recombination (~ 10^{-9} s) is usually much faster in contrast to their transfer rate to the surface of the catalyst to conduct the redox reactions (~ 10^{-3} s to ~ 10^{-8} s). [39]

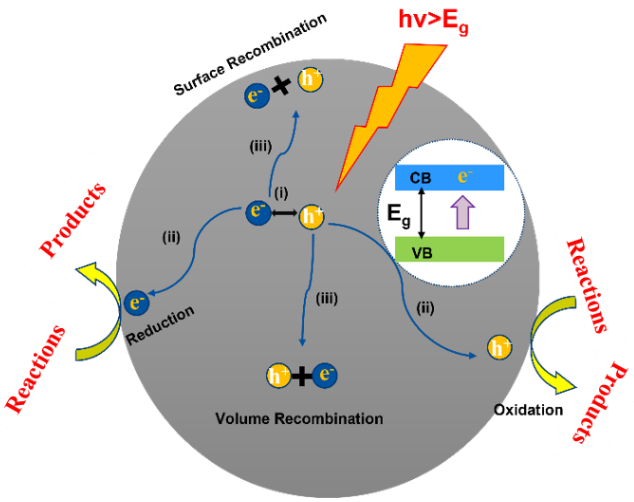

Figure 2.1 Schematic illustration of different steps during the photocatalytic process: (i) generation of electron-hole pairs; (ii) migrations of exciton to the surface-active sites; (iii) instant recombination of electrons and holes. [40]

2.2.1 Heterogeneous semiconductor photocatalyst materials

According to the function of elements in constructing heterogeneous semiconductors, the elements are classified into four groups, shown in Figure 2.2. [35] There are (i) to construct crystal structure and energy structure, (ii) to construct crystal structure but not energy structure, (iii) to form impurity levels as dopants, and (iv) to be used as co-catalysts.

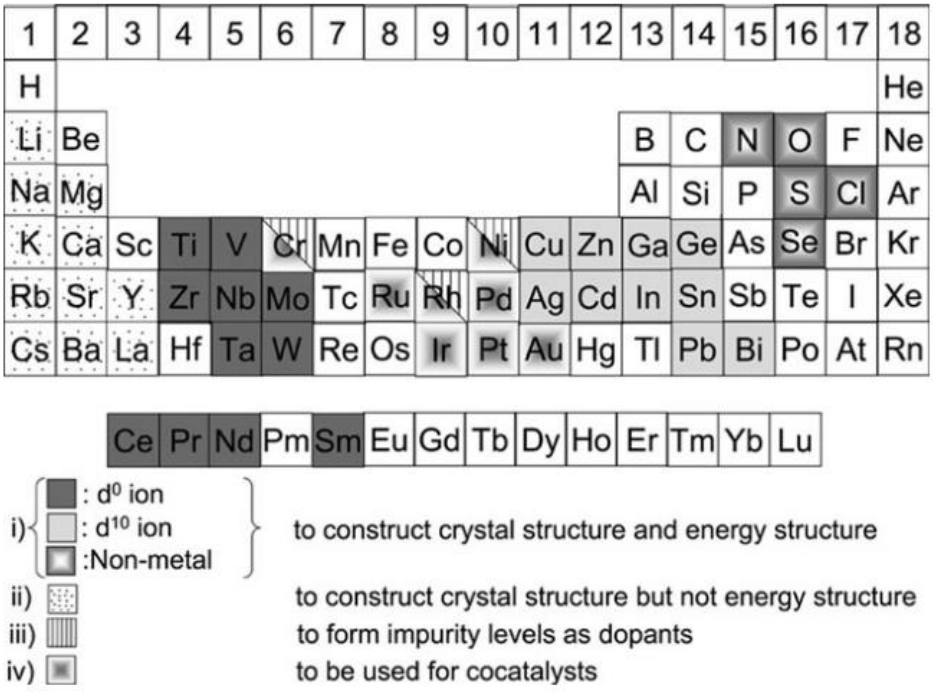

Figure 2.2 Elements constructing heterogeneous photocatalysts. [35]

According to the compositions, the semiconductors (bandgap usually between 0.5 to 3.6 eV) can be divided into elemental and compound semiconductors. The element materials are silicon (Si), germanium (Ge), and tin (Sn) in Group IV, and selenium (Se) and tellurium (Te) in Group VI of the periodic table. Numerous binary and ternary compounds are composed of more than one element from different columns in periodic table, such as gallium arsenide (GaAs, Group III-V), zinc oxide (ZnO, Group II-VI), silver chloride (AgCl, Group I-VII), tin dioxide (SnO_2, Group IV-VI), antimony oxide (SbO_2, Group V-VI), and chalcopyrite ($CuFeS_2$, Group I-III-VI). According to the positive (hole) and negative (electron) carriers, semiconductors can be divided into p-type and n-type semiconductors. Semiconductors can be classified as direct or indirect band gap based on whether the maximum energy of the valence band and the minimum energy of the conduction band occur at the same or different value of electron momentum. The typical semiconductors are summarised in Table 2.1. [18]

Table 2.1 List of Semiconductor Materials from the WIKIPEDIA (2024, March 19).

Column in periodic table	Material	Formula	Band gap (eV)	Gap type
IV	Silicon	Si	1.12	indirect
IV	Germanium	Ge	0.67	indirect
VI	Red selenium	Se	2.05	indirect
	Tin dioxide	SnO_2	3.6	
II-VI	Zinc sulfide	ZnS	3.54 (cubic) /3.91(hexagonal)	direct
II-VI	Zinc oxide	ZnO	3.37	direct
II-VI	Zinc selenide	ZnSe	2.7	direct
II-VI	Cadium selenide	CdSe	1.74	direct
II-VI	Cadmium sulfide	CdS	2.42	direct
		Fe_2O_3	2.20	
Oxide	Titanium dioxide, anatase	TiO_2	3.20	indirect
Oxide	Titanium dioxide, rutile	TiO_2	3.0	direct
Oxide	Titanium dioxide, brookite	TiO_2	3.26	
III-V	Gallium phosphide	GaP	2.26	indirect
III-V	Gallium arsenide	GaAs	1.42	direct
III-V	Gallium antimonide	GaSb	0.73	direct
III-V	Indium phosphide	InP	1.35	direct
	Strontium titanate	$SrTiO_3$	3.3	
		CuO	2.00	
		WO_3	2.80	
Magnetic	Nickel (II) oxide	NiO	3.6-4.0	direct
Oxide	Copper (I) oxide	Cu_2O	2.17	direct
IV-V		g-C_3N_4	2.7	

The width of the band gap in a semiconductor material and also the levels of the CB and VB are important in the photocatalytic redox reaction. If the photocatalytic water splitting is taken as an example, the bottom level of the CB has to be more negative than the redox potential of H^+/H_2O (0 V vs. NHE), while the top level of the valence band should be more positive than the redox potential of O_2/H_2O (1.23 V vs. NHE). Therefore, the theoretical minimum band gap for water splitting is 1.23 eV, and according to the Band gap (eV) = 1240/λ (nm), the absorption light wavelength is 1100 nm. Additionally, for the photoreduction of CO_2, the bottom level of the CB should be negative than the redox potential of CO_2/hydrocarbons (CH_4, CH_3OH, HCOOH), refer to Figure 2.3.

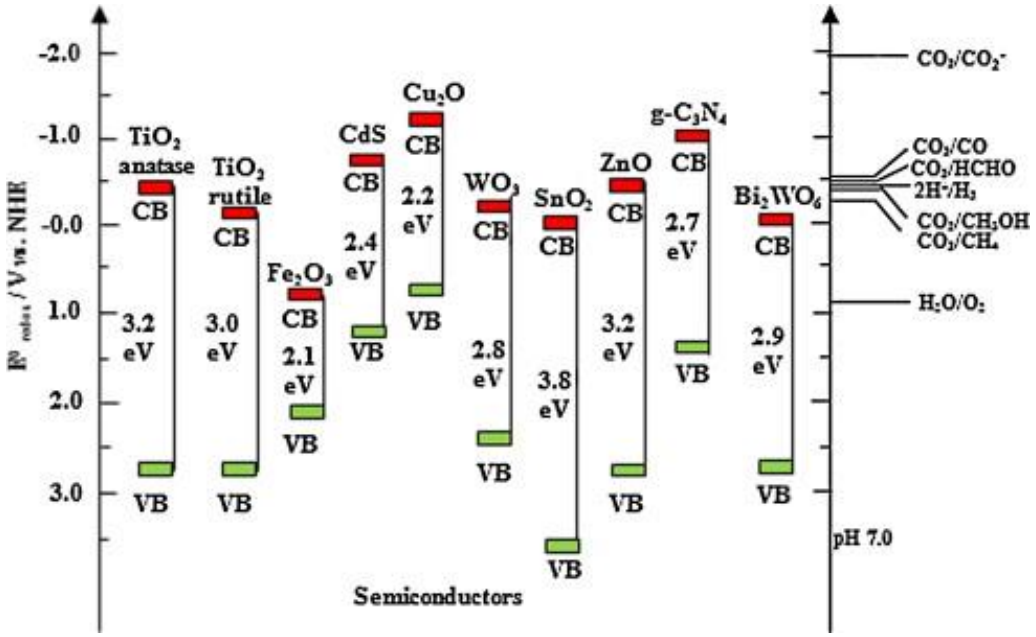

Figure 2.3 Band gap of some photocatalysts with respect to the redox potential of different chemical species measured at pH of 7. [32]

2.2.2 Methods to improve semiconductor photocatalytic properties

According to the photocatalytic process shown in Figure 2.1, an effective photocatalytic system depends on the corresponding requirements: (i) ensuring a sufficiently narrow band gap should be to assimilate the maximum solar spectrum; (ii) achieving high separation and swift transfer of active carriers (e^-/h^+) to the surface of the photocatalyst to minimize their recombination rate; (iii) possessing a robust redox capacity of the active carriers; (iv) having a surface area and morphology that provide numerous active sites for redox reactions. [41] However, intrinsic semiconductor photocatalysts often fail to meet all these requirements, prompting modifications to enhance their photocatalytic properties.

The band gap plays a major role in deciding the optical absorption ability of semiconductor. Semiconductors with bandgap larger than 2.5 eV are usually called wide-band gap semiconductors. The larger the band gap, the more energy is required to excite the electrons from the VB to CB. For example, as shown in Figure 2.4, semiconductors with band gap larger than 3.10 eV are only active under ultraviolet irradiation (UV), which occupies less than 5 % of solar energy. [42]

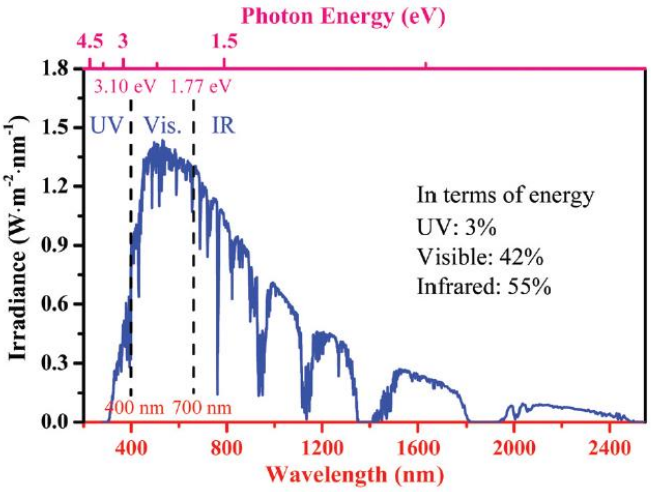

Figure 2.4 Spectrum of sunlight at sea level. [19]

To enhance the absorption of solar irradiation, self-doping or doping with external elements are usually used to tune the band structure. [43] However, doping introduces impurity levels in the band gap of semiconductor, and the dopant atoms become combination centres for activated carriers to inhibit the reaction. Unlike the creation of new band energy by doping, the creation of solid-solution photocatalyst can also lead to changes in the band gap, the crystal structure, as well as the local electronic structure. [44] The integration of plasmonic metal components with semiconductors is regarded as an effective way as the metal nanostructures act as tunable light antennas across the full solar radiation spectrum. [45]

The photocatalytic efficiency also greatly depends on the separation rate of e-/h+ pairs. In pristine photocatalysts, charge transfer occurs through random channels, leading to a high probability of e-/h+ recombination with the bulk or at the catalyst surface, releasing heat. To improve the charge spatial separation and depress exciton recombination, several strategies are proposed. (i) Doping elements as extrinsic defects into their crystal lattice generates impurity states within the optical band gap, which can widen their optical response and also reduces the recombination of charges. However, doping (non-metal doping, metal doping, co-doping) can also acts as a recombination centre for excitons to lower the photocatalytic performance. (ii) Designing vacancies (anion vacancies, cationic vacancies, co-/multi-vacancies) inside the photocatalyst lattice can also help to tune the band gap and transfer the charge carriers. Constructing a heterojunction is an effective strategy to control the separation and migration of charges. This enhances the transfer of charges along the heterojunction boundary, facilitating the movement of majority carriers and inducing the separation of charge carriers; various heterostructures, including Type II, Z-Scheme, and the recently studied S-Scheme semiconductor-semiconductor heterostructures, have been proposed for this purpose. [46] [47]

The reactivity of the photocatalyst is affected by the surface atomic structures. This is as the surface atomic arrangement and coordination intrinsically determine the reactant molecules adsorption,

excited carrier transfer and separation, product molecules desorption. Therefore, tuning crystal facets of photocatalysts is another important factor to optimize the photocatalytic reactivity. [16]

2.2.3 Mechanistic understanding of the plasmonic enhancement

Interest in plasmonic photocatalyst has received an increasing attention during the last decade, with the number of papers has increased rapidly from 2010 till now. Awazu *et al.* started to use the term "plasmonic photocatalysis" for the first time at 2008. [48] A number of studies show that composite plasmonic metal/semiconductors exhibit highly improved performance in photocatalytic reactions compared with their pure semiconductor counterparts. [49]

Combing disparate plasmonic metals with semiconductor nanoparticles is an effective way to extend a semiconductor's excited wavelength range and promote charge separation. [50] [51] In semiconductor-metal heterojunctions, Schottky contacts are exhibited due to the unequal work functions of the conductor and semiconductor, resulting in electron drift and the creation of a Schottky barrier at the interface between these two materials.

While experimental research in this field is still in the exploration stage, the local surface plasmon resonance (LSPR) effect is widely recognized for its significant impact on improving photocatalytic activity of plasmonic metal/semiconductor heterostructures. Under photo illumination, the electron cloud of the metal would respond to the incident light, shown in Figure 2.5. When the incident light carries a changing electromagnetic field to the metal, collective electron oscillation of the electron cloud of the metal would happen, called surface plasmon. The surface plasmon can be classified into surface plasmon polariton (SPP, propagate plasmons along the interface between metal and dielectric), and local surface plasmon resonance (LSPR, non-propagating plasmons in metal nanostructures). LSPR refers to the coherent collective oscillation of free electrons in plasmonic metal nanoparticles, which are more relevant in the field of plasmonic photocatalysis. [52] The electron cloud tends to displace asymmetrically relative to the nuclei by the restoring force arising from Coulomb attraction between electrons and nuclei. Consequently, an electric field is created owing to the redistribution of the charge density, and the direction is opposite to the external one. [53]

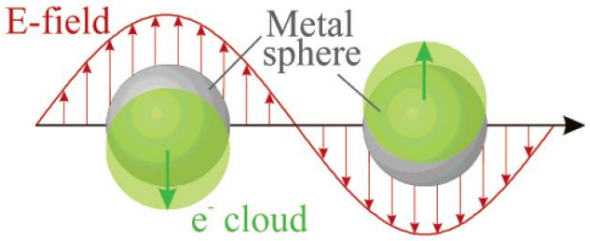

Figure 2.5 Schematic of plasmon oscillation for a metal sphere, showing the displacement of conduction electron charge cloud relative to the nuclei and formed electromagnetic field. [54]

The resonant photon wavelength varies among different metals. For example, Au, Ag and Cu nanostructures exhibit distinct resonant behaviour when interacting with photons of different wavelengths. (Figure 2.6 (a)) The resonant wavelength and LSPR intensity are influenced not only by the nature of metals but also by the size and shape of metallic nanostructures. Figure 2.6 (b) and Figure 2.6 (c) illustrate the resonant response of silver with various shapes and different sizes, respectively. [49] Therefore, the controlled synthesis of nanoparticles plays a crucial role in determining the photocatalytic properties of plasmonic metal/semiconductor heterostructure.

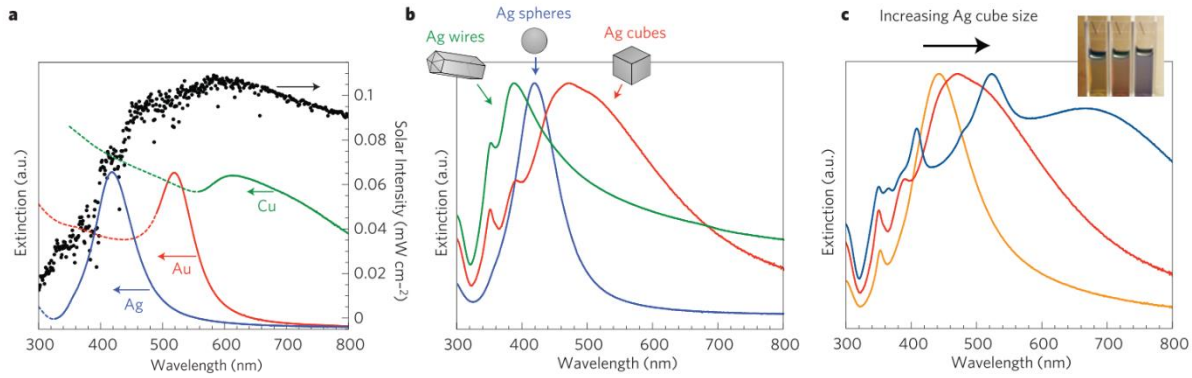

Figure 2.6 (a) Normalized extinction spectra of spherical Ag (38 ± 12 nm diameter), Au (25 ± 5 nm) and Cu (133 ± 23 nm) particles. The intensity of solar radiation is shown in black. Dashed portions of the metal extinction curves indicate interband transitions, meaning there is no surface plasmon resonance in these regions. (b) Normalized extinction spectra for Ag wire (90 ± 12 nm diameter, > 30 aspect ratio), sphere (38 ± 12 nm), and cube nanostructures (79 ± 12 nm edge length). (c) Normalized extinction spectra for Ag nanocubes with various sizes 56 ± 8 nm edge length (orange line), 79 ± 13 nm (red line), and 129 ± 7 nm (blue line). [49]

Despite the significance of plasmonic metal/semiconductor heterostructures, there are disputes regarding the mechanisms behind their plasmonic effect in enhancing the photocatalytic process. The five main mechanisms of plasmonic effect are shown in Figure 2.7: (i) light scattering; (ii) hot-electron injection; (iii) plasmon-induced resonance energy transfer (PIRET); (iv) Local electromagnetic field enhancement (LEMF); (v) plasmonic heating effect. The former three are the major mechanisms, which are mostly used to explain the plasmonic enhanced properties. [46] [49] Almost every reported work attempts to provide a reasonable explanation for the enhanced photocatalytic performance. There is no single prevailing idea, each approach may work under certain conditions and may fail under others. Taking the example of plasmonic metal@Cu_2O core-shell hybrid composites, the hot-electron injection process is the most cited mechanism to explain the improved photocatalytic property [55] [56]. However, it is limited by the electronic band structure alignment of the semiconductor and metal. Cushing *et al*. [57] reported that PIRET may occur between these two materials. However, Li *et al*. [58] reported there is a combination of PIRET and hot-electron injection simultaneously to help generate electron-hole pairs in semiconductor. The detailed processes need to be considered and placed within their proper and relevant contexts. The theory of the plasmonic enhanced photocatalyst is still in its infancy, and it requires further study.

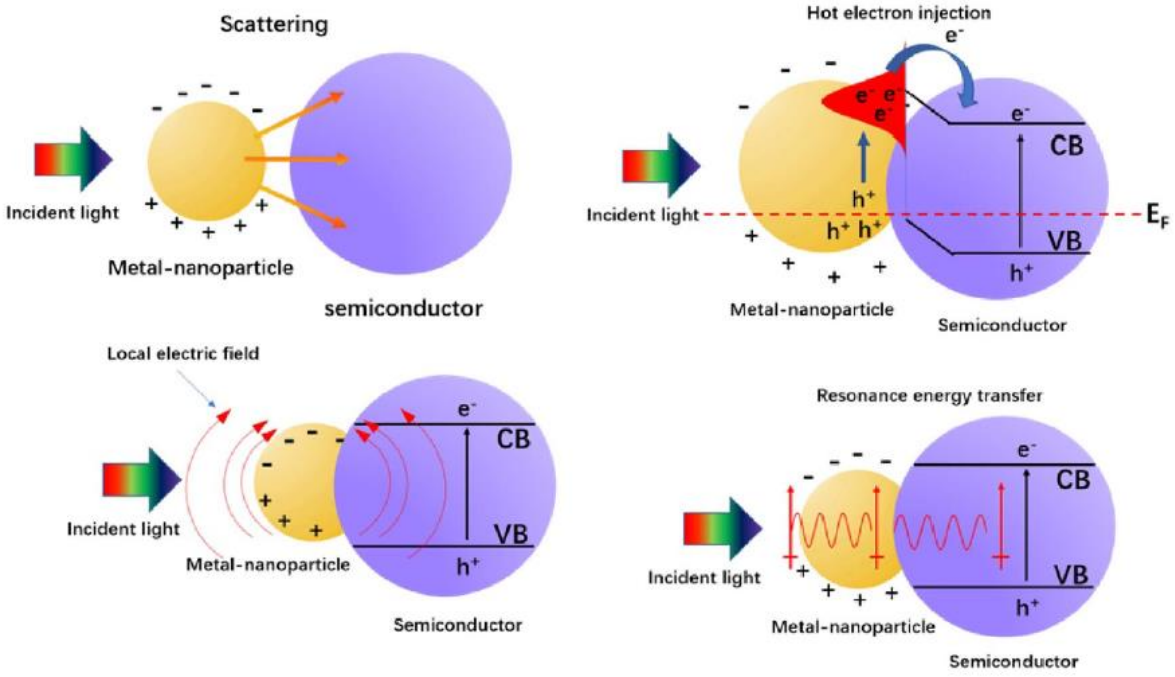

Figure 2.7 Illustration of four different types of metal-semiconductor LSPR. [46]

Much progress has been made in understanding and fine-tuning the plasmonic noble metal/semiconductor structure to get better photocatalytic properties. For example, the light absorption of semiconductors can be increased by adjusting the particle size, [59] [60] morphology, [61] and also the amount of plasmonic metal NPs, [62] explaining by the metal NP scattering. The hot-electron injection can only happen when the plasmonic metal is in direct contact with the semiconductor photocatalyst, where the Schottky barrier is formed. [48] The hot-electron process is also found to relate to the exact energy levels of the hot electrons at various statuses, the external temperature, and interface between these two materials, etc. [63] [64] The non-homogeneous localised electromagnetic field shows the highest intensity at the surface of the plasmonic metal, and decays exponentially with distance from the metal surface ($1/s^4$, s is the distance from the surface) or from the centre of the plasmonic metal ($1/d^6$, d is the distance from the centre). [45] According to the PIRET mechanism, the transfer efficiency proportional depends on (i)the overlap integral of the plasmon resonance and the conduction band, and (ii) the distance between the energy donor (metal) and the energy acceptor (semiconductor). [57] [65]

In order for a photocatalyst to find industrial and commercial application, the following aspects need to be achieved: (i) good catalytic performance for diverse photo-applications; (ii) find a way to scale up to industrial standards; (iii) how to prevent the corrosion of photocatalysts and promote their stability in recyclability runs.

2.2.4 Synthesis method of metal/semiconductor hybrid nanostructures

The photocatalytic property of metal/semiconductor hybrid nanostructures are influenced by factors such as particle size, distribution and morphology of both metal and semiconductor materials, as well as their organised hybrid structure. These influencing parameters strongly depend on the preparation techniques, necessitating well-controlled synthesis procedures for effective exploitation of the properties of metal NPs in combination with semiconductors.[62] It is important to consider to achieve scale-up synthesis process with controlled structure. This section details conventional methods for semiconductor nanostructure synthesis and the incorporation of noble metal NPs into semiconductors.

Numerous conventional synthesis methods, including sol-gel processes, [66] hydrothermal/solvothermal processes, [67] [68] precipitation methods, [69] wet chemical reduction methods, [70] laser ablation, [71] *etc.* are used to prepare semiconductor with various shape morphologies such as nanoparticles, [72]nanorods, [73] nanosheets, [74]and nanowires, [71], as well as various crystal-facet morphologies. [75] Typically, these methods involve high temperatures, pressures, and complicated apparatus. Considering the substantial demand for commercial-scale semiconductor materials, simplified processes are necessary.

For metal/semiconductor hybrid nanostructures, various plasmonic photocatalysts can be roughly classified into three forms based on the contact form: embedded form, encapsulation form, and isolation form. The schematic diagram and corresponding reported hybrid nanostructures are shown in Figure 2.8. [38]

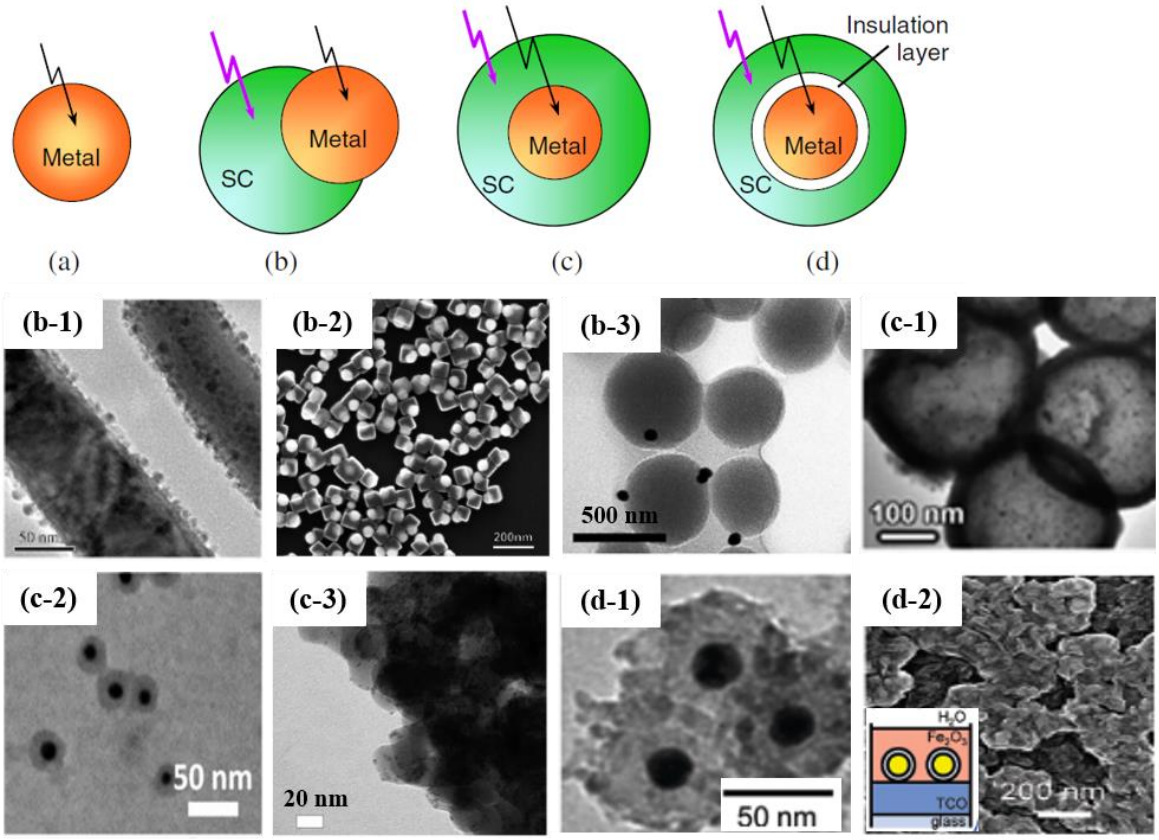

Figure 2.8 Four classifications of the plasmonic photocatalytic systems based on the contact form. (a) Sole-metal form, (b) Embedded form ((b-1) HRTEM images of Au nanoparticles deposit onto the surface of ZnO nanorod. [76] *(b-2) SEM images of Au-Cu_2O Janus nanostructures* [55] *(b-3) TEM images of Au nanoparticles deposited on the surface of TiO_2* [77]*), (c) Encapsulation form ((c-1), Multiple-core @ single-shell, Au@SiO_2 yolk-shell structure.* [78] *(c-2) TEM images of Au (15 nm) @TiO_2 (10 nm) core-shell nanoparticles* [79]*, (c-3) well-dispersed Pd nanoparticles inside SiO_2 matrix* [80]*), and (d) Isolation form ((d-1) HRTEM images of CdS@SiO_2 deposited on Au@SiO_2 particles* [81]*, (d-2) SEM images of placing silica-coated Au particles at the bottom of thin Fe_2O_3 photoelectrode layer.* [82]*) SC stands for semiconductor, purple and back lines stand UV and visible light respectively.* [38]

For the embedded form (Figure 2.8 (b)), metal nanoparticles adhere to the surface of the semiconductor. Semiconductors with various morphologies were firstly synthesised. Then, the metal precursor is mixed with this pre-achieved or purchased semiconductor material, and reducing agents are added. [83] This results in the reduction of the metal precursor to metal nanoparticles on the semiconductors surface in a method called wet-impregnation. Compared to this method, the sol-immobilisation method affords greater control over nanoparticle properties. [84] [85] In this method, metal colloidal solution properties were controlled by adjusting synthesis conditions i.e. temperature, concentration of metal precursor and reducing agent, solvent, reaction time, etc. The tailored metal colloids are then sol-immobilised by adding the semiconductor support under vigorous stirring conditions. [86] Alternatively, the metal nanoparticles can be deposited onto the surface of semiconductor materials by a deposition-precipitation method. [76]

For the encapsulation form (Figure 2.8 (c)), the pre-achieved metal colloidal solution is mixed with the semiconductor precursor, with semiconductor then synthesised and embedding the metal nanoparticles inside to form a core-shell [87] [88], yolk-shell structure [78] or well embedded metal nanoparticles inside semiconductor matrix [80]. The metal nanoparticles are synthesised as core, followed by the surface modification with an insulation coating, and finally coated by the semiconductor material on the surface (Figure 2.8 (d)). [82] For the isolation form, an isolation cell is added to avoid direct electron transfer between metal and semiconductor particle. This system allows the study of influence of size of nanoantenna metal particles as well as the distance between metal and semiconductor on the photocatalytic properties. [81]

In practical production processes, designing and achieving the synthesis of the metal/semiconductor composite nanostructures is mainly conducted at the lab scale and is difficult to replicate on a large scale. Flow reactors offer a solution to this obstacle by providing alternatives routes to execute syntheses under highly controlled process conditions while providing options for large-scale production.

2.3 Flow chemistry and the application to nanoparticle synthesis

Flow chemistry is a process where fluids with the starting materials are continuously pumped through a reactor to produce a stream of product. [89] The solutions are injected into a milli/micro-reactor using a pump or series of pumps, which can either be semi-continuous, requiring refilling, or continuous, which can run indefinitely without the need for refilling. Mixers and unions are used to connect the reactor and enable the introduction of new reagents into the ongoing flow. [90] Compared with traditional batch reactor, micro chemical plants act as a bridge between chemical engineering science (micro area) and process systems engineering (macro area), refer to the Figure 2.9. [91]

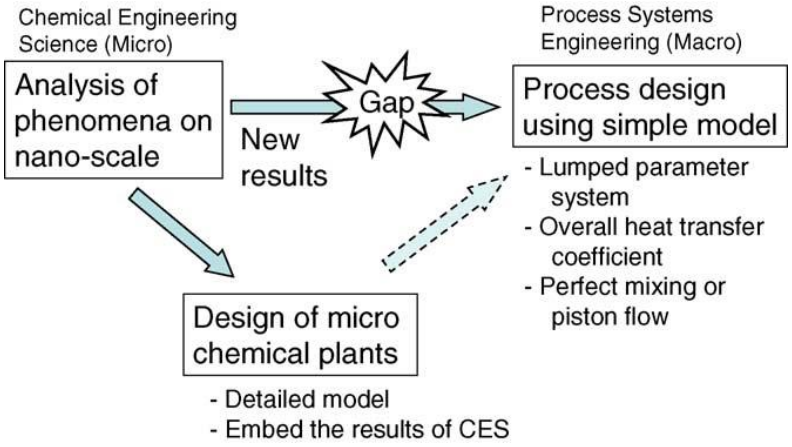

Figure 2.9 Bridge between the micro and macro engineering. [91]

Due to the small characteristic dimensions and the larger surface area to volume ratio, microreactors could provide better mixing and mass/heat transfer as compared to traditional batch reactors. [92] To enhance the mixing performance, the methods usually used involve applying external forces ('active micromixer') or adjusting the reactor inherent hydrodynamic structure ('passive micromixer'). [93] Passive microfluidic devices as compared to active ones, are much simpler and more flexible, because they do not use any external actuator to drive the fluids. Microreactors for nanocrystal synthesis can be classified into two broad categories: capillary- and chip-based systems. [9] Capillary tubings have been used to access small-scale flows within the simplest features since the initial stages. They offer simple and cheap approaches for conducting continuous flow experiments with well-understood hydrodynamics and also easy manipulation of operating parameters such as residence time. [94] Chips are typically fabricated from a plastic, glass or silicon substrate, using soft-lithography, wet etching or micromachining techniques to achieve the internal structure.

There are a variety of passive micromixers with different channel geometries, shown in Figure 2.10, such as 'split-and-recombine' (SAR), [95] lamination-based channel (parallel lamination, [96], [97] multi-lamellae, [97]) curved-channel, [98] obstacle-based pattern, [96] *etc*. These have been designed to enhance mixing by reducing the diffusion length, or stretching or folding the fluid interface by chaotic advection. In the case of SAR micromixers, the main channel is typically split into two sub-channels, leading to an increase in the interfacial area. Furthermore, when the fluid flows through the turns inside the structure, the imbalance between pressure force and centrifugal force induces secondary flow (i.e. Dean vortex), which can enhance the mixing performance dramatically. [95]

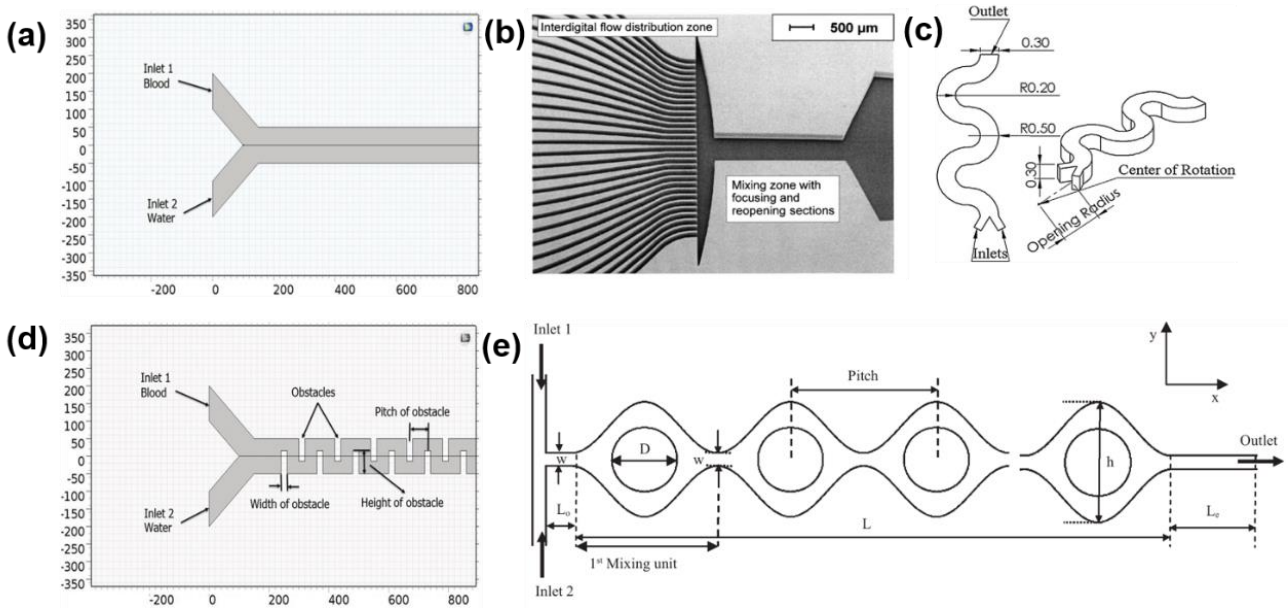

Figure 2.10 Schematic of different micromixer's design (a) Y-type mixer (b) the slit-shaped interdigital mixer (c) curved-channel mixer (d) obstacle-based mixer (e) convergent. [93]

In the research discussed in Chapter 3, the Corning Advanced-Flow^{TM} Reactor (Corning AFR) is used to synthesis Ag nanoparticles. This is a commercial continuous flow reactor comprised of a chain of identical cells with convergence-divergence configuration which could lead to potential enhancement of the mixing performance. Chapter 4 and Chapter 5 emphasise the microfluidic synthesis of semiconductor nanoparticles, specifically SnO_2, SnO_2@Au, and Cu_2O. The primary focus is on achieving a continuous synthesis process with enhanced control over the morphology of these nanoparticles, utilizing a microreactor. In these two chapters, a straightforward capillary microreactor has been employed to facilitate the synthesis process.

2.3.1 Mechanism of nanomaterials synthesis

A profound understanding of particle formation mechanism is essential for tuning their size and morphology. Nucleation and growth are generally used to describe the overall process of formation of solids from a liquid solution as two sequential events, and are also crucial for controlling precise structural characteristics of the final solid. Nucleation is the first step in which building units, *e.g.* atoms, ions, or molecules form a new thermodynamic structure (nuclei) at the atomic or molecular level. This is followed by growth, during which crystal units are incorporated onto the surface of the nuclei, which may also coalesce or aggregate, leading to an increase in size. [99]

Classical Nucleation Theory (CNT) [100] and Non-Classical Nucleation Theories (NCNT) [101] are integrated to elucidate the formation of a new thermodynamic solid nuclei from liquid solution. [102] Nucleation is categorized as homogeneous or heterogeneous based on the presence of foreign bodies. CNT, the most commonly applied mechanism, involves a single-step process wherein nuclei reach the critical size and act as templates for crystal growth. NCNT serve as complementary frameworks to address observed phenomena that do not align with CNT, such as intermediate stages in solution crystallisation. Two major mechanisms are outlined depending on the thermodynamic stability of the intermediates: a two-step nucleation [103] and a pre-nucleation clusters mechanism [104]. Regardless of the nucleation mechanism, critical controlling parameters include temperature, supersaturation, surface free energy, [105] and local solvent environment or ligands environment. [106]

Then following crystal growth has a crucial impact on the final crystal structure and product purity of nanomaterials. [107] Classical and non-classical crystal growth frameworks are combined to give the explanation on crystal growth. Trying to explain the crystal size enlargement can be attributed to layer-by-layer addition of monomers on the existing crystal surface [100] or the assembly of particles by oriented or non-oriented attachment or aggregation separately. [108] [109] [110] Regardless of the mechanism, the crystal growth process is influenced by the thermodynamic parameters, i.e. temperature, pressure, and supersaturation. [99] Therefore, in the synthesis process, homogeneous

reaction environment both in temperature and reactant concentration is really essential to synthesise nanoparticles with uniform properties.

2.3.2 Synthetic approaches for metal nanoparticles

Commonly there are two synthesis approaches in the fabrication of monometallic nanoparticles, i.e., bottom-up and top-down. [111] In the top-down synthesis method, NPs are synthesised by subdividing a bulk substrate. However, the most common methods used recently are bottom-up synthesis methods, such as hydrothermal decomposition, [5] sol-gel, [2] and chemical reduction method [24]. This is as these bottom-up approaches are versatile in designing and synthesising new materials.

Chemical reduction methods have been frequently used to synthesise metal nanomaterials, as they offer good control of the particle size and morphology by changing the type of reducing agent, reaction temperature, reaction time, and concentration of the solution. [112] The first step involves the reduction of metal salts into zerovalent metal atoms, a process that occurs within milliseconds to a few seconds. Then these atoms orient themselves into crystalline structures. The process of nuclei formation and growth is the most important step to control their size and uniformity of NPs. For the synthesis of nanoparticles, in order to achieve small and uniform particles, homogeneously high supersaturation levels and temperature gradient are necessary which are limited by mass and heat transport in the reactor. As nanotechnology moves from academic to actual large-scale manufacturing, there are still several challenges as the control exerted at the nanoscale tends to wane at the meso- and macroscales. [113]

Considering chemical reaction of nanoparticle synthesis is based on the underlying transport process and chemical kinetics, the synthesis process should be considered from both chemistry and engineering. Chemical engineering process contains four processes: momentum transfer, energy transfer, mass transfer and chemical reaction. During the synthesis process in the liquid solution, micro-mixing of reactants on the molecular level is the premise of the reaction process, which often influences the outcome of reactions.

Damköhler number (Da) is a dimensionless number used in chemical engineering to relate the chemical reaction timescale to the transport phenomena rate occurring in a system. [3]

$$Da = \frac{reaction\ rate}{mass\ transport\ rate} \tag{2-1}$$

- If the chemical reaction is very low, $Da < 0.01$, the intrinsic chemical kinetics governs the rate of reaction.

- If the reaction speed and the mixing speed are in the same order of magnitude, both of the mixing performance and intrinsic kinetics govern the rate of reaction.
- If the reaction is very fast or instantaneous, $Da > 100$, the micromixing speed governs the rate of reaction, the yield of production.

In some situations, when the reaction rate is significantly slower than mixing ($Da < 0.01$), the mixing performance has a negligible influence on the chemical reaction. Therefore, a microfluidic reactor, integrated within a small-scale unite, provides identical results to those obtained from a traditional batch reactor housed in a larger vessel or tank. [114] However, in the synthesis process of metal nanoparticles ($Da > 100$), the chemical reduction and nucleation reactions are finished within milliseconds. [115] Consequently, the influence of mixing inhomogeneity, along with associated spatial and temporal variations at the microscopic scale, becomes significant in determining particle size and particle size distribution (PSD). [116] [117] Therefore, the mixing step in the apparatus is a decisive step in the overall process.

In the traditional batch reactor, scaling up poses a challenge as increasing the reactor volume diminishes control over mixing performance, leading to non-uniform nanoparticle properties. The precise control of flow rate, residence time, temperature, concentration in the continuous flow system allows for precise control over size, shape and composition of the nanoparticles. [105] By obtaining optimised conditions for the desired product, it is also possible to achieve large scale production without compromising product quality, while also enhancing green chemistry metrics. [90]

Furthermore, transitioning batch processing into continuous flow allows for controlled synthesis with scalability, reduction of solvent waste and allows for a ‘plug and play’ system to attach inline reactors and real time analysis of the resulting product in an automatable way. [118] In response to the aforementioned challenges in the batch reactor, continuous flow techniques for metal nanoparticle synthesis show a large number of advantages shown in Table 2.2.

Table 2.2. Advantages and Disadvantages of Colloidal Nanoparticle Preparation Methods. [119]

Colloidal nanoparticle preparation method	Advantages	Disadvantages
Colloidal batch methods	Excellent control over particle size, distribution, and morphologies in small scale	Difficult to scale up because of heat and mass transport limitations Safety issues with batch scaling Batch-to-batch variability
Flow fabrication methods	Automatable Efficient heat and mass transfer Superior reproducibility Reduced environmental health and safety risks Higher yields, lower by-products Excellent control over particle size, distribution, morphologies	Industrial scale out has not been demonstrated Not widely adopted Fouling

2.3.3 What's next for continuous microfluidic synthesis of nanoparticles

Although microfluidic synthesis shows undeniable advantages in producing uniform and consistent particles with the desired size and distribution, several future trends for commercial production are outlined below.

The first major problem is the potential of reactor fouling. [120] Fouling is the undesirable buildup of solid materials sticking to the channel walls that results in changes in flow velocity, mixing performance, permeability, heat flux and may lead to complete clogging of the channel at worst. Moreover, the cleaning strategies before operation being resumed is energy- and time-consuming. Addressing fouling is a challenging task because every application of microfluidic devices will encounter this complex issue. Resolving this problem is crucial for achieving continuous synthesis with controlled nanoparticle properties.

Secondly, there has also been a trend towards the use of automated continuous flow systems and algorithms for the self-optimisation of the fabrication of nanomaterials. This trend contributes to optimizing the shapes of materials for various applications which results in improved production speed, reduced waste, and increased quality control. [118] Additionally, machine learning applications extend to predictive maintenance, enabling manufacturers to anticipate and prevent equipment failures before they occur, which can further improve the overall efficiency of continuous flow processing. [121]

Thirdly, achieving the industry-required throughput can be challenging with low volume throughput in a single-channel of microfluidic reactor. A possible solution is to increase the total production yield by numbering-up, each unit microreactor in parallel working simultaneously with shared inputs. [122] However, the complexity arises in simultaneously controlling flows and temperatures in hundreds of microreactors in parallel, making the numbering-up of reaction units challenging for large-scale production. Although some successful cases have been reported using micro- and milli-reactions for nanomaterials production [123] [124], numbering up home-made micro-channel/tubular reactors with non-standardised tubing, connectors, adaptors, *etc.* and non-integrated heating/cooling elements remains a challenge. [10] A notable example of a commercially successful continuous flow reactor is the Advanced-Flow^{TM} Reactor (AFR) developed by Corning, shown in Figure 2.11. This flow reactor is specially designed to enable the conversion from traditional batch to continuous flow chemical processing form lab to industrial-scale production. This system allows for easy production capacity increase by switching to larger modules with limited need for further optimisation, facilitating numbering-up with appropriate fluid distribution. [125]

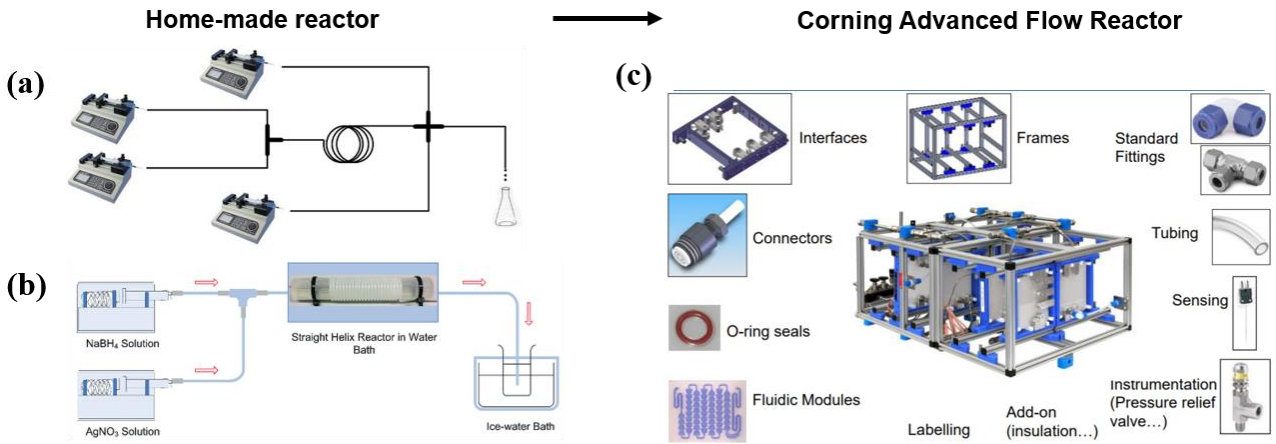

Figure 2.11 Examples schematics of the experimental setup of home-made reactors (a) coil microreactor for synthesis Ag-ZnO NPs [126]*, (b) helical microreactor for synthesising Ag NPs* [115]*, and (c) Corning AFR setup, modules and components.*

2.3.3.1 Scaling-up process using the Corning AFR

A series of Corning reactors are designed and integrated for a smooth and seamless scale-up transition from academia and lab feasibility (Corning NebulaTM Education kits, Lab Reactor System 2 & Low-Flow (Figure 2.12 (b)) to process development (G1 (Figure 2.12 (c)), G1 SiC, G1 Photo) to multi-ton industrial production of chemicals (G3 (Figure 2.12 (d)), G3 Photo, G4 (Figure 2.12 (e)) & G5). All the series reactor units have the same HEART designed cell, as shown in Figure 2.12 (a). Although the channel size (hydraulic diameter around 1 mm) is greater than a typical reactor, the split-and-

recombine heat-shaped cell is able to provide efficient mixing for both homogeneous and heterogeneous systems as well as superior heat and mass transfer. [127] [128]

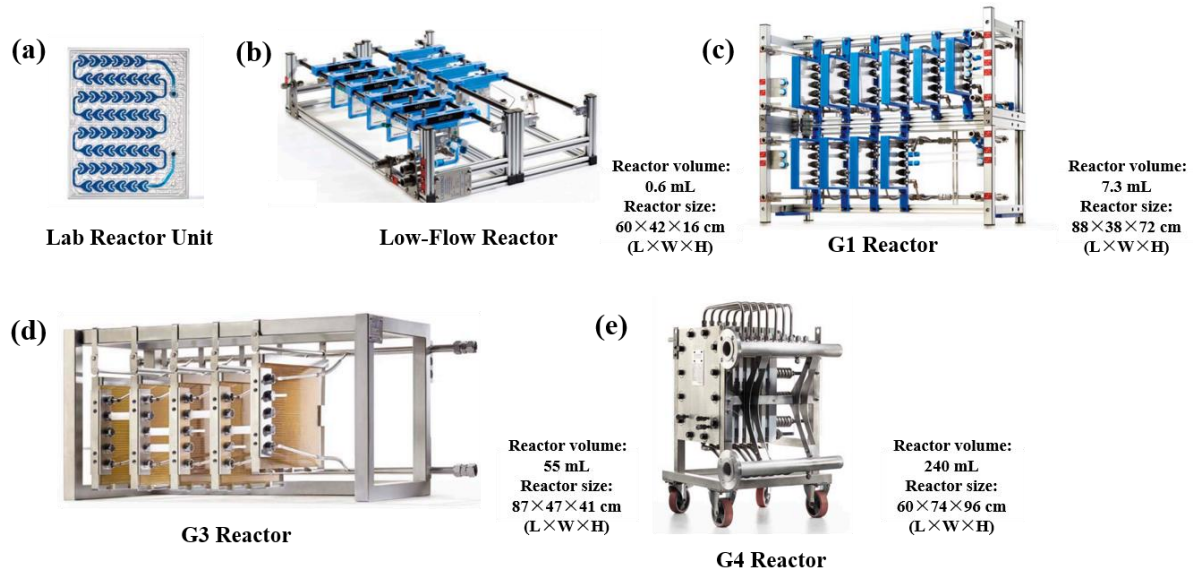

Figure 2.12 Images of Corning (a) Lab Reactor Unit, and set-up of (b) Low-Flow Reactor, (c) G1 Reactor, (d) G3 Reactor, (e) G4 Reactor.

This section provides a review of scale-up synthesis processing. Two methods are employed to increase the product yields in the Corning reactor. The first involves a gradual scale up, with volume change from the 0.6 mL of Low-Flow Reactor to the 240 mL of G4 Reactor. This facilitates a seamless transition between different reactor types due to the similar mixing performance and heat/mass behaviour, achieved by using the heart-shaped static mixing elements. [13] [129] Another method is by numbering-up of each unit reactor in parallel. [130] [131]

Celine *et al.* [132] reported multiphase hydrogenation using heterogeneous catalyst was conducted through a Corning AFR. It showed the high potential for an industrially scale by producing 200 tons / year using almost 20 reactors in parallel. The Corning reactor has also demonstrated effectiveness in continuous synthesis of some organic materials with high yields. Zhang *et al*. [13] scale up a phase-transfer catalyst hypochlorite oxidation reaction from microfluidic spiral microreactor to mesoscale system (i.e. Corning Low Flow Reactor and Advanced Flow Reactor). The production rate increased up to 700 times in the scaling process without sacrificing mass and heat transport performance. Monbaliu *et al.* [15] reported a robust, continuous and safe industrial-scale process i.e. 12,000 t/y for producing the biodiesel additive STBE.

The previous studies using Corning AFR mostly focus on the large-scale production of organic molecules, with only a few papers reported on nanoparticle synthesis. Bianchi *et al.* [129] reported a unique, robust and scalable photochemical flow process for the production of spherical gold NPs on a

water-soluble acylphosphinate photoinitiator exposed to UV irradiation. This protocol reports an effective solution for avoiding gold fouling, hence providing a reliable and robust protocol for long-term operation. The preliminary optimization was undertaken in commercial Corning G3 flow reactor, and the conditions were successfully transported to pilot and lab scale flow reactors, shown in Figure 2.13.

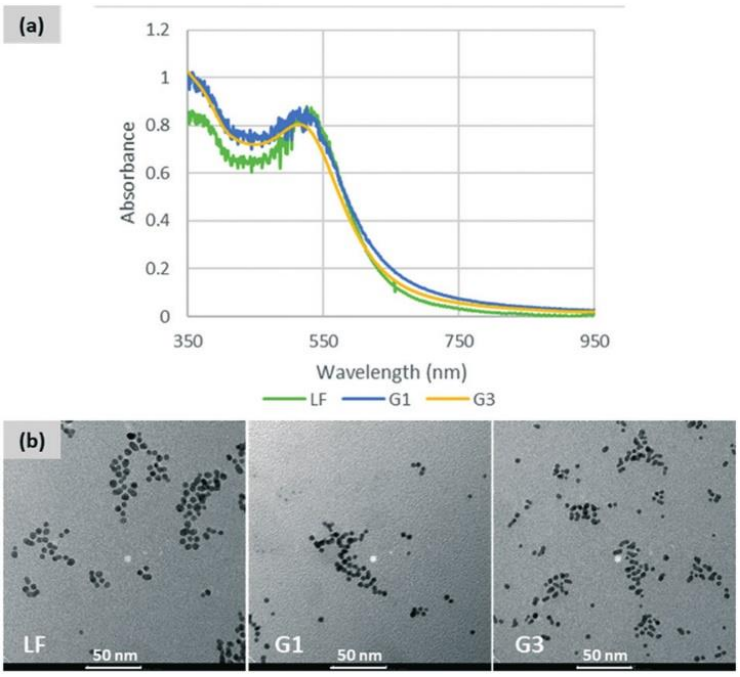

Figure 2.13 Comparison between the Au NPs produced with the Lab photo (LF), G1 photo and G3 photo reactors. (a) UV spectra; (b) TEM images. [129]

However, the influence of mixing performance at various operating conditions on nanoparticle synthesis has never been studied. Hence in the study detailed in Chapter 3, the performance of a Corning AFR on the continuous synthesis of metal NPs is evaluated, taking silver as a case, to build up a synthetic model method for the robust and repeatable synthesis method of metal nanoparticles.

2.4 Continuous synthesis of semiconductor nanoparticles

2.4.1 SnO_2 NPs

Tin (VI) oxide, also known as cassiterite, is amphoteric material. The crystal structure type of SnO_2 is tetragonal with dimensions of the unit cell: $a=b=0.47374$ nm, $c=0.31864$ nm and $\alpha=\beta=\gamma=90^o$. In one unit cell, the tin ion is surrounded by 6 oxygen ions and each oxygen is bordered by 3 tin ions, and its space group is *P42/mnm*. [133], shown in Figure 2.14. Since M.S. Wrighton used a Sb-doped SnO_2 electrode to produce oxygen under UV light in 1976, SnO_2 has successfully aroused researchers' interests. [134] As an important n-type semiconductor with a direct wide band gap (3.60 eV at 300 K),

SnO_2 has been widely used in various photocatalytic reactions due to its long-term stability, high oxidation potential and chemical inertness, non-toxicity, etc. [135]

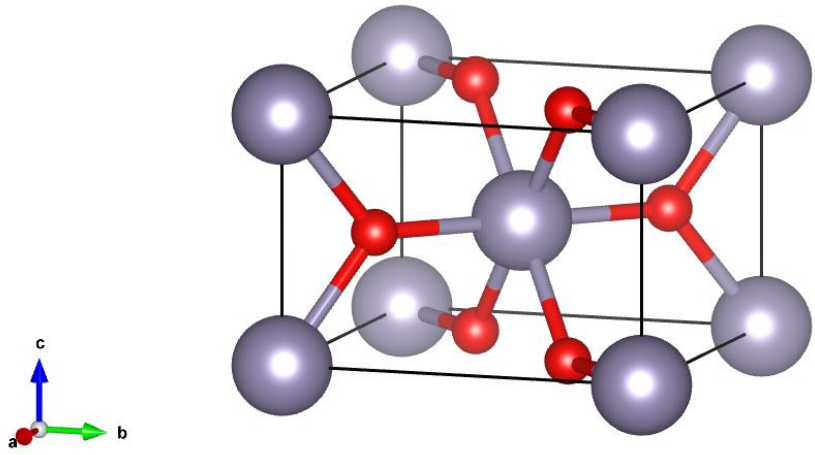

Figure 2.14 The crystal structure of SnO_2 with oxygen (red ball) and tin (grey ball), generated from crystallography open database using VESTA software. [136]

2.4.1.1 The synthesis method of SnO_2 and plasmonic metal SnO_2 nanostructure

Usually, traditional synthesis methods of tin dioxide such as hydro-/solvo-thermal, [137] [138] chemical precipitation, [139] sol-gel [140] *etc.* are commonly used. However, these are not ideal for large-scale commercialisation because they typically require complex equipment, the use of toxic solvents and time-consuming high-temperature or high-pressure processes. [141] Inspired by the work of Weihong Lai *et al.* [141], which showed that the one- to three-dimensional morphology of inorganic materials (i.e. BaF_2, $Mg(OH)_2$, $Co(OH)_2$, $Cu(OH)_2$, $CaCO_3$ etc.) can be adjusted by the electrolytic dissociation of the reactants and the supersaturation of the solutions even at room temperature. In contrast to traditional hydro-/solvo-thermal or sol-gel methods, which typically require high temperatures or pressures, we aim to synthesise SnO2 nanoparticles at low temperature and low pressure. Herein, we achieved SnO_2 nanoparticles by adjusting the supersaturation and the polarity of solution using a microreactor. This is described in Chapter 4.

Synthesis methods for metal/SnO_2 hybrid composites focus on small scale batches nowadays, and they can be classified into four types, shown in Figure 2.15.

(i) The sol-immobilisation method was used to synthesise mesoporous SnO_2 coating on the surface of metal nanoparticles, forming either core-shell or yolk-shell structures. Sodium stannate trihydrate ($Na_2SnO_3 \cdot 3H_2O$) was introduced to the metal colloidal solution (pH=10.5-11, adjusted by NaOH), followed by stirring and heating for several hours. An alternative synthesis method was applied using

a microwave hydrothermal method instead of conventional hydrothermal method to increase the crystallinity. [72] [137] [138][142] [143] [144]

(ii) The sol-immobilisation method was used to fabricate porous non-centrosymmetric Au-SnO_2 hybrid nanostructures. Potassium stannate trihydrate ($K_2SnO_3 \cdot 3H_2O$) was mixed with urea, then the resulting mixture was added to a pre-prepared Au colloid and ethylene glycol. The mixture was then transferred into an autoclave, at 200 ^oC, for periods of time including 10 min, 1 h, 6 h, 12 h. When tested as a photocatalyst, it was found that the degradation rate of RhB increased three times of when using Au/SnO_2 as compared with pristine SnO_2 under visible light. [50]

(iii) The impregnation method was used to fabricate composite materials wherein metal NPs were deposited on the surface of SnO_2. Initially, SnO_2 NPs with different morphologies were hydrothermally synthesised by using $Na_2SnO_3 \cdot 3H_2O$ or $SnCl_4$ as precursors. Then surface-functionalised SnO_2 was mixed with the metal precursor, leading to the formation of metal NPs coated on the SnO_2 surface. [145] [146] [147] [148]

(iv) The one-pot co-precipitation synthesis method was employed to synthesise metal NPs inserted into the SnO_2 matrix. The metal and tin precursors were mixed simultaneously, and the solution was adjusted to have an alkaline property. The mixed solution was heated at high temperature to ensure the simultaneous formation of SnO_2 and metal NPs. [149] [150] [151] [152] [153]

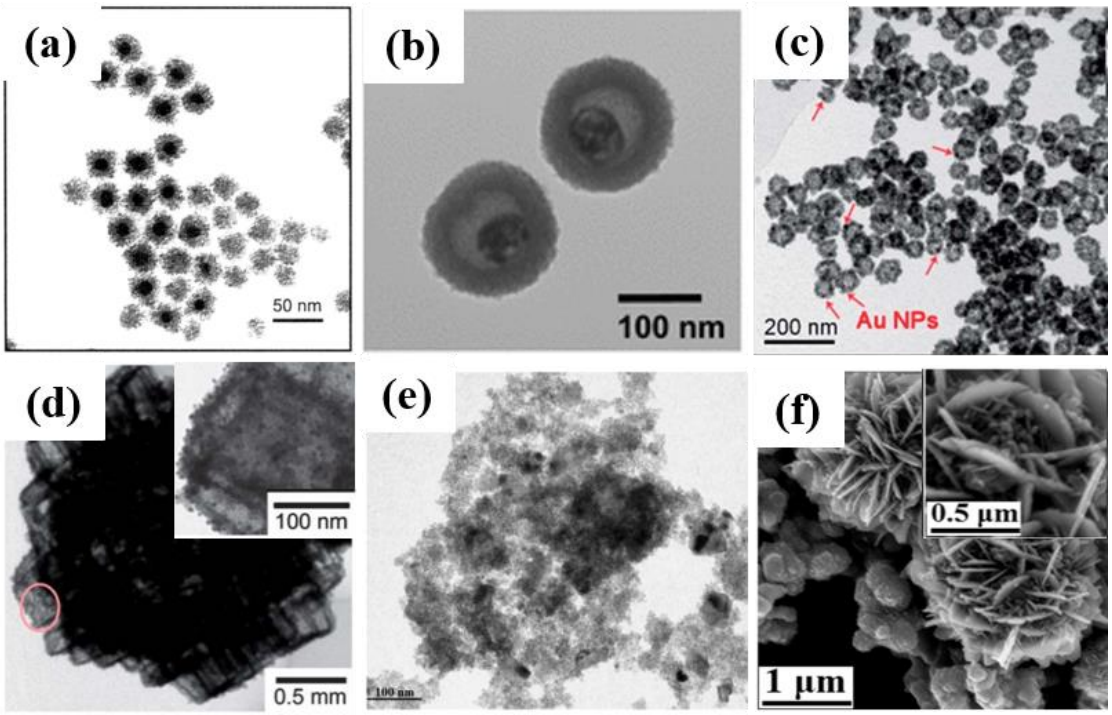

Figure 2.15 TEM images of (a) Au (15 nm) @ SnO_2 (10 nm) core-shell structure, [137] *(b) Au-Ag nanoshell @ SnO_2 Yolk-shell structure,* [144] *(c) Au-SnO_2 non-centrosymmetric hybrid structure,* [50] *(d) Au NPs loaded on dendritic assemblies of SnO_2 hollow hexapods,* [146] *(e) Ag NPs inserted inside the SnO_2 matrix,* [151] *and (f) SEM images of 10 % atomic ratio Ag inserted inside the SnO_2 flower like heterostructures* [152].

However, these semi-continuous synthesis methods for the metal NPs@SnO_2 hybrid nanostructure pose challenges in scaling-up process. To address this issue and enable high-volume production, an investigate into an easy method for the continuous synthesis of Au@SnO_2 in micro-capillary reactor is described in Chapter 5. First the SnO_2 was synthesised in the microreactor, then the Au NPs were added. In order to identify the most effective structure with superior photocatalytic properties, three different methods were explored to incorporate Au NPs with SnO_2: (1) Au NPs coated on the SnO_2 matrixes, (2) Au NPs surrounded by SnO_2 matrixes, and (3) Au NPs embedded with SnO_2 matrixes.

2.4.2 Cu_2O NP

Cu_2O crystallises in a face cubic centered crystal structure ($fcc, Pn\bar{3}m$), with lattice constant a=b=c=4.217 Å, α=β=γ=90°. In the cubic lattice, oxygen atoms are surrounded by tetrahedrally coordinated Cu(I) atoms, shown in Figure 2.16. The number of copper atoms in the unit cell is twice that of the oxygen atoms. [154] Cu_2O is a typical p-type semiconductor with a narrow band gap of 2.17 eV (corresponding to a wavelength of 590 nm for excitation by light), and is one of the most intensively investigated binary transition metal oxides. Besides the well-known merits including low-cost, nontoxicity, abundance and easy synthesis, as compared to other semiconductors, Cu_2O has further advantages: (i) the narrow band gap gives a high optical absorption coefficient, (ii) the corresponding theoretical photocurrent is up to -14.7 mA/cm^2 [155] and a higher carrier mobility with 30-130 cm^2/Vs [156], and (iii) excitons in Cu_2O have a long-lived lifetime of ~10 microseconds. [157]

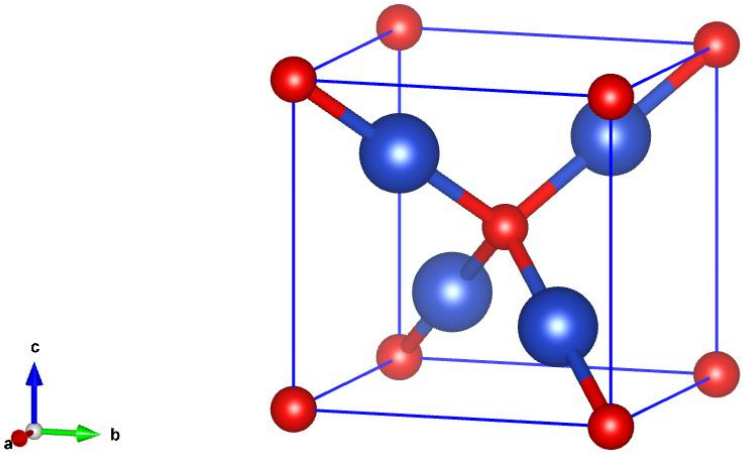

Figure 2.16 The crystal structure of Cu_2O with oxygen (red ball) and copper (blue ball), generated from crystallography open database using VESTA software. [158]

The tailored architecture of Cu_2O crystals has also attracted great research interest due to morphology-dependent physicochemical applications in catalysis, sensing, surface-enhanced Raman scattering, chemical template, solar-to-chemical energy conversion *etc*. [159] Cu_2O micro-/nano-crystals with various architectures have been achieved such as hollow structures, [159] nanowires, [160] thin films, [161] nanoshells, [162] *etc.* Among them, with the face-centred cubic crystal structure, the morphology of Cu_2O can also be controlled by the crystal facets. Polyhedral Cu_2O architectures with low-index facets (including {100}, {111}, and {110}) and high-index facets (such as {211}, {311}, {522}, {332}, {544} etc.) has been achieved by modifying the growth rate ratio (R) between the <100> and <111> directions. [163] [164] Some geometrical configurations of the Cu=O exposed with various low- and high-index facets are shown in Figure 2.17.

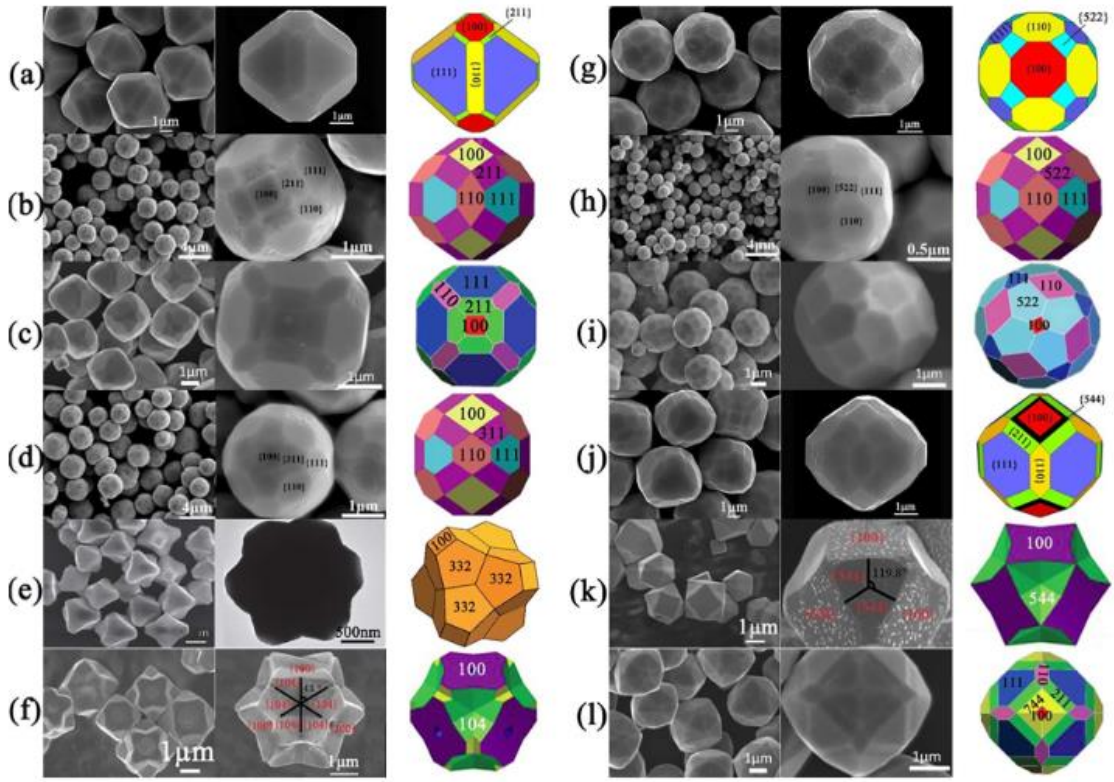

Figure 2.17 Typical SEM, TEM images along with the corresponding simulated geometrical configuration of the Cu_2O crystals partially exposed with different low- and high-index facets. The detailed indexes for these facets are displayed in the simulated polyhedral structures. [163]

2.4.2.1 Recent studies on the synthesis method of Cu_2O NPs

The photocatalytic properties of polyhedon Cu_2O are influenced by various surface atomic structures, which alter band structures and transport properties of donors and acceptors. A key focus of future research is designing crystal structures to enhance photocatalytic property. While successful lab-scale synthesis of plane-controlled Cu_2O nanocrystals has been achieved using techniques such as irradiation [165], hydrothermal and solvothermal methods [166] [167], electrodeposition [168],

sputtering [169] and wet chemical reduction [170] [156] *etc.* challenges remain in achieving reproducibility, high yields, easy scale-up, and controllability. In chemical engineering, synthesising desired particles with a controllable structure on a larger scale is crucial for practical production.

Currently, the "heating-up" method provides an industrially viable route for synthesising cuprous oxide nanoparticles without crystal control. This method involves the thermal decomposition of copper complexes, leading to the formation of copper spherical nanoparticles, which are then further oxidized. [171] The solution-phase reduction reaction is a commonly employed “bottom-up” approach for tailoring the nucleation and growth processes of Cu_2O crystals. This method shows great potential for the industrial scale-up in microfluidic systems and also allows the precise control over the morphology, particle size, and exposure facets under proper experimental conditions.[163] These conditions include the concentration and type of reducing agent [172] [173], the presence of surfactants [174], type of copper sources [175], synthesis time, reaction temperature, and pH value *etc*. [176]

In recent decades, significant advancements in the lab-scale have been made in tailoring the architectures of Cu_2O micro-/ nanocrystals, e.g. hollow and porous structure, 0-D nanodots, 1-D nanowires, 2-D nanoplates, 3-D facet-designed polyhedral by using the solution-phase method. [163] Sui *et al.* [177] controlled the shape evolution of Cu_2O crystals from cubes, truncated octahedra, octahedra, nanospheres, and star-shaped by delicately manipulating the polyvinyl pyrrolidone (PVP) concentration, reaction time, and reaction temperature. Huang *et al.* [178] synthesized a novel series of Cu_2O nanocrystals with a systematic shape evolution form cubic to truncated octahedral and rhombic dodecahedral structures by simply adjusting the amount of reducing agent $NH_2OH.HCl$. Leng *et al.* [179], [180] delicate controlled over the shapes with high-index facets from the 12-facet, to 18-facet, 50-facet through tuning the concentration of OH^- and the volume ratio of polar organic solvent to water. To date, only a limited number of papers have reported on the synthesis of Cu_2O using microfluidic system, and even no one focused on the precise control of its morphology.

Wei *et al.* [181] firstly reported to synthesise Cu_2O nanofluids in tubular microreactor, shown in Figure 2.18 (a). Cu_2O NPs were produced in two steps at 40^{o}C. To enhance the nanofluid stability and prevent the particle aggregation, polyvinyl pyrrolidone (PVP) was premixed with cupric-sulfate ($CuSO_4$) solution. In the first step, $CuSO_4$ with PVP solution and NaOH (sodium hydrate) were pumped through inlet 1 and 2 to form cupric hydroxide ($Cu(OH)_2$). Under heating, $Cu(OH)_2$ quickly decomposed into cupric oxide. Then hydrazine-hydrate ($N_2H_4{\cdot}H_2O$) was injected from inlet 3 to reduce CuO into Cu_2O. It shows that the morphology of particles changed from a spherical shape to polyhedral, starfishlike, and flowerlike by varying the $CuSO_4$ concentration and fluid flow rates.

Al-Antaki *et al.* [182] reported a pulsed laser ablation (PLA) method under continuous flow conditions to synthesis copper (I) and copper (II) oxide nanoparticles using water as the solvent,

shown in Figure 2.18 (b). This new method paves a new simple and high-yield way to synthesis metal oxide NPs with avoiding the use of harsh chemicals. Firstly, a plume of copper was formed after irradiation of a copper rod, following reacts with oxygen in the air to form the Cu_2O NPs. Under continuous flow, water with Cu_2O NPs dispersion was delivered via a jet to the base of the tube. The dispersion of the Cu_2O NPs from the continuous flow process could be produced from CuO NPs by mild heating in an oven at 50 ^oC for 10 h. To explore the possible application for scaling up, they prepared 200 mg Cu_2O NPs over 12 h as well as 200 mg CuO NPs at 50 ^oC. For this method, selectively forming Cu_2O NPs in water in large scale is challenging, as long ablation times mainly result in the formation of larger particles.

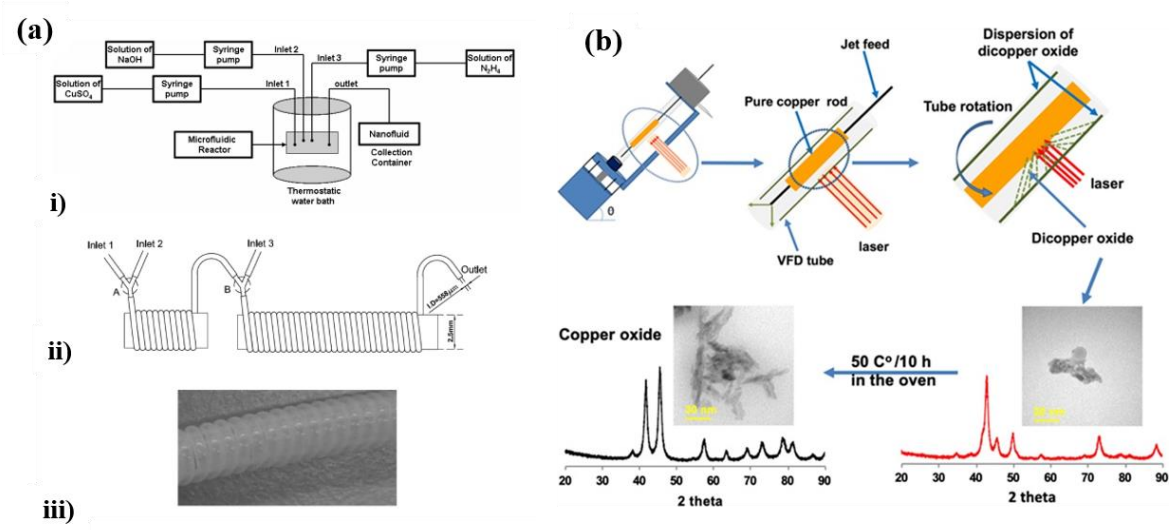

Figure 2.18 (a) Microfluidic one-step chemical solution method for Cu_2O nanofluids synthesis: i) test setup, ii) microfluidic reactor, and iii) PTFE microbore tubing coil, [181] *(b) a vortex fluidic device to synthesis Cu_2O NPs under continuous oxide* [183].

The limited literature on microfluidic synthesis of Cu_2O can be attributed to the fact that the understanding of the underlying mechanisms governing the nucleation and growth processes of Cu_2O nanoparticles with various morphologies is still in its infancy. Furthermore, in-depth understanding of the influence of mass and heat transfer on the various cuprous structure is needed for further investigation. These present obstacles when transitioning from batch processes to microfluidic systems, as it is challenging to achieve precise control over the shapes and sizes of the nanoparticles. While considerable progress has undoubtedly been achieved in the empirical stage of preparing cuprous oxide crystalline nanospheres in the last decades, a combination of empirical and theoretical approaches is needed to advance the field further. [171] In our research, described in Chapter 5, we optimised the continuous synthesis process for Cu_2O nanocrystals with a controlled polyhedral structure using a lab-made capillary reactor. The influences of mixing performance inside the microreactor and solution concentration were systematically investigated to explore their effect in morphology formation as well as size distribution. This simple continuous method for the controllable

evolution of polyhedral Cu_2O opens up new possibilities for the large-scale production of other semiconductor nanomaterial with different facets in a reproducible manner.

Chapter 3. Continuous synthesis of Ag nanoparticles in an advanced-flow reactor

3.1 Introduction

Despite enormous advancements in the synthesis and application of nanomaterials, the key to their commercialisation still lies in the scalable production of nanomaterials. [113] Traditional protocols are typically developed based upon batch processes, which can be easily optimized to yield high-quality products at lab scale. However, meeting the requirements for large scale production becomes challenging due to batch-to-batch variability, and the level of control on the nano- and microscale tends to wane when scaling up to the meso- and macroscale. [105] Continuous flow offers a potential solution to overcome the scale-up challenges attributed to its small characteristic dimensions and a larger surface area-to-volume ratio, which could provide better mixing and mass/heat transfer compared to traditional batch reactors. [92] Moreover, the throughput of these reactors can be increased by numbering up. [122] Despite some successful cases have been reported in the lab using micro- and milli-reactions for nanomaterials production [123] [124], scaling up home-made micro-channel/tubular reactors with non-standardised tubing, connectors, adaptors, *etc.* and non-integrated heating/cooling elements remains a challenge. [10] A notable example of a commercially successful continuous flow reactor is the Advanced-Flow™ Reactor (AFR) developed by Corning. This flow reactor is specially designed to facilitate the transition from traditional batch to continuous flow chemical processing form lab to industrial-scale production. [125] They have been utilised for synthesising both homogeneous and heterogeneous organic molecules on a large scale. However, there is limited research reporting the use in nanomaterials production, particularly for metal NPs. [129] [132]

This chapter evaluated the performance of a Corning® Advanced-Flow™ Reactor (AFR, Lab Reactor Module) for nanomaterials production in a single-phase flow, taking Ag NPs as a case study, to understand the effects of multiscale mixing behaviours on nanoparticle synthesis. The work detailed in this chapter has been published in 'Mixing performance and continuous production of nanomaterials in an advanced-flow reactor'.[184]

3.2 Experiments and methods

3.2.1 Materials

Silver nitrate ($AgNO_3$, Acros Organics), trisodium citrate dihydrate ($C_6H_5Na_3O_7 \cdot 2H_2O$, ≥99 wt.%, Sigma Aldrich), sodium borohydride solution ($NaBH_4$, 12 wt.% in 14 M NaOH, Sigma Aldrich), methylene blue (MB, $C_{16}H_{18}ClN_3S \cdot 3H_2O$, 1% extinction, Fisher Bioreagents), potassium iodide (KI, 99

wt.%, Alfa Aesar), potassium iodate (KIO_3, 99.5 wt.%, Acros Organics), iodine (I_2, >99 wt.%, Alfa Aesar), orthoboric acid (H_3BO_3, >99.8 wt.%, BDH Laboratory Supplies), sodium hydroxide (NaOH, >97.5%, Scientific Laboratory Supplies), sulfuric acid (H_2SO_4, 95-98 wt.%, Honeywell Fluka), and bovine serum albumin (BSA, Sigma Aldrich) were used as received without any further treatment. Deionised (DI) water (resistivity of 18.2 MΩ·cm) purified with Milli-Q ultra-pure water system was used in all experiments.

3.2.2 Corning AFR

Figure 3.1 shows the structure of the Corning AFR (Lab Reactor module, made up of glass). The AFR consists of three highly engineered fluidic layers, i.e., a reaction layer sandwiched between two heat exchange layers (Figure 3.1 (a)). The two heat exchange layers have the same inlet and outlet, and the fluid in these two layers follows the dashed-line walls inside (Figure 3.1 (b)). The reaction layer is composed of a consecutive series of heart-shaped cells with the same geometry (internal volume of 2.7 mL, 18 rows and 197 cells in total, Figure 3.1 (b)). Each cell contains a central U-shaped structure serving as an obstacle which forces the fluid to split and recombine, along with the change of the flow direction (Figure 3.1 (c)). The split and recombine (SAR) principle is a common mechanism employed in static mixers, enhancing mixing even at low Reynolds number by generating multiple fluid layers. [185]

The cross-section of the channel varies continuously along the flow direction, causing a position-dependent velocity profile. For the reaction layer, the AFR has two inlets (inlet 1 and 2 are marked in blue and yellow, respectively, in Figure 3.1 (b)) and one outlet (marked in green in Figure 3.1 (b)). The fluid that enters through inlet 1 is split into two streams (S1 and S3, volumetric flow rate Q_{inlet1}) before combining with the fluid from inlet 2 (S2, volumetric flow rate Q_{inlet2}) in the jet zone, and going into the first cell (Figure 3.1 (c)). The total volumetric flow rate (Q_{total}) and flow rate ratio (R) can be represented as follows:

$$Q_{S1} = Q_{S3} = 0.5Q_{inlet1} \tag{3-1}$$

$$Q_{total} = Q_{inlet1} + Q_{inlet2} = (Q_{S1} + Q_{S3}) + Q_{S2} \tag{3-2}$$

$$R = Q_{inlet1} / Q_{inlet2} = 2Q_{S1}/Q_{S2} = 2Q_{S3}/Q_{S2} \tag{3-3}$$

The designed total flow rates for the reaction layer range from 2 to 10 mL/min, and the operation temperature and pressure ranges are -40 to 200 °C and up to 18 bar, respectively.

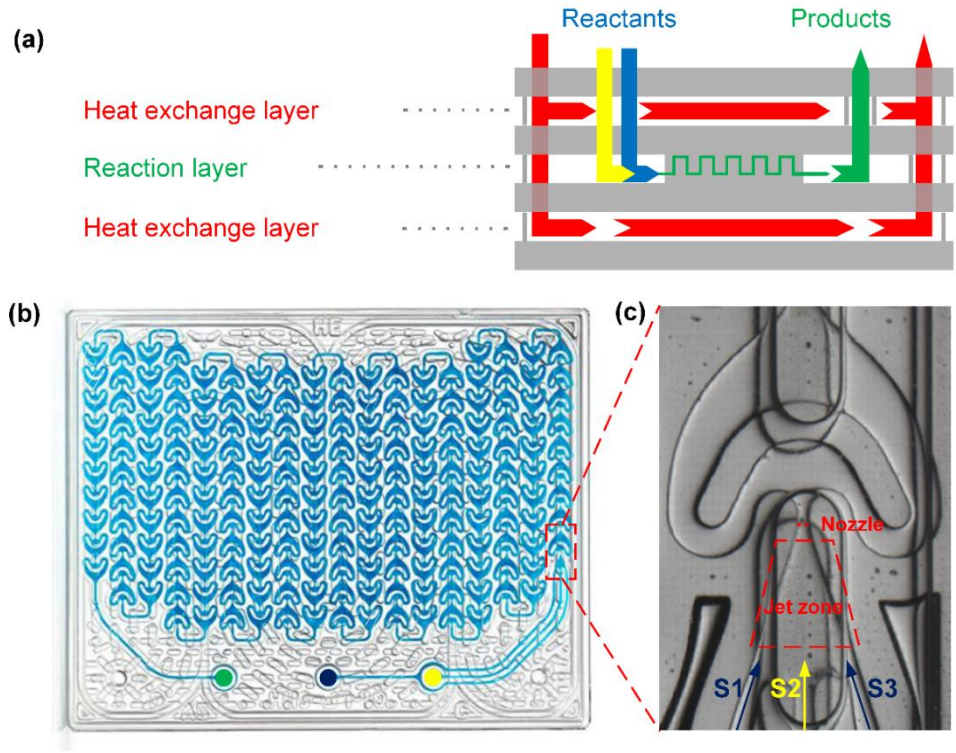

Figure 3.1 (a) Cross-sectional view of the Corning AFR Lab Reactor module showing the two heat exchange layers and the reaction layer; (b) Top view of the Corning AFR Lab Reactor module. The inlets 1 and 2 are marked in dark blue and yellow, respectively and the outlet is in green; (c) Enlarged image of top view of the Corning AFR Lab Reactor module. Streams 1 (S1) and 3 (S3) from inlet 1 mix with stream 2 (S2) from inlet 2 in the jet zone.

3.2.3 Optical visualisation

As the Corning AFR is manufactured with transparent glass, the flow pattern and mixing status in the unit cell can be evaluated by a dye dilution-based characterisation method. The schematic diagram setup is shown in Figure 3.2 (a). To visualize and analyse mixing efficiency, an aqueous MB solution and DI water were injected into the reaction layer using two syringe pumps (Chemyx, Fusion 100) as the two inlet fluids. It can be assumed that the dye solution has the identical density and dynamic viscosity as water. [185] The mixing phenomena of the two liquids were recorded by a CCD camera (15 frames per second) mounted on a stereo microscope (Olympus, SZX16) at room temperature (20-22 ˚C). AFR was illuminated by a LED light source (Olympus, SZX2-ILLT) integrated with the microscope. The resolution of the record images was 2448×2048 pixels with 0.0087 mm/pixel. In this experiment, the reactor was positioned under the lens of the camera horizontally, ignoring the effect of gravity.

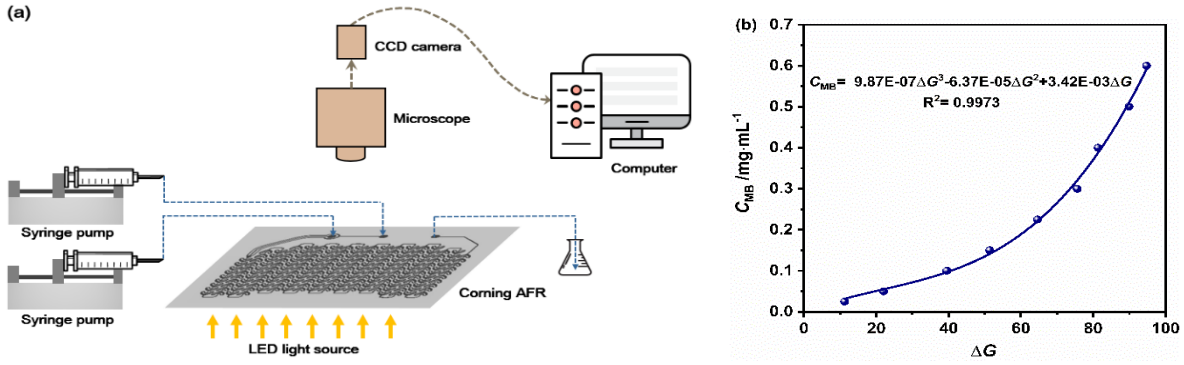

Figure 3.2 (a) Experimental setup for optical visualisation of the AFR using aqueous MB solution and DI water as the working fluids; (b) Relationship between the grey difference and the concentration of MB.

To quantify the mixing performance, calibration solutions with different MB solution concentration levels were prepared (0.025, 0.05, 0.10, 0.15, 0.225, 0.30, 0.40, 0.50 and 0.60 mg/mL). The images were captured when the whole system appeared stable during the process of the solution being pumped through the reactor. Image processing was done using FIJI (a distribution of ImageJ software) with the approach used shown in Figure 3.3.

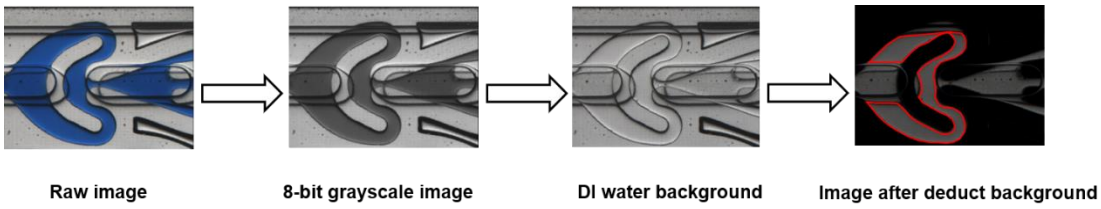

Figure 3.3 Schematic of the procedure for generation of the grey value with three steps. Step 1: the captured raw images convert into 8-bit grayscale image, Step 2: the calibration images are calculated by subtracting the DI water background image, and Step 3: then the grey value was obtained in the region of interest.

The image analysis approach compromised three steps:

(1) The captured raw images were first converted into 8-bit grayscale images, since it is more effective to build the relationship between the combination of red, green and blue channels rather than each colour channel with concentration. [186]

(2) The grayscale value for calibration image was calculated by subtracting the DI water background image, in order to eliminate the bias level set by the camera manufacture and light reflection.

(3) The relationship between the grey value (ΔG) obtained in the region of interest (ROI, marked red in Figure 3.3) and the concentration of MB solution (C_{MB}) was shown in Figure 3.2 (b).

Based on the ΔG-C_{MB} correlation, the concentration distribution profile in the region of interest (ROI) for each mixing experiment could be determined. The degree of mixing is widely quantified by the so-called mixing index (MI), which is an indicator of the quality of the mixing process. [187] Several equations are usually used to calculate MI:

$$\mathrm{MI} = 1 - \frac{\sigma}{\bar{\mathrm{C}}} \tag{3-4}$$

$$\mathrm{MI} = 1 - \frac{\sigma}{\sigma_{\max}} \tag{3-5}$$

$$\sigma = \sqrt{\frac{1}{\mathrm{N}} \times \sum_{\mathrm{i}=1}^{\mathrm{N}} (\mathrm{C_i} - \bar{\mathrm{C}})^2} \tag{3-6}$$

where σ represents the standard deviation of the species concentration in the cross-sectional plane analysed, and *N* is the total number of pixels in the cross-sectional plane analysed. C_i and $\bar{C}$ are the species concentration at the i^{th} pixel and the species concentration for complete mixing, respectively. $\sigma_{\max}$ is the maximum standard deviation of the species concentration, and corresponds to zero mixing.

The mixing index is calculated according to the Equation 3-4, when the flow rate ratio of the two fluids equals to 1. [93] In this case, the mixing index is within the range of 0-1, with 0 indicating total segregation and 1 denoting complete mixing. However, when the flow rate ratio is not 1, the mixing index for the total segregation is not equal to 0, and varies with the flow rate ratio. Table 3.1 provides examples of various flow rate ratios between MB and water along with their final mixing index by using Equation 3-4 and Equation 3-5. Hence, it is difficult to compare the degree of mixing at different flow rate ratios by using Equation 3-4. When studying the effect of the flow rate ratio, Equation 3-5 is always employed, in which $\sigma_{\max}$ is introduced to normalise σ, and the value of $\sigma_{\max}$ is dependent on the flow rate ratio. [185]

Table 3.1 Mixing index (MI) at the inlet with zero mixing for different flow rate ratios.

MB	Water	Q_{MB}/Q_{water}	$\bar{C}$	MI at the inlet (Equation 3-4)	σ_{max}	MI at the inlet (Equation 3-5)
1	1	1	0.50	0	0.50	0
1	0.5	2	0.67	0.29	0.47	0
1	1/3	3	0.75	0.42	0.43	0
1	0.25	4	0.80	0.50	0.40	0

For all flow rate ratios, the mixing index calculated from Equation 3-5 lies between 0 and 1. The higher the mixing index, the greater the degree of mixing. In this section, the effects of the total flow rate and flow rate ratio on the flow and mixing characteristics were studied. The corresponding experimental conditions were listed in Table 3.2. Because the flow rate ratio varied in a wide range from 0.25 to 8, the concentration of MB solution at the inlet was varied accordingly to maintain the outlet concentration of MB a constant, i.e., 0.2 mg/mL and thus achieve a high-contrast visualisation of the mixing process. The mixing indices at different operation parameters were calculated according to Equation 3-5.

Table 3.2 Experimental details for optical visualisation.

Inlet channel 1 (two sub-inlets)		**Inlet channel 2**				
Methylene blue solution (MB)		**Deionized water**	Q_{total}	$R = Q_1/Q_2$	$\overline{C_{MB}}$	σ_{max}
$C_{MB,0}$	Q_1	Q_2				
mg/mL	mL/min	mL/min	mL/min	/	mg/mL	mg/mL
0.300	0.67	0.33	1.00	2	0.200	0.14
0.300	2.00	1.00	3.00	2	0.200	0.14
0.300	3.33	1.67	5.00	2	0.200	0.14
0.300	4.00	2.00	6.00	2	0.200	0.14
0.300	5.33	2.67	8.00	2	0.200	0.14
0.300	6.00	3.00	9.00	2	0.200	0.14
1.000	1.80	7.20	9.00	0.25	0.200	0.4
0.600	3.00	6.00	9.00	0.5	0.200	0.28
0.400	4.50	4.50	9.00	1	0.200	0.2
0.250	7.20	1.80	9.00	4	0.200	0.1
0.225	8.00	1.00	9.00	8	0.200	0.071

The flow pattern and mixing performance inside the reactor cell of the Corning AFR at different total flow rate and flow rate ratio was calculated by the optical visualisation in this section.

3.2.4 Villermaux/Dushman reaction

Due to the limited spatial and temporal resolution of the optical microscope, flow visualisation could mainly provide mixing performance on macro- and meso-scale. Micromixing is on the scale of molecular diffusion, which determine the solution reaction. To quantify the mixing on the microscale, the Villermaux/Dushman method was applied, [188] based on the parallel competing iodide-iodate reaction system:

$$H_2BO_3^- + H^+ \rightarrow H_3BO_3 \quad \text{(quasi-instantaneous)} \tag{3-7}$$

$$5I^- + IO_3^- + 6H^+ \rightarrow 3I_2 + 3H_2O \quad \text{(in the same time scale of micromixing process)} \tag{3-8}$$

$$I_2 + I^- \leftrightarrow I_3^- \quad \text{(instantaneous equilibrium reaction)} \tag{3-9}$$

The neutralization reaction 3-7 is quasi-instantaneous, while the Dushman reaction 3-8 is fast but much slower than reaction 3-7. Dushman reaction is in the same characteristic time scale with the micromixing process. Reaction 3-9 is an instantaneous equilibrium reaction.

In the experiment, a buffered solution (solution A, inlet 2, central flow) $KI/KIO_3/NaOH/H_3BO_3$ was mixed with diluted H_2SO_4 (solution B, inlet 1, two side flow). All the experiments were conducted at room temperature, 20-22 °C.

Under perfect micromixing conditions, the injected acid was instantly dispersed within the reactive medium and consumed by $H_2BO_3^-$ ions via reaction 3-7. Conversely, in situations where the characteristic dissipation time of the injected acid mixing time is in the same range or larger than the reaction time of reaction 3-8, these aggregates result in a local overconcentration of acid. After the complete consumption of $H_2BO_3^-$ ions, the excess acid can react with surrounding I^-/IO_3^- ions. Then the formed I_2 can further react with I^-ions to yield I_3^- ions according to reaction 3-9. The amount of produced I_3^- depends on the micromixing efficiency and was measured by a UV-vis spectrophotometer at 353 nm. There was a linear relationship between the absorbance and the concentration of I_3^-, which accorded with Lambert-Beer's law, and could be expressed as follows:

$$A = \varepsilon b\,[I_3^-] \tag{3-10}$$

where ε is the molar absorptivity of I_3^-, b is the path length. The extinction coefficient εb of I_3^- here is 25.505 $m^3 \cdot mol^{-1} \cdot cm^{-1}$, which is calculated according to the following equations:

The equilibrium constant for the equilibrium reaction between I_2 and KI is a function of temperature:

$$\log_{10} K_B = \frac{555}{T} + 7.355 - 2.575 \log_{10} T \tag{3-11}$$

where T is the temperature in K, and K_B is the equilibrium constant, which can be calculated as follows,

$$K_B = \frac{[I_3^-]}{[I_2][I^-]} \tag{3-12}$$

Rewriting the equation above in terms of the conversion of I_2 generates an equation with only the conversion unknown,

$$K_B = \frac{[I_3^-]}{[I_2][I^-]} = \frac{X_{I_2}[I_2]_0}{(1-X_{I_2})[I_2]_0 \times ([I^-]_0 - X_{I_2}[I_2]_0)} \tag{3-13}$$

where X_{I_2} is the conversion of I_2. With the calculated conversion the concentration of I_3^- can be determined.

During the calibration, a series of aqueous solutions with different I_3^- concentrations were prepared. The raw data is summarised in Table 3.3.

Table 3.3 Experimental details for the determination of extinction coefficient of I_3^-.

Temperature	mass of I_2	$[I_2]_0$	mass of KI	$[I^-]_0$	Volume of the solution	The concentration of I_3^- used	Absorbance of I_3^-
°C	g	mol/m^3	g	mol/m^3	L	mol/m^3	a.u.
23.1	0.0029	0.0457	0.0207	0.499	0.25	0.012	0.319
23.1	0.003	0.0473	0.0282	0.680	0.25	0.015	0.403
23.1	0.0029	0.0457	0.011	0.265	0.25	0.007	0.161
23.1	0.0055	0.0867	0.0286	0.689	0.25	0.028	0.722
23.1	0.0072	0.113	0.0279	0.672	0.25	0.036	0.914

The extinction coefficient was recalculated, and the value was 25505 L·mol^{-1}·cm^{-1}. As shown in Table 3.3, this value was very close to the data reported in the literature. [189] Subsequently, the X_S and corresponding micromixing time was recalculated and the calibration curve is shown in Figure 3.4.

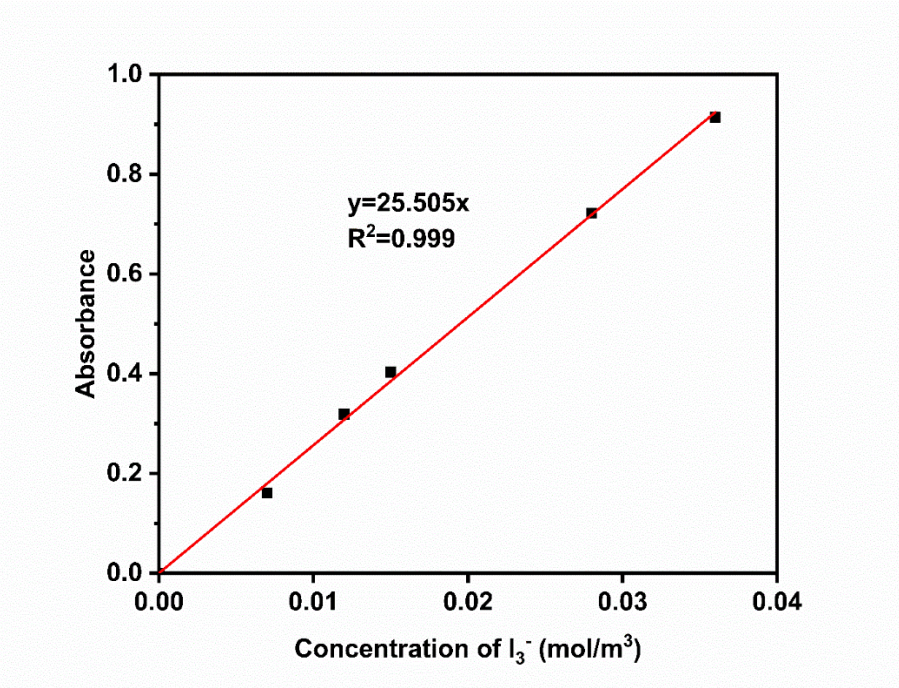

Figure 3.4 The calibration curves used in this work. The unit of the extinction coefficient of I_3^- in this figure was $m^3 \cdot mol^{-1} \cdot cm^{-1}$.

Based on the obtained concentration of I_3^-, the segregation index (X_s) which is defined to quantify the micromixing efficiency can be calculated:

$$X_s = \frac{Y}{Y_{ST}} \tag{3-14}$$

$$Y = \frac{2(V_A+V_B)([I_2]+[I_3^-])}{V_B[H^+]_0} \tag{3-15}$$

$$Y_{ST} = \frac{6[IO_3^-]_0}{6[IO_3^-]_0+[H_2BO_3^-]_0} \tag{3-16}$$

where Y is the ratio of acid mole number consumed by reaction 3-7 to the total acid mole number injected. Y_{ST} is the value of Y in the total segregation case when the micromixing process is infinitely slow. In this case, the H^+ ions are proportionally consumed by the $H_2BO_3^-$ ions and I^-/IO_3^- ions. The selectivity between these two reactions is controlled by the ratio of their concentration, assuming that the reaction will occur quasi-instantaneously with H^+. V_A and V_B are the flow rates of the mixed solution and H_2SO_4 solution, respectively. $[I_2]$ and $[I_3^-]$ are the concentrations of I_2 and I_3^- ions in the reaction effluent, while $[H^+]_0$ is the initial concentration of H^+ ions in H_2SO_4 solution, and $[IO_3^-]_0$ and $[H_2BO_3^-]_0$ are the initial concentrations of IO_3^- and $H_2BO_3^-$ ions in the mixed solution. The value of X_S is within the range of $0 < X_S < 1$ for partial segregation, and X_S equal to 0 is for perfect micromixing, while X_S equal to 1 is for total segregation, respectively.

According to the literature [190], when the flow rate ratio was varied, the following equations must be fulfilled to keep the molar ratios of different ions constant:

$$\frac{3V_A[IO_3^-]_0}{V_B[H^+]_0} = r_1 \tag{3-17}$$

$$\frac{V_A[H_2BO_3^-]_0}{V_B[H^+]_0} = r_2 \tag{3-18}$$

where r_1 and r_2 are constants. The details of the concentrations of different reactants used in this section were summarized in Table 3.4. The two solutions A and B were pumped through the AFR by syringe pumps.

Table 3.4 Experimental details for Villermaux-Dushman method.

Inlet channel 1 (two side flows)		**Inlet channel 2 (central flow)**					**V_{total}**	***R***	**r_1**	**r_2**
H_2SO_4 solution		**Mixed solution**								
$C_{H_2SO_4}$	**V_B**	**$C_{H_2BO_3^-}$**	**C_{NaOH}**	**C_{KI}**	**C_{KIO_3}**	**V_A**				
M	**mL/min**	**M**	**M**	**mM**	**mM**	**mL/min**	**mL/min**	**/**	**/**	**/**
0.018	0.67	0.200	0.100	11.600	2.330	0.33	1.00	2	1.39	0.032
0.018	1.33	0.200	0.100	11.600	2.330	0.67	2.00	2	1.39	0.032
0.018	1.67	0.200	0.100	11.600	2.330	0.83	2.50	2	1.39	0.032
0.018	2.00	0.200	0.100	11.600	2.330	1.00	3.00	2	1.39	0.032
0.018	3.33	0.200	0.100	11.600	2.330	1.67	5.00	2	1.39	0.032
0.018	4.00	0.200	0.100	11.600	2.330	2.00	6.00	2	1.39	0.032
0.018	4.67	0.200	0.100	11.600	2.330	2.33	7.00	2	1.39	0.032
0.018	5.33	0.200	0.100	11.600	2.330	2.67	8.00	2	1.39	0.032
0.018	6.00	0.200	0.100	11.600	2.330	3.00	9.00	2	1.39	0.032
0.060	1.80	0.083	0.042	4.833	0.971	7.20	9.00	0.25	1.39	0.032
0.036	3.00	0.100	0.050	5.800	1.165	6.00	9.00	0.5	1.39	0.032
0.024	4.50	0.133	0.067	7.733	1.553	4.50	9.00	1	1.39	0.032
0.015	7.20	0.333	0.167	19.333	3.883	1.80	9.00	4	1.39	0.032
0.014	8.00	0.600	0.300	34.800	6.990	1.00	9.00	8	1.39	0.032

a: $r_1 = \frac{V_A[H_2BO_3^-]_0}{V_B[H^+]_0}$; b: $r_2 = \frac{V_A[IO_3^-]_0}{V_B[H^+]_0}$

This parallel reaction is sensitive to the pH value in the solution and should be chosen judiciously. If the pH is below pH* (iodine dismutation pH), iodine (I_2) remains stable. Conversely, when the pH exceeds pH*, the iodine formed is thermodynamically unstable and dissociates. [190]

In a segregation situation where acid aggregates, localized zones with pH levels lower than pH* may appear. Within these zones, iodine is formed. These aggregates are progressively dissipated as mixing improves and H^+ ions are consumed. Subsequently, the local pH in these zones finally increases to its final equilibrium pH value. If the final mean pH value is lower than pH*, iodine forms naturally, even under conditions of good mixing. The H^+ ions released by the $H_2BO_3^-/H_3BO_3$ buffer will react to produce iodine. In order to the formation of iodine is only due to bad micromixing, the final mean pH must be greater than pH*. Considering these two situations, the final pH value must be as close as possible to pH*. [188] The final pH value is influenced by both the initial pH of buffer solution and the quantity of sulphuric acid. Typical pH value used are as follows: (1) buffer solution: 8.5 < pH < 9.5; (2) pH* close to 7. Here, the concentrations of different reactants were carefully chosen to maintain the system pH at ca. 8.5 under different parameters. [191]

3.2.5. Determination of micromixing time by incorporation model

As previously discussed, the effectiveness of micromixing, as indicated by the segregation index (X_s), exhibited a strong dependence on the concentration of reactants. This dependency posed challenges when attempting to compare various research studies. Consequently, it became necessary to introduce a parameter, micromixing time, which remained constant regardless of reactant concentration, in order to better elucidate micromixing performance. Several models, including the Inter Exchange with the Mean (IEM) model [192], the Incorporation model [193], and the Engulfment Deformation Diffusion (EDD) model [194] have been proposed to characterize the mixing process. Among these models, the Incorporation model is regarded as a simple and commonly employed approach in both laminar and turbulent micromixing. The parameter known as micromixing time (t_m), integrate to the Incorporation model, serves as a measure of micromixing efficiency because it remains constant under similar hydrodynamic conditions. Consequently, this allows for a straightforward quantification and comparison of micromixing times across different reactor setups. [194]

The incorporation model is applied in conjunction with the iodide-iodate reaction system. According to this model, a finite quantity of acid is divided into aggregates and gradually invaded by environmental fluid that contains iodide and iodate in a basic medium. Acid aggregates grow by progressively incorporating the surrounding medium where neutralisation of $H_2BO_3^-$ ions and Dushman reaction take place. The characteristic time of incorporation, t_m, is assumed to be equal to the micromixing time. The volume of the aggregate grows according to Equation 3-19:

$$V_2 = V_{20}g(t) \tag{3-19}$$

where V_2 is the volume of the acid aggregate, V_{20} is the initial volume of the acid aggregate, and $g(t)$ is the incorporation function with the form:

$$g(t) = exp\ (t/\tau_m) \text{ or } g(t) = 1 + t/\tau_{\mathrm{m}} \tag{3-20}$$

where τ_{m} is the characteristic micromixing time.

The concentrations of the j species can be calculated by the following equation:

$$\frac{dC_j}{dt} = \left(C_{j10} - C_j\right)\frac{1}{g}\frac{dg}{dt} + R_j \tag{3-21}$$

where j species represents various ions in the solution, which include $H_2BO_3^-$, H^+, I^-, IO_3^-, I_2 or I_3^-. R_j is the net production rate of species j for the reaction. When $\mathrm{g(t)} = \exp\left(\mathrm{t}/\tau_{\mathrm{m}}\right)$, Equation 3-21 can be transformed to:

$$\frac{dC_j}{dt} = \frac{C_{j10} - C_j}{\tau_{\mathrm{m}}} + R_j \tag{3-22}$$

With a series of presumed value of micromixing time and known initial concentration of different ions in each solution, Equation 3-22 could be solved by MATLAB (ode15s). The value of time step was fixed at 10^{-8} s, and the integration process was terminated when the H^+ ions were completely consumed with 10^{-8} M as the criterion.

3.2.6 Continuous synthesis and characterisation of Ag nanoparticles (NPs)

The experimental setup for the continuous synthesis of Ag NPs is shown in Figure 3.5. The Ag NPs were prepared via wet chemical method by reducing Ag^+ ions with $NaBH_4$ in the presence of $C_6H_5Na_3O_7$ stabiliser. In a typical procedure, a precursor solution (containing $AgNO_3$ and $C_6H_5Na_3O_7$) and fresh reducing agent ($NaBH_4$ solution) were separately pumped into the AFR by syringe pumps.

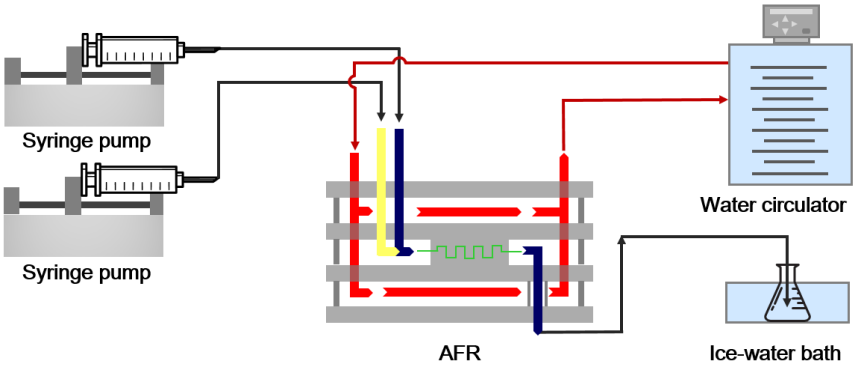

Figure 3.5 Schematic of the experimental setup for the continuous synthesis of Ag NPs in the AFR.

The molar ratio of $C_6H_5Na_3O_7$ to $AgNO_3$, and $NaBH_4$ to $AgNO_3$ were fixed at 3.5 and 6, respectively. The synthetic reaction temperature was controlled at 60 °C by a water circulator (Julabo, FP50-HE) with an external circulation connected to the heat exchanger layers. The reaction effluent flowed straight into a beaker immersed in the ice-water bath to quench the reaction and reduce the mobility and consequent agglomeration of the NPs. The concentrations of $AgNO_3$, $C_6H_5Na_3O_7$ and $NaBH_4$ used for different flow rates, flow rate ratios and feed orientation were summarized in Figure 3.5.

Table 3.5 Experimental details for continuous synthesis of Ag NPs.

Inlet channel 1 (two side flows)		**Inlet channel 2 (central flow)**			Q_{total}	R
$NaBH_4$ solution		**Ag precursor solution**				
C_{NaBH_4}	Q_1	C_{AgNO_3}	C_{Na_3CA}	Q_2		
mM	**mL/min**	**mM**	**mM**	**mL/min**	**mL/min**	**/**
0.450	0.67	0.150	0.525	0.33	1.00	2
0.450	2.00	0.150	0.525	1.00	3.00	2
0.450	4.00	0.150	0.525	2.00	6.00	2
0.450	6.00	0.150	0.525	3.00	9.00	2
1.500	1.80	0.063	0.219	7.20	9.00	0.25
0.900	3.00	0.075	0.263	6.00	9.00	0.5
0.600	4.50	0.100	0.350	4.50	9.00	1
0.375	7.20	0.250	0.875	1.80	9.00	4
0.338	8.00	0.450	1.575	1.00	9.00	8

The UV-vis spectra of the as-prepared Ag NPs were recorded on an Agilent Cary 60 UV-vis spectrophotometer between 300 and 800 nm with a wavelength resolution of 0.5 nm. The transmission electron microscopy (TEM) images of the as-prepared Ag NPs were acquired with a FEI Tecnai TF20 FEGTEM. To avoid post-synthesis agglomeration and maintain uniform particle deposition, the specimens for TEM analysis were prepared following the protocol developed by Michen and co-workers.[195] 50 µL of the as-prepared Ag NPs colloid solution and 50 µL of BSA solution (0.3 mg/mL) were mixed and stored at 4 ºC for 2 h prior to TEM grid preparation. A 5 µL mixture droplet was added to a carbon copper grid (200 mesh) and then dried for 2 h in air.

3.3 Results and discussion

According to the LaMer model, nanoparticle formation undergoes two steps, namely "burst" nucleation followed by diffusion-controlled growth. [100] Both the rates of nucleation and growth affect the nanoparticle size and particle size distribution (PSD), with their dependence on supersaturation, temperature, and surface free energy. [105] In this work, we maintain the temperature and surface free energy, and the variation in supersaturation is the sole factor influencing the final nanoparticle size and PSD. Generally, the mixing process is divided into three stages, i.e. micro-, meso-, and macromixing. [196] [197] Macromixing usually happens by bulk convection on the scale of the reactor, commonly at the length larger than 50 mm, which is how the fluid is distributed across the whole reactor. Mesomixing generates engulfment and vortices, commonly at the length of 0.1-10 mm. Micromixing is on the scale of molecular diffusion. Here in the Corning AFR,

the supersaturation depends on micromixing on the molecular scale, which is preceded by meso- and macromixing, i.e., the reduction of segregation scale controlled by fluid flow. Consequently, to achieve a robust and controllable synthesis of NPs, the understanding and control of fluid flow pattern and mixing behaviour in the reactor are of theoretical and practical importance.

It is widely found that mixing performance is strongly dependent on the process parameters, total flow rate (i.e. Reynolds number [198]), and flow rate ratio (i.e. the position of impingement point [199]). Therefore, in this work, the flow and multiscale mixing behaviours under different process parameters (i.e. total flow rate and flow rate ratio) were studied experimentally. The flow visualisation was conducted for MB-water system to reflect the flow trajectory as well as the mixing process on the meso- and macroscale. [200] Moreover, the mixing on the microscale was quantified by V-D method. Subsequently, the relationship between multiscale mixing behaviour and the average size and PSD of Ag NPs were demonstrated. Since the cells have the same geometry, it could be expected that the flow and mixing characteristics exhibit periodic variation along these cells. Therefore, the following discussion focuses mainly on the flow and mixing behaviour in the first cell.

3.3.1 Flow pattern and quantification of mixing performance on the meso- and macroscale using flow visualisation.

3.3.1.1 The effect of total flow rate

The MB solution entered into the reaction layer from inlet 1 and was split into two side flows (S1 and S3), while the DI water was injected from inlet 2, acting as the central flow (S2). The flow rate ratio was fixed at 2, while the total flow rate varied from 1 to 9 mL·min^{-1}, and at the same time Reynolds number increased from 13 to 117. The Reynolds number is calculated via

$$Re = \frac{\rho V L}{\mu} \tag{3-23}$$

Where Re is the Reynolds number, the ratio of inertial forces to viscous forces. ρ is the density of fluid, 10^3 kg/m^3. V is the velocity of the fluid. L is a characteristic length, here it was calculated based on the hydraulic diameter of the nozzle (Figure 3.1 (c), 0.37 mm in width and 0.40 mm in depth). μ is the dynamic viscosity of the fluid, 2.98×10^{-3} Ns/m^2. In this calculation, the same properties of water were specified for the fluids. Figure 3.6 shows the optical images about concentration contour of fluid mixing at different total flow rates. The central flow of DI water was combined with two side flows of MB solution in the jet zone (hereafter referred as the combined stream). For all total flow rates (1-9 mL·min^{-1}), two distinct interfaces could be observed in the jet zone, indicating a laminar flow behaviour.

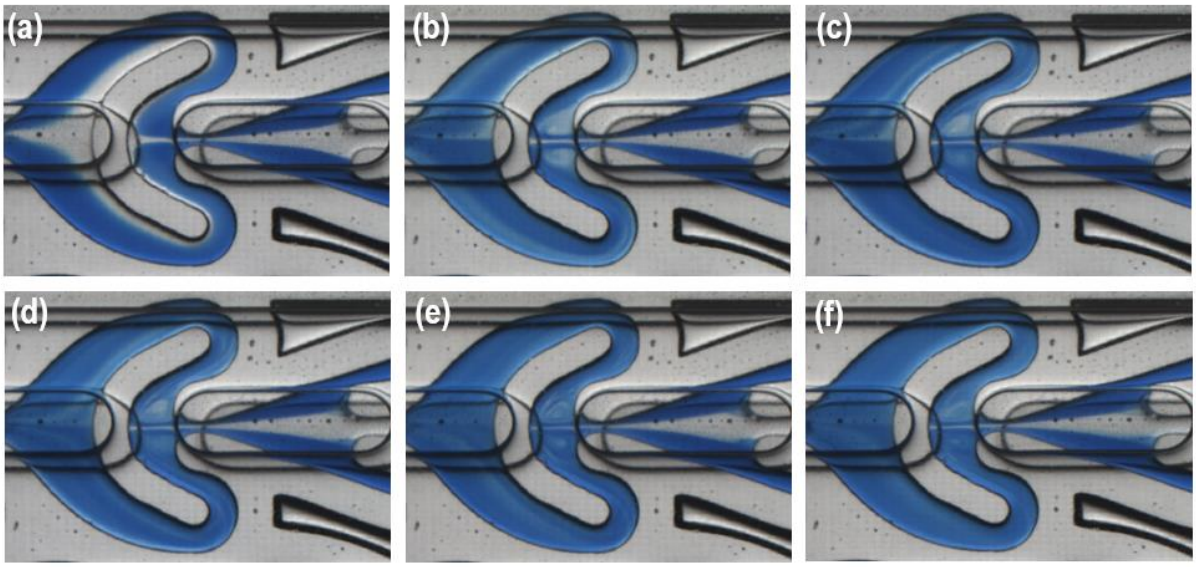

Figure 3.6 Optical microscope images of mixing images obtained at different total flow rates using aqueous MB solution and DI water as the working fluids (a) 1 mL·min^{-1}, (b) 3 mL·min^{-1}, (c) 5 mL·min^{-1}, (d) 6 mL·min^{-1}, (e) 8 mL·min^{-1}, (f) 9 mL·min^{-1}. R = 2.

The width of the central flow was measured (line 1, Figure 3.7 (a)) when the combined stream flowed into the nozzle, and the accurate position where the interface between the central flow and side flow could be distinguished was marked in Figure 3.7 (b).

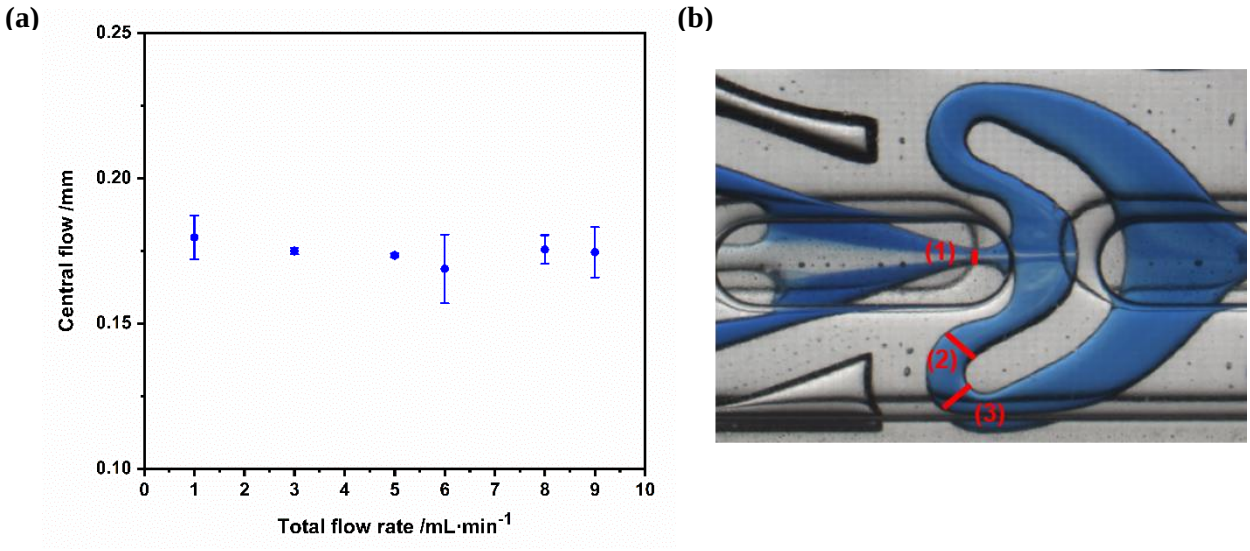

Figure 3.7 (a) The width of the central flow as a function of the total flow rate. R =2. (b) The width was measured on the selected line 1.

As shown in Figure 3.7, the width of the central flow was independent of the total flow rate, implying the initial fluid distribution across the combined stream was identical at different total flow rates. At the total flow rate of 1 mL·min^{-1} (Figure 3.6 (a)), the combined stream was separated into two sub-streams once entering the first cell. In each sub-stream, the DI water and MB solution flowed side by side, maintain a well-defined interface. Remarkably, even at the outlet of the first cell, the interface between the water and MB solution remained very clear. This indicated that the fluid mixing was

dominated by molecular diffusion which was very slow under this condition. Despite a Re number of 39 at the flow rate of 3 mL·min^{-1}, which still positions the flow within the laminar regime, totally different flow and mixing behaviours were observed in comparison to the 1 mL·min^{-1} flow condition. As shown in Figure 3.6 (b), the combined stream went through the nozzle along the initial flow direction and collided with the U-shaped structure, which split the combined stream into two sub-streams. No visible interface between MB solution and DI water could be seen at the end position of the first cell, implying the mixing performance was much better than that at 1 mL·min^{-1}. The improved mixing performance can be attributed to a combination of transverse motions resulting from collisions and expansion vortices. Within the U-shaped structure, collisions generated transverse motions which effectively increased the interfacial area for diffusion and reduced the mass transfer distance. Additionally, two symmetric expansion vortices appeared on both sides of the combined stream. The generation of expansion vortices was pervasive when the cross-section of the channel enlarged abruptly, which can accelerate the mixing process through stretching and folding mechanisms. [201] Moreover, when the fluid flowed through the turning (plane 3, Figure 3.7 (b)) of the heart-shaped cell, transverse advection, known as the Dean vortex, may occurred due to the gradient of the centrifugal force in the cross-section of the channel. The Dean number (*De*) is defined as a control parameter to express the ratio of centrifugal forces to viscous forces and the intensity of Dean vortex, and can be calculated through the following equation [202]:

$$De = Re\sqrt{\frac{D_h}{2R}} \tag{3-24}$$

where *Re* represents the Reynolds number, and D_h and *R* are the hydraulic diameter of the curved channel and the radius of curvature of the curved channel, respectively.

As the total flow rate increased from 1 to 9 mL·min^{-1}, the Dean number increased from 7 to 60 when the fluid flowed through the turning (the Dean number was calculated based on the average radius of curvature of the turning, Table 3.6). According to the literature, when the Dean number is above 20, corresponding to the total flow rate of 3 mL·min^{-1} in this work, a symmetrical vortex pair would be formed. [202] Thus, the Dean vortex generated in the turning at higher total flow rate could further improve the mixing quality.

Table 3.6 Dean numbers at different total flow rates when the fluid passed Plane 3 (turning) in Figure 15.

Q_{total}	D_h /mm	R /mm	Re	De
1	0.88	1.07	13	7
3	0.88	1.07	39	20
5	0.88	1.07	65	33
6	0.88	1.07	78	40
8	0.88	1.07	104	53
9	0.88	1.07	117	60

However, darker striations of MB could still be observed, indicating the mixing at 3 mL·min^{-1} was far away from ideal mixing in the first cell. As the total flow rate further increased, the distribution of MB across the channel became more homogeneous, indicating a better mixing quality. This could be attributed to the enhanced intensities of secondary flows (i.e., transverse motions caused by collision, expansion and Dean vortices) with the increase in Reynolds number. [203]

To demonstrate quantitatively the effect of the total flow rate on the degree of mixing, the mixing index was calculated according to Equation 3-5. For the flow visualisation, the mixing index at the outlet of the heart-shaped cell was difficult to be achieved in this work because of the existence of exchange layers (Figure 3.1). Therefore, the mixing index was determined on a selected plane in the sub-channel (line 2, Figure 3.7 (b)). In Figure 3.8, as the total flow rate increased from 3 to 9 mL·min^{-1}, the mixing index increased slightly from 0.37 to 0.60, which could be attributed to the higher degree of transverse advection in this flow rate range. At higher Re numbers, although the residence time of two fluids to molecular diffusion decreased, the chaotic motion became rapidly and led to the enhancement of the mixing efficiency.

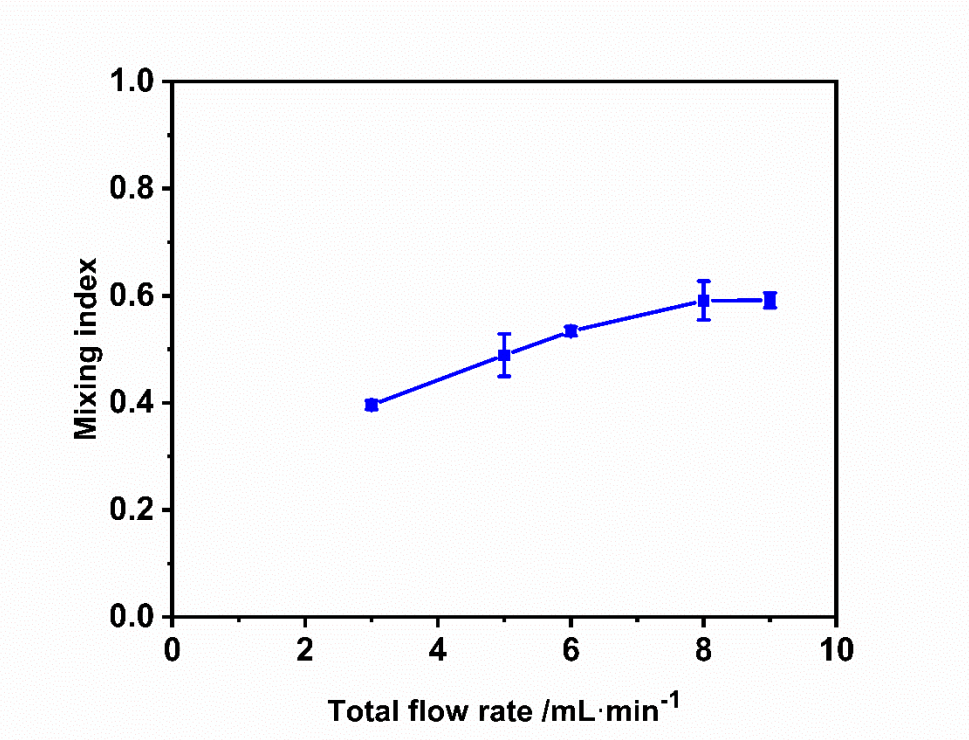

Figure 3.8 Mixing index as a function of the total flow rate. R = 2.

3.3.1.2 The effect of flow rate ratio

In this section, mixing performance was studied at various flow rate ratios ranging from 0.25 to 8 by adjusting the flow rates of MB solution and DI water while maintaining the total flow rate at 9 $mL \cdot min^{-1}$. The MB solution and DI water were pumped into the AFR from inlets 1 and 2, respectively. The optical images of fluid mixing at different flow rate ratios are displayed in Figure 3.9. It can be seen that the flow rate ratio affected the initial MB concentration distribution across the combined stream. The width of the central flow (DI water) was measured in the same position, as shown in Figure.3.7 (b) (line 1). As shown in Figure.3.10, the width of the central flow was gradually narrowed with the increase of the flow rate ratio. As the flow rate ratio increased from 0.25 to 4, the width of the central flow decreased from 0.34 to 0.09 mm. When the flow rate ratio further increased to 8, the width of the central flow could not be distinguished due to the limited camera resolution (0.0087 mm/pixel), and particularly the fast dispersion of MB from the side flow into the central flow arising from the extremely narrow width.

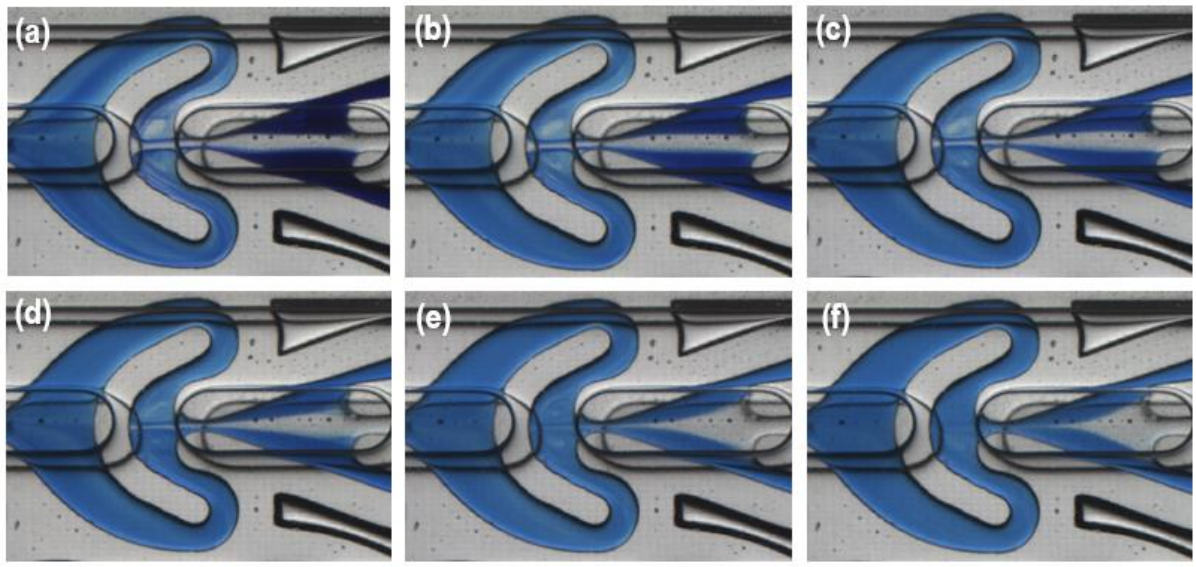

Figure 3.9 Mixing images obtained at different flow ratios: (a) 0.25, (b) 0.5, (c) 1, (d) 2, (e) 4, and (f) 8 using aqueous MB solution and DI water as the working fluids at Q_{total} = 9 mL·min^{-1}.

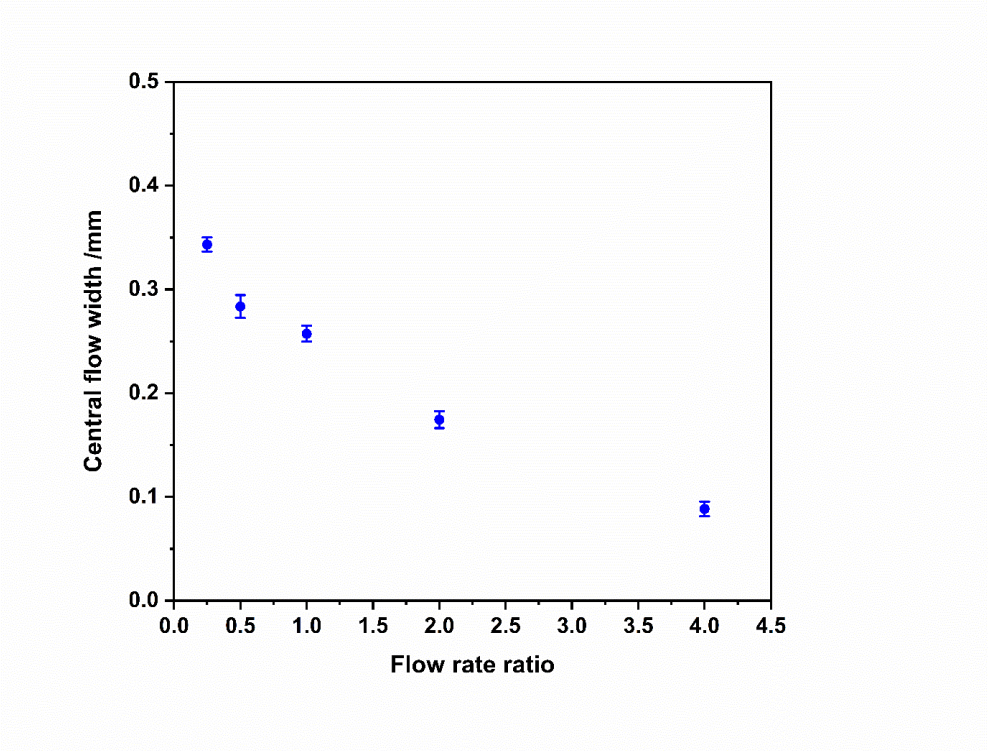

Figure 3.10 The width of the central flow as a function of the flow rate ratio at Q_{total} = 9 mL·min^{-1}.

At the flow rate ratio of 0.25, nearly no MB diffused into the interior of the central flow even before it reached to the U-shaped obstacle. As for the flow rate ratio of 8, MB could quickly diffuse across the central flow because of the narrowest width of the central flow.

The mixing indexes at different flow rate ratios are shown in Figure 3.11. For the flow rate ratios of 4 and 8, the mixing indexes are decreasing to almost 0 when it reaches to 8, indicating that the mixing performance worsens with increasing flow rate ratio. However, in our experiment, MI was calculated

according to the equation (3-5) and (3-6). At these flow rate ratios, the difference between the inlet MB concentration and average MB concentration was small, and the deviation of the grey level caused by the non-uniform light distribution of microscope could not be ignored. Errors exist when the flow rate ratio increases to 4 and 8. Therefore, further validation by an additional method will be needed to calculated the MI at different flow rate ratios.

Hence, it is concluded that the effect of the flow rate ratio on the degree of mixing could primarily be attributed to the different initial MB concentration distributions across the combined stream. This phenomenon, to some extent, is similar to the fact that the feed position affected the mixing performance dramatically in stirred batch reactors. [204] In stirred batch reactors, the stirring impeller generates a nonuniform velocity field across the reactor, affecting the energy dissipation rate. Varying the feed position results in differing local energy dissipation rates where the feeds enter reactor, significantly affecting the macromixing behaviour. In contrast to the total flow rate, the effect of the flow rate ratio on the mixing performance has been rarely investigated and vary across the mixers with different structures, i.e. different mixing mechanism.

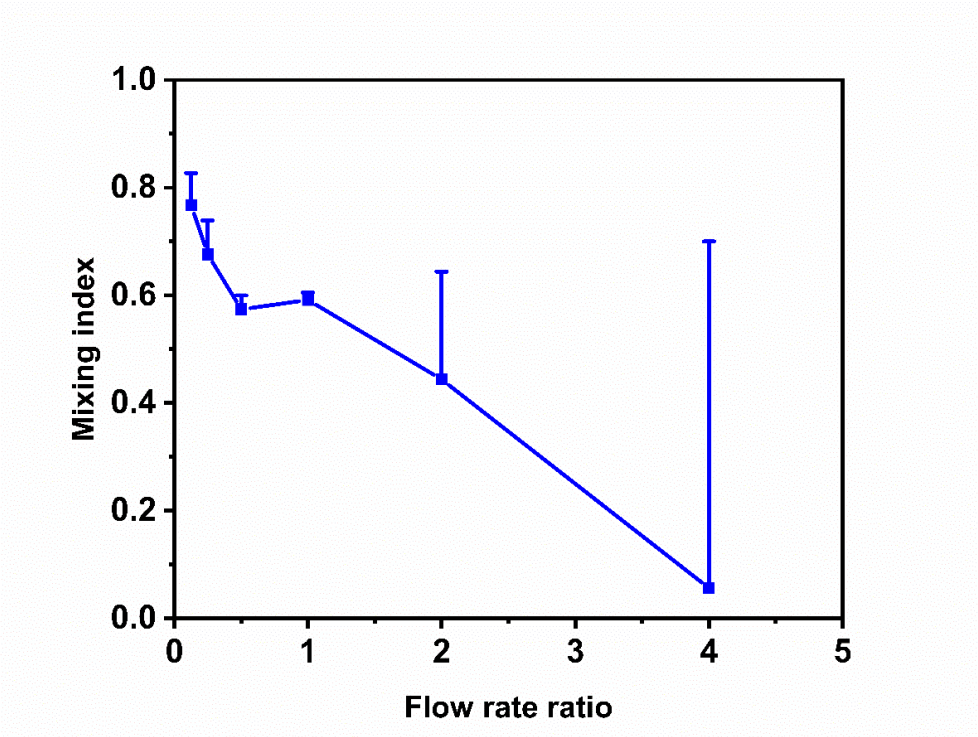

Figure 3.11 The mixing index as a function of the flow rate ratio.

3.3.2 Quantification of the mixing performance on the microscale using Villermaux-Dushman method

Micromixing represents the final stage of mixing, essential for achieving molecular-scale

homogeneity. Given that all the chemical reactions occur at the molecular scale, the efficiency of micromixing within the reactor strongly impacts the reaction performance. The mixing performance on meso- and macromixing has been studied by dye visualisation above, which helped determine the minimum scale of segregation-only dimensions at the molecular-scale achieve the homogenization. [205] A smaller minimum scale of segregation helps to achieve higher micromixing efficiency. Typically, the micromixing efficiency can be evaluated by several fast competitive or consecutive reaction schemes which are sensitive to the micromixing quality. [206] Among these methods, the Villermaux-Dushman method based on the iodide-iodate reaction system has been widely employed to assess the overall micromixing performances of various mixers. [207]

3.3.2.1 The effect of total flow rate

Figure 3.12 (a) shows the plot of the segregation index as a function of the total flow rate with the flow rate ratio of 1, and the concentration of reactants kept constant. When the total flow rate was 1 $mL \cdot min^{-1}$, the segregation index was as high as 0.038, indicating a poor micromixing efficiency. As discussed in Section 3.3.1.1, the mixed solution and sulphuric acid solution flowed side by side at 1 $mL \cdot min^{-1}$. Hence, the competitive reaction system occurred at the interface between two reactant streams and was limited by molecular diffusion. H^+ ions were consumed preferentially by $H_2BO_3^-$ ions at the interface, and the formation of I_2 was limited initially. However, along the flow direction, the unreacted I^- and IO_3^- ions at the interface gradually diffused into the sulphuric acid solution, leading to the formation of a large amount of I_2 and subsequent I_3^- ions, and thus a high segregation index. As the flow ratio increased from 1 to 6 $mL \cdot min^{-1}$, the segregation index decreased significantly from 0.038 to 0.0037. This indicated that a better micromixing performance could be achieved at a higher total flow rate. With the further increase of the total flow rate, only a slight decrease in the segregation index was observed, implying the enhancement effect of the evaluated total flow rate on micromixing was not pronounced over 6 $mL \cdot min^{-1}$. It was evident that the total flow rate showed the same effect on the micromixing performance as that on the meso- and macromixing performances (quantified by the mixing index in Section 3.3.1.1). This was because the intensities of the secondary flows were enhanced with the increase of the total flow rate, leading to an improved meso- and macromixing. A better meso- and macromixing performance could offer a more uniform concentration distribution, which could inhibit the occurrence of Dushman reaction. In conclusion, the enhanced secondary flows could reduce the minimum scale of segregation, which facilitated the mixing on the microscale. The micromixing time decreased from 0.17 to 0.004 s (Figure 3.12 (c)) as the flow rate increased from 1 to 9 mL/min, which is coincide with the enhancement in micromixing performance.

3.3.2.2 The effect of flow rate ratio

Figure 3.12 (b) shows the effect of the flow rate ratio on the segregation index. The segregation index decreased from 0.014 to 0.0016 as the flow rate ratio increased from 0.125 to 1. As the flow rate ratio further increased from 1 to 4, no obvious change in the segregation index was observed. Initially, Villermaux-Dushman method was widely used for evaluating the mixing performances of batch reactors. When this method was implemented to the continuous reactor, Equation 3-17 and 3-18 must be satisfied at different flow rate ratios. In other words, the molar ratio of H^+ ions should be kept unchanged. Hence, the concentration of H^+ ions should increase with the decrease in the flow rate of H_2SO_4 solution. The Dushman reaction was more sensitive to the concentration of H^+ ions compared to the nebulization of $H_2BO_3^-$. [208] Kölbl and co-workers found that the absorption of I_3^- (i.e. segregation index) increased with the increasing concentration of H^+ ions and Dushman reaction mainly happened in H^+ ions-rich region. [209] For microreactors, studying the effect of flow rate ratio, the segregation index decreases with the increasing flow rate of H_2SO_4 solution (i.e. the decreasing H^+ ions concentration). [210] Similar to the previous studies, as shown in Figure 3.12 (b), the segregation index was strongly determined by the concentration of H^+ ions in this study, which varied with the flow rate ratio (the same phenomenon as we discussed in section 3.1.2). When the flow rate ratio was 0.25, the H^+ concentration was as high as 0.12 M, leading to the maximum value of the segregation index. When the flow rate ratio increased from 2 to 8, there was only a slight increase in the concentration of H^+ ions, so the segregation index mainly related to the micromixing performance. Therefore, when the flow rate ratio changed, many factors, including the multiscale mixing performance and initial concentration of reactants, finally affected the reaction behaviour. Here in order to provide a more comprehensive understanding of micromixing performance, the micromixing time has been incorporated as an additional factor. As shown in Figure 3.12 (d), all the micromixing time fluctuated around 0.005 s. Considering the precision of the model, it could be concluded that the micromixing times at different flow rate ratios are of similar magnitudes. Consequently, it was reasonable that the micromixing time was nearly independent of the flow rate ratio.

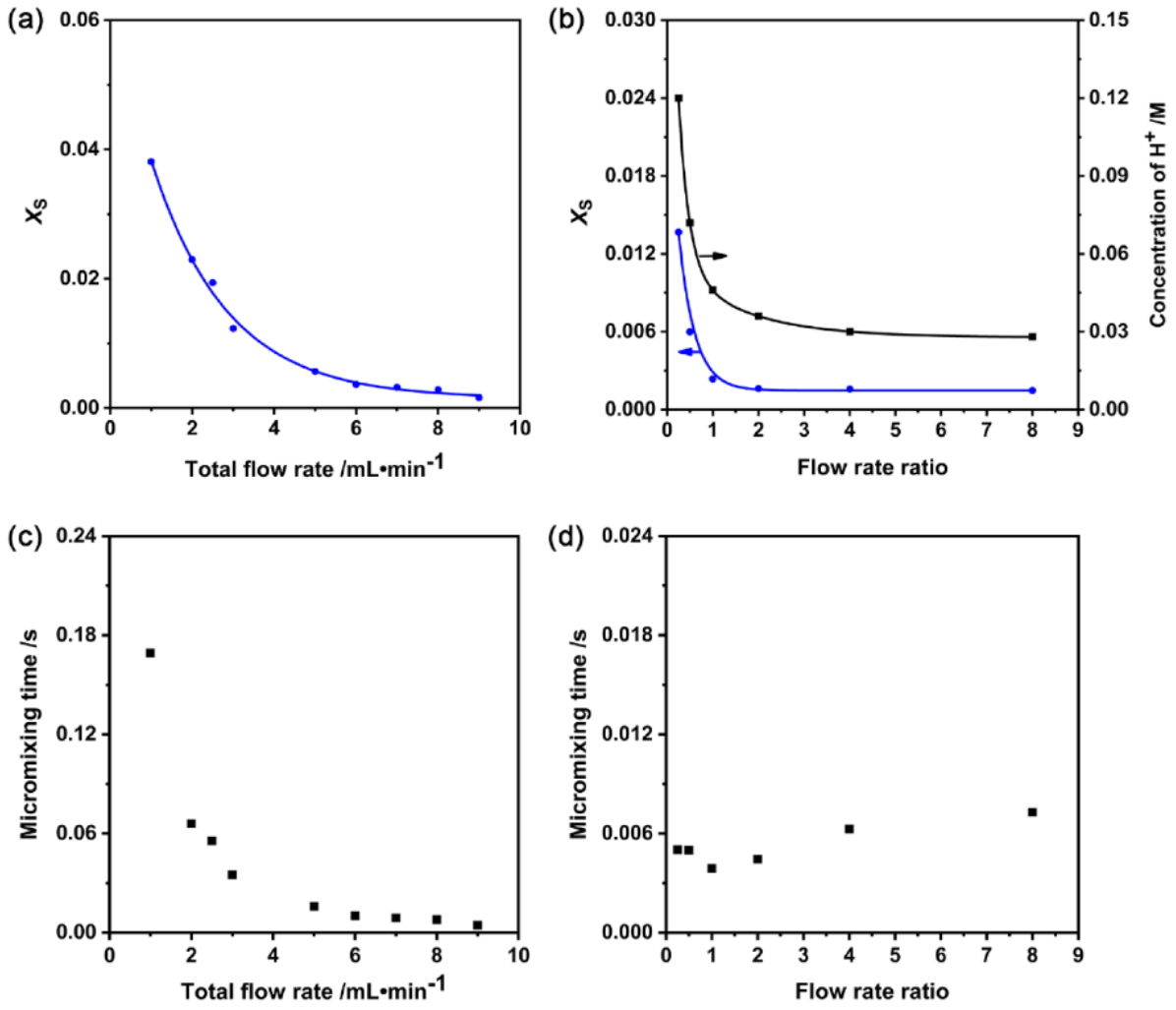

Figure 3.12 Plots of segregation index (X_S) and micromixing time as a function of (a, c) total flow rate, R = 2; (b, d) flow rate ratio, Q_{total} = 9 mL·min^{-1}.

3.3.3 Continuous synthesis of the Ag NPs

The mixing performances at multi-scales in Corning AFR have been discussed in sections 3.3.1 and 3.3.2. This section will evaluate the influence of mixing characteristics on the continuous synthesis of nanomaterials (i.e. spherical Ag NPs as a case), mainly on the average particle size and PSD. Earlier studies have demonstrated that the particle size of Ag NPs is closely related to mixing performance.[211] Better micromixing leads to higher and more uniform local supersaturation instantaneously, and thus fast nucleation rate and smaller average particle size and narrower particle size distribution. The aforementioned results showed that the total flow rate and flow rate ratio had significant effects on the flow and mixing characteristics, so it could be anticipated that these two parameters affected as well the particle size distribution of Ag NPs.

3.3.3.1 The effect of total flow rate

In this experiment, $NaBH_4$ solution was injected into the AFR from inlet 1 (side flow), and Ag precursor solution was injected from inlet 2 (central flow). The total flow rate increased from 1 to 9 $mL \cdot min^{-1}$, and the flow rate ratio was maintained at 1. Figure 3.13 shows the UV-vis spectra of Ag NPs synthesised at different total flow rate, and the corresponding TEM images and PSD at 1 and 9 $mL \cdot min^{-1}$. Both samples exhibited spherical morphologies, and the particle size distribution of as-prepared Ag NPs can be deduced by the full wavelength at half maximum (FWHM), the larger the FWHM, the wider PSD.[22] The UV-vis absorption spectra of Ag NPs synthesised at low total flow rates (1 $mL \cdot min^{-1}$) exhibited an asymmetric shape, i.e. a main peak at ca. 388 nm and a shoulder peak at ca. 410 nm. Correspondingly, a bimodal PSD measured from TEM images was shown in Figure 3.13 (c). As the total flow rate increased from 1 to 9 $mL \cdot min^{-1}$, the shoulder peak of UV-vis absorption spectra in Figure 3.13 (a) gradually disappeared, along with the FWHM decreasing from 65 to 52 nm and the average particle size decreasing from 7.2 ± 3.9 to 4.6 ± 1.8 nm, respectively. The Ag NPs synthesised at 9 $mL \cdot min^{-1}$ showed a symmetrical absorption peak around 388 nm, which was the characteristic absorption peak of spherical Ag NPs, and corresponds to the unimodal PSD in TEM images. This indicated that increasing the total flow rate could obtain uniform particles with a narrow PSD for Ag NPs.

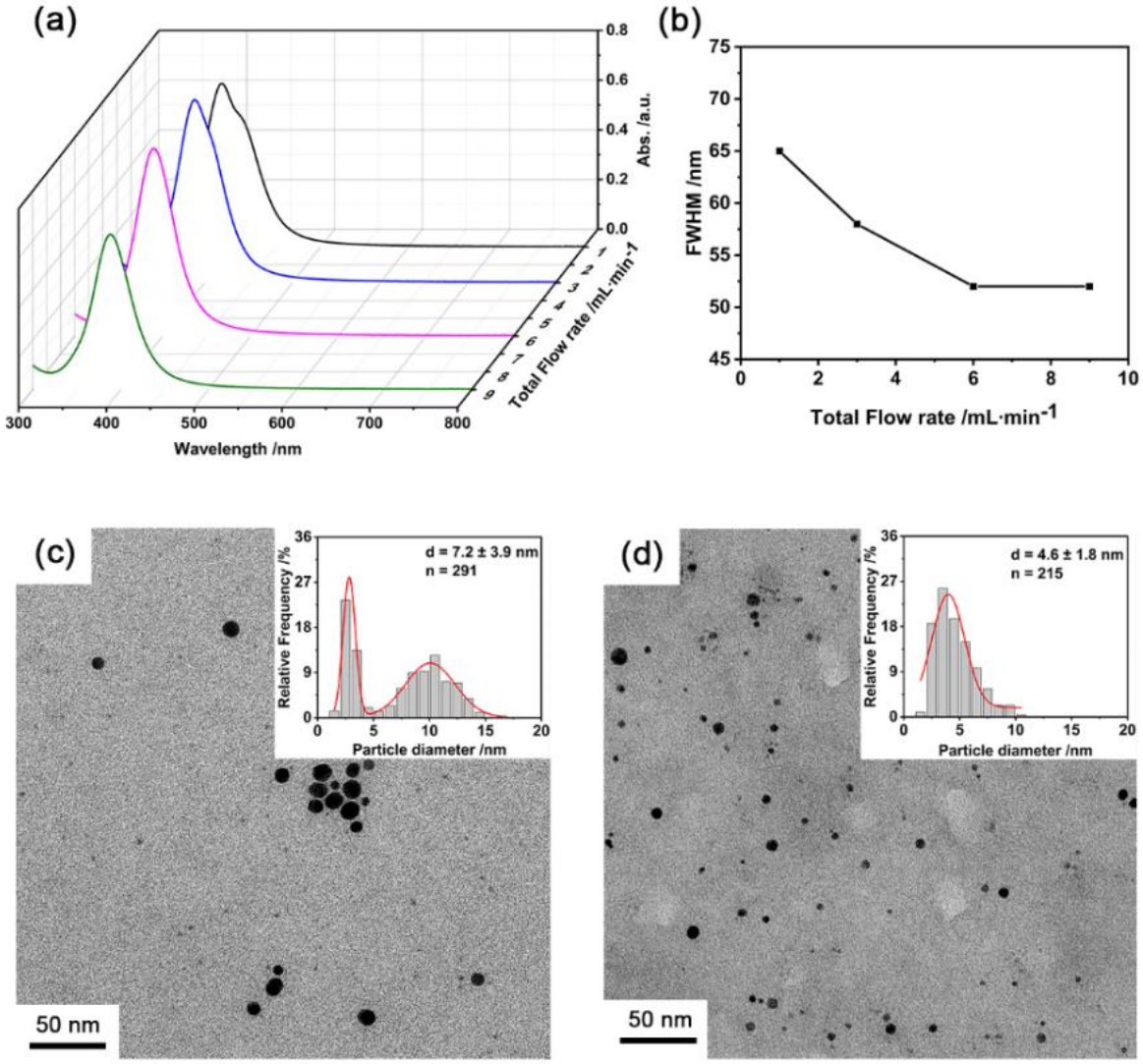

Figure 3.13 (a) UV-vis absorption spectra of Ag NPs synthesised at different total flow rates; (b) FWHM as a function of the total flow rate. The line is given as eye guide only. TEM image and particle size distribution of Ag NPs synthesised at (c) 1 mL·min^{-1} (d) 9 mL·min^{-1}. R = 2.

Taking the results obtained in flow visualisation, and the Villermaux-Dushman protocol into consideration, the effect of the total flow rate could be merely attributed to the change in micromixing performance. The worst micromixng performance at 1 mL·min^{-1} induced the widest PSD. As discussed above, Ag NPs are formed by burst nucleation as described by the classic nucleation mechanism, followed by further diffusion growth, Ostwald ripening or coalescence. [105] At 1 mL·min^{-1}, the $NaBH_4$ solution and Ag precursor solution flowed side by side. The reduction reaction occurred at the interface between these two flows in the beginning. When the supersaturation of Ag atoms exceeded the critical value, nuclei formed. Due to the slow molecular diffusion, both homogenous nucleation and growth on existing nuclei as the nucleation sites could occur. Poor mixing performance caused nuclei to form at different positions along the flow direction, which experienced different growth histories, and hence a wide PSD. When the total flow rate increased, the micromixing

performance became better, thereby uniform reaction environment, leading to a smaller PSD and narrower particle size distribution.

In this section, the molar ratios between $NaBH_4$ and $AgNO_3$ is 6 to 1, and $C_6H_5Na_3O_7$ and $AgNO_3$ were maintained at 3.5 and 1, respectively. According to the literature, Ag^+ ions reacted with BH_4^- ions under the basic environment via the following equation: [212]

$$8Ag^+ + BH_4^- + 8OH^- \rightarrow 8Ag + H_2BO_3^- + 5H_2O \quad (3\text{-}25)$$

It was apparent that a large excess of $NaBH_4$ was used in this study. Although from 1 to 9 $mL \cdot min^{-1}$, the residence time decreased from 162 s to 18 s, the chemical reduction and nucleation reaction happened within milliseconds. Then a small number of crystal units finished growing into particles within seconds. [25] So the particle size and PSD are mainly dependent on mixing performance.

3.3.3.2 The effect of flow rate ratio

In line with the above experiments, the flow rate ratio was varied from 0.25 to 8, while the total flow rate was kept at 9 $mL \cdot min^{-1}$ in this section. Figure 3.14 shows the UV-vis absorption spectra and corresponding TEM images and PSD of Ag NPs synthesised at different flow rate ratios. As the flow rate ratio increased from 0.25 to 8, the FWHM decreased from 70 to 49 nm. This implied that the Ag NPs synthesised at higher flow rate ratio had a narrower PSD. It was further confirmed by the results of TEM, the average particle sizes of Ag NPs synthesised at 0.25 and 8 were 7.5 ± 3.9 and 4.3 ± 1.8 nm, respectively. Evidently, when the flow rate ratio was varied from 2 to 8, the particle size distribution of Ag NPs did not change following the same trend as the multiscale mixing performance. The similar phenomenon has been already found in Villermaux-Dushman method (Section 3.3.2.1).

As discussed in flow visualisation, the central flow exhibited the largest width at the flow rate ratio of 0. 25. As depicted in Figure 3.14, only a minor amount of MB from the side flow diffused into the interior of the central flow and MB concentration at a very low level. Therefore, it could be expected that the diffusion of BH_4^- ions from side flow ($NaBH_4$ solution) into the interior of central flow (Ag precursor solution), or the diffusion of Ag^+ ions from the interior of central flow to the side flow requires a longer time at the flow rate ratio of 0.25, as compared to other flow rate ratios. In this case, the nucleation of Ag NPs happened a longer duration along the flow direction until Ag^+ ions were completely consumed. As a result, Ag NPs with a broader PSD were obtained at the flow rate ratio of 0.25. At the flow rate ratio of 8, the width of the Ag precursor stream was the narrowest, so BH_4^- could migrate quickly across the Ag precursor stream. Although the mixing performance was far away from ideal mixing, most of Ag^+ ions could be reduced in a short period, because excessive $NaBH_4$ was used (the concentration ratio of $NaBH_4$ / Ag^+ is 0.75/1). Consequently, a narrower particle size distribution was obtained at the flow rate ratio of 8 as compared to 0.25. It is concluded that the average size and morphology of nanomaterials could be tuned by changing the width of the central

flow. Similar conclusions have been obtained in earlier studies, Lu and co-workers reported that while changing the flow rate of the side flow, the outer profile of the central flow and the molar ratio of two reactants varied, leading to the formation of Au hybrid materials with different morphologies. [213]

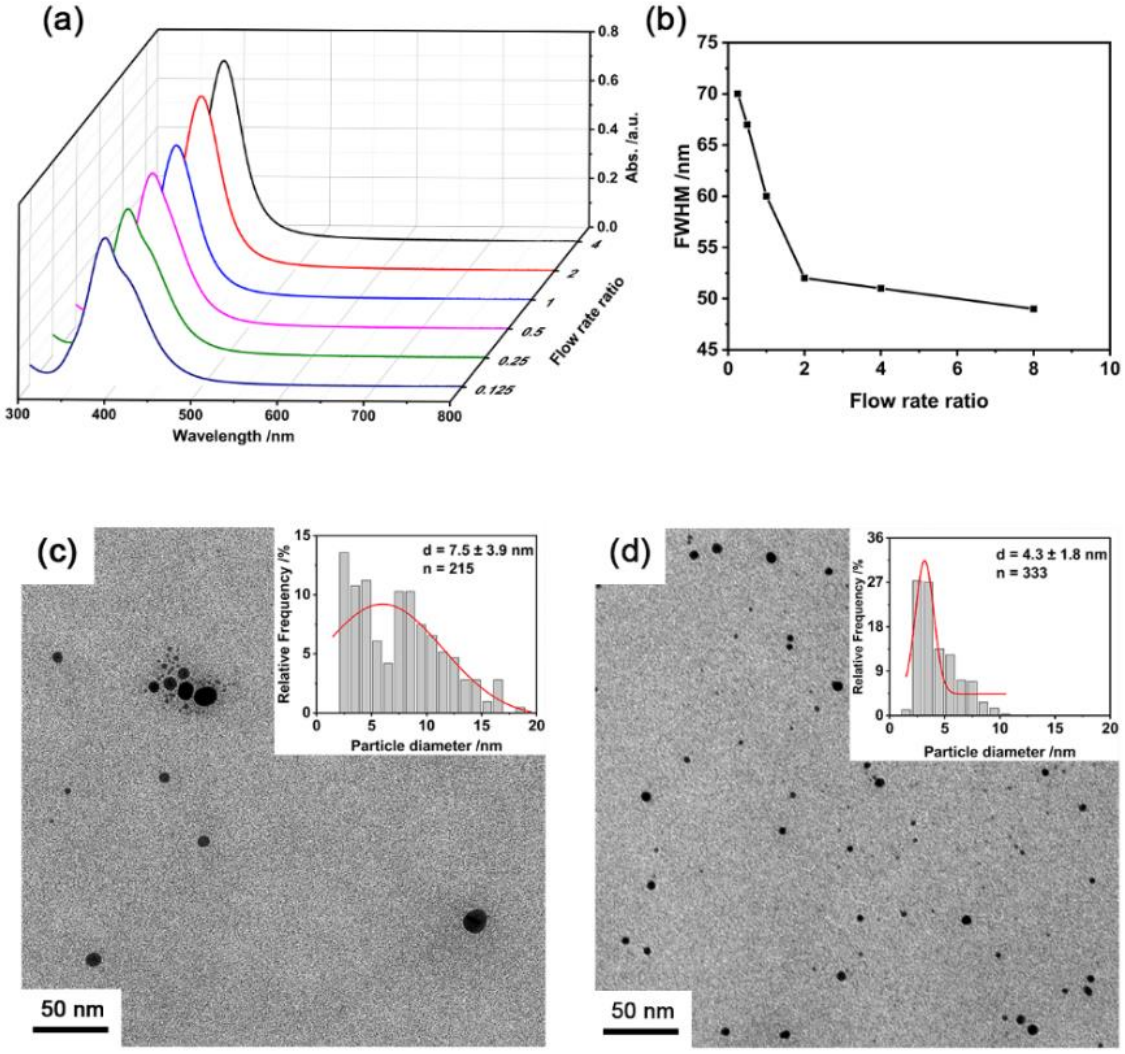

Figure 3.14 (a) UV-vis absorption spectra of Ag NPs synthesised at different flow rate ratios, (b) FWHM as a function of the flow rate ratio. The line is given as eye guide only. TEM image and particle size distribution of Ag NPs synthesised at the flow rate ratio of (c) 0.25 and (d) 8. Q_{total}= 9 mL·min^{-1}.

3.4 Conclusion

In this chapter, the influence of multiscale mixing performances of a Corning AFR Lab Reactor module on silver NPs synthesis has been studied for the first time. Firstly, the flow and mixing characteristics (mainly on the meso- and macroscale) of two miscible liquids in Corning AFR were conducted by dye visualisation for methylene blue-water system. It was found that both the total flow rate (1-9 mL·min^{-1}) and flow rate ratio (0.25-8) significantly affected the flow and mixing characteristics. With the increase in the total flow rate, a flow pattern evolution from laminar flow

(1 $mL \cdot min^{-1}$) to a complex flow containing transverse advection (3-9 $mL \cdot min^{-1}$) was observed. The mixing index increased with the increase in the total flow rate, indicating a better mixing performance. The improved mixing performance at evaluated total flow rate could be attributed to the enhanced secondary flows (i.e. transverse motion caused by the collision with the U-shaped obstacle, expansion vortices and Dean vortices) originating from the unique structural feature of reactor cell. As for the flow rate ratio, it affected the widths of the central and side flows in the jet zone, i.e. initial concentration distribution profile across the combined stream, thereby inducing different mixing performances. The best mixing performance was obtained at the flow rate ratio of 0.25.

Subsequently, the micromixing efficiency which strongly affected the reaction performance was studied by the Villermaux-Dushman method. The segregation index as well as the micromixing time decreased with the increase of the total flow rate, implying a better micromixing efficiency. The flow rate ratio affected the segregation index in a complex manner. Across the flow rate ratio studied, the micromixing performance was related to the diffusion width and solution concentration distribution. When the continuous synthesis of Ag NPs was carried out, a similar phenomenon was observed. As the total flow rate increased, the PSD of Ag NPs became narrower due to the better micromixing efficiency at the higher total flow rate. When the flow rate ratio changed, the PSD of Ag NPs was dependent on the width of the Ag precursor solution rather than the degree of mixing, because an excessive amount of $NaBH_4$ was used. To sum up, the aforementioned results provide a deeper understanding of the flow and mixing characteristics, and their effects on the particle size distribution of Ag NPs in a Coning AFR. This may pave the way for large scale production of size-tunable Ag NPs in the future.

Chapter 4. Continuous synthesis of SnO_2 and Au@SnO_2 NPs in micro-capillary reactor

4.1 Introduction

SnO_2, an important n-type semiconductor with a direct wide bandgap of 3.60 eV at 300 K, has been widely used in various photocatalytic reactions due to its long-term stability, high oxidation potential and chemical inertness, non-toxicity, etc. [135] Traditional synthesis methods of SnO_2 NPs, such as hydro-/solvo-thermal, chemical precipitation, sol-gel methods, typically require complex equipment, the use of toxic solvents, and time-consuming high-temperature or high-pressure processes, making them less suitable for large-scale commercialisation. [137] [137][138] [140] Taking the advantage of microfluidics with excellent heat/mass transfer performance and also scalability potential, we initially synthesised SnO_2 NPs by adjusting the supersaturation and the polarity of solution using a microreactor to achieve the continuous synthesis at low temperature and low pressure.

For the wide-band semiconductors, incorporated plasmonic metal nanostructures are commonly used to enhance their solar-light harvesting in photocatalysis.[65] [214] Traditionally synthetic strategies include sol-immobilisation, impregnation and co-precipitation techniques. [83][84][149] However, these semi-continuous synthesis approaches pose challenges when scaling up production. To address this limitation and enable high-volume production, we initially investigate a straightforward method for the continuous synthesis of Au@SnO_2 in micro-capillary reactor. The solar energy conversion efficiency of this binary composite photocatalysts is determined by the type, material features, geometric arrangement of the building blocks. To identify the most effective structure with superior photocatalytic properties, three different methods were explored to incorporate Au NPs with SnO_2: (1) Au NPs coated on the SnO_2 matrixes, (2) Au NPs surrounded by SnO_2 matrixes, and (3) Au NPs embedded with SnO_2 matrixes.

4.2 General experiments and methods

4.2.1 Chemicals

Tin(IV) chloride pentahydrate ($SnCl_4 \cdot 5H_2O$, Scientific Laboratory Supplies), hydrogen tetrachloroaurate (III) hydrate ($HAuCl_4$, Across Organics), trisodium citrate dihydrate ($C_6H_5Na_3O_7 \cdot 2H_2O$, ≥99 wt%, Sigma Aldrich), sodium borohydride solution ($NaBH_4$, 12 wt% in 14 M NaOH, Sigma Aldrich), Rhodamine B (RhB, $C_{28}H_{31}ClN_2O_3$, 1% extinction, Fisher Bioreagents), sodium hydroxide (NaOH, >97.5%, Scientific Laboratory Supplies), absolute ethanol (C_2H_6O, Sigma-Aldrich) all these chemicals were used as received without further purification. Deionised (DI)

water (resistivity of 18.2 MΩ·cm) used in all experiments was purified with a Milli-Q ultra-pure water system.

4.2.2 Characterisation of nanoparticles

The structure was confirmed by X-ray diffraction (XRD) analysis with a Bruker D8 (Cu-Kα radiation, λ = 0.15418 nm) over the 2θ range of 20°-80°. Transmission electron microscopy (TEM) images were obtained using a FEI Tecnai 20 TF20 FEGTEM, and the Image J software was utilised to obtain the area-equivalent diameter of Au and SnO_2 NPs. To avoid post-synthesis agglomeration problem during drying, the Au NPs specimens for TEM analysis were prepared according to Michen et al.'s protocol. [195] [215] To understand the nucleation process of SnO_2 in the microfluidic reactor, a liquid cell TEM (LCTEM, with SiN_x membranes) was used and images undertaken in FEI Titan^3 Themis G2 TEM. UV-vis optical absorption spectra of the products were obtained by a Cary 5000 UV-Vis-NIR spectrophotometer. The photoluminescence (PL) intensity of the samples was detected using a fluorescence spectrometer (Cary Eclipse, Varian Medical Systems, USA). The UV-vis spectra of the as-prepared Au NPs were recorded on an Agilent Cary 60 UV-vis spectrophotometer between 400-800 nm with a wavelength resolution of 2 nm. The Brunauer-Emmett-Teller (BET) specific surface area of the samples was determined through nitrogen absorption at -196 ^oC. All the samples were degassed at 100 ^oC for 5 h before measurement.

4.2.3 Photocatalytic activity test

The photocatalytic performance of pristine SnO_2 and Au@SnO_2 was evaluated by degradation of Rhodamine B. 30 mg of catalyst powder was added to 100 ml Rhodamine B (RhB) solution (concentration of 10 mg/L). Before irradiation by solar simulator (150 W xenon lamp fitted with an air mass 1.5 global (AM 1.5G) filter, Oriel® Sol3A^{TM}, 1 sun illumination, 100 mW cm^{-2} with light filter > 400 nm), the suspension was stirred in the dark for 60 mins to reach the adsorption equilibrium. 3 mL of the suspension solution were taken out at each 30 min interval and centrifuged for 10 min to obtain the supernatant. The residual concentration of RhB dye in the supernatant was measured by a UV-vis spectrophotometer (Perkin Elmer LAMBDA 265) at 554 nm.

4.3 Synthesis of SnO_2 nanocrystals in batch and microreactor

The hydrothermal method is a widely utilised approach for synthesizing SnO_2 nanoparticles, involving a reaction within an autoclave under elevated pressure and high temperature. The resultant products are white precipitates or clear solutions from the chemical reaction between tin (IV) chloride and sodium hydroxide which are closely linked to the final pH values. At lower pH value, total or partial precipitation of $Sn(OH)_4$ is formed according to the following reaction (Equation 4-1).

Subsequently, through heating within the autoclave, the precipitate $Sn(OH)_4$ decomposes to SnO_2 nanoparticles (Equation 4-2). [216]

$$SnCl_4 + 4\,NaOH = Sn(OH)_4 + 4\,NaCl \quad (4\text{-}1)$$

$$Sn(OH)_4 = SnO_2 + 2\,H_2O \quad (4\text{-}2)$$

When excess OH^- is added, the white precipitate $Sn(OH)_4$ dissolves by reacting with abundant hydroxide ions, with the intermediate hydroxide $Sn(OH)_6^{2-}$ formed (Equation 4-3). Then during the heat treatment of the hydrothermal method, when the solution critical concentration reaches supersaturation, the SnO_2 nuclei are formed spontaneously through a condensation reaction. [216] [217] When the temperature further rises, especially upon reaching the supercritical regime of the solutions, the polarity - distribution of charge within the molecules of the solution - can undergo a shift. This change in polarity influences the way SnO_2 crystals grow, leading to anisotropic growth where the crystals preferentially grow in certain directions. Aref *et al.* [67] reported that SnO_2 crystal growth explodes and anisotropic nanorods formed when the hydrothermal temperature increases to 400 °C. At this temperature, the water's structure transitions to a non-polar state, contributing to the observed effects. Kazuyoshi *et al.* [218] reported the synthesis of cubic-shaped SnO_2 nanocrystals by utilising $SnCl_4$ and NaOH, along with ammonium hydroxide as a surface capping agent, using a hydrothermal method at 150 °C for 24 h.

$$Sn(OH)_4 + 2\,NaOH = Na_2Sn(OH)_6 \quad (4\text{-}3)$$

$$Na_2Sn(OH)_6 = SnO_2 + 2\,NaOH + 2\,H_2O \quad (4\text{-}4)$$

4.3.1 The synthesis of SnO_2 nanocrystals in batch reactor

The aim of this experimental is to synthesise SnO_2 nanocrystals under room-pressure and low-temperature condition. Firstly, we explore the impact of varying concentrations of NaOH and $SnCl_4$ on the production of SnO_2. To achieve this, we conducted a series of experiments in batch reactors at room temperature with 5 mins reaction time, and the photographs of reaction mixtures are shown in Figure 4.1. $SnCl_4$ (0.05 M) was mixed with different concentrations of NaOH solution (the molar ratios of $SnCl_4$ to NaOH range from 1/3 to 1/12) at room temperature. When the pH value was between 1.16 to 10.93 (the molar ratios of $SnCl_4$ to NaOH range around from 1/3 to 1/4.5), total or partial precipitation of $Sn(OH)_4$ was formed according to the following reaction (Equation 4-2). When excess OH^- was added, a clear solution was obtained, and the white precipitate $Sn(OH)_4$ dissolved immediately by reacting with abundant hydroxide ions, the intermediate hydroxide $Sn(OH)_6^{2-}$ formed when pH value reaches up to 10.93 (Equation 4-3).

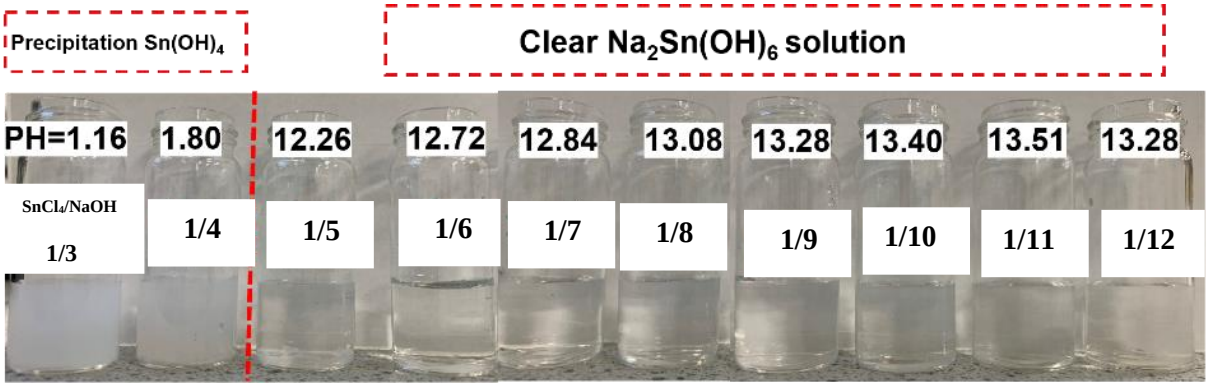

Figure 4. 1 Photographs of reaction mixtures of $SnCl_4$ (0.05M) mix with various concentrations of NaOH solution (the molar ratios of $SnCl_4$ to NaOH range from 1/3 to 1/12) in vials, room temperature, 5 mins of the residence time.

The molar ratio of $SnCl_4$ (0.05 M) to NaOH (0.3 M) was maintained at 6, resulting in a clear mixture solution with a pH value of 12.72. In aqueous solution, $Sn(OH)_6^{2-}$ has higher solubility at room temperature without crystallisation of SnO_2. To induce SnO_2 precipitation, we maintained the reaction temperature at 70ºC, 80ºC, and 90ºC, resulting in successive decreases in precipitation formation time to 17 mins, 7 min 55 s, and finally 5 mins. It shows that as the temperature increases, the solution reaches a critical concentration where SnO_2 nuclei form through agglomeration (Equation 4-4). Furthermore, to investigate the influence of $SnCl_4$ concentration, it was maintained at 0.1 M, 0.05 M, and 0.025 M. The precipitation formation time increased successively from 2 mins 20 s to 5 mins. At the concentration of 0.025 M, there was no precipitation even after 30 mins at a reaction temperature of 90ºC. The experimental findings indicate that elevating both the temperature and $SnCl_4$ concentration improved the precipitation process of SnO_2 nanocrystals.

To further speed up the SnO_2 synthesis process at room temperature, ethanol was added to the solution of $SnCl_4$ and NaOH mixture. SnO_2 white precipitate was formed (confirmed by the XRD result in Figure 4.3 [219]) even at room temperature when the molar ratio of $SnCl_4$ to NaOH ranges at and below 1/6, as shown in Figure 4.2. However, when the concentration ratio of $SnCl_4$/NaOH decreases from 1/7 to 1/12, no precipitation occurs at room temperature. The lack of precipitation attributed to the excess alkali, which suppresses the nucleation of SnO_2. [218] The resultant precipitation was centrifuged (5000 rpm, 30 min) and washed with ethanol and water repeatedly until the absence of chloride ion ($AgNO_3$ test). [220]

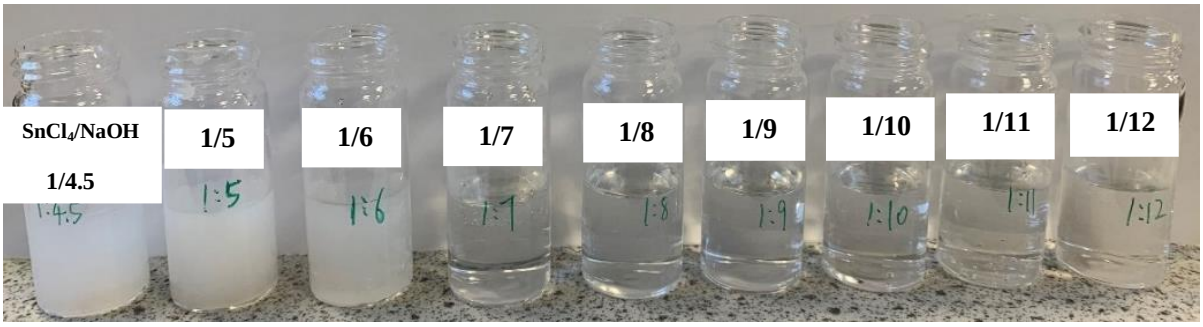

Figure 4.2 Photographs of reaction mixtures of ethanol adding into $SnCl_4$ with different NaOH mixture solution (the molar ratios of $SnCl_4$ to NaOH range from 1/4.5 to 1/12) at room temperature (the volume ratio of ethanol to $SnCl_4$/NaOH mixture is 1/1).

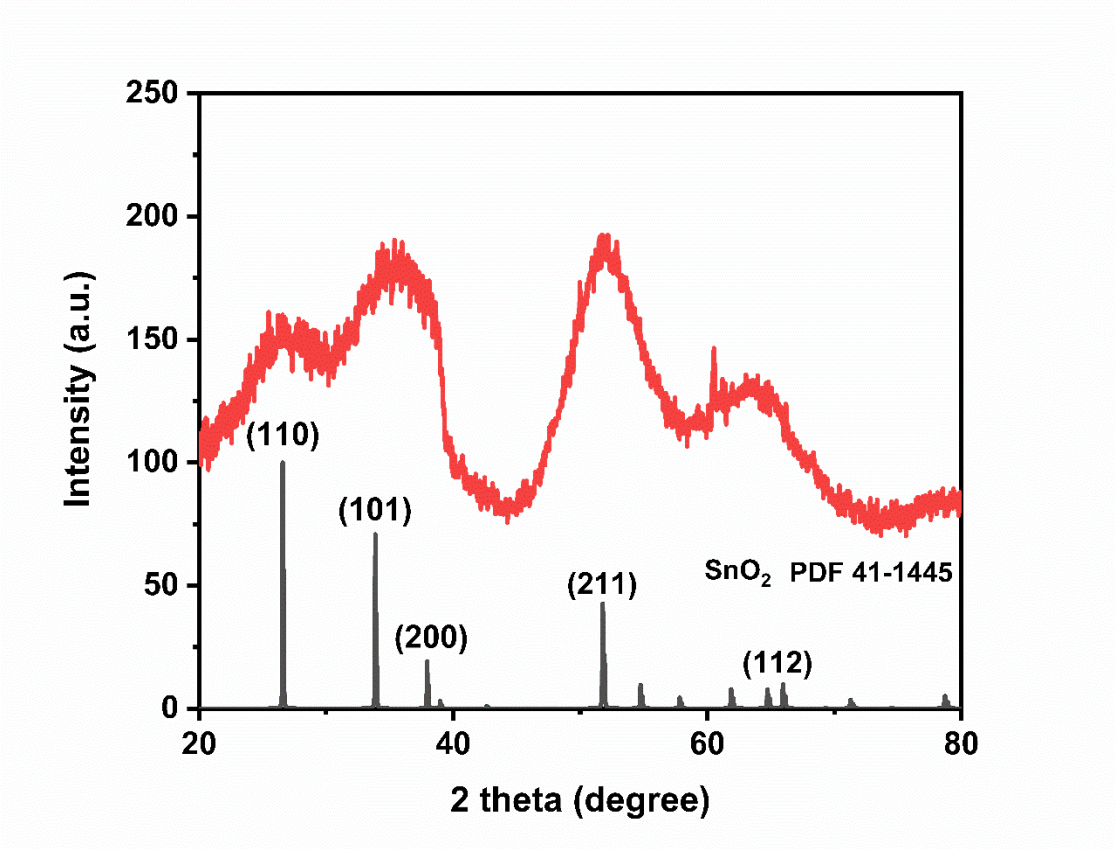

Figure 4.3 XRD pattern of SnO_2 precipitations synthesising by adding ethanol into $SnCl_4$ with NaOH mixture solution at room temperature, with the molar ratio of $SnCl_4$ to NaOH 1/4.5 and the volume ratio of ethanol to $SnCl_4$/NaOH mixture 1/1.

The polar characteristic of the solvent is proposed to influence both nucleation and growth process of semiconductor nanoparticles. For minerals and solid electrolytes [99]:

$$A_\alpha B_\beta = \alpha A^{a+} + \beta B^{b-} \quad (4\text{-}5)$$

$$S = \frac{a_\pm}{a_\pm^*} = \left(\frac{a_A^\alpha a_B^\beta}{K_{sp}}\right)^{1/v} \quad (4\text{-}6)$$

Where $v = \alpha + \beta$ is the total number of ions in each formular unit, $a_{\pm}$ is the mean activity of the ionic species, a_A and a_B are the activities of cation and anion, K_{sp} is the product solubility, S is the supersaturation.

When adding ethanol, the decreased polarity of the solution will rapidly decrease the solubility K_{sp} of SnO_2 and then increase the supersaturation S, so the rapid crystallisation form suddenly with smaller SnO_2 nuclei from the intermediate hydroxides $Na_2Sn(OH)_6$. [221] To observe the precipitation process of SnO_2, in situ liquid cell TEM was used. Dual inlet liquid streams of ethanol and the $SnCl_4$/NaOH mixture solution (the molar ratio is 1/6) were mixed and flowed through a liquid cell chip at room temperature. Amorphous SnO_2 particles nucleated within 1s and then aggregated to diameters of up to hundreds of nanometers, shown in Figure 4.4. However, the spatial resolution of the experiments undertaken does not provide insight into the question of whether nucleation occurs via ion-by-ion attachment, as per 'classic nucleation theory', or whether stable or metastable clusters serve as the primary species of addition, as 'non-classic nucleation theory'. As for the SnO_2, the solution is saturated so quickly when ethanol is added that a high number of nuclei of the precipitates are generated suddenly. So, the high nucleation rate will lead to the formation of small, irregular crystal in a very short time with morphology hard to control. The irradiating electrons have a strong effect on the local pH of the solution and colloid aggregation. [222] To rule out aggregation caused by changes in pH value, the $SnCl_4$/NaOH mixture solution (the molar ratio is 1/6) were mixed and flowed through a liquid cell chip at room temperature without adding ethanol. After 30 s, no aggregation was observed. This implies that the addition of ethanol induces the formation of SnO_2 nanocrystals, and the cause is not attributed to a change in local pH values.

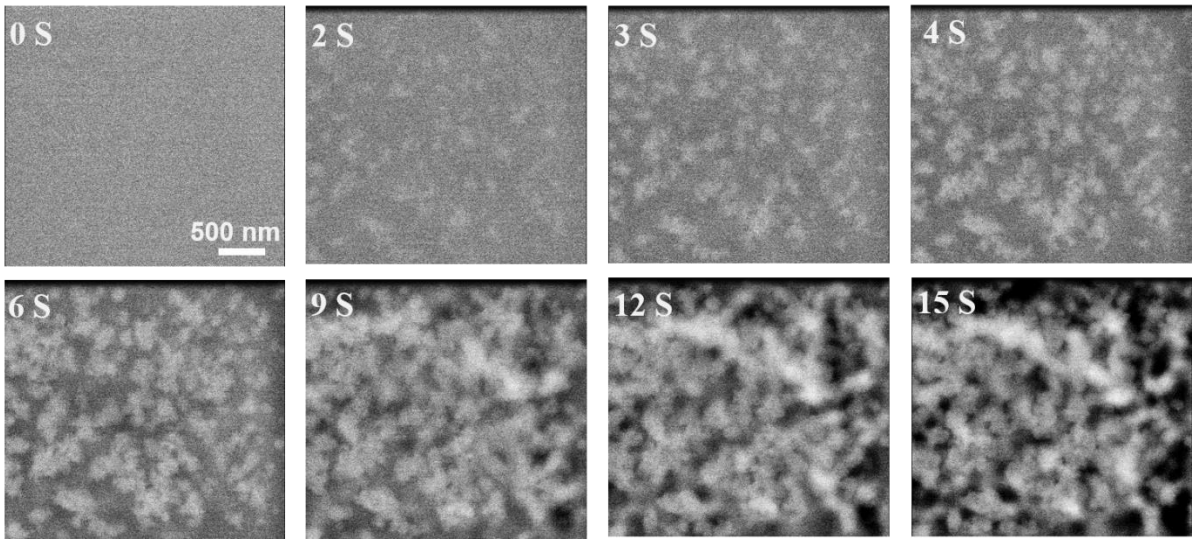

Figure 4.4 STEM images of nucleation and growth process of SnO_2 crystals by adding ethanol monitored by in situ LPTEM at room temperature.

The morphology of nanoparticles can also be influenced by solvent polarity through adding organic solvents. Khoza *et al.* [223] reported that the intermediate hydroxides $Zn(OH)_4^{2-}$ convert into ZnO with varying morphologies when subjected to different polar solvent mediums, water, ethanol, or acetone under microwave heating at 120 °C for 15 mins. Specifically, a mixed solvent of water and ethanol is commonly employed in the hydrothermal method for the formation of SnO_2 nanorods, which elongate their *c* axis to form non-spherical like hierachical nanostructures. It is well accepted that SnO_2 prefer to grow along the [001] direction with the (110) facet, because the surface energy per crystal face can be sequenced as (110) < (100) < (101). [217] [218] The driving forces for the growth of 1D SnO_2 nanorods are believed to originate from the chemical potential in the ethanol/water solution and the inherent crystal structure of SnO_2. [224] In another investigation by Inderan *et al.* [217], a complete conversion from nanospheres to nanoplates and finally nanorods of SnO_2 were successfully synthesised through hydrothermal treatment at 180 °C with different concentration of $SnCl_4 \cdot 5H_2O$ (0.04 M–0.16 M) dissolved in a solution of ethanol and water.

We propose that ethanol can speed up the nucleation of SnO_2 at lower temperatures, prompting small nuclei agglomerate into quasi-spherical (particle size range from 50-300 nm) without undergoing further anisotropic growth. As the temperature increases, the water/ethanol mixture solution could help to form the SnO_2 nanorod structures. To validate this proposition, we obtained SnO_2 in both a microreactor (90 °C, 5 mins) and an autoclave (a 50 mL Teflon-lined stainless-steel vessel, 250 °C, 24 h) by reacting ethanol with $SnCl_4$ (0.05 M) / NaOH (0.3 M) mixture. As shown in Figure 4.5, SnO_2 NPs with both quasi-spherical and nanorod shapes (similar as the morphologies reported in [217] and [224]) were formed in microreactor (Figure 4.5 (a)) and autoclave (Figure 4.5 (b)), respectively.

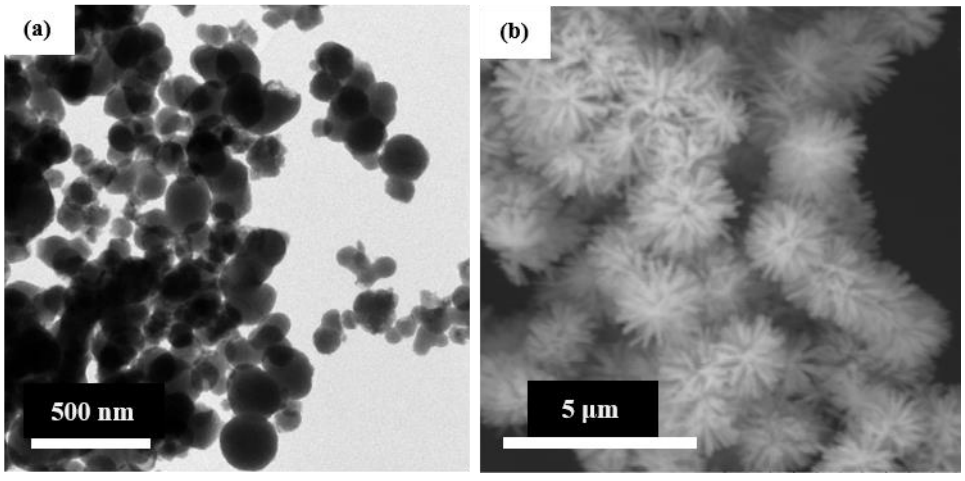

Figure 4.5 (a) TEM image of pristine SnO_2 spherical semiconductor synthesised in microreactor, 90 °C, 5 mins. (b) SEM images of SnO_2 nanorod semiconductor in autoclave, 250 °C, 24 h.

4.3.2 Experimental set-up of SnO_2 nanocrystals in microreactor

Here to scale up the production of SnO_2 nanocrystals, a lab-made microreactor system was made, shown in Figure 4.6. A helical polytetrafluoroethylene tube (250 cm, PTFE, IDEX Health & Science LLC) with 1/16 inch inner diameter and 1/8 inch outer diameter coiled tightly around a cylindrical support (diameter is 20.05 mm). 0.05 M (1.751 g) of $SnCl_4 \cdot 5H_2O$ and 0.3 M (1.2 g) of NaOH (the molar ratio of NaOH/$SnCl_4$ is 6/1) was used as the precursor solution. Two syringe pumps (Chemyx, Fusion 100) were used to deliver the $SnCl_4$/NaOH solution and ethanol each with a flow rate of 0.5 mL/min and a residence time of 5 mins. The two streams were mixed in a T mixer (PEEK, 0.50 mm through hole, IDEX Health & Science LLC). The reactor was immersed in a constant-temperature water batch to maintain a reaction temperature of 90 °C. At the outlet, a nitrogen cylinder was used to control the system pressure to ensure that no bubbles were formed in the system, and the reaction was quenched by using ice bath. The resultant precipitation was centrifuged (5000 rpm, 30 min) and washed with ethanol and water repeatedly until the absence of chloride ion ($AgNO_3$ test). [220]

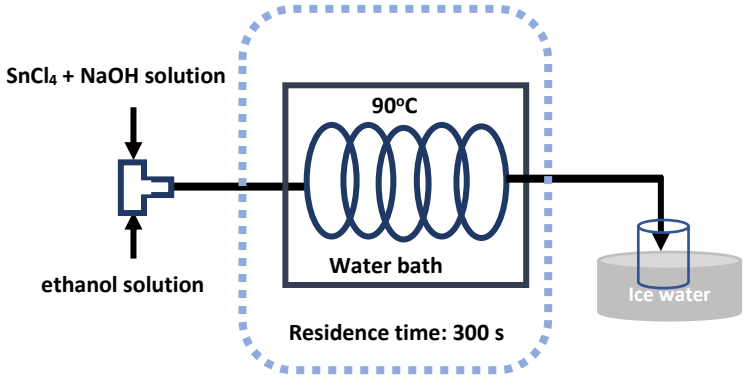

Figure 4.6 Schematic diagram of the experiment setup for SnO_2 semiconductor synthesis.

4.4 The characterisation results and photocatalytic property of SnO_2 synthesising in microreactor

Figure 4.7 (a-c) shows a TEM image of pristine polycrystalline SnO_2 and the corresponding Fast Fourier Transform (FFT) patterns obtained in microreactor. SnO_2 shows a quasi-spherical morphology, and its crystallites display random orientation, causing the lattice fringes to be rotated in different directions. The broad diffraction peaks in the XRD pattern (JCPDS, 41-1445, a tetragonal phase with a $P4_2/mnm$ space group, D_{4h}) imply small grain sizes (Figure 4.7 (d)). The crystallite size measured in TEM image is 3.06 ± 0.51 nm using software Image J, which agrees with grain size (3.12 nm) calculated according to the Scherer's formula. [219]

$$d = 0.89\lambda/\beta cos\theta \qquad (4\text{-}7)$$

where 0.89 is Scherrer's constant for sphere, λ is the X-ray wavelength, θ is the Bragg diffraction angle, and β is the full width at half maximum (FWHM) of the diffraction peaks.

The tetragonal crystal structure was identified by the FFT patterns (shown in Fig. 4-10 (c)), which are indexed to the distinctive (110), (101), (211), and (112) planes of SnO_2. The fringe patterns are in harmony with the peaks observed in the XRD pattern.

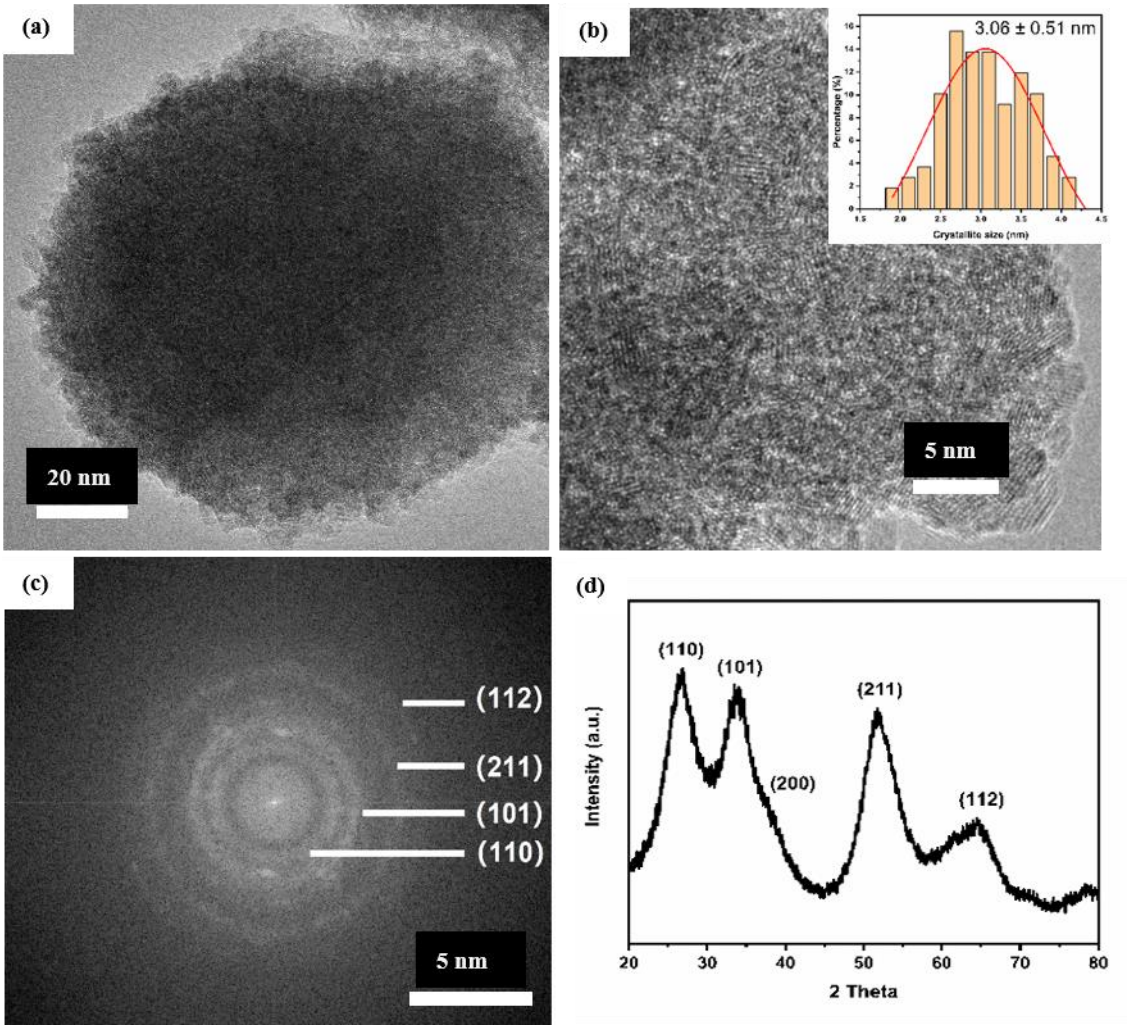

Figure 4.7 (a) TEM image of a large grouping of SnO_2 NPs, with particle size of ~ 130 nm, (b) higher magnification TEM image where individual ~ 3 nm crystalline nanoparticles are visible, (c) corresponding Fourier transformation, (d) XRD pattern of pristine SnO_2 semiconductor synthesised in microreactor, 90 ^oC, 5 mins.

The optical absorption of pristine SnO_2 was monitored through UV/Vis diffuse reflectance spectroscopy, shown in Figure 4.8 (a). The SnO_2 nanoparticles only respond to the UV light and no absorption could be observed in the visible wavelength. The band gap energy was calculated from the UV-vis spectra using the TAUC model. [225] This model relates the absorption coefficient to the energy of the incident photon by the following equation:

$$\alpha(v)hv = k\left(hv - E_g\right)^n \quad (4\text{-}8)$$

Where E_g is the band gap energy, hv is the energy of the incident photon, k is a constant, and $\alpha(v)$ is the absorption coefficient which can be defined by Beer-Lamber's law. The exponent n depends on the type of transition. For SnO_2 NPs, the value of n is 1/2 for the direct allowed transition.

Plots of $\alpha(hv)^2$ versus hv can be derived from the adsorption data in Figure 4.8 (b). The intercept of the tangent to the plot gives an approximation of the band gap energy of the semiconductor. The estimated band gap values of pure SnO_2 is 3.24 eV, which is less than that of the bulk SnO_2 (3.62 eV). The narrowing band gap might be due to the up-shift of the valence band maximum induced by the presence of the oxygen vacancies/defects in the SnO_2. [226] Arik *et al.* studied that the oxygen vacancy defects in semiconductor nanocrystals act as active centres to capture the photoinduced electrons, which will control the electron-hole recombination process and thus their photocatalytic properties. [227]

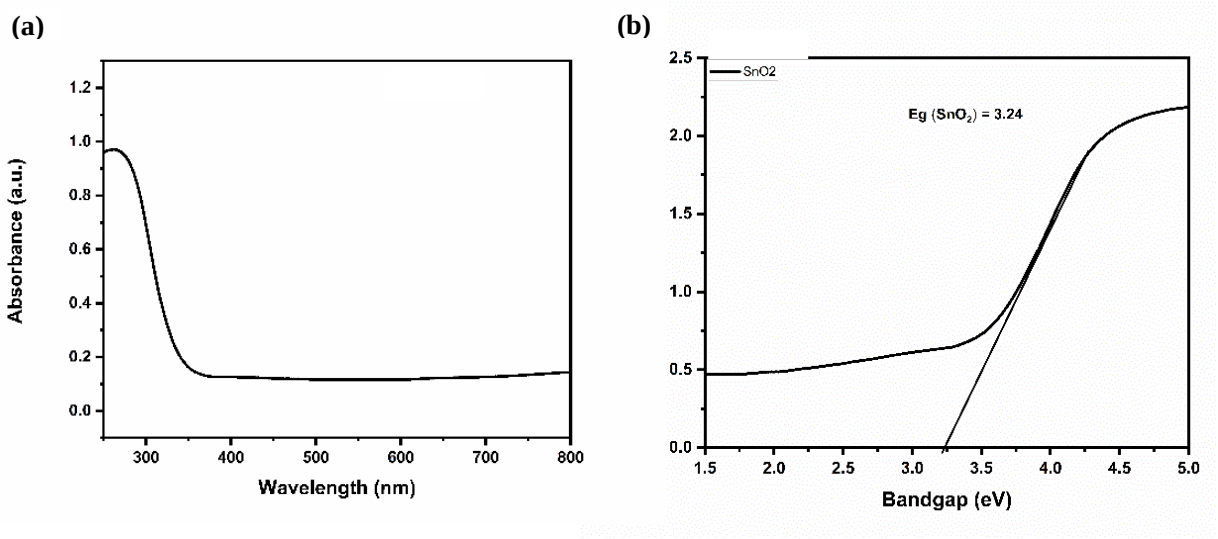

Figure 4.8 (a) Diffuse reflectance UV-visible (DRUV) spectra and (b) Optical band spectra of pristine SnO_2 synthesised in microreactor, 90°C, 5 mins.

The surface-related defects of pristine SnO_2 were investigated by Raman spectroscopy, shown in Figure 4.9. Here the SnO_2 nanocrystal is rutile in nature with the space group D_{4h} and the normal lattice vibration at the Γ point of the Brillouin Zone is given by Equation 4-9 [20][21]:

$$\Gamma = 1\,A_{1g} + 1\,A_{2g} + 1\,A_{1u} + 1\,B_{1g} + 1\,B_{2g} + 2\,B_{1u} + 1\,E_g + 3\,E_u \quad (4\text{-}9)$$

Where B_{1g}, E_g, A_{1g}, and B_{2g} are the Raman active modes. The Raman spectrum of SnO_2 nanoparticles, where peaks at 474, 630, 773 cm^{-1} correspond to E_g, A_{1g}, and B_{2g} vibration modes, respectively. The peak at 577 cm^{-1} which is not detected in the bulk rutile SnO_2 is assigned to the

surface defects of the SnO_2 nanocrystals. [230] Compared with the Raman peaks of bulk rutile SnO_2, the broader Raman peaks is related to the nanocrystalline nature of the prepared SnO_2.

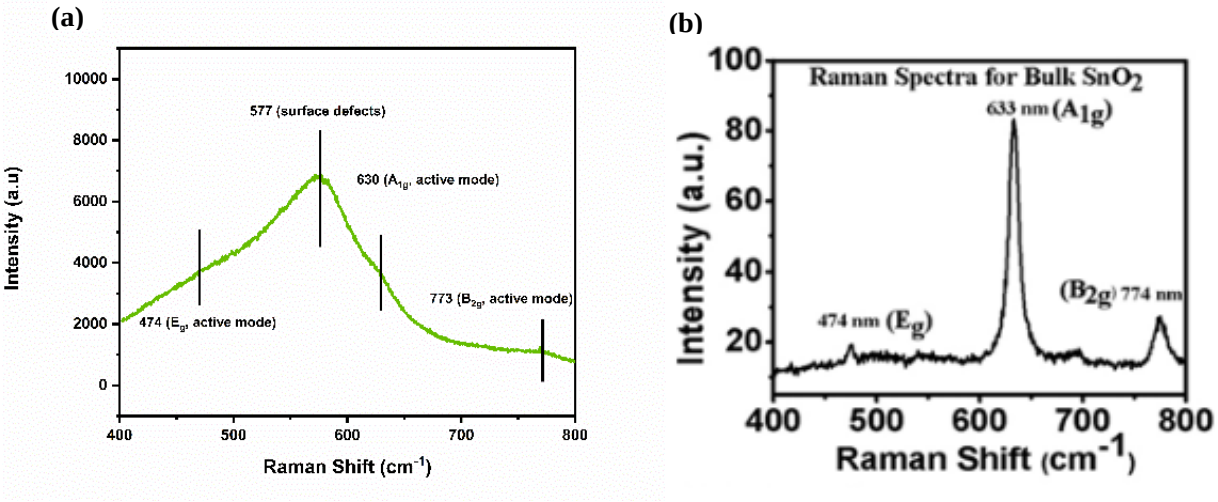

Figure 4.9 Raman spectra of (a) pristine SnO_2 nanoparticles synthesised in microreactor, 90 °C, 5 mins and (b) standard bulk SnO_2, cited from the copyright [227].

In evaluate the photocatalytic performance of SnO_2 nanoparticle, experiments were conducted using Rhodamine Blue (RhB) as a test compound under both visible light and simulated solar light conditions. Figure 4.10 depicts the absorption of RhB measured every 30 mins to assess the photocatalytic property of SnO_2. A blank experiment was investigated as comparison, no RhB was degraded without catalyst under light irradiation. Pure SnO_2, characterised by its wide band gap, exhibited minimal photocatalytic activity under visible light (Figure 4.10 (a)). Under simulated solar light, only slight photocatalytic degradation was observed, however, this performance does not meet the application requirements. [231] The pure SnO_2 materials has the ability to absorb UV light and exhibit some photocatalytic properties, which has been reported before. [227] [232] In conclusion, for the pristine SnO_2 NPs synthesised in the microreactor, their photocatalytic properties need to be tested in the future work.

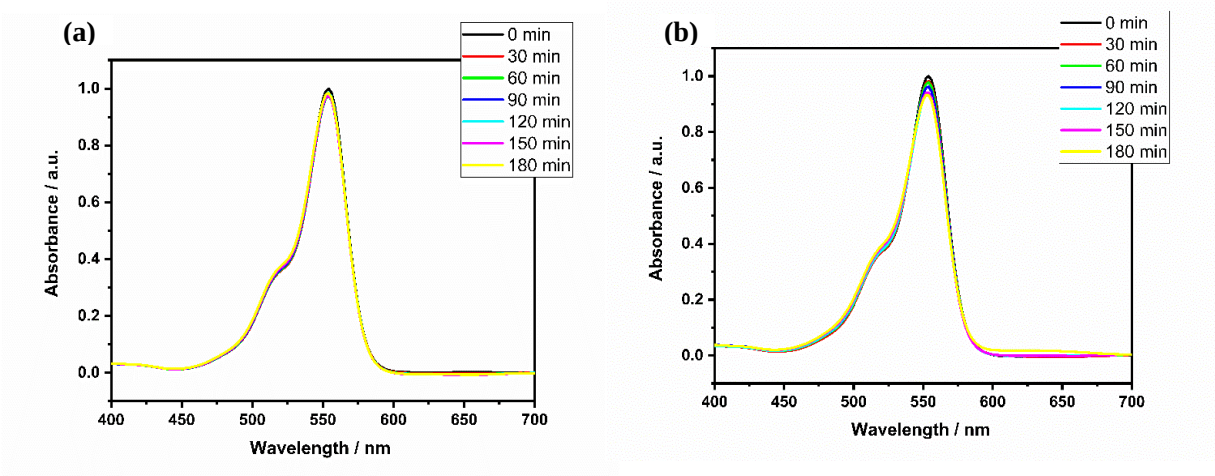

Figure 4.10 The absorption of RhB using SnO_2 nanoparticles as catalysts under (a) visible light and (b) simulated solar light.

4.5 Summary

In this section, the factors of pH value, precursor concentration, temperature, solvent polarity were studied on the nucleation and growth process SnO_2 nanocrystals using hydrothermal method in a batch reactor. To scale up the synthesis of SnO_2 nanocrystals, we transitioned the synthesis from a batch reactor to a microfluidic system for the first time. The system operates at a temperature of 90°C, with residence time of 5 mins, and utilizes ethanol to accelerate the SnO_2 agglomeration. The band gap of SnO_2 nanocrystals synthesised in the microreactor is 3.24 eV lower than the bulk, attributed to the presence of the oxygen vacancy. However, its photocatalytic activity under the visible light and simulated solar light remains negligible.

4.6 Incorporating Au nanoparticles into SnO_2 semiconductor

The pristine SnO_2, as discussed above, exhibits no absorption in the visible light spectrum, thus displaying almost no photocatalytic properties under simulated solar light. Plasmonic metal/semiconductor are regarded as being a very effective way to enhance the solar-light harvesting in the photocatalysis owing to the surface plasmon resonance (SPR) effect and also prevent the hole-electron recombination by charge transfer. [50][51] Mostly the plasmonic metal nanoparticles are noble metals such as Au, Ag, Pt, etc.

The solar energy conversion efficiency of a binary composite photocatalysts is determined by the material composition, material shape and size features as well as the geometric arrangement of the building blocks. Herein, three different ways to incorporate Au NPs with SnO_2 were compared to get the best combination structure: (1) Au NPs coated on the SnO_2 matrixes, (2) Au NPs surrounded by

SnO_2 matrixes, and (3) Au NPs embedded in SnO_2 matrixes. In order to achieve large-scale production of Au@SnO_2, we firstly employ continuous microfluidic methods to synthesise the hybrid Au@SnO_2 composite in a micro-capillary reactor.

4.6.1 Two-stage synthesis method for Au-SnO_2: coating Au NPs on SnO_2 matrixes

In the first stage, the prepared $SnCl_4$ (0.05 M)/NaOH (0.3 M) solution and the ethanol were injected into the microreactor through the T-mixer (PEEK, 0.50 inch through hole, IDEX Health & Science LLC) to get the SnO_2 with the same flow rate 0.5 ml·min^{-1}, 90 ^{o}C, 300 s. To incorporate Au NPs with SnO_2, a freshly prepared precursor aqueous solution (0.019 mM, 0.038 mM, or 0.076 mM $HAuCl_4$) was pumped to mix with the production in previous stage at room temperature for 300 s. Subsequently, the reducing agent solution (($NaBH_4$/$HAuCl_4$ = 12/1, Na_3CA/$HAuCl_4$ = 5/1) was pumped to synthesis Au NPs at 90^{o}C for 180 s, shown in Figure 4.11. The resultant precipitation was quenched in ice water and then centrifuged and washed as producing pristine SnO_2. The theoretical weight ratio of Au NPs to SnO_2 is 0.025 wt%, 0.05wt% and 0.1 wt% assuming all the Au+ has been reduced to Au atoms.

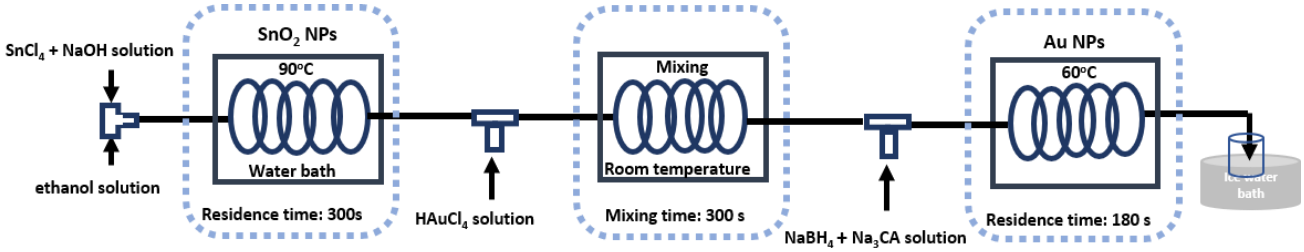

Figure 4.11 Schematic diagram of the experiment setup for Au-SnO_2 two-stage synthesis method.

4.6.2 Two-stage synthesis method for SnO_2-Au: Au NPs surrounded by SnO_2 matrixes

To precisely control the particle size distribution of metal nanoparticles, the preparation process of Au@SnO_2 catalysts comprises two main steps: (i) synthesis of size-controlled Au NPs; (ii) self-assembly assisted precipitation of SnO_2 around the preformed Au NPs. In the first stage, monodispersed Au nanoparticles were prepared in spiral microreactor following a modified protocol [233]. The synthesis process was carried out at 60 ^{o}C using freshly prepared precursor aqueous solution (0.019 mM, 0.038 mM, or 0.076 mM $HAuCl_4$) and reducing agent solution ($NaBH_4$/$HAuCl_4$ = 12/1, Na_3CA/$HAuCl_4$ = 5/1). Both solutions were introduced into reactor using syringe pumps with volumetric flow rate 0.5 ml·min^{-1}, and with a residence time of 180 s.

In the second stage, the obtained Au colloid solution was directly fed into cross-type mixer (PEEK, 0.20 inch through hole, IDEX Health & Science LLC). At the same time, the prepared $SnCl_4$ / NaOH solution and the ethanol were injected into with the same flow rate 0.5 ml·min^{-1}, shown in Figure 4.12. The theoretical weight ratio of Au NPs to SnO_2 is 0.025 wt%, 0.05wt% and 0.1 wt%.

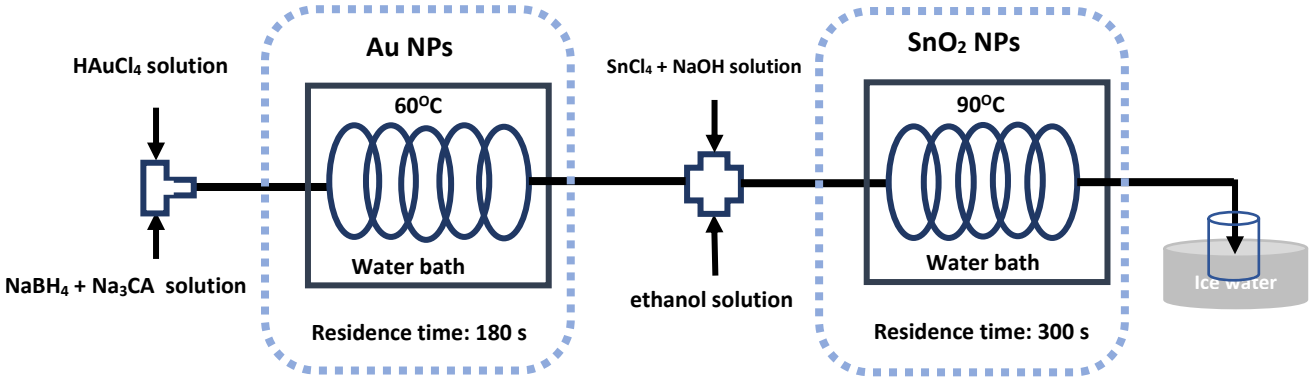

Figure 4.12 Schematic diagram of the experiment setup for SnO_2-Au two-stage synthesis method.

4.6.3 One-pot synthesis method for SnO_2-Au: Au NPs embedded in SnO_2 matrixes

A third method was attempted in an aim to achieve high dispersion of Au NPs and SnO_2 nanocrystals with an intimate contact by preparing both components cooperatively. Three solution inlets of precursor solution ($HAuCl_4$ (0.019 mM, 0.038 mM, or 0.076 mM), $SnCl_4$ (0.05M) and NaOH (0.3 M)), ethanol and reducing agent ($NaBH_4$/$HAuCl_4$ = 12/1, Na_3CA/$HAuCl_4$ = 5/1) were pumped via cross-type mixer into the microreactor, shown in Figure 4.13. The SnO_2 can be precipitated out from the solution with Au NPs formed after the reduction of Au^+. The Au NPs would be trapped inside the precipitated SnO_2 with good mixing. The theoretical weight ratio of Au NPs to SnO_2 is 0.025 wt%, 0.05wt% and 0.1 wt%.

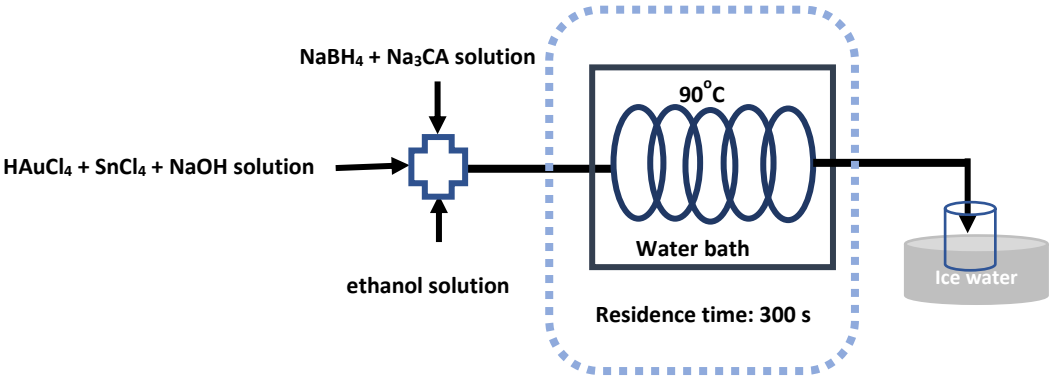

Figure 4.13 Schematic diagram of the experiment setup for one-pot SnO_2-Au synthesis method.

4.7 Results and discussion

4.7.1. Au NPs coated on the SnO_2 matrixes

Figure 4.14 illustrates the overall microstructure of the composite material, depicting Au NPs adhering to the surface of SnO_2 nanocrystals. The method employed (Figure 4.11) achieved a theoretical weight content of SnO_2 to Au around at 0.05 wt%. Hence, establishing a robust bond between plasmonic metal nanoparticles and the semiconductor surface is crucial for enhancing their photocatalytic properties. However, in the preparation process of this SnO_2-Au structure, after centrifugation the Au NPs and SnO_2 became separated. Following multiple washing steps, the Au NPs were eventually removed. Therefore, this method is not conducive to obtaining a well-formed plasmonic metal and semiconductor composite structure.

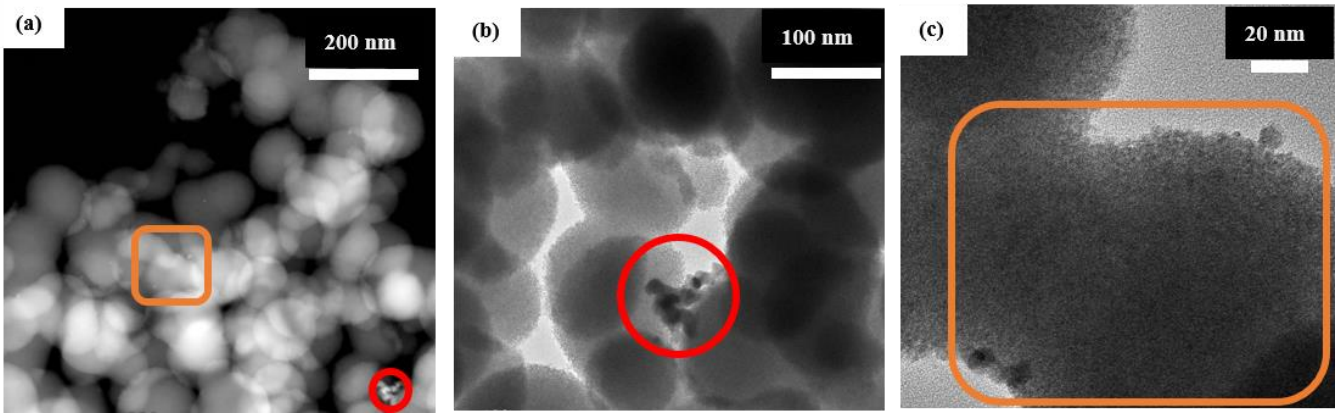

Figure 4.14 (A) HAADF-STEM images of SnO_2@Au nanostructure with the amplified TEM images in marked area (red circle-(B), rectangle-(C)).

4.7.2 Au NPs surrounded by SnO_2 matrixes

To achieve a stable hybrid composite of Au NPs and SnO_2 matrixes to improve their synergistic coupling efficiency, the composite materials, where Au NPs are surrounded by SnO_2, were produced using a SnO_2-Au two-stage synthesis method in section 4.6.2, as depicted in Figure 4.12. In the first stage, Au NPs were synthesised using a wet chemical reduction method in the microreactor setup. Subsequently, in the second stage, SnO_2 matrixes were formed and encapsulated the Au NPs within them. After centrifugation, the combination of materials remains stable. However, after several additional washes, the Au NPs separate from the SnO_2 matrixes. The colour of Au NPs is purple, while the colour of SnO_2 is grey-white. Following several centrifugation cycles, it was observed that the purple colour concentrating at the bottom of the materials, indicating decreased stability between

these two materials. To investigate the impact of the weight ratio of Au NPs to SnO_2, three different concentrations of $HAuCl_4$ at 0.038 mM, 0.076 mM, and 0.152 mM were used, aiming for theoretical ratios of 0.025 wt%, 0.05 wt%, and 0.1 wt%, respectively. The LSPR position of Au NPs colloids centre at 520-526 nm, shown in Figure 4.15.

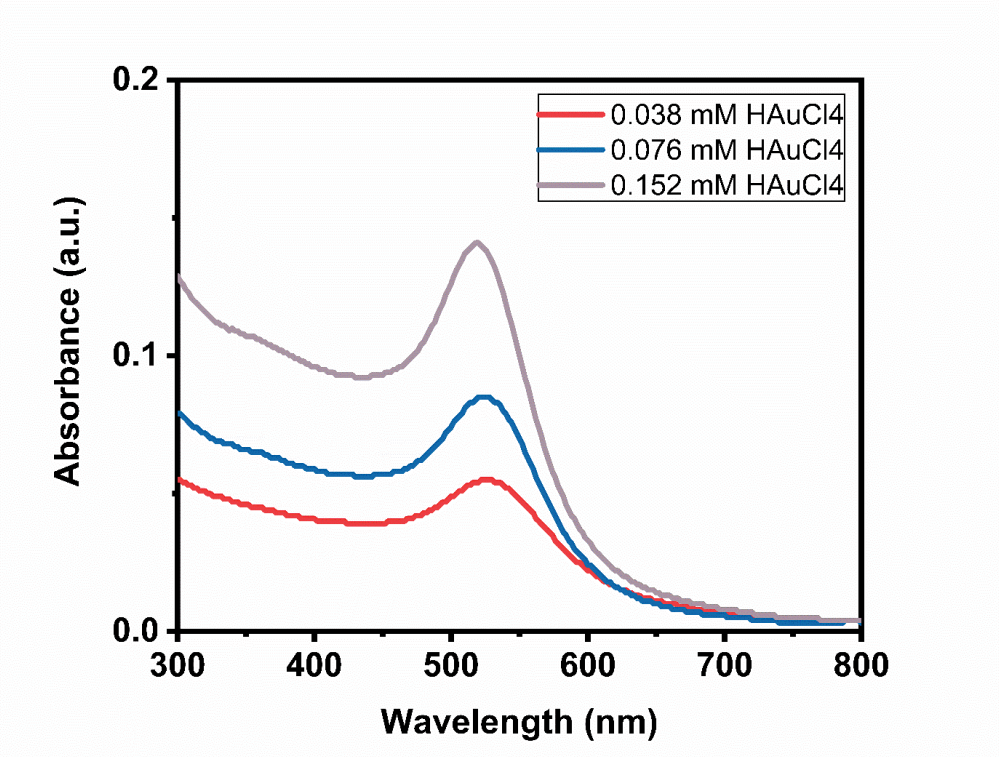

Figure 4.15 UV-vis absorption spectra of Au NPs synthesised at different precursor concentration. A: 0.038 mM, B: 0.076 mM, C: 0.152 mM.

To observe the combination mode of the Au@SnO_2 structure, STEM images of 0.05 wt% Au-SnO_2 were utilised, as shown in Figure 4-16 (a) and (b). While Au NPs (with average particle size 15 nm) were embedded within the SnO_2 matrixes, it is evident that the Au did not tightly integrate with SnO_2, revealing noticeable gaps between these two materials. The XRD result in Figure 4.16 (c) did not show obvious Au NPs peaks. This could be attributed to the lower weight content of Au NPs inside. Additionally, the (200) peak in the SnO_2 pattern overlaps with the main reflection of Au, further complicating the identification of Au NPs peaks.

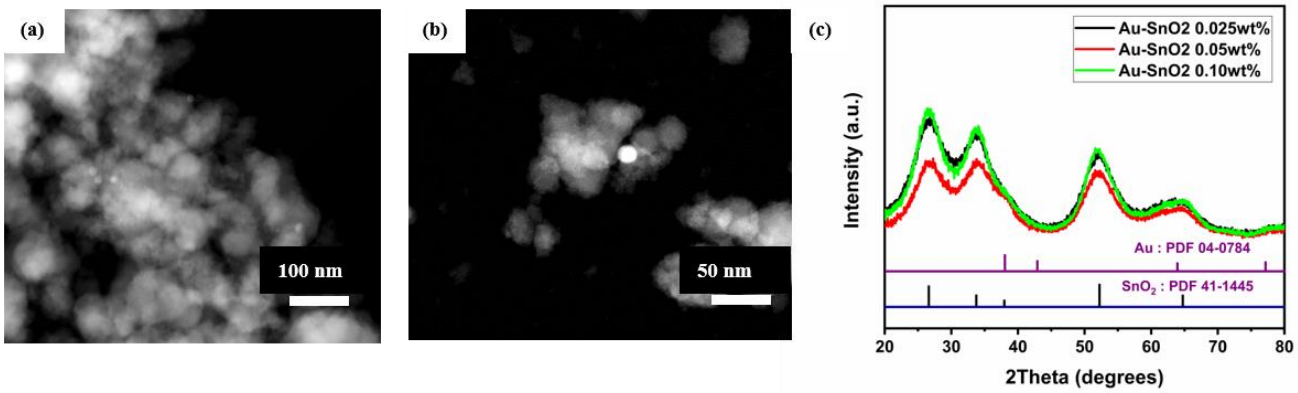

Figure 4.16 (a) (b) STEM images and (c) XRD pattern of 0.05 wt% Au- SnO_2 nanostructure. [219][234]

4.7.3 Au NPs embedded with SnO_2 matrixes

To enhance the contact interface between Au NPs and SnO_2, a one-pot synthesis method was employed to synthesize Au NPs embedded within SnO_2 matrixes, as illustrated in Figure 4.13. The gold precursor ($HAuCl_4$) and tin precursor ($SnCl_4$) were mixed together firstly. Subsequently, ethanol and the reducing agents ($NaBH_4$ and Na_3CA) were added, facilitating the simultaneous formation of Au NPs and SnO_2 in the reaction. To observe the combination mode of the one-pot structure, STEM images of 0.05 wt% SnO_2-Au were utilized, as shown in Figure 4.17 (a) and (b). The Au NPs embedded within the SnO_2 matrixes, without gaps between these two materials. The particle size of Au NPs is not uniform, ranging from 5 to 20 nm. The lack of uniformity maybe attributed to the complex reaction environment, making it challenging for the Au NPs to control their particle size when interacting with SnO_2 nanocrystals. From the XRD result (Figure 4.17 (c)), no obvious Au NPs peaks were observed, the reason maybe the low weight content of Au NPs.

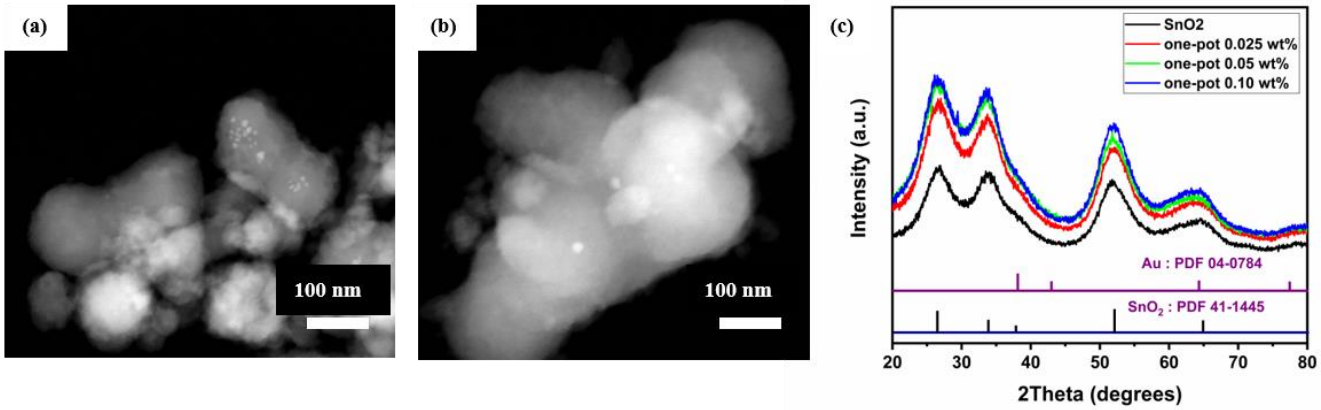

Figure 4.17 (a)(b) STEM images and (c) XRD pattern of one-pot 0.05 wt% SnO_2-Au nanostructures.

4.7.4 The photocatalytic property of Au@SnO_2 structure

For the photocatalytic property of semiconductors, factors such as the adsorption of pollutants, light harvesting, and the charge transportation and separation are crucial. In the following section, the surface areas of materials are discussed as key factors of pollutant adsorption. The light absorption ranges of Au-SnO_2 and one-pot SnO_2-Au nanomaterials were illustrated by the band gap. Additionally, the photoluminescence spectra studied to show their electron separation and recombination properties.

4.7.4.1 The surface area of the pristine SnO_2 and Au@SnO_2 structure

The nitrogen adsorption-desorption isotherm and corresponding size distribution of the pristine SnO_2 and Au@SnO_2 samples were shown in Figure 4.18. The nitrogen adsorption-desorption isotherm loops exhibit no distinct saturated adsorption plateau (type IV curves), indicating irregular pore structures within pristine SnO_2, Au-SnO_2, and one-pot SnO_2-Au nanostructures. [146] These pores are likely attributed to the spaces among the grain stacking in the SnO_2 matrixes. Additionally, the feature of the isotherm changed when adding Au NPs, indicating the insertion of Au NPs were mainly filling into the pores of the SnO_2 matrixes. The increase contact area with pollutants will improve the photocatalytic activity. [235] However, the surface areas of Au@SnO_2 did not exhibit significant increasement compared with the pristine SnO_2 nanoparticles, indicating that surface area alone may not be the key factors influencing their photocatalytic property differences.

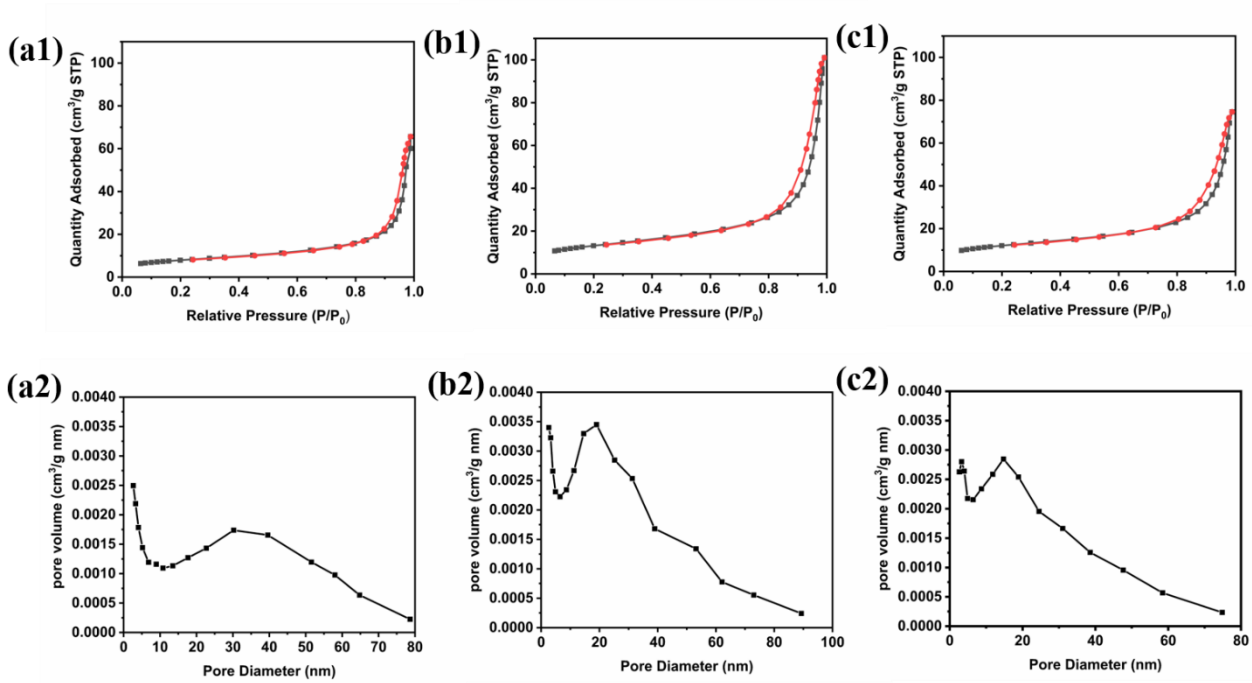

Figure 4.18 Nitrogen adsorption-desorption isotherm of (a1) pristine SnO_2, (b1) Au-SnO_2, (c1) one-pot SnO_2-Au and pore size distribution of (a2) pristine SnO_2, (b2) Au-SnO_2, (c2) one-pot SnO_2-Au.

4.7.4.2 The band gap of the pristine SnO_2 and Au@SnO_2 structure

The pristine SnO_2 nanomaterials synthesised in the microreactor exhibit inter-band absorption, which was cut off at about 350 nm, as depicted in Figure 4.19 (a). For the Au@SnO_2 structure, the UV-vis absorption band of Au NPs shows a shift from 520 nm to 550 nm. The LSPR band of plasmonic metal is not only dependent on the morphology of nanoparticles themselves but also sensitive to the refractive index of the surrounding environment. [72] This shift can be attributed to an increase dielectric contrast, as the refractive index of water is 1.33 and SnO_2 is 2.0. [57] Additionally, the broadening LSPR band of Au NPs could be attributed to particle aggregation and clustering in the synthesis process. [236] Plots of $\alpha(hv)^2$ versus hv was shown in Figure 4.19 (b), and the estimated band gap values of Au- SnO_2 with different Au content was 3.04 eV (0.025 wt%), 2.92 eV (0.05 wt%), and 2.59 eV (0.1 wt%) respectively. The reduced band gap observed in the Au-SnO_2 hybrid composite, in comparison to the pristine SnO_2, is likely due to the excitation of the gold surface plasmon. This excitation can alter the carrier density, thereby influencing the energy of the band gap.[50] [237] [238]

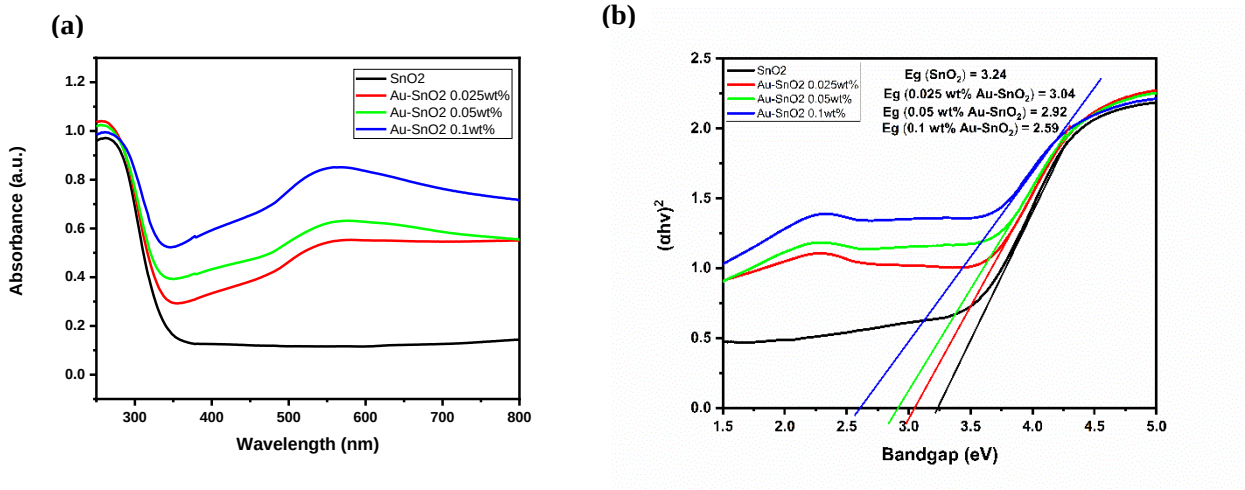

Figure 4.19 (a) Diffuse reflectance UV-visible (DRUV) spectra and (b) Optical band spectra of Au- SnO_2 nanostructure.

For the one-pot SnO_2@Au structure, the LSPR band of Au NPs showed a shift from 520 nm to 560 nm, as illustrated in Figure 4.20 (a). In this method, as the Au NPs and SnO_2 formed simultaneously, the formation process became more complicated. The particle size of Au NPs in the one-pot method is not as uniform as these synthesised in the separated method. The shift of LSPR could be attributed to the Au NPs themselves and also the increased dielectric constant inside the SnO_2 matrixes. [57] [72] Plots of $\alpha(h\nu)^2$ versus $h\nu$ was shown in Figure 4.20 (b), and the estimated band gap values of SnO_2-Au with different Au contents were 3.19 eV (0.025 wt%), 3.04 eV (0.05 wt%), and 3.14 eV (0.1 wt%) respectively. Although the materials introduced visible light photo-response plasmonic Au NPs, the band gap in these materials with three different Au NPs contents did not change significantly compared to pristine SnO_2 (3.24 eV). This could be attributed to the fact that the low content of inserted Au NPs did not significantly influence the carrier density of the SnO_2 matrixes. [50]

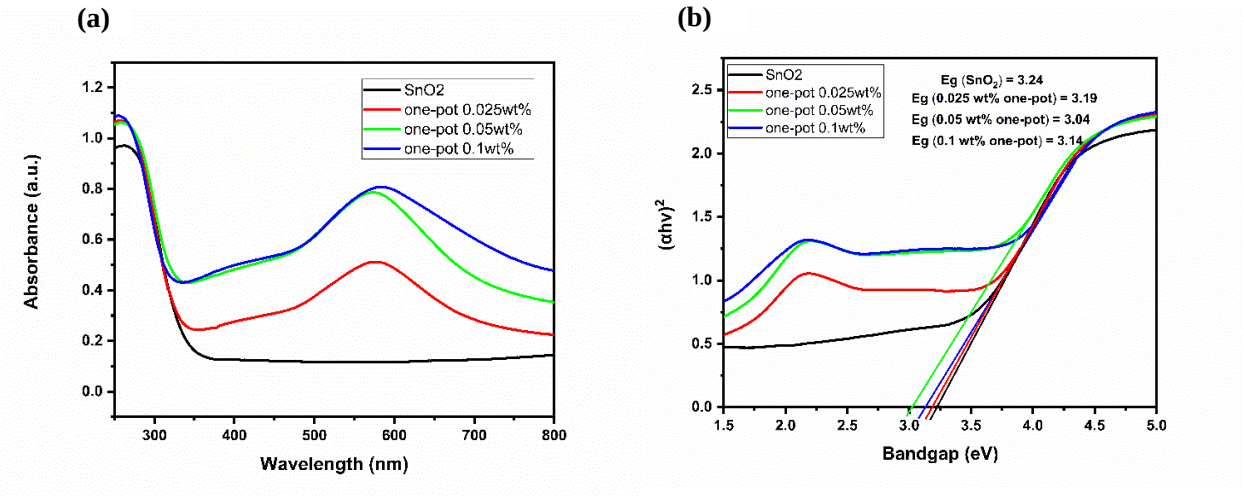

Figure 4.20 (a) Diffuse reflectance UV-visible (DRUV) spectra and (b) Optical band spectra of one-pot SnO_2-Au nanostructure.

4.7.4.3 Photoluminescence spectra of the pristine SnO_2 and Au@SnO_2 structure

Photoluminescence spectroscopy gives information about the electron-hole pairs recombination, defect peaks and charge carrier trapping in semiconductors. The rate of electron-hole recombination is decided by the intensity of the photoluminescence peak. The higher the intensity of the spectrum, the higher rate of electron-hole recombination is. [226] However, to enhance the photocatalytic performance, the increased number of photo-generated electrons and holes need to participate in the photocatalytic reaction. [239] On the other hand, a lower intensity indicates that more excited electrons in semiconductor are trapped or transferred to the metal through the interface, which indicates efficient charge separation. The room temperature photoluminescence spectra of the three samples-pristine SnO_2, Au-SnO_2 and one-pot SnO_2-Au with weight ratio of Au/SnO_2 0.05 wt% are shown in Figure 4.21 with an excitation wavelength of 606 nm. Only the one-pot sample shows a

slightly reduced PL intensity than pristine SnO_2, indicating Au NPs plays a minor role in trapping the photo-generated electrons from SnO_2, potentially contributing to charge separation.

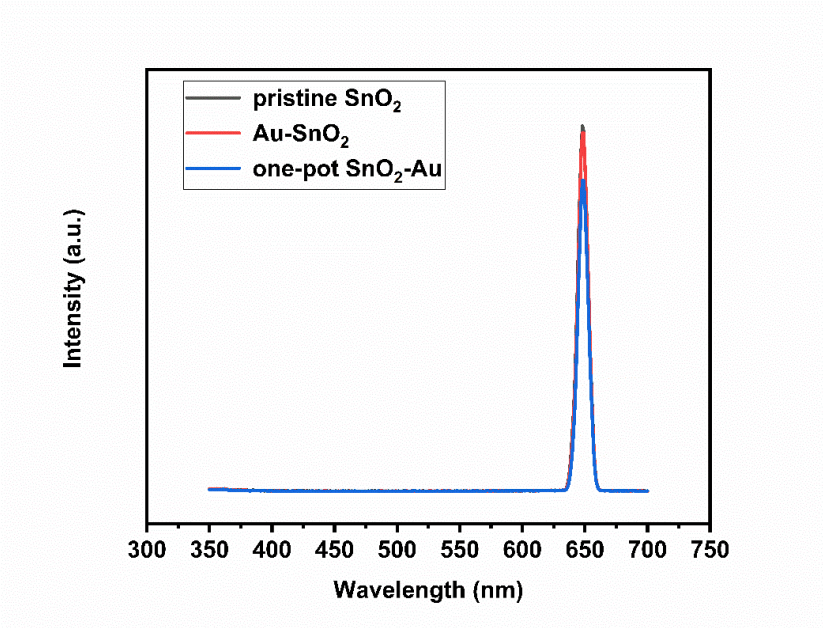

Figure 4.21 Photoluminescence spectra of (A) pristine SnO_2, (B) Au-SnO_2, (C) one-pot SnO_2-Au.

4.7.4.4 The degradation rate of the pristine SnO_2 and Au@SnO_2 structure on RhB

The photocatalytic activity of SnO_2 and Au@SnO_2 structure for the RhB degradation under visible light is observed in Figure 4.22. The degradation rate of RhB without catalysts was taken as a blank experiment, revealing almost no degradation happened in the absence of catalysts.

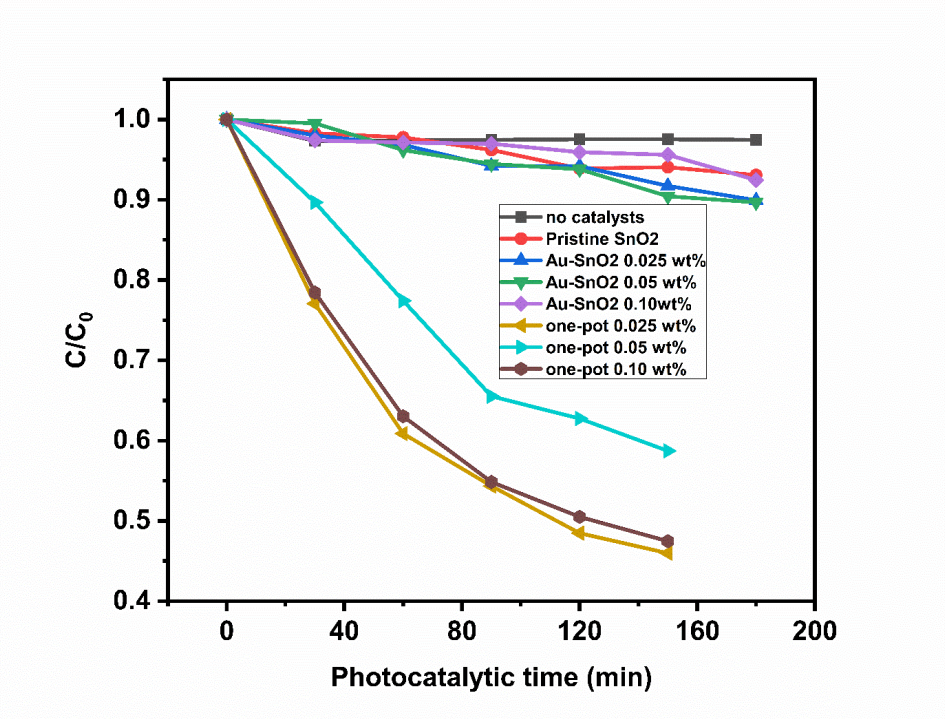

Figure 4.22 RhB photocatalytic degradation of pristine SnO_2, Au-SnO_2, and one-pot SnO_2-Au.

To quantitatively compare the photocatalytic activities of these Au@SnO_2 nanoparticles, the reaction rate constants (k) were calculated using the pseudo first-order model (Equation 4-10) used to describe photocatalytic degradation.

$$\ln(C_0/C) = kt \qquad (4\text{-}10)$$

The linear relationships of $\ln(C_0/C)$ versus irradiation time (t) indicate that each photodegradation process follows first-order kinetics. The rate constants are shown in Table 4.1.

Table 4.1 The kinetic rate of RhB photocatalytic degradation of pristine SnO_2, Au-SnO_2, and one-pot SnO_2-Au.

Pristine SnO_2 (min^{-1})	**Method 1: Au-SnO_2 (min^{-1})**	**Method 2: one-pot SnO_2-Au (min^{-1})**
$4.3*10^{-4}$	0.025 wt% Au $5.8*10^{-4}$	0.025 wt% Au $6.6*10^{-3}$
	0.05 wt% Au $6.1*10^{-4}$	0.05 wt% Au $3.7*10^{-3}$
	0.1 wt% Au $3.6*10^{-4}$	0.1 wt% Au $6.3*10^{-3}$

The band gap of Au-SnO_2 is lower than the pristine SnO_2 due to the increased carrier density from gold surface plasmons. However, due to the unintimate contact between Au and SnO_2, the degradation rate of Au-SnO_2 doesn't improve significantly compared to the pristine SnO_2. In the one-pot Au-SnO_2 structure, Au NPs do improve the photocatalytic properties of SnO_2 structure. However, due to the lower weight ratio of Au/SnO_2 from 0.025 wt% to 0.1 wt%, a significantly lower overall degradation rate was achieved on the order of 10 to the power of negative three. Some errors in the kinetic rate of

RhB photocatalytic degradation cannot be ignored when comparing these three different weight ratios. Specifically, the degradation rate constant of one-pot 0.1 wt% SnO_2-Au for RhB under visible light is 0.0063 min^{-1}, surpassing the reported results by Bathula *et al.* [68] Their study achieved SnO_2 quantum dot/Au NPs via a one-pot solvothermal method at 100 ^oC for 18 h, yielding a rate constant k is 0.019 min^{-1} with Au/SnO_2 is 4.69 wt%.

The degradation process of RhB initiates with N-de-ethylation and the chromophore cleavage, which leads to the opening of the molecular rings and subsequent generation of a series of intermediate oxidation products. Eventually, smaller molecules undergo mineralisation until they transform into the final products of CO_2 and H_2O. [232] Figure 4.23 illustrates the degradation process of RhB using one-pot 0.1 wt% Au-SnO_2 in our experiment. The absorption peaks display slight hypsochromic shifts, indicating the likely formation of a series of N-de-ethylated intermediates in a stepwise manner. Even after 420 minutes, some peaks persist, suggesting the presence of organic intermediates that have not completely degraded into CO_2 and H_2O. [240] In summary, although the one-pot Au-SnO_2 structure does improve the photocatalytic properties compared with pristine SnO_2 due to the intimate contact of these two materials, the incomplete degradation of RhB as well as the low degradation rate imply that the photocatalytic property is not optimal. Further experiments need to be designed to improve it.

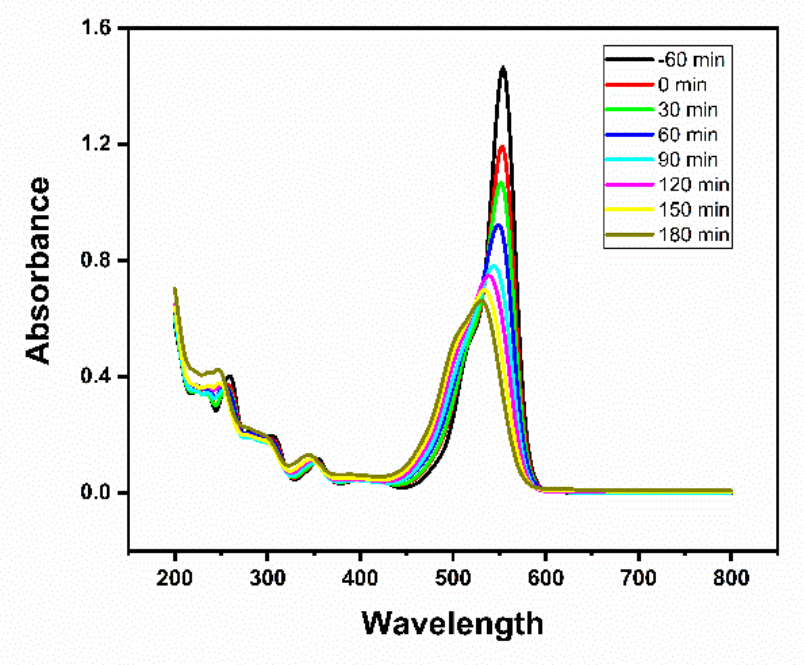

Figure 4.23 Click or tap here to enter text.Absorption spectra for photocatalytic degradation of RhB using one-pot 0.05 wt% Au-SnO_2.

Herein, incorporating Au NPs inside SnO_2 matrix using the one-pot method enhances the photocatalytic property through two main processes: (ii) hot-electron injection and (iv) Local electromagnetic field enhancement (LEMF) process. The hot-electron injection occurs only when the plasmonic metal is in direct contact with the semiconductor, and the energy of hot carrier surpasses

the Schottky barrier. For the LEMF process, the enhanced charge separation of semiconductor will only happen when the energy of local electric field higher than their band gap. [45] In our research, the randomly inside located Au NPs through the one-pot synthesis method will only work when the excited carriers of SnO_2 migrate to their surface-active sites to take part in reduction or oxidation chemical reactions.

4.9 Conclusion

SnO_2 nanocrystals can be synthesised using hydrothermal and solvothermal method. In this chapter, we synthesised SnO_2 NPs at low-temperature and low-pressure conditions by adjusting pH value, temperature, precursor concentration, and solvent polarity. Additionally, to scale up the synthesis process, we initially transitioned the synthesis method from a batch reactor to a microfluidic system. As a wide band-gap semiconductor, SnO_2 primarily obsorbs UV light, which constitutes only a small fraction (below 5%) of the solar light spectrum.

To improve the photocatalytic properties across the entire solar spectrum, plasmonic gold nanoparticles were incorporated to the SnO_2 NPs. A microfluidic method was firstly explored for continuous synthesis, studying three incorporation structures for optimal photocatalytic property: (1) Au NPs coated on the SnO_2 matrixes, (2) Au NPs surrounded by SnO_2 matrixes, and (3) Au NPs embedded with SnO_2 matrixes. Synthesising SnO_2 nanocrystals in the first step, then sol-immobilising Au NPs on the surface of SnO_2 matrixes did not yield effective integration. After several times centrifugation, these two materials separated. Although embedding pre-synthesised Au NPs inside SnO_2 matrixes locks them in place, there still remains a noticeable gap between these two materials. Due to the unintimate contact, the degradation rate of Au-SnO_2 did not improve significantly compared to the pristine SnO_2.

In the one-pot synthesis method with simultaneous synthesis of SnO_2 and Au NPs, Au NPs do improve the photocatalytic properties of SnO_2 under simulated solar light. However, lower weight ratios of Au/SnO_2 (0.025 wt%, 0.05 wt%, and 0.1 wt%) result in a significantly lower overall degradation rate. Even after 420 minutes, some organic intermediates still exist and have not been completely degraded into CO_2 and H_2O. Therefore, the primary focus for further study is achieving an intimate combination structure of SnO_2@Au with the proper plasmonic metal weight content.

Chapter 5. Continuous synthesis of Cu_2O polyhedral nanoparticles with shape evolution in microtube reactor

5.1 Introduction

Crystal facet engineering of semiconductor metal oxide nanocrystals has attracted significant attention due to the capability to manipulate facet-selective performance in various photoelectric applications. [241] [242] Cuprous oxide (Cu_2O), a visible light-driven p-type semiconductor with a narrow bandgap of 1.9-2.2 eV, shows promising potential in photocatalytic applications. [174] [243] With the face-centered cubic crystal structure ($Pn\bar{3}m$), Cu_2O polyhedron could achieve low-index facets and/or high-index facets by modifying the growth rate ratio (R) between the <100> and <111> directions. [163] Hence, in addition to the particle size and shape, the exposed crystal-index facets of Cu_2O nanoparticles plays a pivotal role in determining their catalytic properties. [154] [244] While the most common synthesis methods of Cu_2O nanocrystals are primarily based on batch-reactor systems in laboratory settings, [245] scaling up this traditional batch system poses challenges, as mixing time and thermal transport do not scale linearly with the volume of the reaction solution in the batch vessel. [184] [246]. Until now, only a few papers have described the synthesis of Cu_2O using the microfluidic method, [181] [183] however, these studies lack the precise control of the final copper nanoparticle morphology.

This chapter details on the systematic and precise shape control of Cu_2O nanocrystals using a lab-made capillary reactor. The morphological evolution of Cu_2O polyhedron from cube to octahedra, and finally to rhombic dodecahedra was achieved by adjusting the concentration of $NH_2OH{\cdot}HCl$ and NaOH. This evolution of the Cu_2O nanocrystal has been interpreted from both thermodynamic and kinetic perspectives. This simple continuous method for the controllable evolution of polyhedral Cu_2O opens up new possibilities for the large-scale production of other semiconductor nanomaterial with different facets in a reproducible manner.

5.2 Experiments and methods

5.2.1 Materials

Anhydrous copper (II) chloride ($CuCl_2$, 97%, Fluorochem), hydroxylamine hydrochloride ($NH_2OH{\cdot}HCl$, 99%, Fluorochem), sodium hydroxide (NaOH, >97.5%, Scientific Laboratory Supplies), and sodium dodecyl sulfonate (SDS, $C_{12}H_{25}NaSO_4 \geqslant 98.5$ %, Sigma-Aldrich) were purchased and used as received without any further purification. Ultrapure deionized water (resistivity of 18.2 MΩ·cm) was used in all experiments.

5.2.2 Batch and continuous microfluidic synthesis of Cu_2O nanocrystals via method 1

5.2.2.1 Batch synthesis of Cu_2O nanocrystals via method 1

The batch reaction was adjusted from the method reported by Huang *et al*. [178] Firstly, 10 mL copper precursor aqueous solution containing $CuCl_2$ (5×10^{-3} M) and capping surfactant SDS (3×10^{-2} M) was mixed with 10 mL NaOH (1.8×10^{-2} M) for a reaction time of 20 s. Blue $Cu(OH)_2$ precipitation was formed on the first step. Then various concentrations of reducing agent $NH_2OH{\cdot}HCl$ in 6.7 mL (a 4×10^{-3} M, b 9.2×10^{-3} M, c 1.2×10^{-2} M, d 2.4×10^{-2} M) was added to achieve systematic shape evolution from cubic to rhombic dodecahedral structures in a reaction time of 20 s. By increasing the concentration of NaOH from 1.8×10^{-2} M to 7.2×10^{-2} M, truncated cube, truncated octahedra and octahedra were obtained. The total volume of solvent was fixed at 26.7 mL. The reaction was undertaken at a temperature of 32 ^{o}C by immersing reaction vials in a water bath. A stirrer bar with a length of 10 mm was placed in the reaction vial with a stirring speed of 250 revolutions/min. The reaction temperatures were controlled using stirred water bath and IKA RCT basic stirrer hotplates equipped with IKA ETS-D5 temperature controller (uncertainty of $\pm$0.1 K). Then the product solutions were kept in the water bath 32^{o}C for 2 h for nanocrystal growth. After aging, the samples were washed and centrifuged with 1:1 volume ratio of water and ethanol several times to remove the SDS surfactant. Finally, the sample was dried in a vacuum drying oven at 60^{o}C for 6 h to obtain a solid product. For the scaled-up batch reaction, the solvents were scaled up by a factor of 3. Reaction procedures were kept the same as the small-scale batch reactions. The concentrations of all solutions are calculated based on their volume in the final solution.

5.2.2.2 Continuous synthesis of Cu_2O nanocrystals via method 1

In order to achieve a continuous synthesis method, cuprous oxide nanoparticles were synthesised in a polytetrafluoroethylene (PTFE, IDEX Health & Science LLC) helical tubular reactor with either a narrow 1/32 inch I.D. (internal diameter) (1/16 inch O.D. (outer diameter)) or wide 1/16 inch I.D. (1/8 inch O.D.). The reactor tubing was coiled around a circular plastic cylinder (diameter ~ 21 mm). In this system, cuprous oxide with tunable crystal shapes were synthesised in two stages (Fig. 5.1). In the first stage, the precursor aqueous solution containing $CuCl_2$ (5×10^{-3} M) and capping surfactant SDS (3×10^{-2} M) mix with various concentrations of NaOH, 1.8×10^{-2} M, 3.6×10^{-2} M, 5.4×10^{-2} M, and 7.2×10^{-2} M. Both solutions were pumped into reactor 1 using a syringe pump (Chemyx, Fusion 100) with volumetric flow rate 3 mL min^{-1}, at 32^{o}C, with residence time 20 s. The two streams were mixed in a T mixer (PEEK, 0.508 mm through hole, IDEX Health & Science LLC). The reduction reaction and Cu_2O seed formation took place in reactor 2 at 32^{o}C where an additional reducing agent $NH_2OH{\cdot}HCl$

(a 4×10^{-3} M, b 9.2×10^{-3} M, c 1.2×10^{-2} M, d 2.4×10^{-2} M) was introduced using a syringe pump and mixed with the solution from reactor 1. The volumetric flow rate of $NH_2OH{\cdot}HCl$ was set to be 2 mL min^{-1} with the total residence time in step 2 was 20 s. Afterward, the outlet solutions were maintained in a 32°C water bath for 2 hours for nanocrystal growth, the same as in the batch reactor.

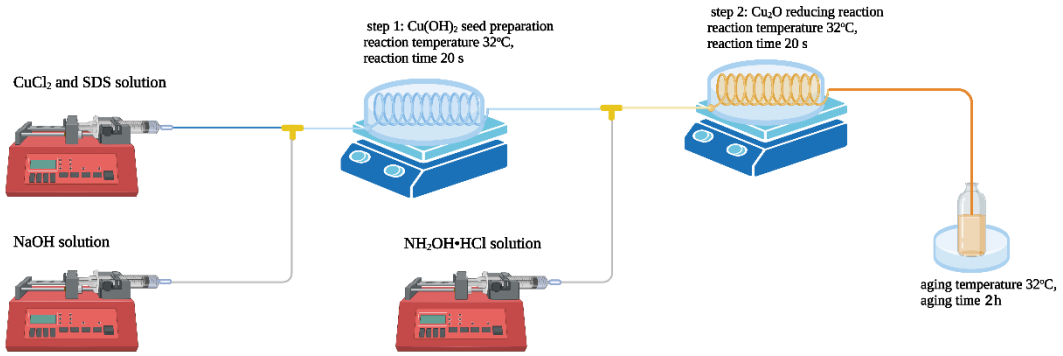

Figure 5.1 Schematic for continuous preparation of Cu_2O nanoparticles of the experimental setup in method 1.

5.2.3 Batch and continuous microfluidic synthesis of Cu_2O nanocrystals via method 2

In method 2, all the precursor concentration of $CuCl_2$, SDS, NaOH, and $NH_2OH{\cdot}HCl$ was kept the same with method 1 in both batch and microreactor (narrow 1/32 inch I.D. or wide 1/16 inch I.D., the schematic of experimental setup was shown in Fig. 5.2). The difference lies in the sequence of adding the reducing agent $NH_2OH{\cdot}HCl$, and NaOH, which were swapped compared to method 1. In the first stage, $NH_2OH{\cdot}HCl$ was mixed with copper precursor within 20 s residence time, 32°C. In the second stage, NaOH was pumped into the second reactor with 20 s residence time, 32°C.

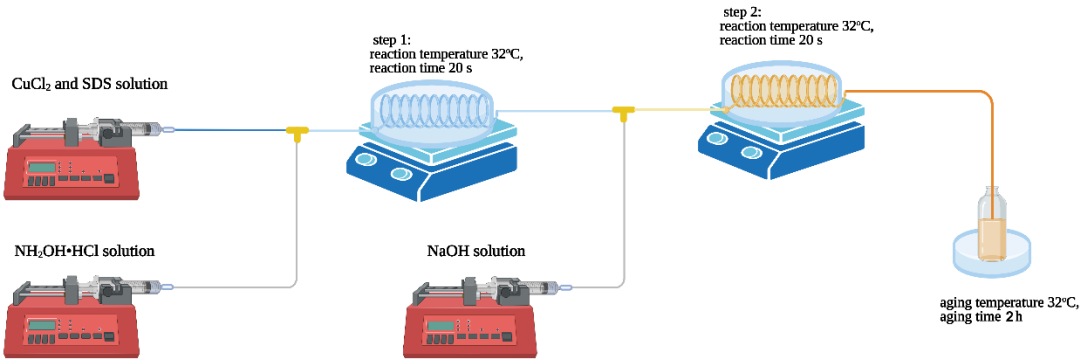

Figure 5.2 Schematic for continuous preparation of Cu_2O nanoparticles of the experimental setup in method 2.

5.2.4 T-mixer and Vortex-mixer

For the synthesis of Cu_2O nanoparticles with rapid nucleation, the choice of mixers also plays a crucial role in determining the final particle size and polydispersity. As the mixing performance inside the mixer is a key factor in this regard. Two mixers were utilized in this study: the T-mixer from IDEX Health & Science LLC, featuring with swept volume 17.5 μL and a through hole 0.05 inches (refer to Figure 5.3(a)), and a two-inlet vortex mixer designed by Professor Nik Kapur's group (refer to Figure 5.3(c)), inspired by the multi-inlet vortex mixer reported by Feng et al. [247] A simplified two-disk design was employed for ease of machining and mixer assembly outside (refer to Figure 5.3(b)).

In the T-mixer, fluids were manually pumped from syringes, leading to the merging of two streams into a mixing stream. The merging process, with a distinct interface between two solutions, occurs in a laminar fashion at the junction, depending on the Reynolds number. [200] The details of this two-inlet vortex were still confidential and will be published by the Kapur group. A rough estimate of the mixing performance of these two mixers can be obtained by evaluating the pressure drop, as the pressure drop i.e. energy dissipation is roughly proportional to the mixing performance. [248] In this experiment, three syringe pumps (Chemyx, Fusion 100) were used to pump the solution through. Attempting to use the two-vortex mixer resulted in pump failure, indicating that the system pressure exceeded the pump pressure range. This suggests that the two-inlet mixer exhibits better mixing performance than the T-mixer. However, to establish a quantitative relationship between the particle size of the Cu_2O nanoparticles and the mixing performance, further research is necessary.

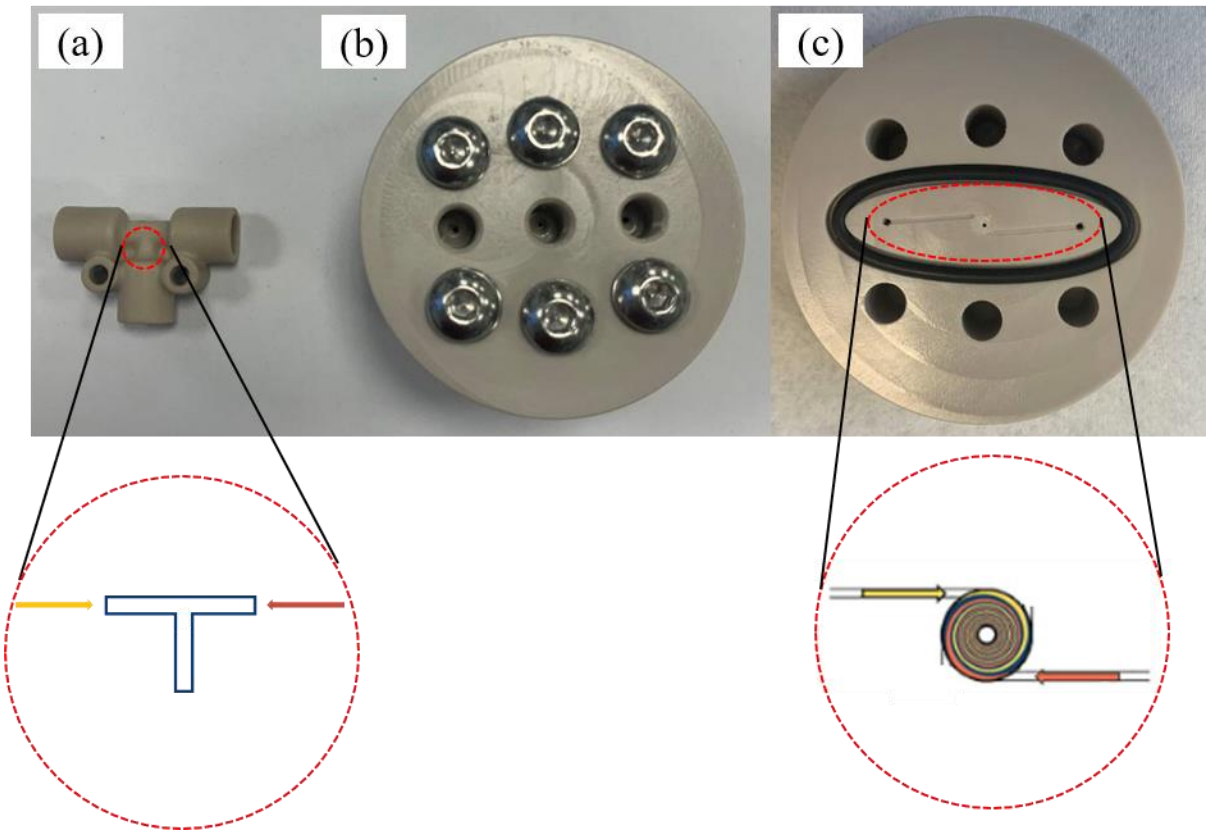

Figure 5.3 Images of (a) the T-mixer, (b) external of two-inlet vortex mixer, and (c) internal of two-inlet vortex mixer. Insets: zoom-in schematics of the T-mixer and the two-inlet vortex mixer

5.2.5 Materials Characterisation

Powder X-ray diffraction patterns were recorded using a Bruker D8 (Cu-Kα radiation, λ = 0.15418 nm) over the 2θ range of 25°-85° with the step size 0.041°. The surface morphologies of the samples were characterised by scanning electron microscopy (SEM, Hitachi SU8230, carbon coating) and transmission electron microscopy (TEM, FEI Tecnai 20 TF20 FEGTEM). To precisely examine early-stage shape and structure by TEM, the samples were added to TEM grids, rapidly frozen to capture the native state and subsequently sublimed following the procedure previously developed. [249] Particle sizes were measured by using ImageJ, with more than 100 particles measured for each sample. UV-visible absorption spectra of the as-prepared Cu_2O NPs were recorded on an Agilent Cary 60 UV-vis spectrophotometer between 300-800 nm with a wavelength resolution of 2 nm. pH value was tested by SevenCompact™ S220 PH meter (uncertainty of ±0.002). To test the concentration of Cu^{2+} remaining in the supernatant, inductively coupled plasma mass spectrometry (Thermo Scientific iCAP RQ plus ICP-MS) was used. In order to reduce the concentration of supernatant to a more suitable range for ICP-MS analysis, all samples were further diluted by a factor of 50 using 2% v/v HNO_3. Subsequently, the actual Cu^{2+} concentration was calculated by multiplying the obtained value by 50.

5.3 Results and discussion

5.3.1 Batch synthesis of Cu_2O nanoparticles via method 1

The morphological evolution of Cu_2O nanocrystals in batch was achieved by varying the concentrations of NaOH and $NH_2OH{\cdot}HCl$ as shown in Figure 5.4. In the batch reactor, by varying the concentrations of reducing agent $NH_2OH{\cdot}HCl$ from 4×10^{-3} M, 9.2×10^{-3} M, 1.2×10^{-2} M to 2.4×10^{-2} M, the Cu_2O crystal vary from nanocube (Cube-Cu_2O, Figure 5.4 (A)-a1, 6 square {100} faces), intermediate structures exhibiting with corner-truncated rhombic dodecahedra (corner-truncated RD-Cu_2O, Figure 5.4 (A)-b1, 6 square {100}, 8 triangular {111},12 rectangle {110} faces) and {100}-truncated rhombic dodecahedra ({100}-truncated RD-Cu_2O, Figure 5.4 (A)-c1, 6 square {100}, 12 rectangle {110} faces), and eventually to rhombic dodecahedra (RD-Cu_2O, Figure 5.4 (A)-d1, 12 rectangle {110} faces) at the concentration of NaOH 1.8×10^{-2} M. Once C_{NaOH} reached 7.2×10^{-2} M, truncated cube (truncated Cube-Cu_2O, Figure 5.4 (A)-a4, b4), truncated octahedra (truncated Oct-Cu_2O, Figure 5.4 (A)-c4) and also perfect octahedra (Oct-Cu_2O, Figure 5.4 (A)-d4) enclosed exclusively by triangular {111} was obtained.

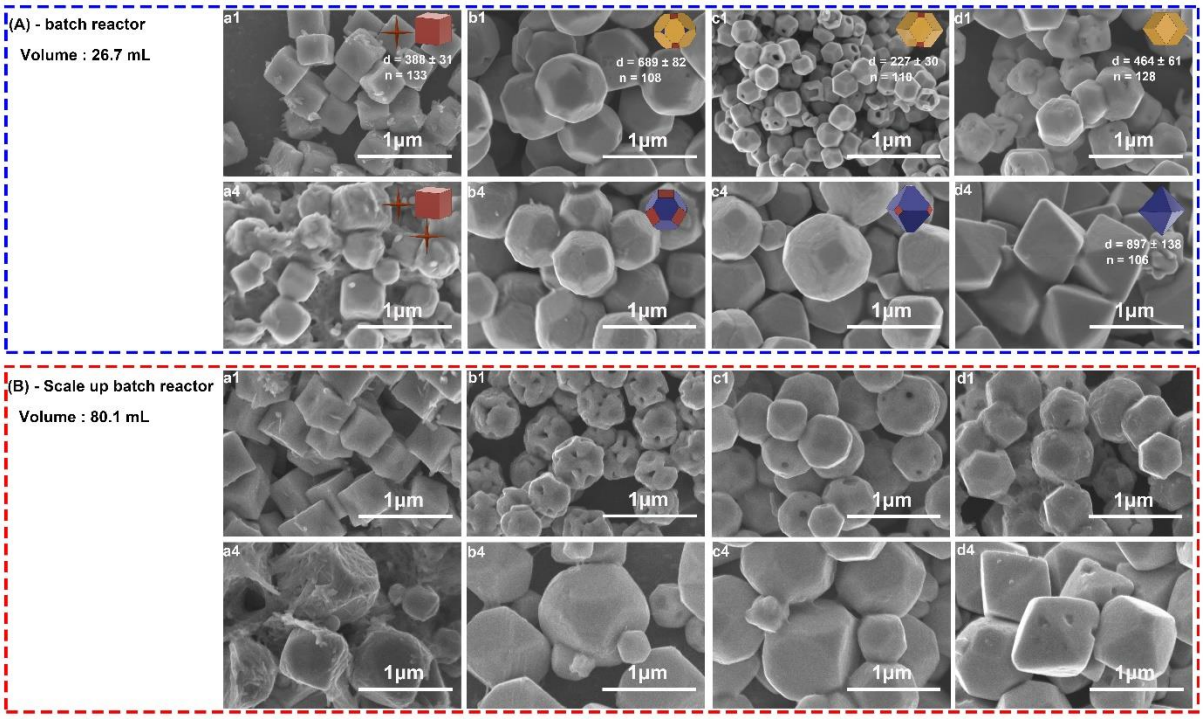

Figure 5.4 Morphology evolution of Cu_2O nanocrystals as shown by SEM images (a1) Cube-Cu_2O, (b1) corner-truncated RD-Cu_2O, (c1) {100}-truncated RD-Cu_2O, (d1) RD-Cu_2O; (a4) Cube-Cu_2O, (b4) Cube-Cu_2O, (c4) truncated Oct-Cu_2O, (d4) Oct-Cu_2O as shown by SEM images under various NaOH and $NH_2OH{\cdot}HCl$ concentrations in (A) batch reactor and (B) scale up batch reactor in method 1. d is the diameter of nanoparticles, measured in nanometres, and n is the number of particles measured.

The crystallographic structure of Cu_2O nanoparticles produced in batch reactor (Figure 5.4 (A)) has been confirmed by XRD measurements, shown in Figure 5.5. All the diffraction peaks are well indexed to the peaks of standard cubic structure Cu_2O (JCPDS card No. 05-0667), except the willow-like crystals formed with Cube-Cu_2O, which introduced tiny CuO crystal (JCPDS card No. 45-0937) shown in sample a4. [250]

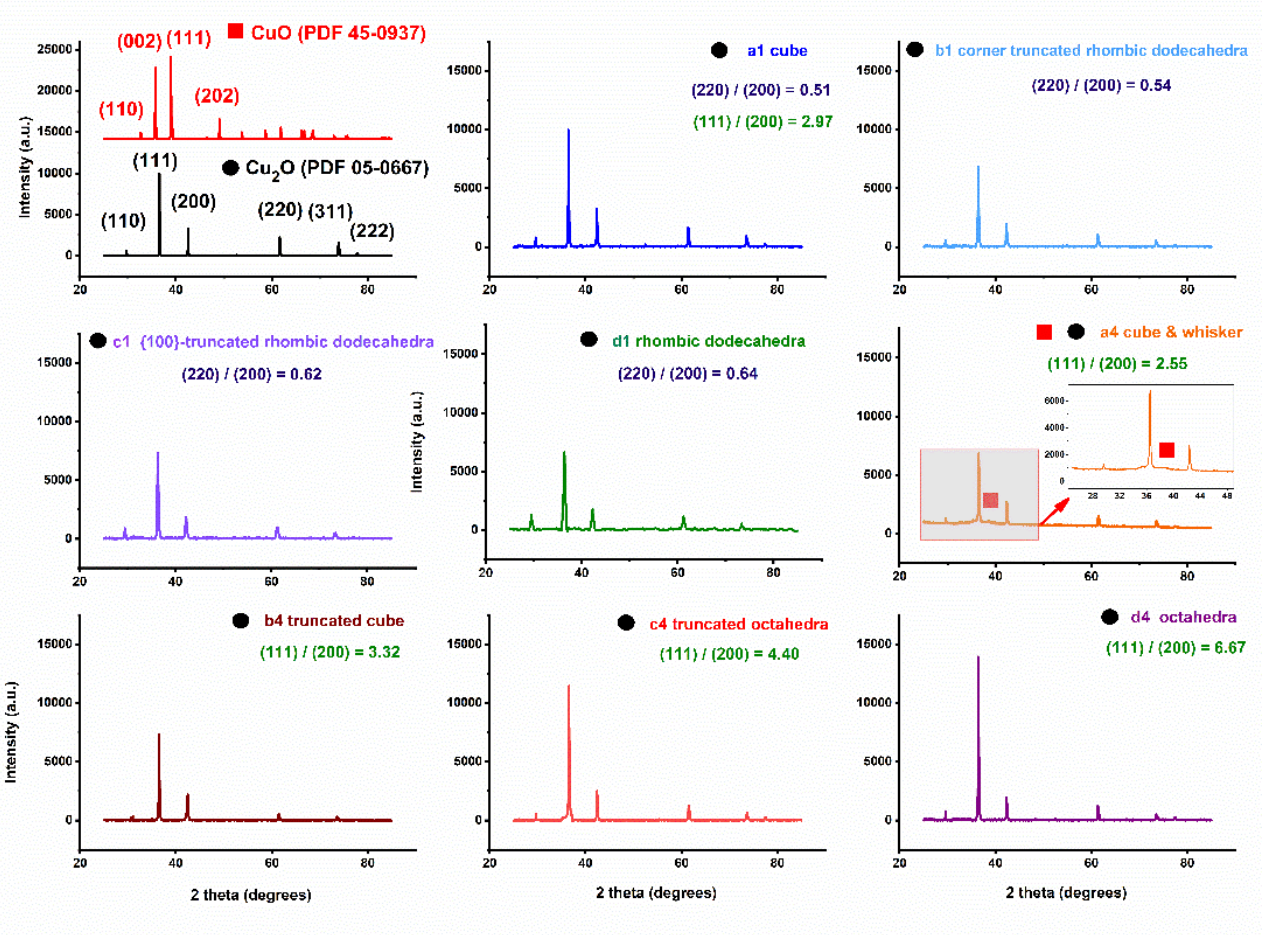

Figure 5.5 XRD of Cu_2O nanocrystals from database (top left) and from the batch reactor (a1) Cube-Cu_2O, (b1) corner-truncated RD-Cu_2O, (c1) {100}-truncated RD-Cu_2O, (d1) RD-Cu_2O; (a4) Cube-Cu_2O, (b4) Cube-Cu_2O, (c4) truncated Oct-Cu_2O, (d4) Oct-Cu_2O in method 1.

The slight diffraction intensity differences evidenced the anisotropic growth of the Cu_2O NPs. Compared with other morphologies, Cub-Cu_2O showed an enhanced (200) peak due to the surface {100} facets. The intensity ratio of the (220)/(200) increases from 0.51 of the cub-Cu_2O (Figure 5.4 (A)-a1), 0.54 of the corner-truncated RD-Cu_2O (Figure 5.4 (A)-b1), 0.62 of {100}-truncated RD-Cu_2O (Figure 5.4 (A)-c1) and 0.65 of RD-Cu_2O was as a result of their {110} facets (Figure 5.4 (A)-d1). The intensity ratio of the (111)/(200) increase from 2.97 of cub-Cu_2O (Figure 5.4 (A)-a1), 3.32 of the corner-truncated RD-Cu_2O (Figure 5.4 (A)-b4), 4.40 of {100}-truncated RD-Cu_2O (Figure 5.4 (A)-c4) and 6.67 of RD-Cu_2O (Figure 5.4 (A)-d4) was as a result of their increased {110} facets bounded on the particle surface. [251] For small-scale batch syntheses, the particle size of Cu_2O

nanoparticles of a1-d4 are quite uniform, with particle size deviation around 10%, shown in Figure 5.4 and Table 5.1. In batch reactions scaled up by a factor of 3 (80.1 mL of reagents), the particle morphology became non-uniform with different crystal facet ratios (Figure 5.4 (B)), which attribute to the poor heat and mass transfer in these batch reactions.

5.3.2 Continuous synthesis of Cu_2O nanoparticles via method 1

In order to establish a reproducible continuous method for Cu_2O nanoparticles with uniform particle size and morphology, we developed a continuous synthesis method using a microfluidic flow reactor within 1/16 inch I.D. The Reynold number in the tube (1/16 inch I.D.) is around 136, which is much lower than the threshold value of 2000. The microtube are generally within the laminar flow regime, and the mixing performance is mainly driven by the molecular diffusion. As both the concentration of $NH_2OH{\cdot}HCl$ and NaOH are important to the final crystal shapes, a 4×4 matrix of various Cu_2O nanoparticle shapes were achieved using the wide tube (1/16 inch I.D.), shown in Figure 5.6.

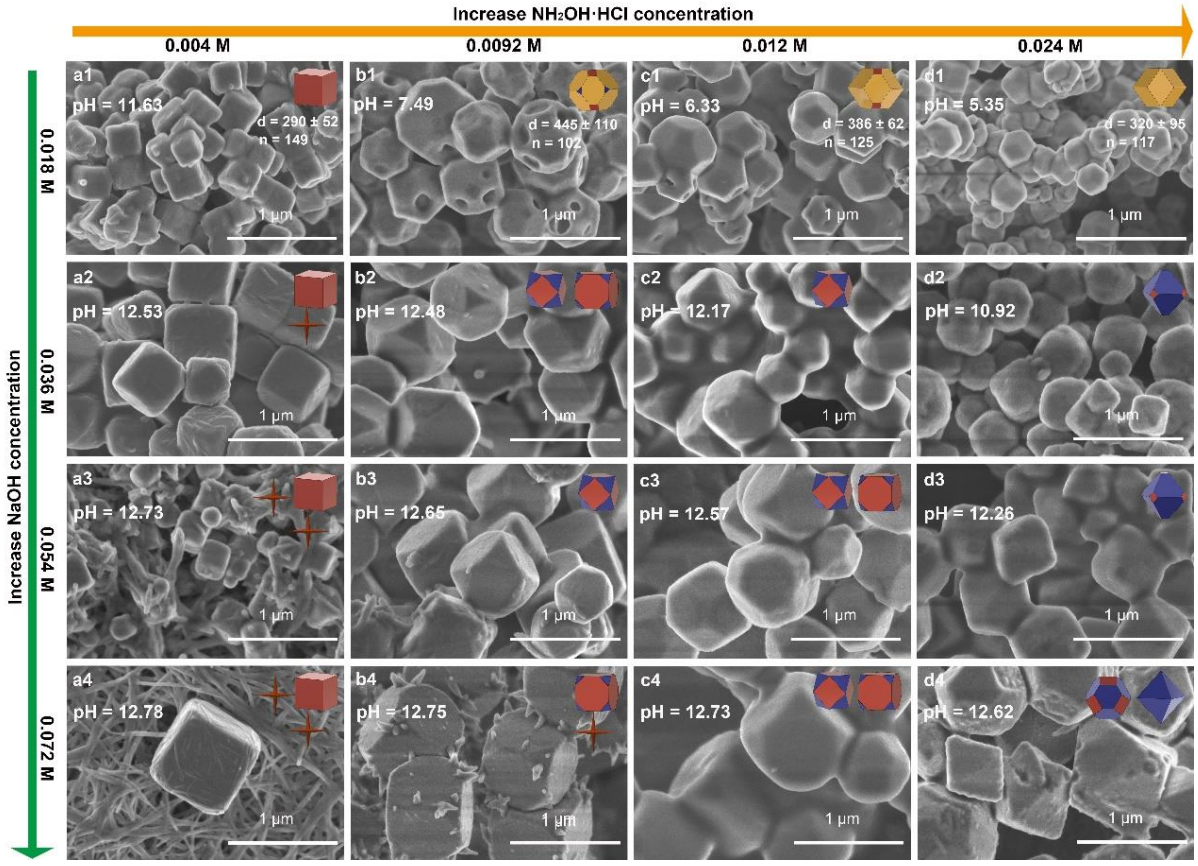

Figure 5.6 Morphology evolution of Cu_2O nanocrystals as shown by SEM images from a1 to d4 under various NaOH concentration from 0.018 M to 0.072 M (shown in y axis) and $NH_2OH.HCl$ concentrations from 0.004 M to 0.024 M (shown in x axis) using method 1 with the microtubing of 1/16 inch I.D with T-mixer, 32°C, residence time in step 1 and step 2 are both 20 s.

When the C_{NaOH} was 1.8×10^{-2} M, more {110} planes could be achieved as increasing the concentration of $NH_2OH{\cdot}HCl$ causes the shape evolution from cube to rhombic dodecahedra

(Figure 5.6 sample a1, b1, c1 to d1). The shape evolution was the same as in the batch reactor and the corresponding the pH value decreased from 11.63 to 5.35. As the C_{NaOH} increased from 1.8×10^{-2} M to 3.6×10^{-2} M, the {110} planes disappeared, with only the {100} and {111} planes observed, resulting in a systematic transformation from cubic to octahedral growth habit in the Cu_2O particles. [252] As C_{NaOH} reached to 3.6×10^{-2} M, the shape of the samples transformed from cube into truncated octahedra with pH value decreasing from 12.53, to 12.48, to 12.17 and finally to 10.92. Once C_{NaOH} reached 7.2×10^{-2} M, perfect octahedra enclosed exclusively by triangular {111} was obtained with $C_{NH_2OH\cdot HCl}$ at 2.4×10^{-3} M with the pH value at 12.62. It is evident that {111} facets become more prominent with the increase of C_{NaOH}, while {110} facets were observed only in the acidic solution. $NH_2OH\cdot HCl$ is a crucial and multi-purpose agent which acts as both reducing agent and to control the pH value as well. However, the size deviation from sample a1 to d1 increased to around 20% compared the 10% in the batch reactor, shown in Figure 5.7 and Table 5.1. For sample a2 to d4, there was a clear trend in shape evolution from cubes to truncated cubes, truncated octahedra, and ultimately octahedra. Nevertheless, it's important to note that the particle morphology did not exhibit uniformity within the microreactor with tube 1/16 inch I.D.

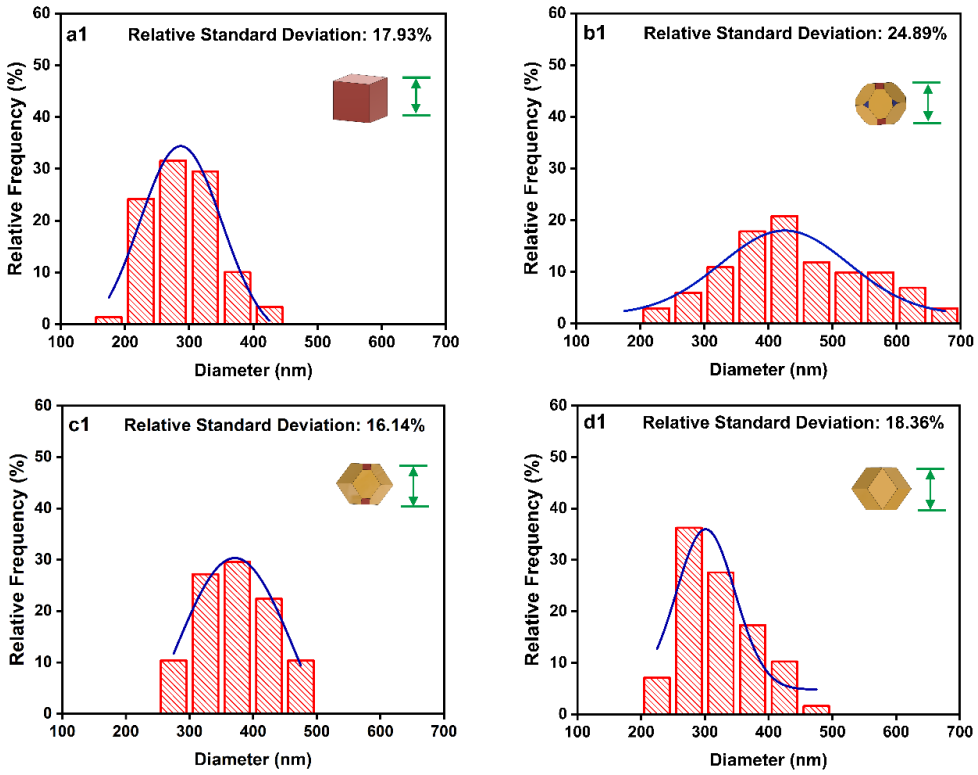

Figure 5.7 Size distribution histograms of Cu_2O nanoparticles morphology: (a1) nanocube, (b1) all-corner-truncated rhombic dodecahedra, (c1) {100}-truncated rhombic dodecahedra, (d1) rhombic dodecahedra in wide tube (I.D. 1/16 inch) using method 1 with T-T mixer.

For the synthesis process in method 1, taking the cube, octahedra and dodecahedra for example, a three-step procedure is proposed to describe the formation of Cu_2O nanocrystals, shown in Figure 5.8-5.10. Initially, copper chloride solution was pre-mixed with SDS in water. The pale blue characteristic of the aquo complex of Cu (II) is retained during complexation (Equation 5-1), suggesting no reduction of copper ions in the solution. [253] Then, upon the addition of NaOH to the mixture of Cu(II)-SDS, the resulting solution rapidly turned turbid light bluish, indicating the formation of $Cu(OH)_2$ precipitate (Equation 5-2). [176][178] Finally, $Cu(OH)_2$ was reduced to Cu_2O monomers using the reducing agent $NH_2OH{\cdot}HCl$ (Equation 5-3), as evidenced by an instant solution colour change. [244] Subsequently, the Cu_2O monomers aggregated to form nuclei seeds via a nucleation process. [254] These seeds underwent further growth and re-construction, giving rise to various intermediate structures.

$$CuCl_2 + 2\,Na(C_{12}H_{25}OSO_3) \rightleftharpoons NaCu(C_{12}H_{25}OSO_3)_2 + 2\,NaCl \quad (5\text{-}1)$$

$$Cu(C_{12}H_{25}OSO_3)_2 + 2\,NaOH \rightleftharpoons Cu(OH)_2 \downarrow + 2\,Na(C_{12}H_{25}OSO_3) \quad (5\text{-}2)$$

$$2\,Cu(OH)_2 + 2\,NH_2OH \cdot HCl \rightleftharpoons Cu_2O + N_2 + 5\,H_2O + 2\,HCl \quad (5\text{-}3)$$

$$Sm{:}\ 2\,CuCl_2 + 4\,NaOH + 2\,NH_2OH \cdot HCl \rightleftharpoons Cu_2O \downarrow + N_2 + 5\,H_2O + 2\,HCl + 4\,NaCl \quad (5\text{-}4)$$

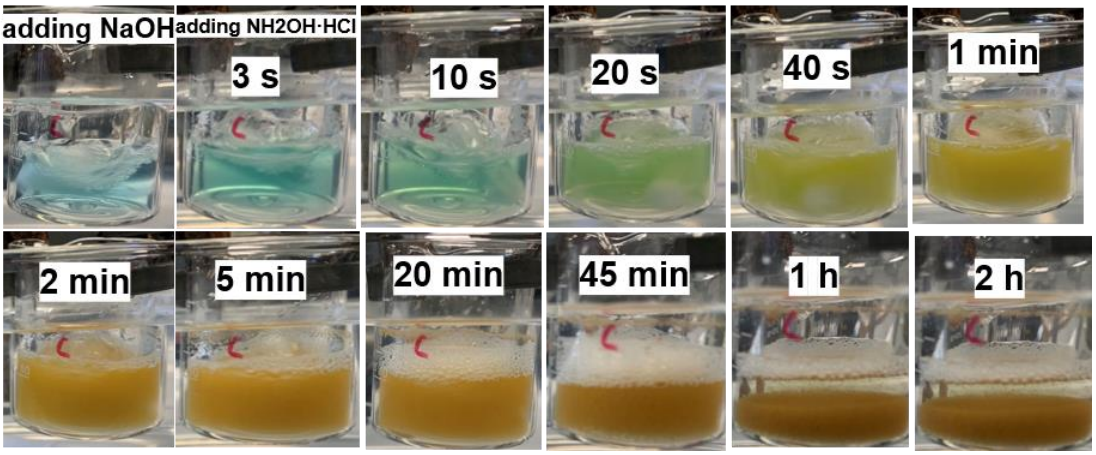

Figure 5.8 The change in the solution colour as a function of reaction time in the synthesis of Cu_2O nanocube in the batch reactor in method 1.

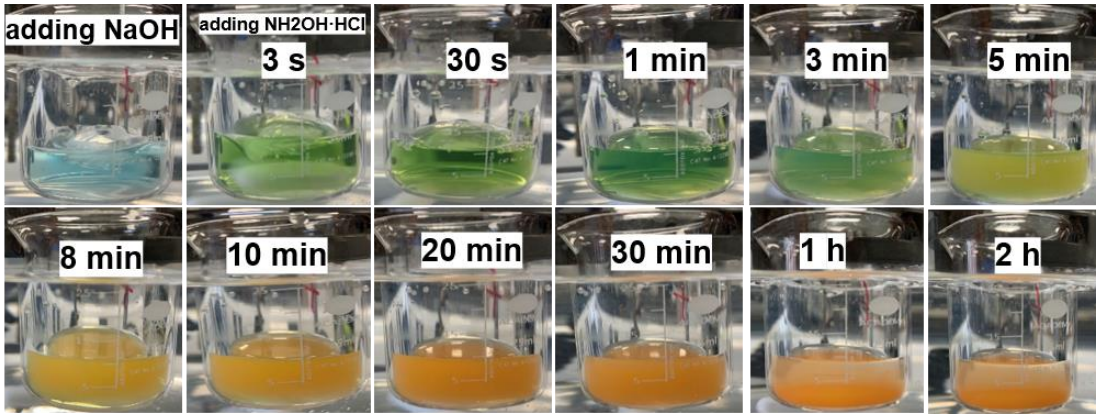

Figure 5.9 The change in the solution colour as a function of reaction time in the synthesis of Cu_2O rhombic dodecahedra in the batch reactor in method 1.

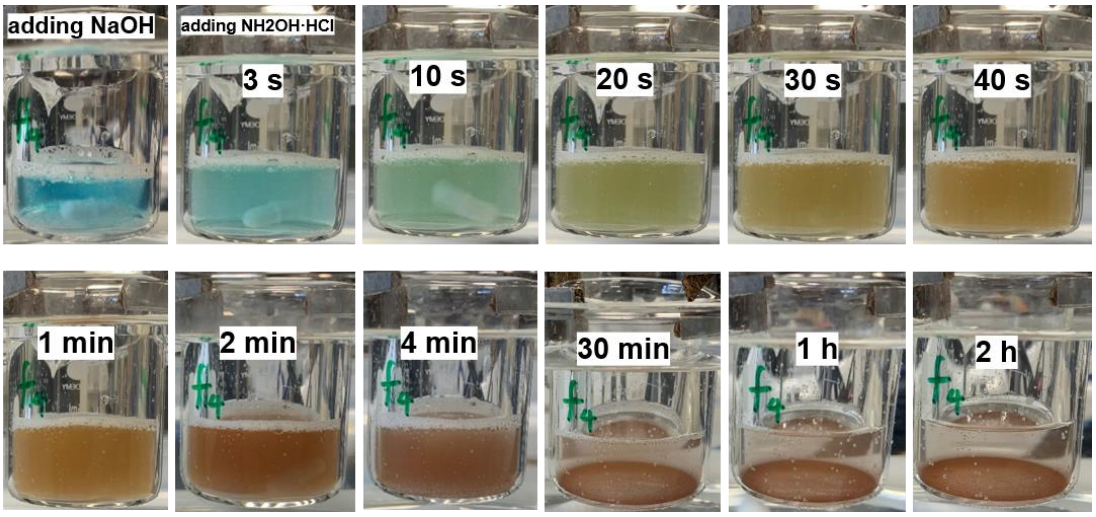

Figure 5.10 The change in the solution colour as a function of reaction time in the synthesis of Cu_2O octahedra in the batch reactor in method 1.

During the synthesis of Cu_2O nanoparticles, in the first step, when the NaOH concentration was 1.8×10^{-2} M, no considerable precipitation of $Cu(OH)_2$ was observed, shown in Fig. 5.11. $Cu(OH)_2$ precipitation in vials and corresponding $Cu(OH)_2$ 'slugs' ($Cu(OH)_2$ precipitation solid particles) were observed in the microtube when NaOH concentration was increased to 3.6×10^{-2} M.

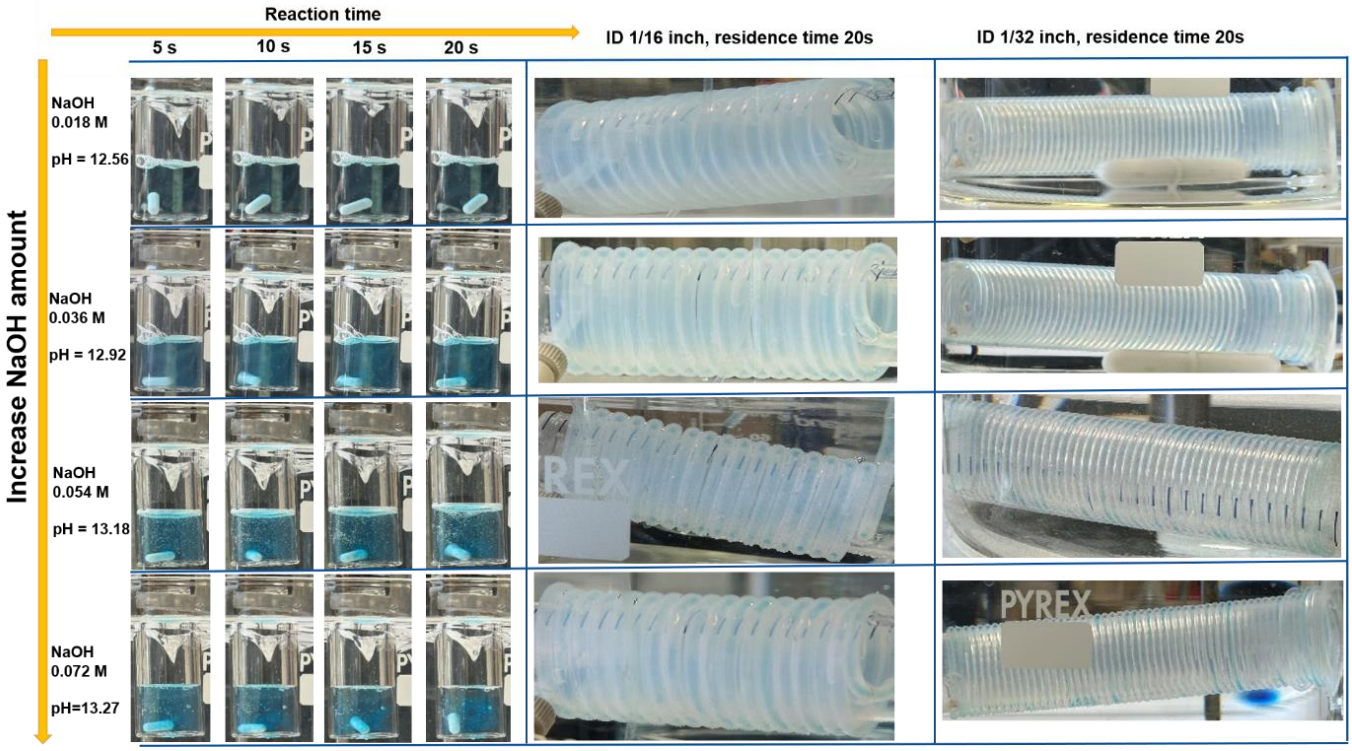

Figure 5.11 $CuCl_2$-SDS reacted with different concentrations of NaOH to form $Cu(OH)_2$ precipitation in both vials and microreactors with temperature 32 °C.

Based on Equation 5-2, a concentration of 1×10^{-2} M NaOH is required for the formation of $Cu(OH)_2$ precipitation when the concentration of $CuCl_2$ was 5×10^{-3} M. In this experimental setup, NaOH concentrations of 1.8×10^{-2} to 7.2×10^{-2} M were utilized, representing concentrations 1.8 and 7.2 times higher than the calculated requirement. As the solubility product constant (K_{sp}) of $Cu(OH)_2$ is around 2×10^{-20}, the transfer of Cu^{2+} ions into $Cu(OH)_2$ is theoretically expected to occur almost completely at these four different concentrations of NaOH. However, as the concentrations of NaOH increased, the precipitation of $Cu(OH)_2$ became more evident in the batch vessel and microreactor. This can be attributed to the presence of anionic surfactant SDS [255]. The SDS micelles form around the cationic Cu^{2+} which trap a certain amount of Cu^{2+} inside the micelles, thus reducing the amount of Cu^{2+} participate the precipitation reaction. During the reduction reaction process, the mixing performance between $Cu(OH)_2$ and the reducing agent $NH_2OH{\cdot}HCl$ plays a crucial role in determining the concentration gradients of Cu_2O monomers, which in turn affect the final particle size and morphologies. As the precipitation $Cu(OH)_2$ increases, the mixing efficiency between $Cu(OH)_2$ with

$NH_2OH{\cdot}HCl$ deteriorates, resulting in non-uniform particle size and shapes of Cu_2O nanocrystals (shown in Figure 5.6 a2-d4).

To enhance the mixing performance, a tube with a reduced inner diameter of 1/32 inch was employed (Reynold number is 271.75). The particle size and shape exhibit greater uniformity with lower relative standard deviation (shown in Figure 5.12, Figure 5.13, Table 5.1), for the samples a1-Cube-Cu_2O (218 nm, 12.34%), b1-corner-truncated RD-Cu_2O (404 nm, 9.99%), c1-{100}-truncated RD-Cu_2O (510 nm, 10.58%), and d1-RD-Cu_2O (571 nm, 12.87%) when compared to the wider microreactor (I.D. 1/16 inch). In the wide tube, the particle sizes were 290 nm with a relative standard deviation of 17.93% (a1-Cube-Cu_2O), 445 nm with 24.89% (b1-corner-truncated RD-Cu_2O), 386 nm with 16.14% (c1-{100}-truncated RD-Cu_2O), and 320 nm with 18.36% (d1-RD-Cu_2O). As case of sample d4, Cu_2O nanoparticles still exhibited non-uniform morphologies in wide tube, showing characteristic shapes of both truncated cube and octahedra. However, when the narrower tube was employed, it resulted in the production of nearly perfect octahedral Cu_2O nanoparticles with particle sizes of 896 nm. Nonetheless, there was still a relatively wide standard deviation of 21.19%, which indicates that a higher mixing performance will be required. As the reduction reaction of $NH_2OH{\cdot}HCl$ and $Cu(OH)_2$ occurs instantaneously, the reaction takes place even at the mixing point of the mixer. To ensure better concentration homogeneity, a two-inlet vortex mixer is utilized as a replacement for the T-mixer. In step 2, with the same flow rate, the rapid initial mixing between $Cu(OH)_2$ with $NH_2OH.HCl$ enhances the uniformity of Cu_2O nano-octahedra with a size of 501 nm, with lower relative standard deviation of 10.55% (Figure 7 d4-1).

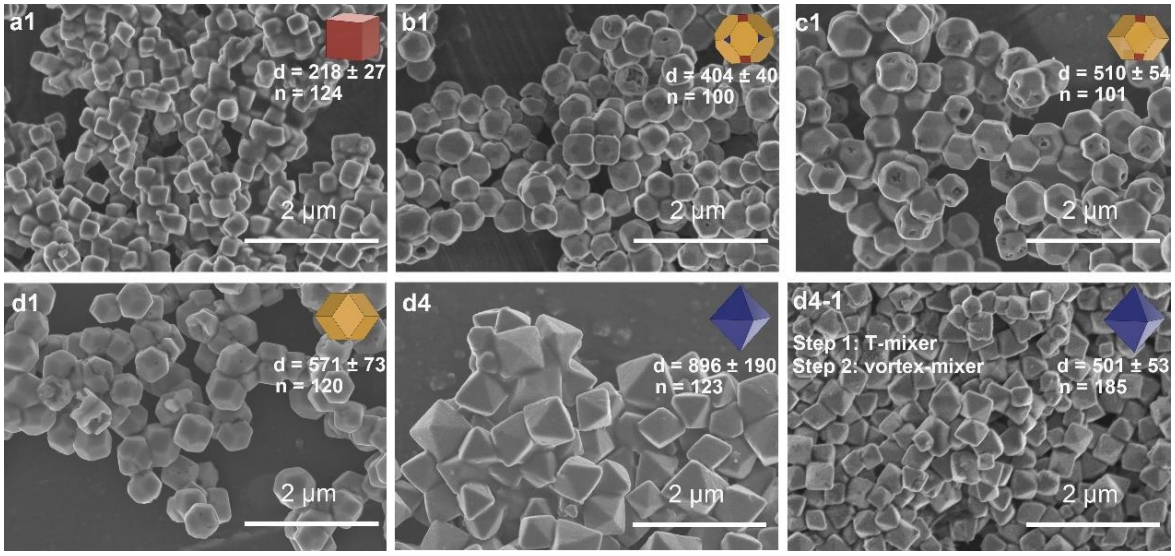

Figure 5.12 SEM images of Morphological evolution under various NaOH and $NH_2OH{\cdot}HCl$ concentrations using method 1 with the microtubing of 1/32 inch I.D with T-mixer in both step 1 and step 2 (a1-d4), and T-mixer in step 1 and vortex-mixer in step 2 (d4-1), 32 ^oC, residence time in step 1 and step 2 are both 20 s.

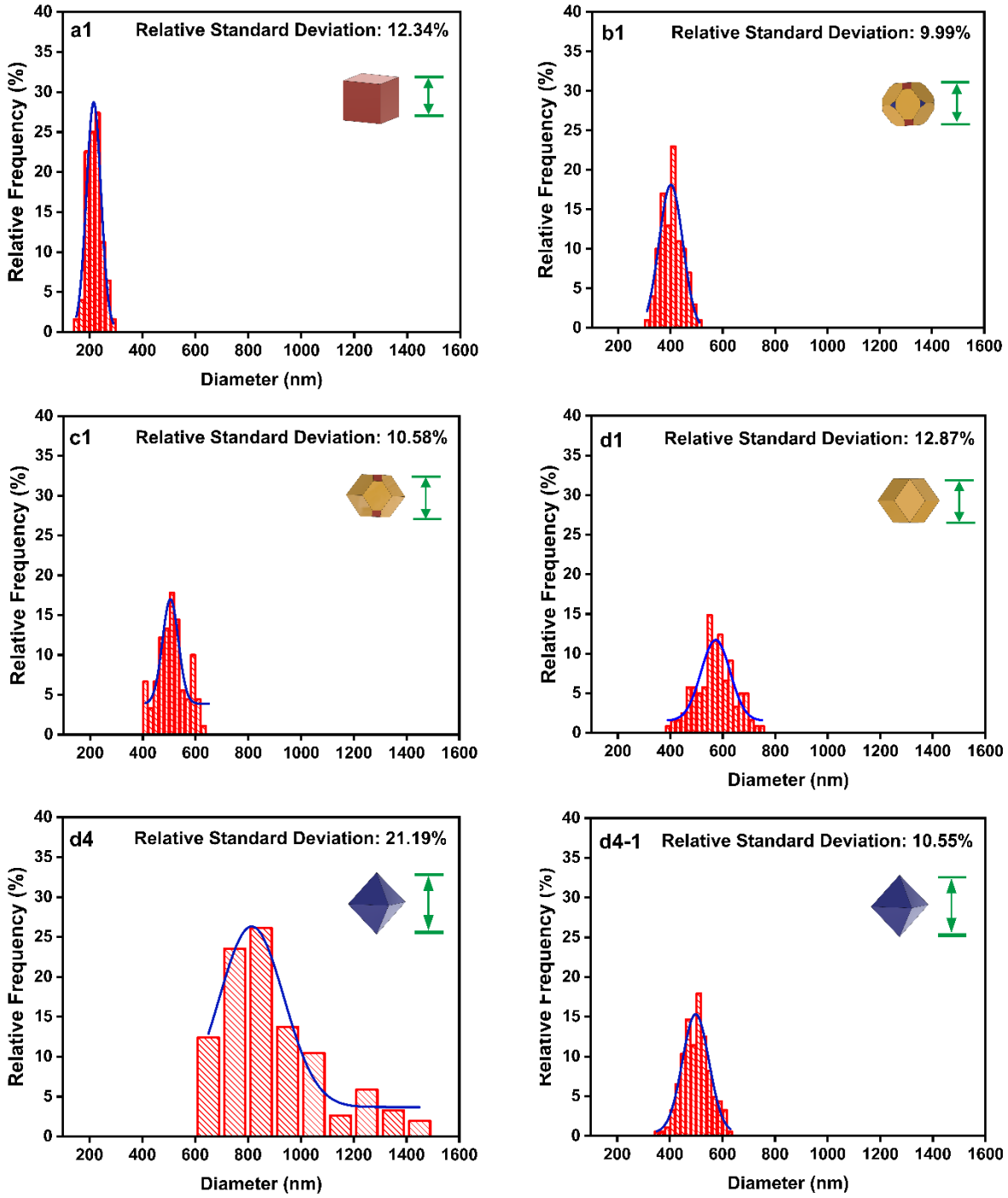

Figure 5.13 Size distribution histograms of Cu_2O nanoparticles in tube (I.D. 1/32 inch) using method 1 with T-T mixer (a1) nanocube, (b1) all-corner-truncated rhombic dodecahedra, (c1) {100}-truncated rhombic dodecahedra, (d1) rhombic dodecahedra, (d4) octahedra and (d4-1) octahedra with T-vortex mixer.

The particle sizes of a1-cube-Cu_2O, b1-corner-truncated RD-Cu_2O, c1-{100}-truncated RD-Cu_2O, d1-RD-Cu_2O, and d4-Oct--Cu_2O in batch and microreactor (1/16 inch I.D., 1/32 inch I.D. respectively) are shown in Figure 5.14 and Table 5.1. In the case of a1-cube and b1-corner-truncated RD, the particle size decreased from the batch reactor, to the wide microreactor (1/16 inch I.D), and further to the narrow microreactor (1/32 inch I.D.). On the contrary, the particle size of c1-{100}-truncated RD

increased from the batch reactor, wide microreactor, and narrow microreactor. For the sample of d1-RD, the particle size is not related to the mixing performance in batch and microreactor. Non-uniform Oct-Cu_2O nanoparticles were formed in wide microreactor. Compared with the batch reactor, similar particle size was achieved in narrow microreactor with T-T mixer with larger particle size deviation. Enhanced mixing performance was achieved by using T-Vortex mixer instead, which achieve uniform Oct-Cu_2O with smaller particle size. From a kinetic perspective, the final shape and particle size is related to the nucleation and growth manner. [163] In this rapid reduction chemical reaction, the degree of supersaturation of Cu_2O monomers is tied to the mixing performance within reactor. The concentration and temperature gradients inside the reactor would lead to the non-uniform particle size and morphology. [256] To investigate the relationship between mixing performance inside the reactor with the final particle size of Cu_2O nanoparticles, we studied the morphology evolution process of three typical shapes: Cube-Cu_2O, RD-Cu_2O, and Oct-Cu_2O at different time scales in the following section.

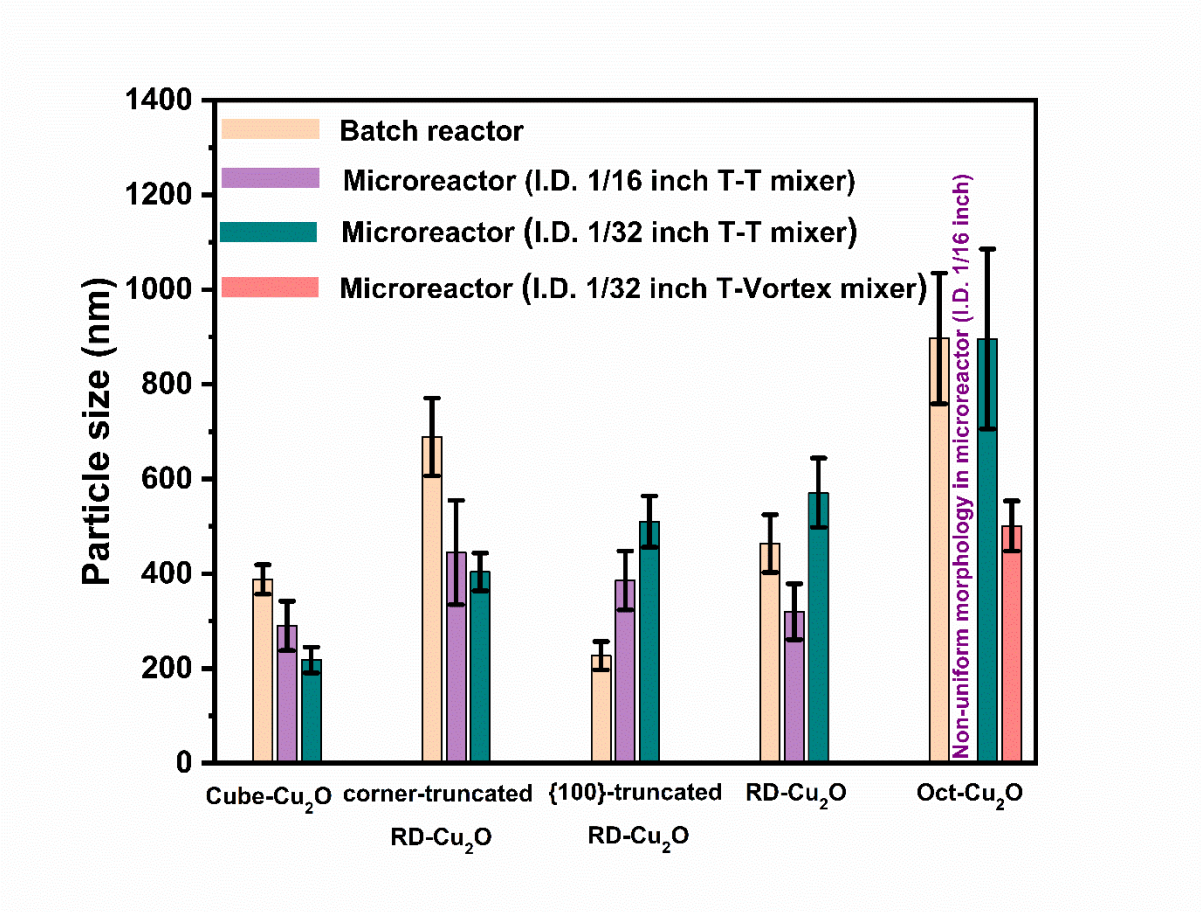

Figure 5.14 Average particle size and relative standard deviation of the Cu_2O nanoparticles from batch reactor and microreactor with 1/16 inch and 1/32 inch respectively from method 1.

Table 5.1 Average particle size and relative standard deviation of the Cu_2O nanoparticles synthesized in batch reactor and microreactor with 1/16 inch I.D. and 1/32 inch I.D. respectively using in method 1.

Sample	Shape	Average Particle Size (nm)	Relative Standard Deviation	Mixer in Step1/Step 2
Fig. 5.3 a1 batch	Cube	388 ± 31	10.39%	
Fig. 5.5 a1-1/16 inch		290 ± 52	17.93%	T/T-mixer
Fig. 5.11 a1-1/32 inch		218 ± 27	12.34%	T/T-mixer
Fig. 5.3 b1 batch	Corner-truncated rhombic dodecahedra	689 ± 82	11.85%	
Fig. 5.5 b1-1/16 inch		445 ± 110	24.89%	T/T-mixer
Fig. 5.11 b1-1/32 inch		404 ± 40	9.99%	T/T-mixer
Fig. 5.3 c1 batch	{100}-truncated rhombic dodecahedra	227 ± 30	13.2%	
Fig. 5.5 c1-1/16 inch		386 ± 62	16.14%	T/T-mixer
Fig. 5.11 c1-1/32 inch		510 ± 54	10.58%	T/T-mixer
Fig. 5.3 d1 batch	Rhombic dodecahedra	464 ± 61	13.25%	
Fig. 5.5 d1-1/16 inch		320 ± 95	18.36%	T/T-mixer
Fig. 5.11 d1-1/32 inch		571 ± 73	12.87%	T/T-mixer
Fig. 5.3 d4-batch	Octahedra	897 ± 138	15.35%	
Fig. 5.5 d4-1/16 inch	Octahedra/truncated cube	Shape uniform	-------	T/T-mixer
Fig. 5.11 d4-1/32 inch	Octahedra	896± 190	21.19%	T/T-mixer
Fig. 5.11 d4-1-1/32 inch	Octahedra	501± 53	10.55%	T/Vortex-mixer

5.3.3 Discussion

5.3.3.1 Nucleation, growth, and shape re-construction of Cu_2O nanoparticles

The progression of colour changes in the solution of Cube-Cu_2O, RD-Cu_2O, and Oct-Cu_2O, is depicted in Figure 5.8-5.10 over a two-hour period in the batch reactor. At the first stage, after the addition of NaOH, blue light precipitation of $Cu(OH)_2$ was observed. After the introduction of $NH_2OH{\cdot}HCl$ to start nanocrystal growth, the solution colour turned from light blue to different colours at different morphology, signifying distinct nucleation and growth processes associated with various Cu_2O morphologies. To study their nucleation and growth process, the TEM images of Cube-, RD-, and Oct-Cu_2O produced in the narrow microtube were used to show the instantaneous particle morphology. Samples were prepared for TEM at these time points same as in the batch reactor, shown in Figure 5.15. In the batch reactor during the synthesis of Cu_2O nanocubes, the solution shifted from light blue to green blue immediately after the introduction of $NH_2OH.HCl$ due to Cu_2O seed formation, shown in Figure 5.8. After 20 s the solution color transitioned to green yellow, which then evolved into light yellow within 1 min. Subsequently, at 2 mins the solution color changed into deep yellow, and there is no obvious further solution color change afterward. Similarly, within the microreactor, the nanocubes grew in size from ~150 nm at 20 s to ~210 nm at 1 min with a noticeably rough surface (Figure 5.15). It is worth noting that even at 20 s, the crystal facets of {100} had already formed. At 1 min, the particle size was already similar to the final particle size at 2 hrs with ~219 nm. The primary change occurring during the time period was the gradual smoothing of rough surface, which continued to improve within 2 hrs.

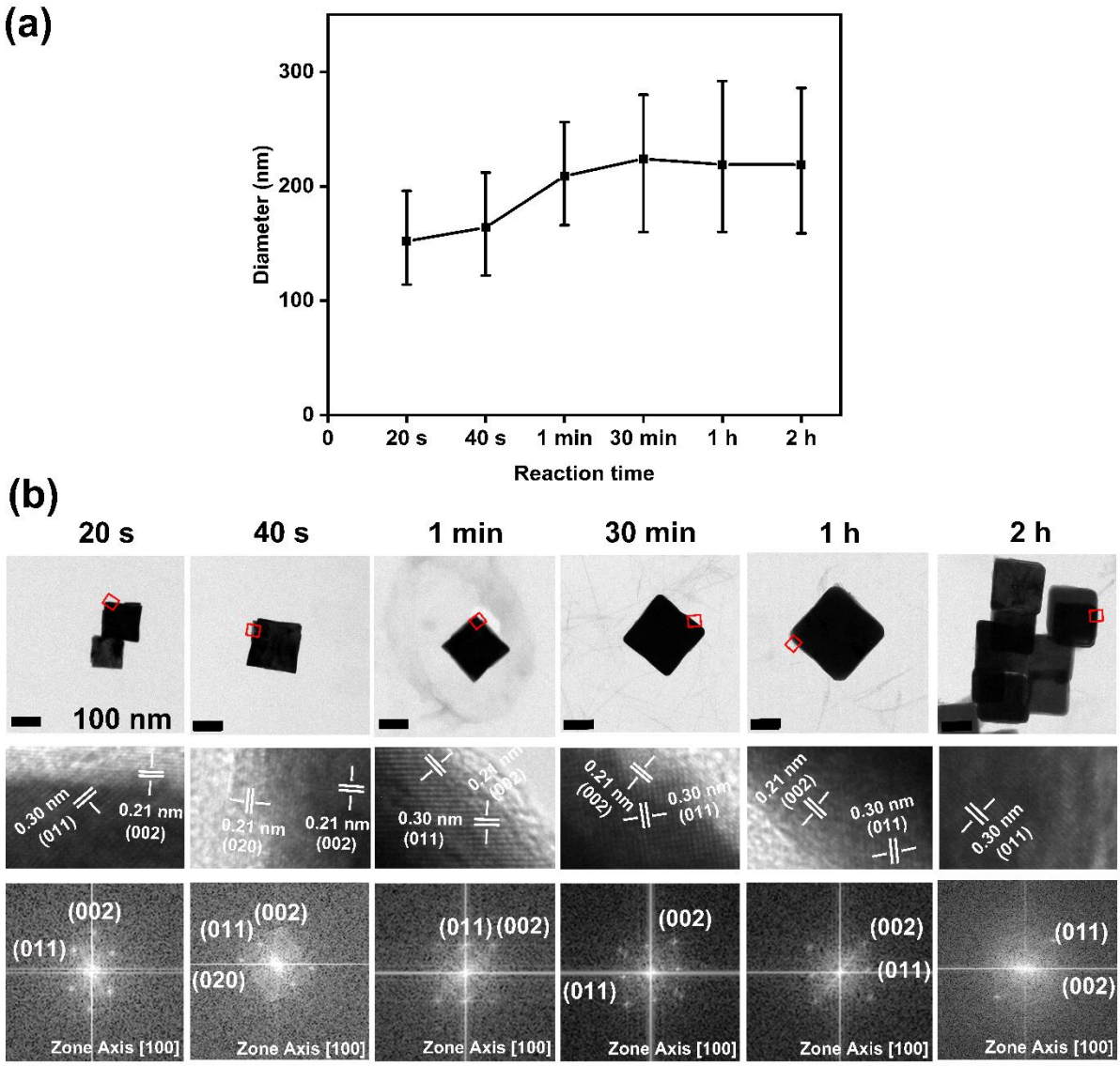

Figure 5.15 Cu_2O nanocubes made via microreactor method 1 (a) Plot of the particle size as a function of reaction times: 20 s, 40 s, 1 min, 30 min, 1 h, and 2 h, (b) TEM images of low magnification showing particle shape and high magnification with lattice fringes and corresponding FFT patterns.

In the synthesis of Cu_2O rhombic dodecahedra, the solution colour changed from light blue to green following addition of $NH_2OH{\cdot}HCl$. The solution colour changes at a much slower rate, and was still green after 1 min of reaction, yellow between 5 to 8 min, and orange from 10 to 60 min of reaction in batch reactor, shown in Figure 5.9. Consequently, the crystal formation process of rhombic dodecahedra exhibits a slower growth rate compared to cubic Cu_2O nanoparticles, shown in Figure 5.16. At 1 min, Cu_2O crystals haven't formed yet, the only imaged particles were those of salts which quickly damaged under the electron beam. At 5 mins, quasi-spherical nanoparticles with {111} facets were formed. Cu_2O nanoparticles tended to aggregate together into quasi-spherical intermediate structures and subsequently evolved into rhombic dodecahedra via a ripening mechanism. At 30 mins,

the particle has almost reach to the final particle size ~580 nm with {100} facets. After the reaction time reach to 2 hrs, perfect rhombic dodecahedra with all surface facets of {110} were achieved. In contrast to the {100} facets of Cu_2O nanoparticles, the {110} facets exhibit a higher density of atomic steps and abundant unsaturated coordination sites. From this experiment, we can tell in the formation of nanocrystals via precipitation reactions, slowing down the reaction rates is crucial to achieve high-energy facets in this kinetic-controlled process.

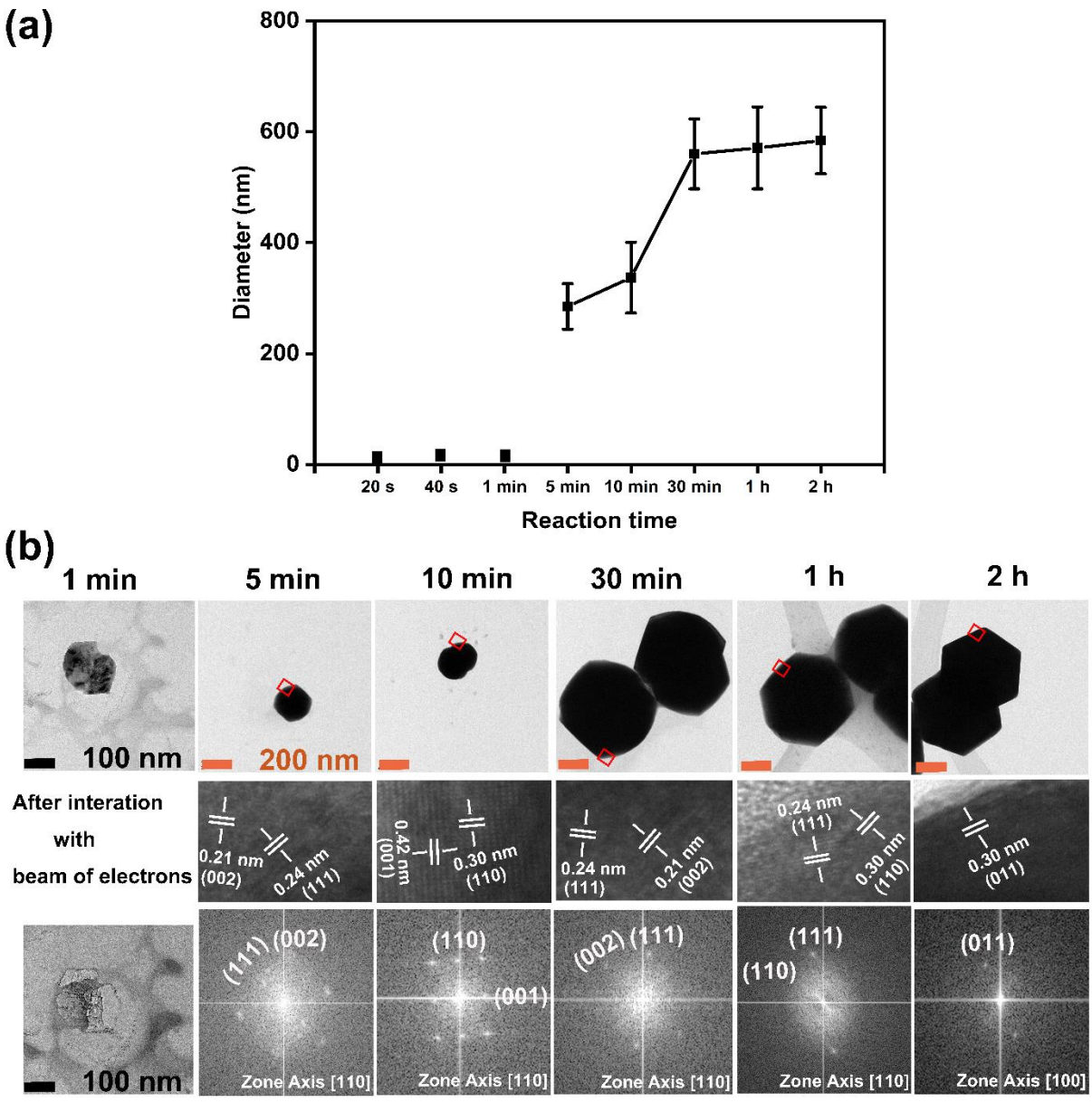

Figure 5.16 Cu_2O rhombic dodecahedra made via microreactor method 1 (a) Plot of the particle size as a function of reaction times: 20 s, 40 s, 1 min, 5 min, 10 min, 30 min, 1 h, and 2 h, (b) TEM images of low magnification showing particle shape and high magnification with lattice fringes and corresponding FFT patterns.

In the synthesis of octahedral Cu_2O nanoparticles, a higher concentration of NaOH 7.2×10^{-2} M was needed compared with 1.8×10^{-2} M in the shape of cube and rhombic dodecahedra. When a higher concentration of NaOH was added, a turbid light bluish precipitation formed in the batch reactor, shown in Figure 5.10. The solution colour changed to yellow blue at 10 s reaction and yellow brown at 1 min after the addition of $NH_2OH{\cdot}HCl$. At 2 min, the solution colour became dark brown and no obvious colour change afterward. The octahedra has the fast growth rate, at 20 s the particle size has already reached ~570 nm, which is consistent during 1 h, shown in Figure 5.9. Both the {110} and {111} facets have been formed as shown in Figure 5.17 (b). After 1 min, the {110} truncated octahedra slowly evolve into octahedra with the disappearing {110} facets without change in particle size. After 2 h, octahedra with perfect {111} facets have been achieved.

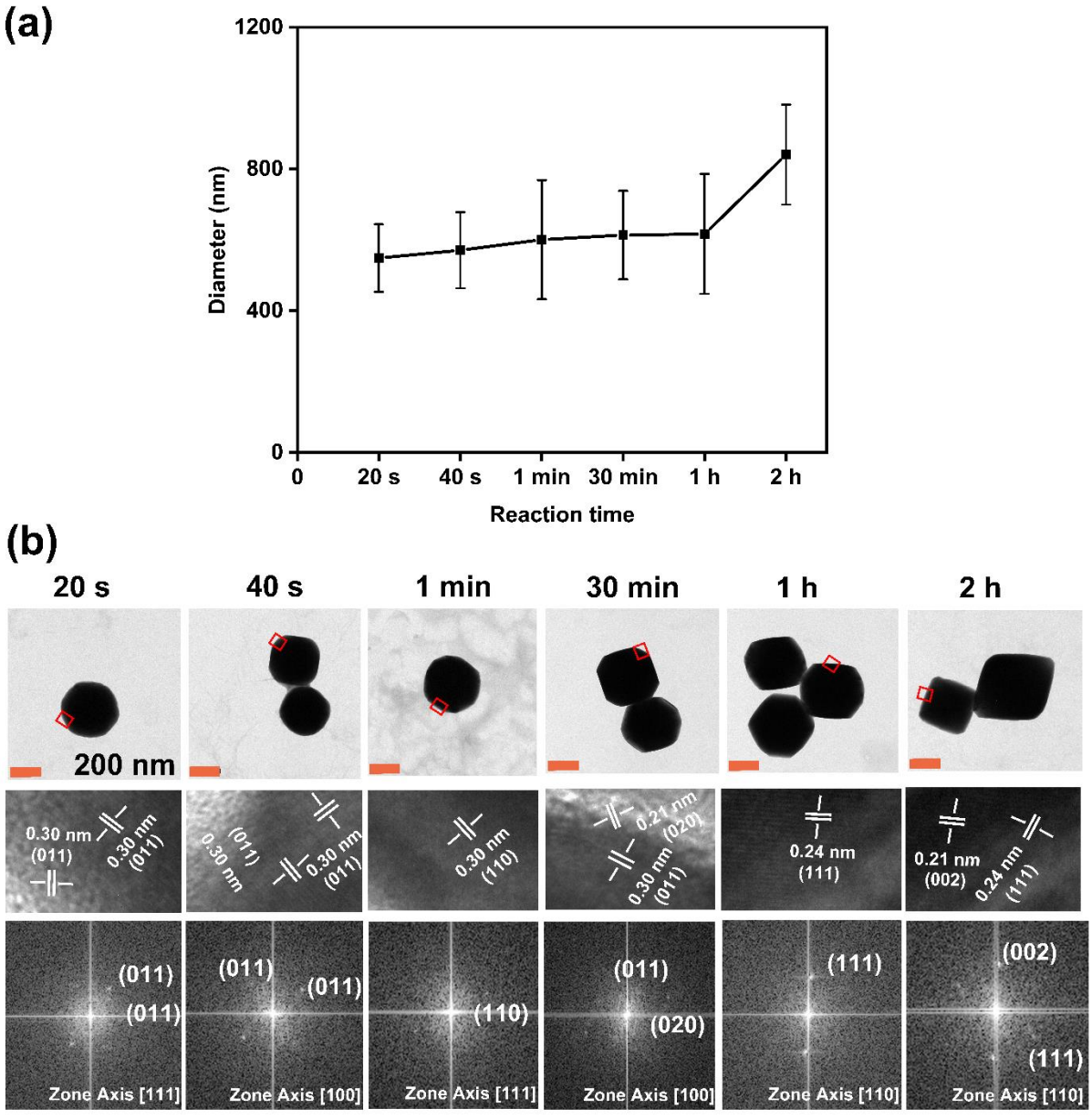

Figure 5.17 Cu_2O octahedra made via microreactor method 1 (a) Plot of the particle size as a function of reaction times: 20 s, 40 s, 1 min, 30 min, 1 h, and 2 h, (b) TEM images of low magnification showing particle shape and high magnification with lattice fringes and corresponding FFT patterns.

To show the synthesis process of Cu_2O nanoparticles, a schematic illustration of geometrical shape-evolution from cube to dodecahedra in different concentrations of NaOH and $NH_2OH{\cdot}HCl$ is shown in Figure 5.18. To these three morphologies, the synthesis process of Cu_2O nanocrystals includes nucleation, growth, and surface re-construction. As the reaction time increased, seed particles continuously adsorb onto the intermediate structures to allow further growth as evidenced by an increase particle size. In the final ripening step, these intermediate structures evolve into different polyhedral architectures via surface reconstruction, aimed at minimizing the overall energy of the reaction system. [257] In this context, achieving the thermodynamically stable morphology relies on factors such as reduction rate, surface molecular diffusion rate, and synthesis time. For the cube-Cu_2O and Oct-Cu_2O, at 20 s, the crystal particle size is already similar to the final particle size at 2 hrs, which means the mixing performance within this 20 s is very important to determine the final particle size. The mixing performance in batch is primarily achieved through mechanical stirring, which can generate bulk fluid movement and turbulent flow. Turbulent flow can increase the opportunity of particle aggregation to increase the final particle size compared with the laminar flow in microreactor, which makes the particle size of cube-Cu_2O in the narrow tube microreactor (1/32 inch I.D.) is smaller than that in the batch reactor. However, for the Oct-Cu_2O, better mixing in the microreactor will be further needed to get $Cu(OH)_2$ precipitation mixing with $NH_2OH{\cdot}HCl$. For the RD-Cu_2O, during the 20 s, no nucleation has been observed, indicating the mixing performance between batch and microreactor did not have such influence on the final particle size. Therefore, the microreactor is particularly well-suited for applications requiring precise control of rapid reactions in small-scale chemical processes.

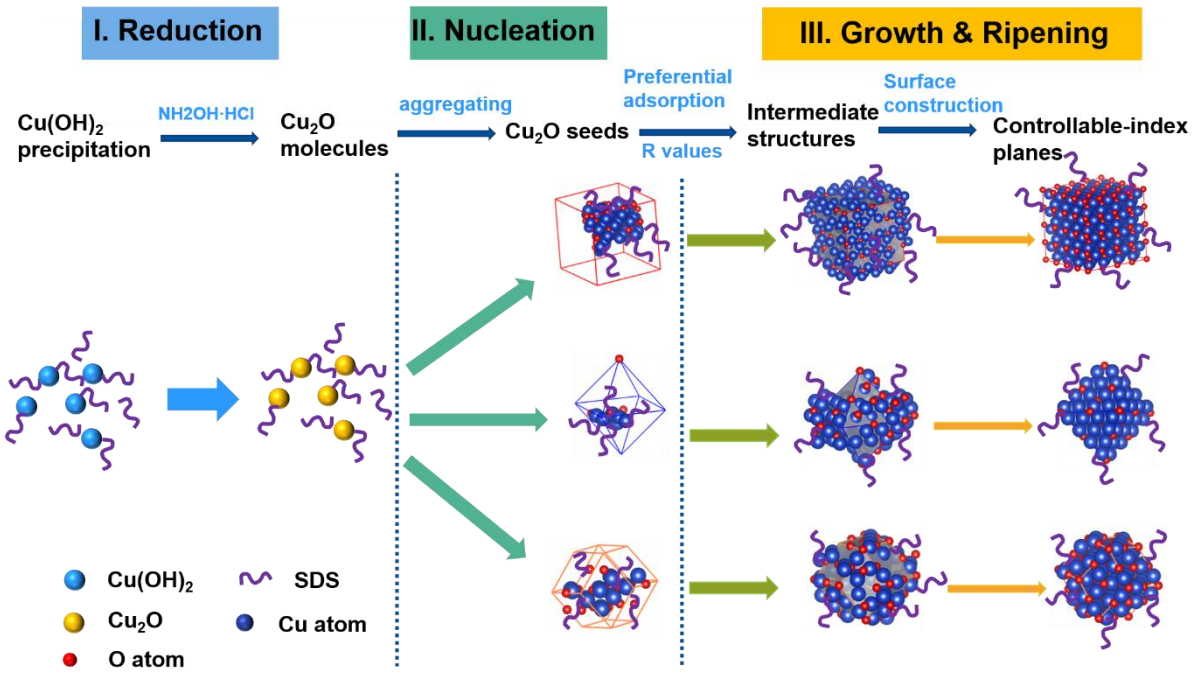

Figure 5.18 Schematic showing the three different approaches to control the shape of Cu_2O nanocrystals using SDS as a capping agent in method 1.

5.3.3.2 The shape evolution of Cu_2O nanoparticles

The growth rate of a crystal perpendicular to a specific plane is directly proportional to its surface energy. As a result, the final facets of Cu_2O could be adjusted according to their respective facet surface energies. [258] [259] According to the Gibbs-Wulff theorem (ΔG), the morphological evolution of crystals is driven by continuously decreasing the total surface energy, and finally terminates at the minimum surface energy point in the given reaction conditions. [260] Huang *et al*. [261] reported that the variation in ΔG, resulting from the different concentrations of cadmium acetate and potassium hydroxide, led to morphological evolution of cadium oxide from stellated octahedra, octahedra, and {100}-truncated octahedra. The various crystal morphologies of cesium lead halide were also obtained by varying the relative reagent amount and thus the different reaction free energy in Peng *et al*.'s paper. [262] For the Cu_2O nanoparticles synthesis in the solution-phase system, different-index facets have been reported by adjusting the R value by changing the concentration of reagents [164] [263], capping agents [175], and anions of the copper salts [264], etc. In practice, however, the shape that evolves is too complex to be tracked accurately. [265]

The different driving force of solidification processes at different conditions is created from the difference in Gibbs free energy between the solid and metastable liquid states. In our system, we try to build the relationship between Gibbs free energy and final shapes of Cu_2O with {100}, {111}, and {110} facets. Using the equation $\Delta G = \Delta G^0 + RT\ lnQ$, we can compute the standard Gibbs free

energy ΔG^0 at the reaction temperature of 307 K, considering specific concentration of NaOH and the reducing agent $NH_2OH{\cdot}HCl$ (see the calculations below).

Gibbs free energy calculation

$$CuCl_2 + 2\,Na(C_{12}H_{25}OSO_3) \rightleftharpoons NaCu(C_{12}H_{25}OSO_3)_2 + 2\,NaCl \quad (5\text{-}1)$$

$$Cu(C_{12}H_{25}OSO_3)_2 + 2\,NaOH \rightleftharpoons Cu(OH)_2 \downarrow + 2\,Na(C_{12}H_{25}OSO_3) \quad (5\text{-}2)$$

$$2\,Cu(OH)_2 + 2\,NH_2OH \cdot HCl \rightleftharpoons Cu_2O + N_2 + 5\,H_2O + 2\,HCl \quad (5\text{-}3)$$

$$Sum\text{: } 2\,CuCl_2 + 4\,NaOH + 2\,NH_2OH \cdot HCl \rightleftharpoons Cu_2O \downarrow + N_2 + 5\,H_2O + 2\,HCl + 4\,NaCl \quad (5\text{-}4)$$

$$Cu(OH)_2 \rightleftharpoons CuO + H_2O \quad (5\text{-}5)$$

$$\text{Or } Sum\text{: } 3\,CuCl_2 + 6\,NaOH + 2\,NH_2OH \cdot HCl \rightleftharpoons Cu_2O \downarrow + Cu(OH)_2 \downarrow + N_2 + 5\,H_2O + 2\,HCl + 4\,NaCl \quad (5\text{-}6)$$

$$\text{Or } Sum\text{: } 3\,CuCl_2 + 6\,NaOH + 2\,NH_2OH \cdot HCl \rightleftharpoons Cu_2O \downarrow + CuO \downarrow + N_2 + 6\,H_2O + 2\,HCl + 6\,NaCl \quad (5\text{-}7)$$

$$\Delta G = \Delta G^0 + RT\,lnQ = -RT\,lnK + RT\,lnQ$$

In which T = 305 K, R = 8.31451 J/K mol, Q is the reaction quotient, which is 0 at the beging of the reaction. K is the Equilibrium Constant. When the reaction finished, ΔG will become 0, so the final Q is equal to K.

For the samples a1-a4, b1-b4, c1-c4, and d1-d4 obtained from the wide microtube, the concentration of Cu^{2+} in the liquid supernatant after centrifuge was obtainded by ICP-MS, shown in Table 5.2. The sample a1 Cub-Cu_2O is considered as an example to calculate the ΔG^0. The concentration of $CuCl_2$ is 0.005 M, NaOH is 0.018 M, and $NH_2OH{\cdot}HCl$ is 0.004 M. As the concentration of Cu^{2+} in the liquid supernatant is 6.33×10^{-6} mol/L, it is assumed that the reation (5-2) proceed completely. The reaction (5-6) or (5-7) should be applied to calculate the ΔG^0:

$$\Delta G^0 = -RT\,ln\,K$$

$$K = Q = \frac{[HCl]^2}{[CuCl_2]^3[NaOH]^6[NH_2OH \cdot HCl]^2}$$

Then

$$K = \frac{[0.00333]^2}{[0.00001]^3[0.008]^6[0.000673]^2}\,M^{-9}$$

So K is 9.17×10^{28} and ΔG^0 is -169.10 KJ/mol for Cube-Cu_2O.

As for the sample d1 RD-Cu_2O, the concentration of $CuCl_2$ is 0.005 M, NaOH is 0.018 M, and $NH_2OH{\cdot}HCl$ is 0.024 M. As the the concentration of Cu^{2+} in the liquid supernatant is 1.23×10^{-3} mol/L, it is assumed that the reation (5-2) doesn't proceed completely, and the reaction (5-4) should be applied to calculate the ΔG^0:

$$\Delta G^0 = -RT\ ln\ K$$

$$K = Q = \frac{[HCl]^2}{[CuCl_2]^2[NaOH]^4[NH_2OH \cdot HCl]^2}$$

Then

$$K = \frac{[0.00377]^2}{[0.00123]^2[0.01046]^4[0.02023]^2}\ M^{-9}$$

So K is 1.92×10^{12} and ΔG^0 is -71.72 KJ/mol for RD-Cu_2O.

As for the sample d4 Oct-Cu_2O, the concentration of $CuCl_2$ is 0.005 M, NaOH is 0.072 M, and $NH_2OH{\cdot}HCl$ is 0.024 M. As the the concentration of Cu^{2+} in the liquid supernatant is 9.04×10^{-6} mol/L, it is assumed that the reation (2) proceed completely, and the reaction (5-6) or (5-7) should be applied to calculate the ΔG^0:

$$\Delta G^0 = -RT\ ln\ K$$

$$K = Q = \frac{[HCl]^2}{[CuCl_2]^3[NaOH]^6[NH_2OH \cdot HCl]^2}$$

Then

$$K = \frac{[0.00333]^2}{[0.00001]^3[0.062]^6[0.02067]^2}\ M^{-9}$$

So K is 4.55×10^{20} and ΔG^0 is -120.62 KJ/mol for Oct-Cu_2O.

The concentrations of HCl, $CuCl_2$, NaOH, and $NH_2OH{\cdot}HCl$ according to the Equation 5-4, 5-6, and 5-7 and the corresponding equilibrium constant and Gibbs free energy driving force of sample a1-d4 are shown in Table 5.2.

Table 5.2 The concentration of Cu^{2+} in the liquid supernatant of sample a1-d4 after centrifuge by the ICP-MS test and the corresponding equilibrium constant K and Gibbs free energy driving force.

Sample	Shape	Cu^{2+} (ICP-MS) mol/L	HCl mol/L	NaOH mol/L	$NH_2OH{\cdot}HCl$ mol/L	K=Q	ΔG KJ/mol
a1	Cube	6.33×10^{-6}	0.00499	0.00802	0.000673	9.17×10^{28}	-169.11
a2	Cube	3.25×10^{-6}	0.00499	0.02602	0.000673	7.87×10^{25}	-151.20
a3	Cube	1.70×10^{-6}	0.00499	0.04402	0.000673	3.35×10^{24}	-143.20
a4	Cube	2.04×10^{-6}	0.00499	0.06202	0.000673	4.29×10^{23}	-137.99
b1	Corner-truncated RD	2.03×10^{-5}	0.00498	0.00804	0.00422	8.33×10^{17}	-104.64
b2	Truncated cube	3.78×10^{-6}	0.00499	0.02602	0.00587	1.03×10^{24}	-140.22
b3	Truncated cube	4.13×10^{-6}	0.00499	0.04402	0.00587	4.41×10^{22}	-132.22
b4	Truncated cube	6.26×10^{-6}	0.00499	0.06202	0.00587	5.64×10^{21}	-127.00
c1	{100}-truncated RD	1.13×10^{-4}	0.00489	0.00822	0.00711	8.56×10^{15}	-93.03
c2	Truncated cube	4.46×10^{-6}	0.00499	0.02602	0.00867	4.74×10^{23}	-138.24
c3	Truncated cube	5.98×10^{-6}	0.00499	0.04402	0.00867	2.02×10^{22}	-130.24
c4	Truncated cube	9.13×10^{-6}	0.00499	0.06202	0.00867	2.58×10^{21}	-125.02
d1	Octahedra	1.23×10^{-3}	0.00377	0.01046	0.02023	1.92×10^{12}	-71.72
d2	Truncated Octahedra	2.28×10^{-5}	0.00498	0.02604	0.02068	1.03×10^{22}	-128.54
d3	Truncated Octahedra	8.66×10^{-6}	0.00499	0.04402	0.02067	3.56×10^{21}	-125.83
d4	Octahedra	9.04×10^{-6}	0.00499	0.06202	0.02067	4.55×10^{20}	-120.62

ΔG^0 = -137.99 to -169.11 KJ/mol for Cube-Cu_2O;

ΔG^0 = -71.72 KJ/mol for the RD-Cu_2O;

ΔG^0 = -120.62 KJ/mol for the Oct-Cu_2O.

ΔG^0 for intermediate structure like the truncated cube is from -125.02 to -140.22 KJ/mol, ΔG^0 for truncated octahedra is from -125.83 to -128.54 KJ/mol, and ΔG^0 for truncated RD is from -104.64 to -93.03 KJ/mol

Table 5.3 The pH values and ΔG^0 of samples a1-d4 with different concentration of NaOH and $NH_2OH.HCl$ in wide tube (1/16 inch I.D.)

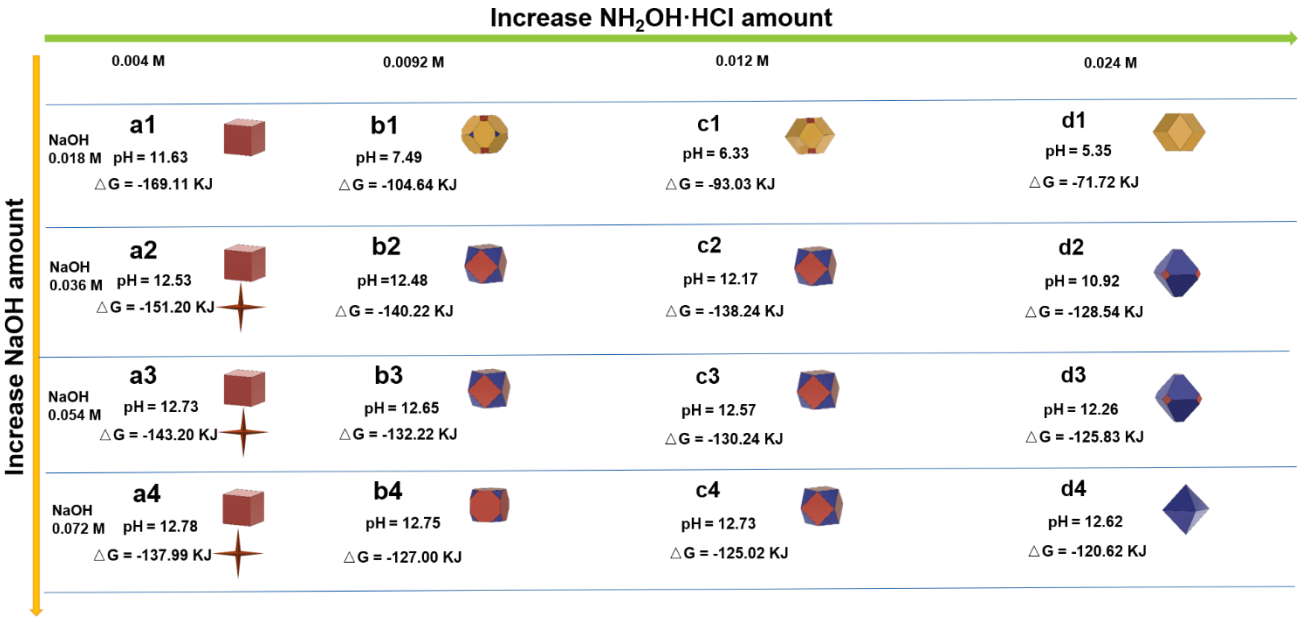

Figure 5.19 illustrates a plot of ΔG^0 versus final pH values of the samples a1 to d4 according to Table 5.3. Rhombic dodecahedra and truncated rhombic dodecahedra form at pH value below than 8 with higher ΔG^0 from -104.64 to 71.72 KJ/mol compares with other shapes. Comparative analysis with cube & whisker and truncated cube reveals that octahedra and truncated-octahedra exhibit higher ΔG^0 with minimal variation in pH values. In our system, the nucleation time of Cu_2O nanoparticles follows the trend of cube {100} (fastest), octahedra {111}, and dodecahedra {110} (slowest), which corresponds with the crystallization process observed in Figure 5.15-5.17.

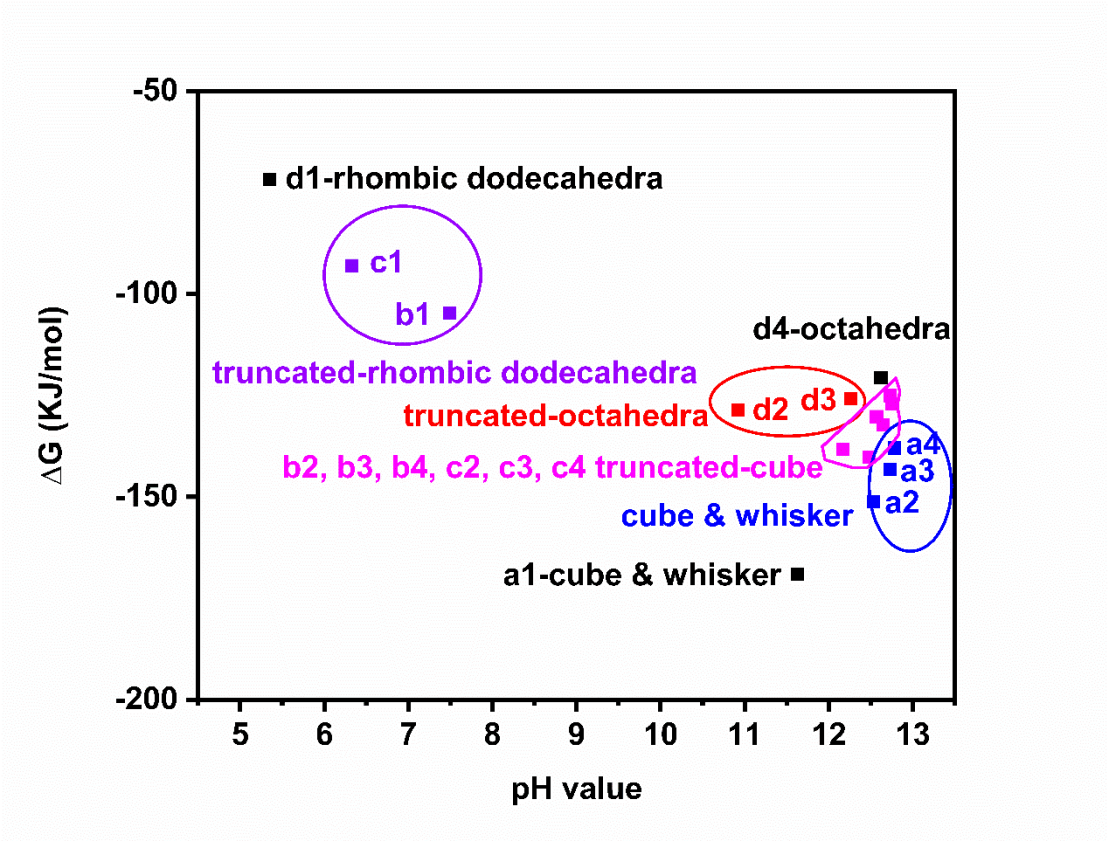

Figure 5.19 A plot of ΔG versus pH value in the formation of different Cu_2O particle shapes in method 1.

5.3.4 Batch and continuous synthesis of Cu_2O nanoparticles via method 2

Theoretically, the equilibrium final shapes of crystals are only determined by the Gibbs-Wulff theory. [266] To prove the relationship between the Gibbs free energy and final crystal morphology, a second method ('method 2') with a simple procedural change compared with method 1 was used. In this method, $NH_2OH{\cdot}HCl$ was added firstly to the Cu(II) solution instead, followed by NaOH. Other reaction conditions, *e.g.* residence time, temperature, concentration were kept the same as method 1. Here in the wide microreactor with I.D. 1/16 inch, the same shape evolution with smooth particle surface of Cu_2O was achieved as the method 1 using the same reaction condition, shown in Figure 5.20.

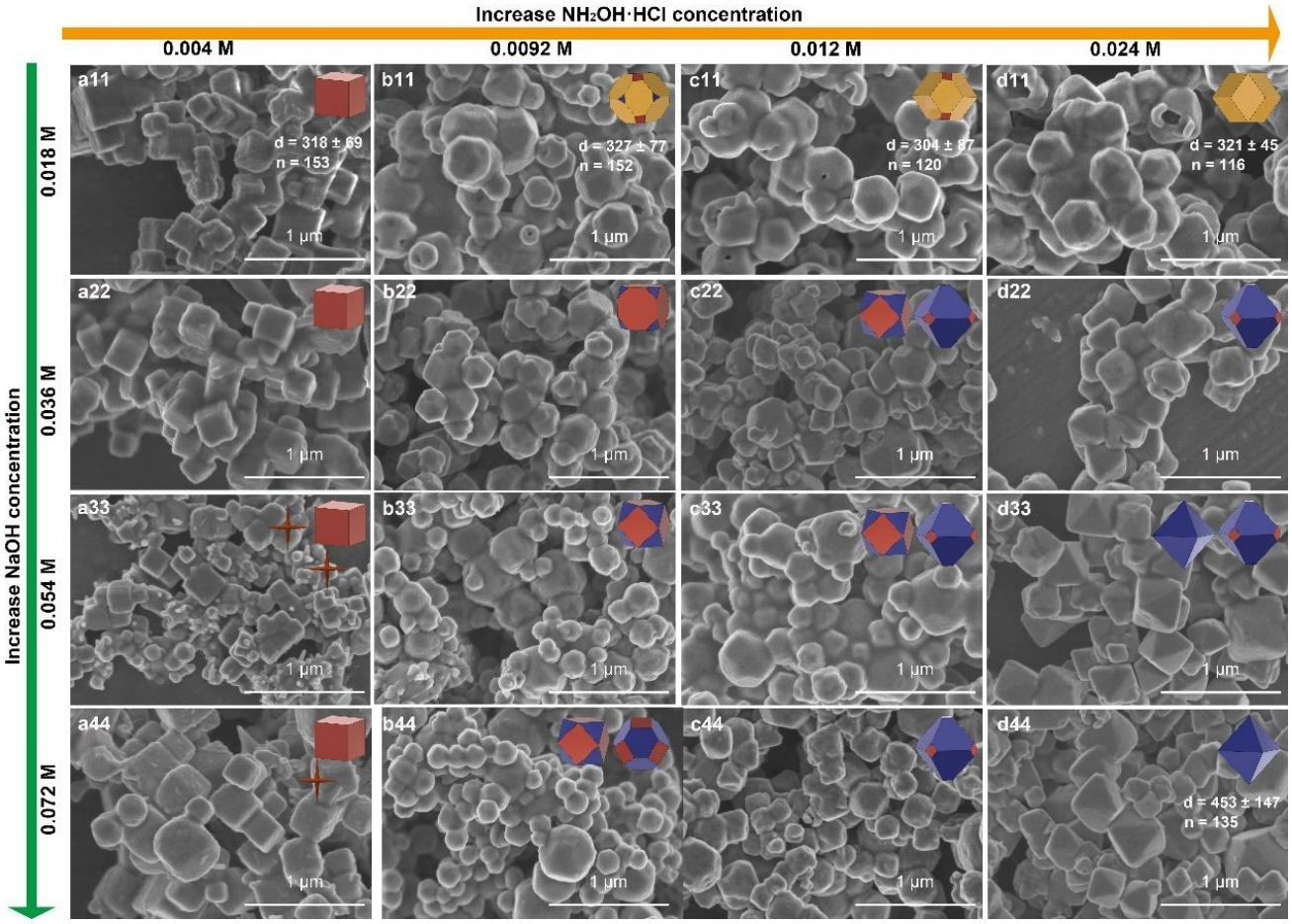

Figure 5.20 Morphology evolution as shown by SEM images from a11 to d44 under various NaOH concentration from 0.018 M to 0.072 M (shown in y axis) and $NH_2OH.HCl$ concentrations from 0.004 M to 0.024 M (shown in x axis) with the microtubing of 1/16 inch I.D with T-mixer, 32°C, residence time in step 1 and step 2 are both 20 s in method 2.

The particle sizes of a11, b11, c11, d11 were measured at 318 nm, 327 nm, 304 nm, and 321 nm with relative standard deviation of 21.74%, 23.47%, 28.67%, and 14.04%, shown in Figure 5.21. As the concentration of NaOH increased, the intermediate structure of truncated cube and octahedra Cu_2O exhibited poor morphology uniform of Cu_2O, shown in samples from Figure 5.20 a22 to d44. While both method 1 and method 2 can produce the same shape evolution of Cu_2O, the particle sizes obtained under the same reaction conditions in these two methods differ as the final crystal shapes and exposed facets of crystal are determined by the interplay between thermodynamics and kinetics. [163] The inconsistencies of particle sizes in these two methods could be attributed to kinetic factors. [267]

The particle sizes of a11, b11, c11, and d44 via method 2 are lower than that of a1, b1, c1 and d1 via method 1, which maybe because the intermediate $Cu(OH)_2$ precipitation formed via method 1 could increase the final Cu_2O particle sizes. For the sample d1, as the pH was below than 7, no Cu(OH)2 precipitation were formed, so the difference of particle size maybe related to the real reaction kinetics.

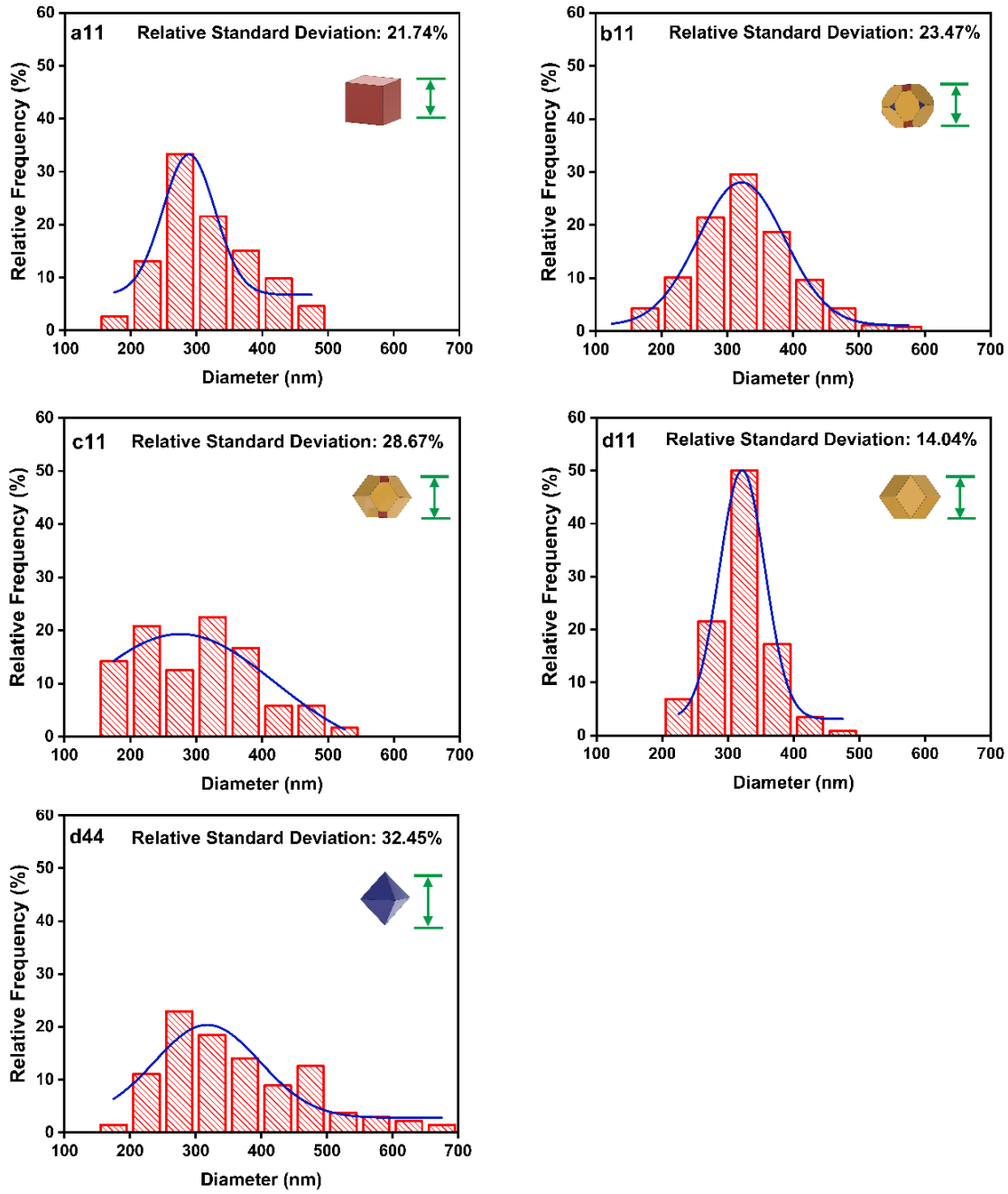

Figure 5.21 Size distribution histograms of Cu_2O nanoparticles morphologies: (a11) nanocube, (b11) all-corner-truncated rhombic dodecahedra, (c11) {100}-truncated rhombic dodecahedra, (d11) rhombic dodecahedra, (d44) octahedra in tube (I.D. 1/16 inch) using method 2 with T-T mixer. Measured to the data in Figure 5.20.

Huang *et. al*.'s research reported using method 2 can produce Cu_2O with rough surfaces using a batch method (in a beaker), similar to the result obtained here via batch synthesis shown in Figure 5.22. Huang indicated that the initial morphology of $Cu(OH)_2$ crystals in method 1 influences the promotion of sharp-faceted Cu_2O nanocrystals formation, with Cu_2O growth initiating at multiple points during the reduction process, and merging of these growth points results in the formation of

smooth, well-defined nanoparticles. [243] Here, Cu_2O nanoparticles with a smooth surface could be achieved in the wide microreactor (I.D. 1/16 inch); it is supposed that the mixing performance inside the reactor has an influence on the final size and shapes of Cu_2O nanoparticles in method 2. The rough surface formed in the batch method 2 can be attributed to the uneven growth rates of crystal facets. The selective adsorption of capping agents on different facets of the crystal can modify their surface energies, thereby enabling control over the growth rate of each facet. [259] [263] We would suppose that the turbulent mixing performance inside the beakers in batch method 2 would induce the uneven selective absorption of capping agents on different facets, which subtly affect the final morphologies of Cu_2O nanocrystals.

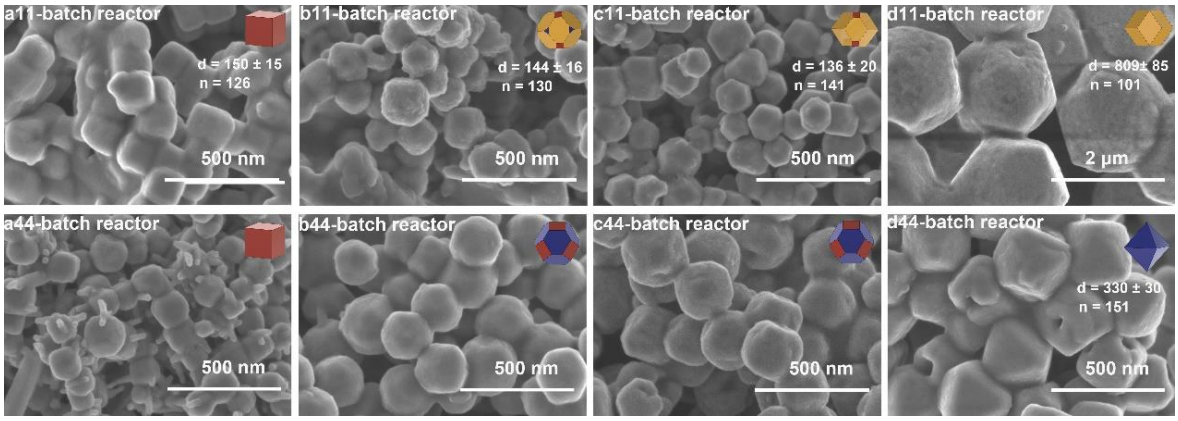

Figure 5.22 Morphology evolution of Cu_2O nanocrystals as shown by SEM images under various NaOH and $NH_2OH.HCl$ concentrations using method 2 in batch reactor with volume of 26.7 mL.

To enhance the mixing performance, a narrow microtube with a diameter of 1/32 inch was utilised instead, shown in Fig. 5.22. As a result, the relative standard deviation for samples a11, b11, c11, d11, and d44 decreased from 21.74% to 9.99%, 23.47% to 12.97%, 28.67% to 12.77%, 14.04% to 9.72%, and 29.97% to 22.43%, respectively, compared to using a tube with a 1/16 inch diameter, shown in Table 5.4, Figure 5.24.

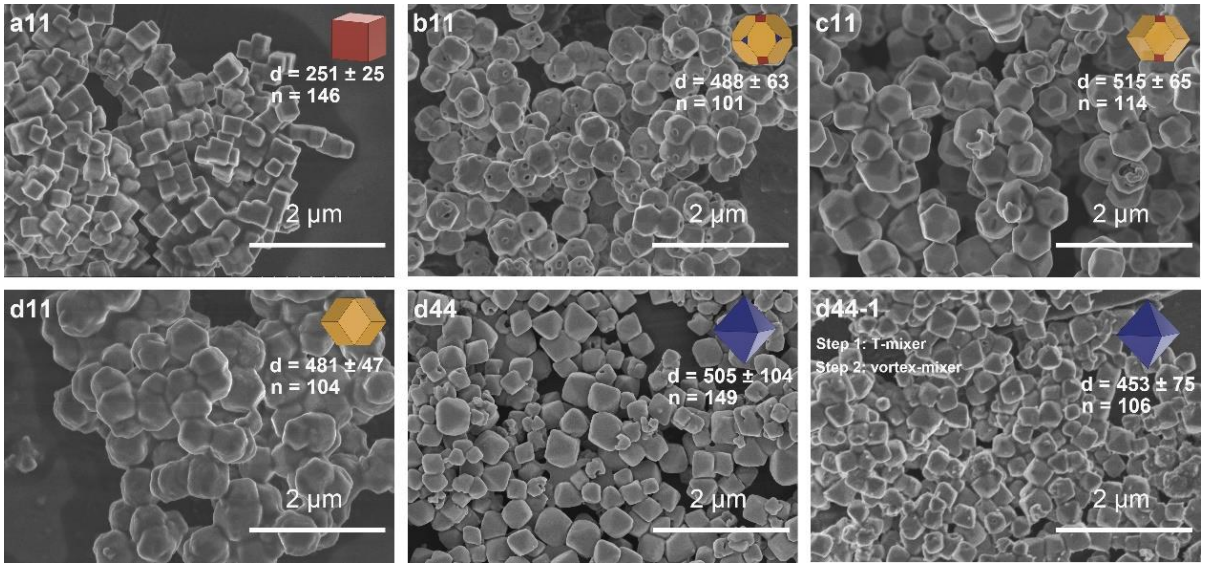

Figure 5.23 Morphology evolution under various NaOH and $NH_2OH{\cdot}HCl$ concentrations using method 2 with the microtubing of 1/32 inch I.D with T-mixer in both step 1 and step 2 (a11-d44), and T-mixer in step 1 and vortex-mixer in step 2 (d44-1), 32 ^oC, residence time in step 1 and step 2 are both 20 s.

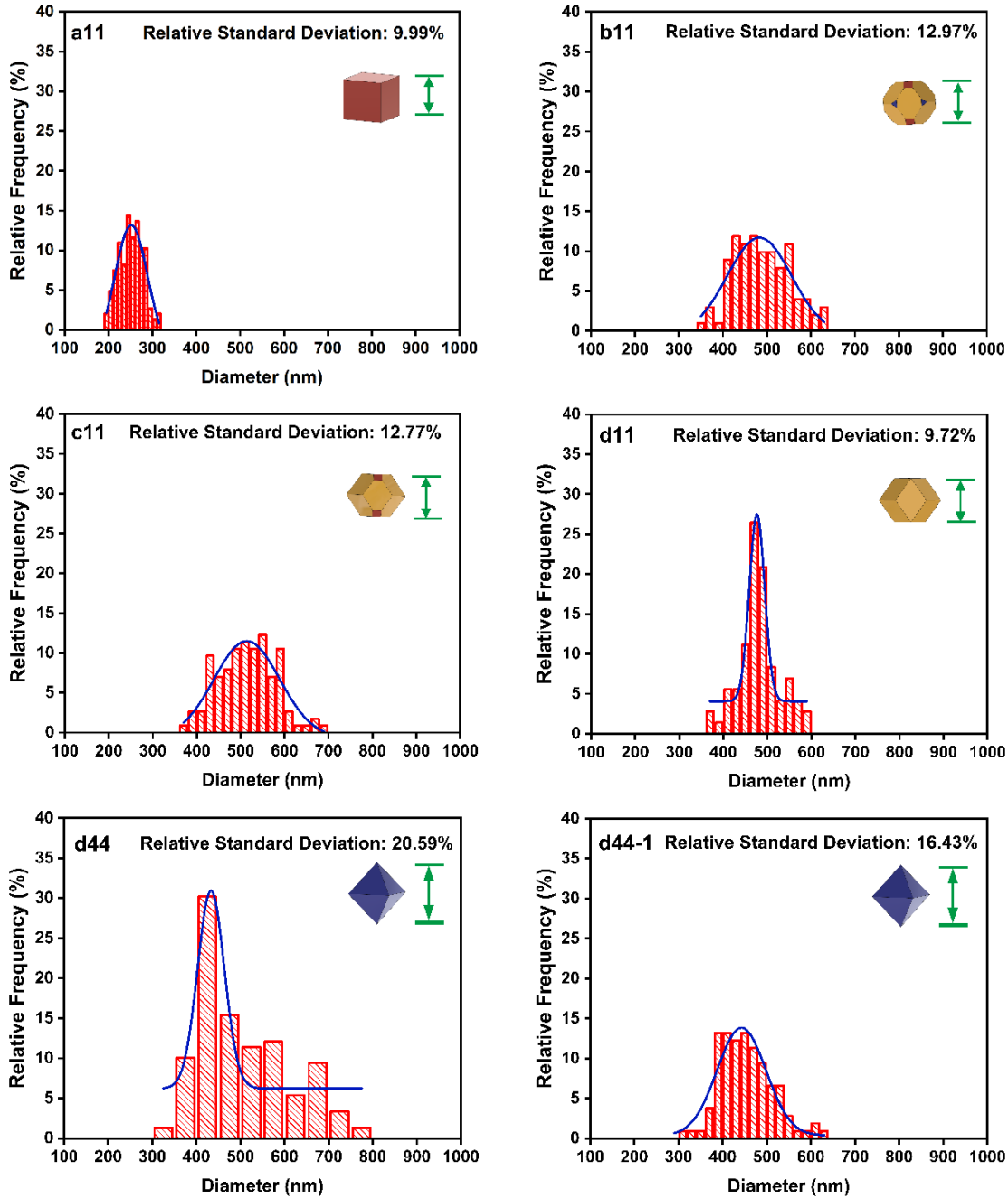

Figure 5.24 Size distribution histograms of Cu_2O nanoparticles in tube (I.D. 1/32 inch) using method 1 with T-T mixer (a11) nanocube, (b11) all-corner-truncated rhombic dodecahedra, (c11) {100}-truncated rhombic dodecahedra, (d11) rhombic dodecahedra, (d44) octahedra and (d44-1) octahedra with T-vortex mixer.

However, despite using the 1/32 inch microtube, the deviation for sample d44 remained relatively high at 22.43%. This is likely due to the increased concentration of NaOH, leading to more reduction of Cu^{2+} to Cu_2O crystal units. Achieving a uniform particle size distribution would require improved mixing performance to ensure uniform concentration. To improve the mixing performance further, a vortex mixer was employed in the second step. Consequently, a more uniform distribution of

octahedral Cu_2O nanoparticles was achieved, reducing the relative standard deviation from 22.43% to 13.30%.

The particle sizes of a11-cube-Cu_2O, b11-corner-truncated RD-Cu_2O, c11-{100}-truncated RD-Cu_2O, d11-RD-Cu_2O, and d44-Oct-Cu_2O in batch and microreactor (1/16 inch I.D., 1/32 inch I.D. respectively) are shown in Figure 5.25 and Table 5.3. For the method 2, when $NH_2OH{\cdot}HCl$ was introduced to the Cu(II)-SDS complex, no noticeable colour change occurred, indicating that the reduction process was still inhibited. Only after the subsequent treatment with NaOH, an immediate change in solution colour was observed, indicating the reduction of Cu^{2+} to Cu_2O monomers occurred abruptly upon the addition of NaOH. Then these seed particles quickly aggregate into larger particles.

In the case of b1- corner-truncated RD, c1-{100}-truncated RD, and d4-Oct, the particle sizes increased from the batch reactor, to the wide microreactor (1/16 inch I.D)., and further to the narrow microreactor (1/32 inch I.D.). The reason is that turbulent mixing in the batch reactor can help to reduce the particle size than laminar mixing in the microreactor. The enhanced molecular diffusion rate in narrow microreactor can lead to the uniform increased particle size. As for the sample d1-RD, the particle size increase from the wide microreactor, to the narrow microreactor and further to the batch reactor. This maybe because within the 20 s residence time, no Cu_2O was formed. So the enhanced mixing performance could increase crystal nucleation agglomeration and further increase the final particle size.

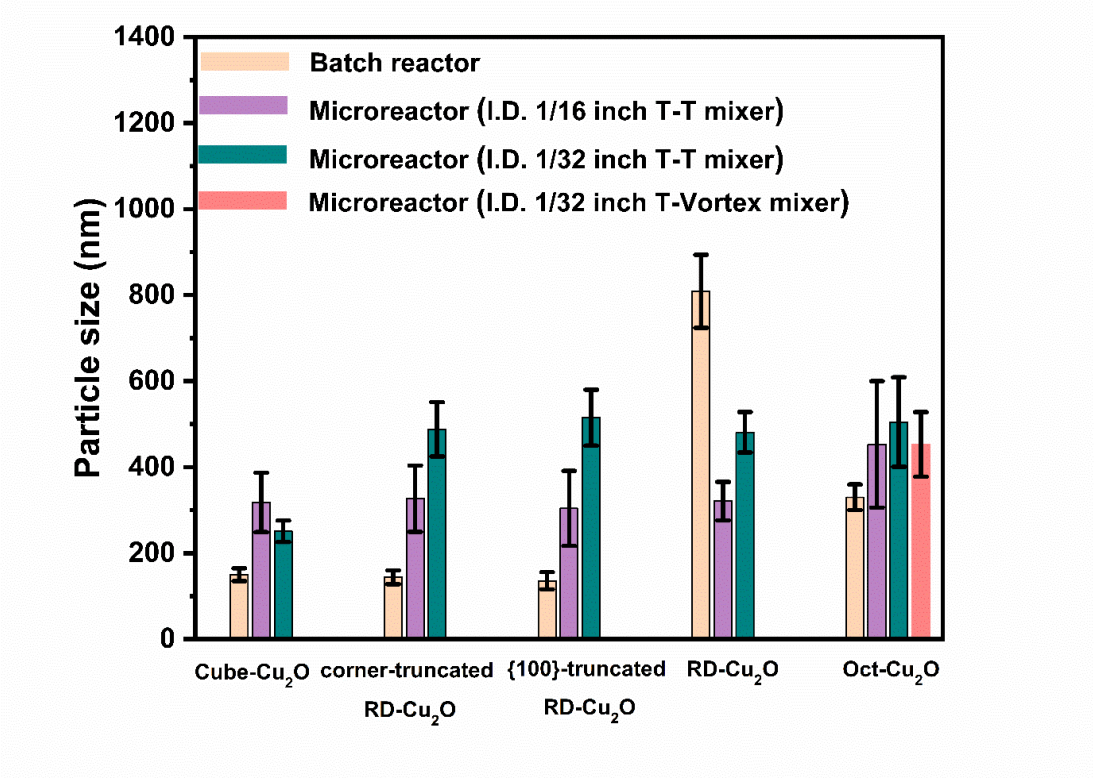

Figure 5.25 Average particle size and relative standard deviation of the Cu_2O nanocrystals from batch reactor and microreactor with 1/16 inch and 1/32 inch respectively via method 2.

Table 5.3Average particle size and relative standard deviation of the Cu_2O nanocrystals synthesized in batch and microreactor with 1/16 inch and 1/32 inch respectively using in method 2, shapes shown in Fig. 5.19, Fig. 5.21 and Fig. 5.22.

Sample	Shape	Average Particle Size	Relative Standard Deviation	Mixer in Step1/Step 2
Fig. 5.19 a11-batch		150 ± 15	10.00%	
Fig. 5.21 a11-1/16 inch	Cube	318 ± 69	21.74%	T/T-mixer
Fig. 5.22 a11-1/32 inch		251 ± 25	9.99%	T/T-mixer
Fig. 5.19 a11-batch		144 ± 16	10.92%	
Fig. 5.21 b11-1/16 inch	Corner-truncated rhombic dodecahedra	327 ± 77	23.47%	T/T-mixer
Fig. 5.22 b11-1/32 inch		488 ± 63	12.97%	T/T-mixer
Fig. 5.19 a11-batch		136 ± 20	14.44%	
Fig. 5.21 c11-1/16 inch	{100}-truncated rhombic dodecahedra	304 ± 87	28.67%	T/T-mixer
Fig. 5.22 c11-1/32 inch		515 ± 65	12.77%	T/T-mixer
Fig. 5.19 a11-batch		809 ± 85	10.5%	
Fig. 5.21 d11-1/16 inch	Rhombic dodecahedra	321 ± 45	14.04%	T/T-mixer
Fig. 5.22 d11-1/32 inch		481 ± 47	9.72%	T/T-mixer
Fig. 5.19 d44- batch		330 ± 30	9.04%	
Fig. 5.21 d44-1/16 inch	Octahedra	453± 147	32.45%	T/T-mixer
Fig. 5.22 d44-1/32 inch		505 ± 104	20.59%	T/T-mixer
Fig. 5.22 d44-1-1/32 inch		453 ± 75	16.43%	T/Vortex-mixer

5.4 Conclusion

In this work Cu_2O nanocrystals has been successfully synthesised, exhibiting a shape evolution from cube, octahedra, and rhombic dodecahedra, achieved by changing the concentration of $NH_2OH{\cdot}HCl$ and NaOH. Cu_2O synthesis was transferred from batch hydrothermal synthesis to a continuous synthesis using a microreactor. The crystallisation of the three-low crystal facets {100} (fastest rate), {111}, {110} (slowest rate) were determined by the Gibbs free energy driving force, measuring -169.11 KJ/mol, -120.62 KJ/mol, and -71.72 KJ/mol respectively. To prove the relationship between the Gibbs free energy and final crystal morphology, method 2 with a simple procedural change compared with method 1 was used. In this method, the final particle shapes of Cu_2O nanoparticles are the same as in method 1, but with different particle sizes. The final morphology of nanoparticle is influenced not only by thermodynamic but also by kinetics, which is closely related to the mixing performance inside the reactor. To investigate the nucleation and growth process, TEM images of Cube-, RD-, and Oct-Cu_2O via method 1 were analysed, revealing instantaneous particle morphology within 2 hours. Nucleation occurred within 20 s residence time for Cube- and Oct-Cu_2O, with turbulent flow in the beaker favouring particle aggregation and resulting in larger final particle sizes compared to the laminar flow in the microreactor. Notably, the particle size of Cube-Cu_2O in the narrow tube microreactor (1/32 inch I.D.) is smaller than that in batch reactor. Further optimisation of mixing in the microreactor may be necessary for Oct-Cu_2O, as improved mixing is required for $Cu(OH)_2$ precipitation to mix effectively with $NH_2OH{\cdot}HCl$. In contrast, for the RD-Cu_2O, no nucleation occurred during the 20 s residence time, suggesting that the mixing performance between batch and microreactor had minimal influence on the final particle size.

Chapter 6. Conclusions and recommendations for further work

6.1 Conclusions

In order to develop a robust and controllable platform for the continuous synthesis of nanomaterials, several challenges had to be addressed and overcome. One challenge involved achieving industry-required yields with low volume throughput in a single-channel of microfluidic reactor. Additionally, the scope of the microfluidic synthesis method was extended to other metal oxides (i.e. semiconductors), to explore the possibility of obtaining nanoparticles with controlled morphology and uniform particle size.

Corning serial AFR reactors, designed for seamless scale-up from traditional batch to continuous flow processing, enable the transition from lab to industrial-scale production. Despite numerous studies on homogeneous and heterogeneous organic molecules, limited research has focused on applications for metal NP production. Moreover, the influence of mixing performance at various operating conditions on nanoparticle synthesis has never been studied. Hence in **Chapter 3**, we evaluated the performance of a Corning AFR (Lab Reactor Module) for metal nanoparticles production, taking Ag NPs as a case study. The instantaneous chemical reduction reaction of Ag precursor, involving burst nucleation and growth process, impacts final nanoparticle size and distribution, heavily influenced by supersaturation. Supersaturation is created through molecular-scale mixing (micromixing) which is preceded by the reduction of segregation scale of fluid flow (meso- and macro-mixing). Therefore, understanding fluid flow patterns and mixing behaviour inside the reactor is crucial for achieving robust and controllable nanoparticle synthesis. Chapter 3 investigated the flow and mixing characteristics inside the Lab Module of Corning AFR at varying total flow rate (1-9 $mL \cdot min^{-1}$) and flow rate ratio (0.25-8). Dye visualisation using methylene blue-water system examined flow patterns and mixing at meso- and macroscales, while micromixing performance was quantified by the Villermaux-Dushman method. The discussion of flow and multi-scale mixing AFR informed the evaluation of its performance for continuous Ag NP synthesis. In summary, this study showed how the flow and multiscale mixing performance affect the average particle size and PSD, paving the way for large-scale production of size-tunable Ag NPs in the further work.

For semiconductor NPs, their photo-properties are influenced by their size, shape and also crystal-facet morphologies. Conventional synthesis methods typically involve high temperatures, pressures, and sometimes complicated apparatus. Considering the significant demand for commercial-scale semiconductor materials, simplified processes are necessary. Flow chemistry offers a solution by allowing control of the synthesis process through adjustment of reaction parameters in solution, while also facilitating large-scale production. In **Chapter 4** and **Chapter 5**, we utilized flow chemistry for the first time to synthesise SnO_2 and Cu_2O NPs. For the SnO_2 NPs, the effects of pH value, precursor

concentration, temperature, and solvent polarity on the synthesis process of SnO_2 nanocrystals were initially studied in a batch reactor. To scale up the synthesis, this was transitioned from a batch reactor to a microfluidic system operating at 90 ^oC, with residence time of 5 mins. To speed up the SnO_2 agglomeration, ethanol was added into the $SnCl_4$ and NaOH mixture solution by decreasing the polarity of the solution, leading to the increased supersaturation and rapid formation of amorphous SnO_2 crystal without morphology control.

The band gap of SnO_2 nanocrystals synthesised in the microreactor (**Chapter 4**) is 3.24 eV, this is lower than the bulk, and is attributed to the presence of oxygen vacancies. However, its photocatalytic activity under visible light and simulated solar light remains negligible. Combing disparate plasmonic metal NPs with semiconductor NPs is an effective method to improve the photocatalytic property by extending the semiconductor's excited wavelength. The photocatalytic property of metal/semiconductor hybrid nanostructures is influenced by factors such as particle size, distribution and morphology of both metal and semiconductor materials, as well as their organized hybrid structures. Thus, designing novel photocatalysts with high property and find a way to scale up to industrial standards is imperative. In conventional synthetic strategies, semiconductor and metal NPs are synthesised separately, and methods like sol-immobilisation, impregnation and co-precipitation are commonly used to combine these binary composites. However, these semi-continuous synthesis methods for the plasmonic metal@semiconductor hybrid nanostructure pose challenges in scaling up while maintaining precise control over nanostructures. To address this issue and enable high-volume production, a straightforward continuous method of Au@SnO_2 in micro-capillary reactor was firstly studied in **Chapter 4**. To identify the most effective structure with superior photocatalytic properties, three different methods with varying procedures were explored to incorporate Au NPs with SnO_2: (1) Au NPs coated on the SnO_2 matrixes (method 1), (2) Au NPs surrounded by SnO_2 matrixes (method 2), and (3) Au NPs embedded with SnO_2 matrixes (method 3). Synthesising SnO_2 nanocrystals first and then sol-immobilising Au NPs on the surface of SnO_2 matrixes did not yield effective integration using method 1. Similarly, embedding pre-synthesised Au NPs inside SnO_2 matrixes resulted in noticeable gaps between these two materials using method 2. Due to the unintimate contact, their photocatalytic property did not significantly improve compared to pristine SnO_2. Simultaneous synthesis SnO_2 and Au NPs using the one-pot synthesis method did improve the photocatalytic property due to the intimate contact. However, lower weight ratios of Au/SnO_2 result in negligible degradation rate of dye solution. Achieving an intimate combination structure of SnO_2@metal NPs with the proper plasmonic metal weight content will be the focus of future research.

For Cu_2O (a p-type semiconductor with a narrow band gap of 2.17 eV), its photocatalytic property is determined by crystal facets, owing to its body-centered cubic lattice structure. Synthesis of Cu_2O

NPs in an increased-volume batch reactor resulted in more nonuniform morphology compared with a smaller batch reactor, which revealed that crystal morphology is influenced by mass transfer conditions inside the reactor. Challenges persist in achieving reproducible, high yields, easy scale-up, and controllable production processes using traditional batch reactor. In **Chapter 5**, we optimized a continuous synthesis process for Cu_2O NPs with controlled polyhedral structures using a lab-made capillary reactor. Shape evolution from cube to Oct, and RD was achieved by adjusting the concentration of $NH_2OH{\cdot}HCl$ and NaOH. It was found that the final NP morphology is influenced not only by thermodynamics but also by kinetics, closely related to the mixing performance inside the reactor. To investigate the nucleation and growth process, instantaneous TEM images of Cube-, RD-, and Oct-Cu_2O morphology were analysed within 2 hours. Nucleation occurred within 20 s residence time for Cube- and Oct-Cu_2O, with turbulent flow in the beaker favouring particle aggregation and resulting in larger final particle sizes compared to the laminar flow in the microreactor. Notably, the particle size of Cube-Cu_2O in the narrow tube microreactor (1/32 inch I.D.) is smaller than that in the batch reactor. Further optimisation of mixing in the microreactor may be necessary for Oct-Cu_2O, as improved mixing is required for $Cu(OH)_2$ precipitation to mix effectively with $NH_2OH{\cdot}HCl$. In contrast, for the RD-Cu_2O, no nucleation occurred during the 20 s residence time, suggesting that the mixing performance between batch and microreactor had minimal influence on the final particle size. This simple continuous method for the controllable evolution of polyhedral Cu_2O opens up new possibilities for large-scale production of other semiconductor nanomaterials with different crystal-facets in a reproducible manner.

6.2 Recommendations for future work

It is recommended that the future research will primarily focus on the synthesis of metal and semiconductor NPs, with emphasis on two aspects: optimizing material design and transitioning from lab-scale batch synthesis to microreactors for high-yield production without compromising product quality. (A) For metal NPs, achieving high yields using microfluidic reactors will be a focal point. Regarding the continuous synthesis of semiconductors in microreactors, significant opportunities for exploration lie ahead: (B) the development for the design of targeted photocatalyst materials; and (C) new synthesis methods of the photocatalyst materials in a simple way and high yields.

(i) Based on current research findings, an optimised continuous synthetic protocol of Ag NPs in Corning AFR was reported in one-single solution process. Due to the internal heat-shaped unit cell inside Corning AFR, a seamless transition from lab-optimized processes to various scales of production could be achieved, while preserving consistent mixing and mass/heat transfer performance. Transitioning the synthetic protocol of Ag NPs, as well as other metal NPs from lab to industrial scale represents a significant opportunity for the future study.

(ii) Regarding pristine semiconductors, their photocatalytic properties are related to their particle size, shape as well as crystal-facet morphology. The future work will summarise into three aspects:

(1) Exploring the transfer of more semiconductor materials from batch to microfluidic reactors with controllable particle size, shape or crystal morphology, as well as continuous synthesis with high yields will be a key focus.

(2) For Cu_2O NPs with various crystal morphologies (cube, octahedra and dodecahedra), optimization of mixing in the microreactor is crucial, particularly for octahedral morphology. Improved mixing is required for $Cu(OH)_2$ precipitation to mix effectively with $NH_2OH{\cdot}HCl$ due to the fast nucleation process. Experimentation with a vortex-mixer instead of a T-mixer has shown promising results in enhancing mixing performance at the point of intersection of $Cu(OH)_2$ precipitation solution and $NH_2OH{\cdot}HCl$, resulting in increased uniformity of Oct-Cu_2O. Further investigation is required to compare the mixing performance between T-mixer and vortex-mixer as well as the influence on the particle size of the Oct-Cu_2O.

(3) Focusing on pristine SnO_2 NPs synthesising in microreactor, their photocatalytic properties under UV light should be test. Focusing on Cu_2O NPs themselves, the future emphasis lies in fine-tuning and designing crystallographic polyhedral architecture with high photocatalytic property. High-index facets usually have the high activities, therefore, designing and illustrating the formation mechanism of Cu_2O architectures primarily exposed to high-index facets could be significant in expanding their potential applications. [268] Additionally, controlled synthesis of nano-structural Cu_2O with varied surfaces is still in its infancy, which highlight the urgent need for simple synthetic strategies enabling the controlled synthesis of Cu_2O nanostructures primarily exhibiting high-index facets. [163]

(iii) As for the plasmonic metal semiconductor, there are several key areas worthy of further study:

(1) Progress in designing ideal materials is accompanied by increased understanding of the photocatalytic process in this hybrid structure. Although five mechanisms of the plasmonic effect have been proposed to explain the enhanced photocatalysis (as mentioned in Chapter 2), research on the mechanisms of plasmonic-enhanced photocatalyst is still in the infancy and requires further study. Experimental research combined with theoretical predictions will be crucial for understanding the structural-property relationship.

(2) Further challenges include expanding the selection of materials by the development of new combinations, architectures, and higher complexity with ideal photocatalytic property. [269] The

magnitude of SPR-enhanced photocatalytic property is related to the optical properties of both metal and semiconductor building blocks, as well as their geometric composite arrangements. Hence, well-designed plasmonic metal-semiconductor heterojunction are key to achieving high energy-conversion rates. [49] For example, in the case of the Cu_2O NPs, a narrow band-gap semiconductor, various designs such as metal core (Au, Ag, Pt, Pd, Cu, *etc.*)/Cu_2O shell (cube, octahedra, dodecahedra, sphere, *etc.*) [268] [270] [271], Janus, non-centrally located core-shell, and anchored structures have been explored. [69] [272] [273][55], [274] Future research will focus on designing new metal@Cu_2O composite hybrid structure. For the Au@SnO_2 NPs described in Chapter 4, the lower photocatalytic activity of the one-pot Au/SnO_2 composite may be due to the small amount of Au NPs inside the composites, as well as the combination structure of Au with SnO_2. Randomly dispersed metal nanoparticles into a semiconductor matrix result in a large variation in the SPR position and local electromagnetic field distribution, making it difficult to control the photocatalytic property. To improve the photocatalytic property, two approaches can be considered: increasing the content of Au NPs and improving the Au NPs and SnO_2 combination mode.

(3) Finally, considering the huge demand of commercial scale, the focus will be on developing cost-effective and straightforward synthetic process of semiconductor-metal hybrid composites with advanced photocatalytic properties.

References

[1] V. Mody *et al.*, “Introduction to metallic nanoparticles,” *J Pharm Bioallied Sci*, vol. 2, no. 4, p. 282, 2010, doi: 10.4103/0975-7406.72127.

[2] J. N. Tiwari *et al.*, “Zero-dimensional, one-dimensional, two-dimensional and three-dimensional nanostructured materials for advanced electrochemical energy devices,” *Prog Mater Sci*, vol. 57, no. 4, pp. 724–803, 2012, doi: 10.1016/j.pmatsci.2011.08.003.

[3] V. Sebastian, “Toward continuous production of high-quality nanomaterials using microfluidics: nanoengineering the shape, structure and chemical composition,” *Nanoscale*, vol. 14, no. 12, pp. 4411–4447, 2022, doi: 10.1039/d1nr06342a.

[4] P. G. Jamkhande *et al.*, “Metal nanoparticles synthesis: An overview on methods of preparation, advantages and disadvantages, and applications,” *J Drug Deliv Sci Technol*, vol. 53, no. June, p. 101174, 2019, doi: 10.1016/j.jddst.2019.101174.

[5] Y. Wang *et al.*, “Bottom-up and top-down approaches to the synthesis of monodispersed spherical colloids of low melting-point metals,” *Nano Lett*, vol. 4, no. 10, pp. 2047–2050, 2004, doi: 10.1021/nl048689j.

[6] L. Gutierrez *et al.*, “Comparative study of the synthesis of silica nanoparticles in micromixer-microreactor and batch reactor systems,” *Chemical Engineering Journal*, vol. 171, no. 2, pp. 674–683, 2011, doi: 10.1016/j.cej.2011.05.019.

[7] C. H. Chang *et al.*, “Synthesis and post-processing of nanomaterials using microreaction technology,” *Journal of Nanoparticle Research*, vol. 10, no. 6, pp. 965–980, 2008, doi: 10.1007/s11051-007-9355-y.

[8] V. S. Cabeza, “High and Efficient Production of Nanomaterials by Microfluidic Reactor Approaches,” X.-Y. Yu, Ed., Rijeka: IntechOpen, 2016, p. Ch. 17. doi: 10.5772/64347.

[9] T. W. Phillips *et al.*, “Nanocrystal synthesis in microfluidic reactors: Where next?,” *Lab Chip*, vol. 14, no. 17, pp. 3172–3180, 2014, doi: 10.1039/c4lc00429a.

[10] M. Qiu *et al.*, “Numbering-up of capillary microreactors for homogeneous processes and its application in free radical polymerization,” *React Chem Eng*, vol. 4, no. 2, pp. 351–361, 2019, doi: 10.1039/c8re00224j.

[11] L. Zhang *et al.*, “Continuous and scalable production of well-controlled noble-metal nanocrystals in milliliter-sized droplet reactors,” *Nano Lett*, vol. 14, no. 11, pp. 6626–6631, 2014, doi: 10.1021/nl503284x.

[12] J. Sui *et al.*, “Continuous Synthesis of Nanocrystals via Flow Chemistry Technology,” *Small*, vol. 16, no. 15, pp. 1–23, 2020, doi: 10.1002/smll.201902828.

[13] Y. Zhang *et al.*, “Scale-up investigation of the continuous phase-transfer-catalyzed hypochlorite oxidation of alcohols and aldehydes,” *Org Process Res Dev*, vol. 18, no. 11, pp. 1476–1481, 2014, doi: 10.1021/op500158h.

[14] B. Buisson *et al.*, “Slurry hydrogenation in a continuous flow reactor for pharmaceutical application,” *Chim Oggi*, vol. 27, no. 6, pp. 12–16, 2009.

[15] J. C. M. Monbaliu *et al.*, "Effective production of the biodiesel additive STBE by a continuous flow process," *Bioresour Technol*, vol. 102, no. 19, pp. 9304–9307, 2011, doi: 10.1016/j.biortech.2011.07.007.

[16] G. Liu *et al.*, "Crystal facet engineering of semiconductor photocatalysts: Motivations, advances and unique properties," *Chemical Communications*, vol. 47, no. 24, pp. 6763–6783, 2011, doi: 10.1039/c1cc10665a.

[17] J. Li *et al.*, "Semiconductor-based photocatalysts and photoelectrochemical cells for solar fuel generation: A review," *Catal Sci Technol*, vol. 5, no. 3, pp. 1360–1384, 2015, doi: 10.1039/c4cy00974f.

[18] F. Zhang *et al.*, "Recent advances and applications of semiconductor photocatalytic technology," *Applied Sciences (Switzerland)*, vol. 9, no. 12, 2019, doi: 10.3390/app9122489.

[19] L. Zhang *et al.*, "Characterization of semiconductor photocatalysts," *Chem Soc Rev*, vol. 48, no. 20, pp. 5184–5206, 2019, doi: 10.1039/c9cs00172g.

[20] V. V. Pokropivny *et al.*, "Classification of nanostructures by dimensionality and concept of surface forms engineering in nanomaterial science," *Materials Science and Engineering C*, vol. 27, no. 5-8 SPEC. ISS., pp. 990–993, 2007, doi: 10.1016/j.msec.2006.09.023.

[21] J. Jeevanandam *et al.*, "Review on nanoparticles and nanostructured materials: History, sources, toxicity and regulations," *Beilstein Journal of Nanotechnology*, vol. 9, no. 1, pp. 1050–1074, 2018, doi: 10.3762/bjnano.9.98.

[22] C. S. Seney *et al.*, "Correlation of Size and Surface-Enhanced Raman Scattering Activity of Optical and Spectroscopic Properties for Silver Nanoparticles," *The Journal of Physical Chemistry C*, vol. 113, no. 1, pp. 74–80, Jan. 2009, doi: 10.1021/jp805698e.

[23] N. Venkatesh, "Metallic Nanoparticle: A Review," *Biomed J Sci Tech Res*, vol. 4, no. 2, pp. 3765–3775, 2018, doi: 10.26717/bjstr.2018.04.0001011.

[24] J. Polte *et al.*, "Nucleation and growth of gold nanoparticles studied via in situ small angle X-ray scattering at millisecond time resolution," *ACS Nano*, vol. 4, no. 2, pp. 1076–1082, 2010, doi: 10.1021/nn901499c.

[25] J. Polte *et al.*, "Formation mechanism of colloidal silver nanoparticles: Analogies and differences to the growth of gold nanoparticles," *ACS Nano*, vol. 6, no. 7, pp. 5791–5802, 2012, doi: 10.1021/nn301724z.

[26] S. Nishimura *et al.*, "In situ time-resolved xafs study on the formation mechanism of Cu nanoparticles using poly(N-vinyl-2-pyrrolidone) as a capping agent," *Langmuir*, vol. 26, no. 6, pp. 4473–4479, 2010, doi: 10.1021/la904248z.

[27] I. Hammami *et al.*, "Gold nanoparticles: Synthesis properties and applications," *J King Saud Univ Sci*, vol. 33, no. 7, 2021, doi: 10.1016/j.jksus.2021.101560.

[28] R. Xu *et al.*, "Shape-dependent catalytic activity of silver nanoparticles for the oxidation of styrene," *Chem Asian J*, vol. 1, no. 6, pp. 888–893, 2006, doi: 10.1002/asia.200600260.

[29] A. Müller *et al.*, "Shape and Surface Morphology of Copper Nanoparticles under CO_2 Hydrogenation Conditions from First Principles," *Journal of Physical Chemistry C*, vol. 125, no. 1, pp. 396–409, 2021, doi: 10.1021/acs.jpcc.0c08261.

[30] H. Tong *et al.*, "Nano-photocatalytic materials: Possibilities and challenges," *Advanced Materials*, vol. 24, no. 2, pp. 229–251, 2012, doi: 10.1002/adma.201102752.

[31] A. FUJISHIMA *et al.*, "Electrochemical Photolysis of Water at a Semiconductor Electrode," *Nature*, vol. 238, no. 5358, pp. 37–38, 1972, doi: 10.1038/238038a0.

[32] O. Ola *et al.*, "Review of material design and reactor engineering on TiO_2 photocatalysis for CO_2 reduction," *Journal of Photochemistry and Photobiology C: Photochemistry Reviews*, vol. 24, pp. 16–42, 2015, doi: 10.1016/j.jphotochemrev.2015.06.001.

[33] A. Houas *et al.*, "Photocatalytic degradation pathway of methylene blue in water," *Appl Catal B*, vol. 31, no. 2, pp. 145–157, 2001, doi: 10.1016/S0926-3373(00)00276-9.

[34] L. Chen *et al.*, "High piezo/photocatalytic efficiency of Ag/Bi_5O_7I nanocomposite using mechanical and solar energy for N2 fixation and methyl orange degradation," *Green Energy and Environment*, vol. 8, no. 1, pp. 283–295, 2023, doi: 10.1016/j.gee.2021.04.009.

[35] A. Kudo *et al.*, "Heterogeneous photocatalyst materials for water splitting," *Chem Soc Rev*, vol. 38, no. 1, pp. 253–278, 2009, doi: 10.1039/b800489g.

[36] D. Friedmann *et al.*, "Heterogeneous photocatalytic organic synthesis: State-of-the-art and future perspectives," *Green Chemistry*, vol. 18, no. 20, pp. 5391–5411, 2016, doi: 10.1039/c6gc01582d.

[37] M. Zürch *et al.*, "Direct and simultaneous observation of ultrafast electron and hole dynamics in germanium," *Nat Commun*, vol. 8, 2017, doi: 10.1038/ncomms15734.

[38] X. Zhang *et al.*, "Plasmonic photocatalysis," *Reports on Progress in Physics*, vol. 76, no. 4, 2013, doi: 10.1088/0034-4885/76/4/046401.

[39] Z. Xiong *et al.*, "A review on modification of facet-engineered TiO_2 for photocatalytic CO_2 reduction," *Journal of Photochemistry and Photobiology C: Photochemistry Reviews*, vol. 36, pp. 24–47, 2018, doi: 10.1016/j.jphotochemrev.2018.07.002.

[40] Z. Zhang *et al.*, "Band bending in semiconductors: Chemical and physical consequences at surfaces and interfaces," *Chem Rev*, vol. 112, no. 10, pp. 5520–5551, 2012, doi: 10.1021/cr3000626.

[41] I. Ahmad *et al.*, "Semiconductor photocatalysts: A critical review highlighting the various strategies to boost the photocatalytic performances for diverse applications," *Adv Colloid Interface Sci*, vol. 311, no. November 2022, p. 102830, 2023, doi: 10.1016/j.cis.2022.102830.

[42] H. Yan *et al.*, "Band structure design of semiconductors for enhanced photocatalytic activity: The case of TiO_2," *Progress in Natural Science: Materials International*, vol. 23, no. 4, pp. 402–407, 2013, doi: 10.1016/j.pnsc.2013.06.002.

[43] S. C. Erwin *et al.*, "Doping semiconductor nanocrystals," *Nature*, vol. 436, no. 7047, pp. 91–94, 2005, doi: 10.1038/nature03832.

[44] Y. Liu *et al.*, "Composition dependence of the photocatalytic activities of $BiOCl_{1-x}Br_x$ solid solutions under visible light," *Chemistry - A European Journal*, vol. 17, no. 34, pp. 9342–9349, 2011, doi: 10.1002/chem.201100952.

[45] P. Zhang *et al.*, “Mechanistic Understanding of the Plasmonic Enhancement for Solar Water Splitting,” *Advanced Materials*, vol. 27, no. 36, pp. 5328–5342, 2015, doi: 10.1002/adma.201500888.

[46] M. Liu *et al.*, “Heterostructure nanocomposite with local surface plasmon resonance effect enhanced photocatalytic activity-a critical review,” *J Phys D Appl Phys*, vol. 55, no. 4, 2022, doi: 10.1088/1361-6463/ac2cac.

[47] Q. Xu *et al.*, “S-Scheme Heterojunction Photocatalyst,” *Chem*, vol. 6, no. 7, pp. 1543–1559, 2020, doi: 10.1016/j.chempr.2020.06.010.

[48] N. Wu, “Plasmonic metal-semiconductor photocatalysts and photoelectrochemical cells : a review,” pp. 2679–2696, 2018, doi: 10.1039/c7nr08487k.

[49] S. Linic *et al.*, “Plasmonic-metal nanostructures for efficient conversion of solar to chemical energy,” *Nat Mater*, vol. 10, no. 12, pp. 911–921, 2011, doi: 10.1038/nmat3151.

[50] W. Wu *et al.*, “Non-centrosymmetric Au-SnO_2 hybrid nanostructures with strong localization of plasmonic for enhanced photocatalysis application,” *Nanoscale*, vol. 5, no. 12, pp. 5628–5636, 2013, doi: 10.1039/c3nr00985h.

[51] Y. Li *et al.*, “Preparation of spherical silver and tin dioxide nanocomposites with the high photocatalytic performance by laser-induced deposition in liquid medium,” *J Alloys Compd*, vol. 900, p. 163522, 2022, doi: 10.1016/j.jallcom.2021.163522.

[52] L. Mascaretti *et al.*, “Hot electron and thermal effects in plasmonic photocatalysis,” *J Appl Phys*, vol. 128, no. 4, 2020, doi: 10.1063/5.0013945.

[53] P. Zhang *et al.*, “Mechanistic Understanding of the Plasmonic Enhancement for Solar Water Splitting,” *Advanced Materials*, vol. 27, no. 36, pp. 5328–5342, 2015, doi: 10.1002/adma.201500888.

[54] K. L. Kelly *et al.*, “The Optical Proerties of Metal Nanoparticles: The Influence of Size, Shape, and Dielectric Environment,” *Journal of physical chemistry B*, vol. 107, no. 3, pp. 668–677, 2003, doi: 10.1080/00094056.2009.10521700.

[55] W. Xu *et al.*, “Continuous Tuning of Au–Cu_2O Janus Nanostructures for Efficient Charge Separation,” *Angewandte Chemie - International Edition*, vol. 59, no. 49, pp. 22246–22251, 2020, doi: 10.1002/anie.202010613.

[56] X. Wu *et al.*, “Au@Cu_2O stellated polytope with core-shelled nanostructure for high-performance adsorption and visible-light-driven photodegradation of cationic and anionic dyes,” *J Colloid Interface Sci*, vol. 469, pp. 138–146, 2016, doi: 10.1016/j.jcis.2016.01.064.

[57] S. K. Cushing *et al.*, “Photocatalytic activity enhanced by plasmonic resonant energy transfer from metal to semiconductor.,” *J Am Chem Soc*, vol. 134, no. 36, pp. 15033–15041, Sep. 2012, doi: 10.1021/ja305603t.

[58] S. K. Cushing *et al.*, “Ag@Cu_2O Core-Shell Nanoparticles as Visible-Light Plasmonic Photocatalysts,” *ACS Catal*, vol. 3, pp. 47-51, 2015. Doi: 10. 1021/cs300672f.

[59] P. K. Jain *et al.*, “Noble metals on the nanoscale: Optical and photothermal properties and some applications in imaging, sensing, biology, and medicine,” *Acc Chem Res*, vol. 41, no. 12, pp. 1578–1586, 2008, doi: 10.1021/ar7002804.

[60] J. H. Hodak *et al.*, "Photophysics of nanometer sized metal particles: Electron-phonon coupling and coherent excitation of breathing vibrational modes," *Journal of Physical Chemistry B*, vol. 104, no. 43, pp. 9954–9965, 2000, doi: 10.1021/jp002256x.

[61] P. Christopher *et al.*, "Enhancing photochemical activity of semiconductor nanoparticles with optically active Ag nanostructures: Photochemistry mediated by Ag surface plasmons," *Journal of Physical Chemistry C*, vol. 114, no. 19, pp. 9173–9177, 2010, doi: 10.1021/jp101633u.

[62] S. T. Kochuveedu *et al.*, "A study on the mechanism for the interaction of light with noble metal-metal oxide semiconductor nanostructures for various photophysical applications," *Chem Soc Rev*, vol. 42, no. 21, pp. 8467–8493, 2013, doi: 10.1039/c3cs60043b.

[63] S. Sun *et al.*, "Interference-induced broadband absorption enhancement for plasmonic-metal@semiconductor microsphere as visible light photocatalyst," *ACS Catal*, vol. 4, no. 12, pp. 4269–4276, 2014, doi: 10.1021/cs501399a.

[64] C. Clavero, "Plasmon-induced hot-electron generation at nanoparticle/metal-oxide interfaces for photovoltaic and photocatalytic devices," *Nat Photonics*, vol. 8, no. 2, pp. 95–103, 2014, doi: 10.1038/nphoton.2013.238.

[65] D. B. Ingram *et al.*, "Predictive model for the design of plasmonic metal/semiconductor composite photocatalysts," *ACS Catal*, vol. 1, no. 10, pp. 1441–1447, 2011, doi: 10.1021/cs200320h.

[66] B. B. Lakshmi *et al.*, "Sol-Gel Template Synthesis of Semiconductor Oxide Micro- and Nanostructures," *Chemistry of Materials*, vol. 9, no. 11, pp. 2544–2550, 1997, doi: 10.1021/cm970268y.

[67] A. Mamakhel *et al.*, "Continuous flow hydrothermal synthesis of rutile SnO_2 nanoparticles: Exploration of pH and temperature effects," *Journal of Supercritical Fluids*, vol. 166, pp. 1–8, 2020, doi: 10.1016/j.supflu.2020.105029.

[68] B. Babu *et al.*, "Novel in-situ synthesis of Au/SnO_2 quantum dots for enhanced visible-light-driven photocatalytic applications," *Ceram Int*, vol. 45, no. 5, pp. 5743–5750, 2019, doi: 10.1016/j.ceramint.2018.12.040.

[69] S. P. Kim *et al.*, "Photocatalytic activity of SnO_2 nanoparticles in methylene blue degradation," *Mater Res Bull*, vol. 74, pp. 85–89, 2016, doi: 10.1016/j.materresbull.2015.10.024.

[70] Y. Zhang *et al.*, "Shape effects of Cu_2O polyhedral microcrystals on photocatalytic activity," *Journal of Physical Chemistry C*, vol. 114, no. 11, pp. 5073–5079, 2010, doi: 10.1021/jp9110037.

[71] J. Hu *et al.*, "Laser-ablation growth and optical properties of wide and long single-crystal SnO_2 ribbons," *Adv Funct Mater*, vol. 13, no. 6, pp. 493–496, 2003, doi: 10.1002/adfm.200304327.

[72] N. Zhou *et al.*, "Mesoporous SnO_2-coated metal nanoparticles with enhanced catalytic efficiency," *ACS Appl Mater Interfaces*, vol. 7, no. 8, pp. 4844–4850, 2015, doi: 10.1021/am508803c.

[73] A. Kar *et al.*, "Recent development of core-shell SnO_2 nanostructures and their potential applications," *J Mater Chem C Mater*, vol. 2, no. 33, pp. 6706–6722, 2014, doi: 10.1039/c4tc01030b.

[74] Y. Q. Guo *et al.*, "Solution route to SnO_2 crystals with controllable morphology," *Appl Surf Sci*, vol. 258, no. 6, pp. 1958–1963, 2012, doi: 10.1016/j.apsusc.2011.06.037.

[75] W. Tu *et al.*, "State-of-the-art advancements of crystal facet-exposed photocatalysts beyond TiO_2: Design and dependent performance for solar energy conversion and environment applications," *Materials Today*, vol. 33, no. March, pp. 75–86, 2020, doi: 10.1016/j.mattod.2019.09.003.

[76] X. Liu *et al.*, "Strong metal-support interactions between gold nanoparticles and ZnO nanorods in CO oxidation," *J Am Chem Soc*, vol. 134, no. 24, pp. 10251–10258, 2012, doi: 10.1021/ja3033235.

[77] C. Zhang *et al.*, "Plasmonic metal/semiconductor hybrid nanomaterials for solar to chemical energy conversion," *Journal of Energy Chemistry*, vol. 63, pp. 40–53, 2021, doi: 10.1016/j.jechem.2021.08.036.

[78] A. Li *et al.*, "Rational design of yolk-shell nanostructures for photocatalysis," *Chem Soc Rev*, vol. 48, no. 7, pp. 1874–1907, 2019, doi: 10.1039/c8cs00711j.

[79] M. Wang *et al.*, "Nonepitaxial growth of uniform and precisely size-tunable core/shell nanoparticles and their enhanced plasmon-driven photocatalysis," *J Mater Chem A Mater*, vol. 4, no. 19, pp. 7190–7199, 2016, doi: 10.1039/c6ta01838f.

[80] L. de Rogatis *et al.*, "Embedded phases: A way to active and stable catalysts," *ChemSusChem*, vol. 3, no. 1, pp. 24–42, 2010, doi: 10.1002/cssc.200900151.

[81] T. Torimoto *et al.*, "Plasmon-enhanced photocatalytic activity of cadmium sulfide nanoparticle immobilized on silica-coated gold particles," *Journal of Physical Chemistry Letters*, vol. 2, no. 16, pp. 2057–2062, 2011, doi: 10.1021/jz2009049.

[82] I. Thomann *et al.*, "Plasmon enhanced solar-to-fuel energy conversion," *Nano Lett*, vol. 11, no. 8, pp. 3440–3446, 2011, doi: 10.1021/nl201908s.

[83] M. Matamoros-Ambrocio *et al.*, "A comparative study of gold impregnation methods for obtaining metal/semiconductor nanophotocatalysts: Direct turkevich, inverse turkevich, and progressive heating methods," *Catalysts*, vol. 8, no. 4, 2018, doi: 10.3390/catal8040161.

[84] A. Villa *et al.*, "Sol immobilization technique: A delicate balance between activity, selectivity and stability of gold catalysts," *Catal Sci Technol*, vol. 3, no. 11, pp. 3036–3041, 2013, doi: 10.1039/c3cy00260h.

[85] S. M. Rogers *et al.*, "Supported metal nanoparticles with tailored catalytic properties through sol-immobilisation: Applications for the hydrogenation of nitrophenols," *Faraday Discuss*, vol. 208, pp. 443–454, 2018, doi: 10.1039/c7fd00216e.

[86] A. Furube *et al.*, "Ultrafast plasmon-induced electron transfer from gold nanodots into TiO_2 nanoparticles," *J Am Chem Soc*, vol. 129, no. 48, pp. 14852–14853, 2007, doi: 10.1021/ja076134v.

[87] Y. Zhang *et al.*, "Facile aqueous synthesis and comparative evaluation of TiO_2-semiconductor and TiO2-metal nanohybrid photocatalysts in antibiotics degradation under visible light," *RSC Adv*, vol. 13, no. 47, pp. 33187–33203, 2023, doi: 10.1039/d3ra06231g.

[88] X. Ma *et al.*, "New insight into the role of gold nanoparticles in Au@ CdS core-shell nanostructures for hydrogen evolution," *Small*, vol. 10, no. 22, pp. 4664–4670, 2014, doi: 10.1002/smll.201401494.

[89] G. M. Whitesides, "The origins and the future of microfluidics," *Nature*, vol. 442, no. 7101, pp. 368–373, 2006, doi: 10.1038/nature05058.

[90] J. Britton *et al.*, "Multi-step continuous-flow synthesis," *Chem Soc Rev*, vol. 46, no. 5, pp. 1250–1271, 2017, doi: 10.1039/c6cs00830e.

[91] S. Hasebe, "Design and operation of micro-chemical plants - Bridging the gap between nano, micro and macro technologies," *Comput Chem Eng*, vol. 29, no. 1, pp. 57–64, 2004, doi: 10.1016/j.compchemeng.2004.07.020.

[92] J. ichi Yoshida *et al.*, "'Impossible' Chemistries Based on Flow and Micro," *J Flow Chem*, vol. 7, no. 3–4, pp. 60–64, 2017, doi: 10.1556/1846.2017.00017.

[93] M. Bayareh *et al.*, "Active and passive micromixers: A comprehensive review," *Chemical Engineering and Processing - Process Intensification*, vol. 147, no. December 2019, pp. 1–19, 2020, doi: 10.1016/j.cep.2019.107771.

[94] S. Marre *et al.*, "Synthesis of micro and nanostructures in microfluidic systems," *Chem Soc Rev*, vol. 39, no. 3, pp. 1183–1202, 2010, doi: 10.1039/b821324k.

[95] A. P. Sudarsan *et al.*, "Multivortex micromixing," *Proc Natl Acad Sci U S A*, vol. 103, no. 19, pp. 7228–7233, 2006, doi: 10.1073/pnas.0507976103.

[96] K. Karthikeyan *et al.*, "Numerical Modeling and Parametric Optimization of Micromixer for Low Diffusivity Fluids," *International Journal of Chemical Reactor Engineering*, vol. 16, no. 3, pp. 1–11, 2018, doi: 10.1515/ijcre-2016-0231.

[97] S. Hardt *et al.*, "Laminar mixing in different interdigital micromixers: II. Numerical simulations," *AIChE Journal*, vol. 49, no. 3, pp. 578–584, 2003, doi: 10.1002/aic.690490305.

[98] A. Shamloo *et al.*, "Analyzing mixing quality in a curved centrifugal micromixer through numerical simulation," *Chemical Engineering and Processing - Process Intensification*, vol. 116, pp. 9–16, 2017, doi: 10.1016/j.cep.2017.03.008.

[99] K. J. Wu *et al.*, "Nucleation and growth in solution synthesis of nanostructures – From fundamentals to advanced applications," *Prog Mater Sci*, vol. 123, no. May 2021, p. 100821, 2022, doi: 10.1016/j.pmatsci.2021.100821.

[100] V. K. Lamer *et al.*, "Theory, Production and Mechanism of Formation of Monodispersed Hydrosols," *J Am Chem Soc*, vol. 72, no. 11, pp. 4847–4854, 1950, doi: 10.1021/ja01167a001.

[101] L. Fornaro *et al.*, "Pre-nucleation and particle attachment of bismuth tri-iodide onto graphene substrates," *J Cryst Growth*, vol. 533, no. October 2019, p. 125454, 2020, doi: 10.1016/j.jcrysgro.2019.125454.

[102] S. Karthika *et al.*, "A Review of Classical and Nonclassical Nucleation Theories," *Cryst Growth Des*, vol. 16, no. 11, pp. 6663–6681, 2016, doi: 10.1021/acs.cgd.6b00794.

[103] P. R. Ten Wolde *et al.*, "Enhancement of protein crystal nucleation by critical density fluctuations," *Science (1979)*, vol. 277, no. 5334, pp. 1975–1978, 1997, doi: 10.1126/science.277.5334.1975.

[104] D. Gebauer *et al.*, "Stable prenucleation calcium carbonate clusters," *Science (1979)*, vol. 322, no. 5909, pp. 1819–1822, 2008, doi: 10.1126/science.1164271.

[105] S. G. Kwon *et al.*, "Formation mechanisms of uniform nanocrystals via hot-injection and heat-up methods," *Small*, vol. 7, no. 19, pp. 2685–2702, 2011, doi: 10.1002/smll.201002022.

[106] S. Mozaffari *et al.*, "Colloidal nanoparticle size control: Experimental and kinetic modeling investigation of the ligand-metal binding role in controlling the nucleation and growth kinetics," *Nanoscale*, vol. 9, no. 36, pp. 13772–13785, 2017, doi: 10.1039/c7nr04101b.

[107] A. S. Myerson *et al.*, *Crystals and crystal growth*. 2019. doi: 10.1017/9781139026949.002.

[108] S. P. Shields *et al.*, "Nucleation control of size and dispersity in aggregative nanoparticle growth. A study of the coarsening kinetics of thiolate-capped gold nanocrystals," *Chemistry of Materials*, vol. 22, no. 10, pp. 3212–3225, 2010, doi: 10.1021/cm100458b.

[109] H. Zheng *et al.*, "Observation of Single Colloidal Platinum Nanocrystal Growth Trajectories," *Science (1979)*, vol. 324, no. 5932, pp. 1309–1312, 2009.

[110] V. N. Richards *et al.*, "Pathway from a molecular precursor to silver nanoparticles: The prominent role of aggregative growth," *Chemistry of Materials*, vol. 22, no. 11, pp. 3556–3567, 2010, doi: 10.1021/cm100871g.

[111] N. Toshima *et al.*, "Bimetallic nanoparticles - Novel materials for chemical and physical applications," *New Journal of Chemistry*, vol. 22, no. 11, pp. 1179–1201, 1998, doi: 10.1039/a805753b.

[112] K. Sugano *et al.*, "Mixing speed-controlled gold nanoparticle synthesis with pulsed mixing microfluidic system," *Microfluid Nanofluidics*, vol. 9, no. 6, pp. 1165–1174, 2010, doi: 10.1007/s10404-010-0637-9.

[113] "A matter of scale," *Nat Nanotechnol*, vol. 11, no. 9, p. 733, 2016, doi: 10.1038/nnano.2016.180.

[114] R. L. Hartman, *et al.*, "Deciding whether to go with the flow: Evaluating the merits of flow reactors for synthesis," *Angewandte Chemie - International Edition*, vol. 50, no. 33, pp. 7502–7519, 2011, doi: 10.1002/anie.201004637.

[115] K. J. Wu *et al.*, "Synthesis of narrow sized silver nanoparticles in the absence of capping ligands in helical microreactors," *React Chem Eng*, vol. 2, no. 2, pp. 116–128, 2017, doi: 10.1039/c6re00202a.

[116] M. Wuithschick *et al.*, "Size-controlled synthesis of colloidal silver nanoparticles based on mechanistic understanding," *Chemistry of Materials*, vol. 25, no. 23, pp. 4679–4689, 2013, doi: 10.1021/cm401851g.

[117] N. K. V. Nadimpalli *et al.*, "A coupled CFD-PBM and thermodynamic analysis of continuous supercritical hydrothermal synthesis of nanoparticles," *Journal of Supercritical Fluids*, vol. 136, no. November 2017, pp. 164–179, 2018, doi: 10.1016/j.supflu.2018.02.011.

[118] B. L. Hall *et al.*, "Autonomous optimisation of a nanoparticle catalysed reduction reaction in continuous flow," *Chemical Communications*, vol. 57, no. 40, pp. 4926–4929, 2021, doi: 10.1039/d1cc00859e.

[119] E. J. Roberts *et al.*, "Continuous Flow Methods of Fabricating Catalytically Active Metal Nanoparticles," *ACS Appl Mater Interfaces*, vol. 11, no. 31, pp. 27479–27502, 2019, doi: 10.1021/acsami.9b07268.

[120] T. Van De Laar *et al.*, "Transition-state theory predicts clogging at the microscale," *Sci Rep*, vol. 6, no. April, pp. 1–8, 2016, doi: 10.1038/srep28450.

[121] Y. Xie *et al.*, *Toward autonomous laboratories: Convergence of artificial intelligence and experimental automation*, vol. 132, no. May 2022. Elsevier Ltd, 2023. doi: 10.1016/j.pmatsci.2022.101043.

[122] D. Conchouso *et al.*, "Three-dimensional parallelization of microfluidic droplet generators for a litre per hour volume production of single emulsions," *Lab Chip*, vol. 14, no. 16, pp. 3011–3020, 2014, doi: 10.1039/c4lc00379a.

[123] J. B. Wacker *et al.*, "Controlled synthesis of fluorescent silica nanoparticles inside microfluidic droplets," *Lab Chip*, vol. 12, no. 17, pp. 3111–3116, 2012, doi: 10.1039/c2lc40300e.

[124] L. Panariello *et al.*, "Highly reproducible, high-yield flow synthesis of gold nanoparticles based on a rational reactor design exploiting the reduction of passivated Au(iii)," *React Chem Eng*, vol. 5, no. 4, pp. 663–676, 2020, doi: 10.1039/c9re00469f.

[125] E. Rossi *et al.*, "Scalable in situ diazomethane generation in continuous-flow reactors," *Org Process Res Dev*, vol. 16, no. 5, pp. 1146–1149, 2012, doi: 10.1021/op200110a.

[126] S. Tao *et al.*, "Continuous synthesis of hedgehog-like Ag-ZnO nanoparticles in a two-stage microfluidic system," *RSC Adv*, vol. 6, no. 51, pp. 45503–45511, 2016, doi: 10.1039/c6ra06101j.

[127] E. D. Lavric *et al.*, "Advanced-Flow TM glass reactors for seamless scale-up," *Chemistry Today*, vol. 27, no. 3, pp. 45–48, 2009.

[128] M. J. Nieves-Remacha *et al.*, "Hydrodynamics of liquid-liquid dispersion in an advanced-flow reactor," *Ind Eng Chem Res*, vol. 51, no. 50, pp. 16251–16262, 2012, doi: 10.1021/ie301821k.

[129] P. Bianchi *et al.*, "Scalable and robust photochemical flow process towards small spherical gold nanoparticles," *React Chem Eng*, vol. 5, no. 7, 2020, doi: 10.1039/d0re00092b.

[130] G. S.Calabrese *et al.*, "From Batch to Continuous Flow Processing in Chemicals Manufacturing," *AIChE Journal*, vol. 57, no. 4, pp. 828–834, 2011, doi: 10.1002/aic.

[131] Z. Dong *et al.*, "Scale-up of micro- and milli-reactors: An overview of strategies, design principles and applications," *Chemical Engineering Science: X*, vol. 10, p. 100097, 2021, doi: 10.1016/j.cesx.2021.100097.

[132] B. Buisson *et al.*, "Slurry hydrogenation in a continuous flow reactor for pharmaceutical application," *Chim Oggi*, vol. 27, no. 6, pp. 12–16, 2009.

[133] T. Entradas *et al.*, "Synthesis of sub-5 nm Co-doped SnO_2 nanoparticles and their structural, microstructural, optical and photocatalytic properties," *Mater Chem Phys*, vol. 147, no. 3, pp. 563–571, 2014, doi: 10.1016/j.matchemphys.2014.05.032.

[134] M. S. Wrighton *et al.*, "Photoassisted Electrolysis of Water by Ultraviolet Irradiation of an Antimony Doped Stannic Oxide Electrode," *J Am Chem Soc*, vol. 98, no. 1, pp. 44–48, 1976, doi: 10.1021/ja00417a009.

[135] C. Sun *et al.*, "Recent intensification strategies of SnO_2-based photocatalysts: A review," *Chemical Engineering Journal*, vol. 427, no. August 2021, p. 131564, 2022, doi: 10.1016/j.cej.2021.131564.

[136] K. Maenetja *et al.*, "Electronic stability study of tin dioxide as a catalyst for lithium-air batteries," *MATEC Web of Conferences*, vol. 388, p. 02001, 2023, doi: 10.1051/matecconf/202338802001.

[137] G. Oldfield *et al.*, "Au@SnO_2 Core-Shell Nanocapacitors," *Advanced Materials*, no. 20, pp. 1519–1522, 2000.

[138] Y. T. Yu *et al.*, "Examination of Au/SnO2 core-shell architecture nanoparticle for low temperature gas sensing applications," *Sens Actuators B Chem*, vol. 157, no. 2, pp. 444–449, 2011, doi: 10.1016/j.snb.2011.04.088.

[139] M. H. Xu *et al.*, "Facile synthesis of highly ethanol-sensitive SnO2 nanosheets using homogeneous precipitation method," *Sens Actuators B Chem*, vol. 145, no. 2, pp. 875–878, 2010, doi: 10.1016/j.snb.2010.01.002.

[140] M. Aziz *et al.*, "Structure of SnO_2 nanoparticles by sol-gel method," *Mater Lett*, vol. 74, no. 41, pp. 62–64, 2012, doi: 10.1016/j.matlet.2012.01.073.

[141] W. H. Lai *et al.*, "Morphology tuning of inorganic nanomaterials grown by precipitation through control of electrolytic dissociation and supersaturation," *Nat Chem*, vol. 11, no. 8, pp. 695–701, Aug. 2019, doi: 10.1038/s41557-019-0298-6.

[142] S. H. Lee *et al.*, "Monodisperse SnO_2-coated gold nanoparticles are markedly more stable than analogous SiO_2-coated gold nanoparticles," *ACS Appl Mater Interfaces*, vol. 5, no. 7, pp. 2479–2484, 2013, doi: 10.1021/am302740z.

[143] P. Rai *et al.*, "Synthesis of plasmonic Ag@SnO_2 core-shell nanoreactors for xylene detection," *RSC Adv*, vol. 5, no. 23, pp. 17653–17659, 2015, doi: 10.1039/c4ra13971b.

[144] C.-H. Li *et al.*, "Optically Tunable Tin Oxide-Coated Hollow Gold–Silver Nanorattles for Use in Solar-Driven Applications," *ACS Omega*, vol. 5, no. 37, pp. 23769–23777, Sep. 2020, doi: 10.1021/acsomega.0c02818.

[145] M. Lei *et al.*, "Controlled preparation of hollow SnO_2@M (M = Au, Ag) heterostructures through template-assist method for enhanced photocatalysis," *Colloids Surf A Physicochem Eng Asp*, vol. 482, pp. 276–282, 2015, doi: 10.1016/j.colsurfa.2015.06.018.

[146] H. You *et al.*, "Gold nanoparticle doped hollow SnO_2 supersymmetric nanostructures for improved photocatalysis," *J Mater Chem A Mater*, vol. 1, no. 12, pp. 4097–4104, 2013, doi: 10.1039/c3ta01099f.

[147] Y. V. Kaneti *et al.*, "Experimental and theoretical studies on noble metal decorated tin oxide flower-like nanorods with high ethanol sensing performance," *Sens Actuators B Chem*, vol. 219, pp. 83–93, 2015, doi: 10.1016/j.snb.2015.04.136.

[148] M. M. Khan *et al.*, "Visible light-induced enhanced photoelectrochemical and photocatalytic studies of gold decorated SnO_2 nanostructures," *New Journal of Chemistry*, vol. 39, no. 4, pp. 2758–2766, 2015, doi: 10.1039/c4nj02245a.

[149] B. Feng *et al.*, "Self-template synthesis of mesoporous Au-SnO_2 nanospheres for low-temperature detection of triethylamine vapor," *Sens Actuators B Chem*, vol. 356, no. January, p. 131358, 2022, doi: 10.1016/j.snb.2021.131358.

[150] Y. Wang *et al.*, "Fabrication and gas sensing properties of Au-loaded SnO_2 composite nanoparticles for highly sensitive hydrogen detection," *Sens Actuators B Chem*, vol. 240, pp. 664–673, 2017, doi: 10.1016/j.snb.2016.09.024.

[151] T. Sinha *et al.*, "Green and Environmentally Sustainable Fabrication of Ag-SnO_2 Nanocomposite and Its Multifunctional Efficacy As Photocatalyst and Antibacterial and Antioxidant Agent," *ACS Sustain Chem Eng*, vol. 5, no. 6, pp. 4645–4655, Jun. 2017, doi: 10.1021/acssuschemeng.6b03114.

[152] X. Wang *et al.*, "Self-assemble flower-like SnO_2/Ag heterostructures: Correlation among composition, structure and photocatalytic activity," *Colloids Surf A Physicochem Eng Asp*, vol. 419, pp. 140–146, 2013, doi: 10.1016/j.colsurfa.2012.11.050.

[153] M. Li *et al.*, "Enhanced Electrochemical Reduction of CO_2 to CO on Ag/SnO_2 by a Synergistic Effect of Morphology and Structural Defects," *Chem Asian J*, vol. 16, no. 18, pp. 2694–2701, 2021, doi: 10.1002/asia.202100718.

[154] H. E. Rude *et al.*, "Toward Informed Design of Nanomaterials: A Mechanistic Analysis of Structure-Property-Function Relationships for Faceted Nanoscale Metal Oxides," *ACS Nano*, vol. 14, no. 12, pp. 16472–16501, 2020, doi: 10.1021/acsnano.0c08356.

[155] A. Paracchino *et al.*, "Highly active oxide photocathode for photoelectrochemical water reduction," *Nat Mater*, vol. 10, no. 6, pp. 456–461, 2011, doi: 10.1038/nmat3017.

[156] A. M. Mohammed *et al.*, "Review of various strategies to boost the photocatalytic activity of the cuprous oxide-based photocatalyst," *J Environ Chem Eng*, vol. 9, no. 2, p. 105138, 2021, doi: 10.1016/j.jece.2021.105138.

[157] D. Snoke, "Coherent Exciton Waves," *Science (1979)*, vol. 273, no. 5280, pp. 1351–1352, 1996, doi: 10.1126/science.273.5280.1352.

[158] A. Živković *et al.*, "Density functional theory study explaining the underperformance of copper oxides as photovoltaic absorbers," *Phys Rev B*, vol. 99, no. 3, pp. 1–10, 2019, doi: 10.1103/PhysRevB.99.035154.

[159] Y. Shang *et al.*, "Facet-Controlled Synthetic Strategy of Cu_2O-Based Crystals for Catalysis and Sensing," *Advanced Science*, vol. 2, no. 10, 2015, doi: 10.1002/advs.201500140.

[160] C. Yu *et al.*, "Multi-branched Cu_2O nanowires for photocatalytic degradation of methyl orange," *Mater Res Express*, vol. 5, no. 3, 2018, doi: 10.1088/2053-1591/aab516.

[161] I. S. Brandt *et al.*, "Electrodeposition of Cu_2O: growth, properties, and applications," *Journal of Solid State Electrochemistry*, vol. 21, no. 7, pp. 1999–2020, 2017, doi: 10.1007/s10008-017-3660-x.

[162] H. Wang *et al.*, "Cuprous oxide nanoshells exhibit geometrically tunable optical properties," *ACS National Meeting Book of Abstracts*, no. 4, pp. 3257–3267, 2011.

[163] S. Sun *et al.*, "Cuprous oxide (Cu_2O) crystals with tailored architectures: A comprehensive review on synthesis, fundamental properties, functional modifications and applications," *Prog Mater Sci*, vol. 96, pp. 111–173, 2018, doi: 10.1016/j.pmatsci.2018.03.006.

[164] S. Sun *et al.*, "The crystal-facet-dependent effect of polyhedral Cu_2O microcrystals on photocatalytic activity," *Catal Sci Technol*, vol. 2, no. 5, pp. 925–930, 2012, doi: 10.1039/c2cy00530a.

[165] M. Torras *et al.*, "Copper Oxide Nanocubes Wrapping Metals by Microwave Synthesis," *Cryst Growth Des*, vol. 21, no. 9, pp. 5027–5035, 2021, doi: 10.1021/acs.cgd.1c00462.

[166] J. Seidler *et al.*, "Novel cuprous oxide morphologies using amino acids and carboxylic acids as structure directing agents in a simple hydrothermal method," *Mater Lett*, vol. 292, p. 129553, 2021, doi: 10.1016/j.matlet.2021.129553.

[167] J. Zeng *et al.*, "Novel Insights into Sb-Cu Catalysts for Electrochemical Reduction of CO_2," *Appl Catal B*, vol. 306, no. January, p. 121089, 2022, doi: 10.1016/j.apcatb.2022.121089.

[168] P. Marathey *et al.*, "Photoelectrochemical characteristics of electrodeposited cuprous oxide with protective over layers for hydrogen evolution reactions," *Int J Hydrogen Energy*, vol. 46, no. 30, pp. 16431–16439, 2021, doi: 10.1016/j.ijhydene.2020.07.271.

[169] K. Ungeheuer *et al.*, "Cuprous Oxide Thin Films Implanted with Chromium Ions—Optical and Physical Properties Studies," *Int J Mol Sci*, vol. 23, no. 15, 2022, doi: 10.3390/ijms23158358.

[170] S. S. Sawant *et al.*, "Synthesis of cuprous oxide (Cu_2O) nanoparticles - A review," *Journal of Nano- and Electronic Physics*, vol. 8, no. 1, pp. 1–5, 2016, doi: 10.21272/jnep.8(1).01035.

[171] P. Lignier *et al.*, "Scalable strategies for the synthesis of well-defined copper metal and oxide nanocrystals," *Chem Soc Rev*, vol. 41, no. 5, pp. 1708–1720, 2012, doi: 10.1039/c1cs15223h.

[172] X. Liang *et al.*, "Facile synthesis and shape evolution of single-crystal cuprous oxide," *Advanced Materials*, vol. 21, no. 20, pp. 2068–2071, 2009, doi: 10.1002/adma.200802783.

[173] W. C. Huang *et al.*, "Synthesis of Cu_2O nanocrystals from cubic to rhombic dodecahedral structures and their comparative photocatalytic activity," *J Am Chem Soc*, vol. 134, no. 2, pp. 1261–1267, 2012, doi: 10.1021/ja209662v.

[174] C. H. Kuo *et al.*, "Facile synthesis of Cu_2O nanocrystals with systematic shape evolution from cubic to octahedral structures," *Journal of Physical Chemistry C*, vol. 112, no. 47, pp. 18355–18360, 2008, doi: 10.1021/jp8060027.

[175] C. H. Kuo *et al.*, "Seed-mediated synthesis of monodispersed Cu_2O nanocubes with five different size ranges from 40 to 420 nm," *Adv Funct Mater*, vol. 17, no. 18, pp. 3773–3780, 2007, doi: 10.1002/adfm.200700356.

[176] C. H. Kuo *et al.*, "Fabrication of truncated rhombic dodecahedral Cu_2O nanocages and nanoframes by particle aggregation and acidic etching," *J Am Chem Soc*, vol. 130, no. 38, pp. 12815–12820, 2008, doi: 10.1021/ja804625s.

[177] Y. Sui *et al.*, "Low temperature synthesis of Cu_2O crystals: Shape evolution and growth mechanism," *Cryst Growth Des*, vol. 10, no. 1, pp. 99–108, 2010, doi: 10.1021/cg900437x.

[178] W. C. Huang *et al.*, "Synthesis of Cu_2O nanocrystals from cubic to rhombic dodecahedral structures and their comparative photocatalytic activity," *J Am Chem Soc*, vol. 134, no. 2, pp. 1261–1267, 2012, doi: 10.1021/ja209662v.

[179] M. Leng *et al.*, "Polyhedral 50-facet Cu_2O microcrystals partially enclosed by {311} high-index planes: Synthesis and enhanced catalytic CO oxidation activity," *J Am Chem Soc*, vol. 132, no. 48, pp. 17084–17087, 2010, doi: 10.1021/ja106788x.

[180] J. Pal *et al.*, "Crystal-plane-dependent etching of cuprous oxide nanoparticles of varied shapes and their application in visible light photocatalysis," *Journal of Physical Chemistry C*, vol. 117, no. 46, pp. 24640–24653, 2013, doi: 10.1021/jp409271r.

[181] X. Wei *et al.*, "Technical note microfluidic method for synthesizing Cu_2O nanofluids," *J Thermophys Heat Trans*, vol. 24, no. 2, pp. 445–448, 2010, doi: 10.2514/1.48984.

[182] A. H. M. Al-Antaki *et al.*, "Continuous Flow Copper Laser Ablation Synthesis of Copper(I and II) Oxide Nanoparticles in Water," *ACS Omega*, vol. 4, no. 8, pp. 13577–13584, 2019, doi: 10.1021/acsomega.9b01983.

[183] A. H. M. Al-Antaki *et al.*, "Continuous Flow Copper Laser Ablation Synthesis of Copper(I and II) Oxide Nanoparticles in Water," *ACS Omega*, vol. 4, no. 8, pp. 13577–13584, 2019, doi: 10.1021/acsomega.9b01983.

[184] M. Yang *et al.*, "Mixing performance and continuous production of nanomaterials in an advanced-flow reactor," *Chemical Engineering Journal*, vol. 412, May 2021, doi: 10.1016/j.cej.2021.128565.

[185] V. Viktorov *et al.*, "Numerical study of fluid mixing at different inlet flow-rate ratios in Tear-drop and Chain micromixers compared to a new H-C passive micromixer," *Engineering Applications of Computational Fluid Mechanics*, vol. 10, no. 1, pp. 183–193, 2016, doi: 10.1080/19942060.2016.1140075.

[186] S. W. Lee *et al.*, "A split and recombination micromixer fabricated in a PDMS three-dimensional structure," *Journal of Micromechanics and Microengineering*, vol. 16, no. 5, pp. 1067–1072, 2006, doi: 10.1088/0960-1317/16/5/027.

[187] I. Shah *et al.*, "Experimental and numerical analysis of Y-shaped split and recombination micro-mixer with different mixing units," *Chemical Engineering Journal*, vol. 358, no. September 2018, pp. 691–706, 2019, doi: 10.1016/j.cej.2018.09.045.

[188] M. C. Fournier *et al.*, "A new parallel competing reaction system for assessing micromixing efficiency - Experimental approach," *Chem Eng Sci*, vol. 51, no. 22, pp. 5053–5064, 1996, doi: 10.1016/0009-2509(96)00270-9.

[189] M. Fournier *et al.*, "Assessing Micromixing Efficiency--Determination of Micromixing Time By a Simple Mixing," *Chem Eng Sci*, vol. 51, no. 23, pp. 5187–5192, 1996, [Online]. Available: http://dx.doi.org/10.1016/S0009-2509(96)00340-5

[190] P. Guichardon *et al.*, “Characterisation of micromixing efficiency by the iodide-iodate reaction system. Part I: Experimental procedure,” *Chem Eng Sci*, vol. 55, no. 19, pp. 4233–4243, 2000, doi: 10.1016/S0009-2509(00)00068-3.

[191] P. Guichardon *et al.*, “Characterisation of micromixing efficiency by the iodide-iodate reaction system. Part II: Kinetic study,” *Chem Eng Sci*, vol. 55, no. 19, pp. 4245–4253, 2000, doi: 10.1016/S0009-2509(00)00069-5.

[192] R. O. Fox, “On the relationship between Lagrangian micromixing models and computational fluid dynamics,” *Chemical Engineering and Processing: Process Intensification*, vol. 37, no. 6, pp. 521–535, 1998, doi: 10.1016/S0255-2701(98)00059-2.

[193] Y. Su *et al.*, “Ideal micromixing performance in packed microchannels,” *Chem Eng Sci*, vol. 66, no. 13, pp. 2912–2919, 2011, doi: 10.1016/j.ces.2011.03.024.

[194] Y. Wu *et al.*, “Intensification of micromixing efficiency in a ceramic membrane reactor with turbulence promoter,” *J Memb Sci*, vol. 328, no. 1–2, pp. 219–227, 2009, doi: 10.1016/j.memsci.2008.12.010.

[195] B. Michen *et al.*, “Avoiding drying-artifacts in transmission electron microscopy: Characterizing the size and colloidal state of nanoparticles,” *Sci Rep*, vol. 5, 2015, doi: 10.1038/srep09793.

[196] X. Lin *et al.*, “Determination of the Micromixing Scale in a Microdevice by Numerical Simulation and Experiments,” *Chem Eng Technol*, vol. 39, no. 5, pp. 909–917, 2016, doi: 10.1002/ceat.201500651.

[197] B. K. Johnson *et al.*, “Chemical processing and micromixing in confined impinging jets,” *AIChE Journal*, vol. 49, no. 9, pp. 2264–2282, 2003, doi: 10.1002/aic.690490905.

[198] T. Xie *et al.*, “Numerical and experimental investigations of chaotic mixing behavior in an oscillating feedback micromixer,” *Chem Eng Sci*, vol. 171, pp. 303–317, 2017, doi: 10.1016/j.ces.2017.05.040.

[199] M. Rahimi *et al.*, “CFD study on effect of channel confluence angle on fluid flow pattern in asymmetrical shaped microchannels,” *Comput Chem Eng*, vol. 73, pp. 172–182, 2015, doi: 10.1016/j.compchemeng.2014.12.007.

[200] S. H. Wong *et al.*, “Micro T-mixer as a rapid mixing micromixer,” *Sens Actuators B Chem*, vol. 100, no. 3, pp. 359–379, 2004, doi: 10.1016/j.snb.2004.02.008.

[201] M. A. Ansari *et al.*, “A novel passive micromixer based on unbalanced splits and collisions of fluid streams,” *Journal of Micromechanics and Microengineering*, vol. 20, no. 5, 2010, doi: 10.1088/0960-1317/20/5/055007.

[202] A. A. Mouza *et al.*, “Mixing performance of a chaotic micro-mixer,” *Chemical Engineering Research and Design*, vol. 86, no. 10, pp. 1128–1134, 2008, doi: 10.1016/j.cherd.2008.04.009.

[203] M. Sadegh Cheri *et al.*, “Simulation and experimental investigation of planar micromixers with short-mixing-length,” *Chemical Engineering Journal*, vol. 234, pp. 247–255, 2013, doi: 10.1016/j.cej.2013.08.067.

[204] M. Assirelli *et al.*, "Macro- and micromixing studies in an unbaffled vessel agitated by a Rushton turbine," *Chem Eng Sci*, vol. 63, no. 1, pp. 35–46, 2008, doi: 10.1016/j.ces.2007.07.074.

[205] X. Lin *et al.*, "Determination of the Micromixing Scale in a Microdevice by Numerical Simulation and Experiments," *Chem Eng Technol*, vol. 39, no. 5, pp. 909–917, 2016, doi: 10.1002/ceat.201500651.

[206] K. Kunowa *et al.*, "Characterization of mixing efficiency in polymerization reactors using competitive-parallel reactions," *Macromol Symp*, vol. 259, pp. 32–41, 2007, doi: 10.1002/masy.200751305.

[207] D. K. Lim *et al.*, "Nanogap-engineerable raman-active nanodumbbells for single-molecule detection," *Nat Mater*, vol. 9, no. 1, pp. 60–67, 2010, doi: 10.1038/nmat2596.

[208] A. Kölbl *et al.*, "The iodide iodate reaction method: The choice of the acid," *Chem Eng Sci*, vol. 65, no. 5, pp. 1897–1901, 2010, doi: 10.1016/j.ces.2009.11.032.

[209] A. Kölbl *et al.*, "Kinetic investigation of the Dushman reaction at concentrations relevant to mixing studies in stirred tank reactors," *Chem Eng Sci*, vol. 93, pp. 47–54, 2013, doi: 10.1016/j.ces.2013.01.067.

[210] M. Guo *et al.*, "Mixing Performance and Application of a Three-Dimensional Serpentine Microchannel Reactor with a Periodic Vortex-Inducing Structure," *Ind Eng Chem Res*, vol. 58, no. 29, pp. 13357–13365, 2019, doi: 10.1021/acs.iecr.9b01573.

[211] X. Z. Lin *et al.*, "Synthesis of silver nanoparticles in a continuous flow tubular microreactor," *Nano Lett*, vol. 4, no. 11, pp. 2227–2232, 2004, doi: 10.1021/nl0485859.

[212] K. J. Wu *et al.*, "Synthesis of narrow sized silver nanoparticles in the absence of capping ligands in helical microreactors," *React Chem Eng*, vol. 2, no. 2, pp. 116–128, 2017, doi: 10.1039/c6re00202a.

[213] M. Lu *et al.*, "Shape-controlled synthesis of hybrid nanomaterials via three-dimensional hydrodynamic focusing," *ACS Nano*, vol. 8, no. 10, pp. 10026–10034, 2014, doi: 10.1021/nn502549v.

[214] M. M. Abouelela *et al.*, "A review on plasmonic nanoparticle-semiconductor photocatalysts for water splitting," *J Clean Prod*, vol. 294, p. 126200, 2021, doi: 10.1016/j.jclepro.2021.126200.

[215] K. J. Wu *et al.*, "Continuous synthesis of tuneable sized silver nanoparticles: Via a tandem seed-mediated method in coiled flow inverter reactors," *React Chem Eng*, vol. 3, no. 3, pp. 267–276, 2018, doi: 10.1039/c7re00194k.

[216] F. C. Vásquez *et al.*, "Shape and size controlled growth of SnO2 nano-particles by efficient approach," *Superlattices Microstruct*, vol. 90, pp. 274–287, 2016, doi: 10.1016/j.spmi.2015.12.014.

[217] V. Inderan *et al.*, "Synthesis and characterisations of SnO2 nanorods via low temperature hydrothermal method," *Superlattices Microstruct*, vol. 88, pp. 396–402, 2015, doi: 10.1016/j.spmi.2015.09.031.

[218] K. Sato *et al.*, "Hydrothermal growth of tailored SnO2 nanocrystals," *Cryst Growth Des*, vol. 13, no. 4, pp. 1685–1693, 2013, doi: 10.1021/cg400013q.

[219] S. M. Yakout, "Inclusion of cobalt reinforced Ag doped SnO_2 properties: electrical, dielectric constant, magnetic and photocatalytic insights," *Journal of Materials Science: Materials in Electronics*, vol. 30, no. 18, pp. 17053–17065, 2019, doi: 10.1007/s10854-019-02052-y.

[220] G. wen Chu *et al.*, "Preparation of SnO_2 nanoparticles using a helical tube reactor via continuous hydrothermal route," *Chemical Engineering Journal*, vol. 253, pp. 78–83, 2014, doi: 10.1016/j.cej.2014.05.016.

[221] V. Saasa *et al.*, "Effect of varying ethanol and water compositions on the acetone sensing properties of WO_3 for application in diabetes mellitus monitoring," *Mater Res Express*, vol. 7, no. 3, 2020, doi: 10.1088/2053-1591/ab7d58.

[222] N. M. Schneider *et al.*, "Electron-Water interactions and implications for liquid cell electron microscopy," *Journal of Physical Chemistry C*, vol. 118, no. 38, pp. 22373–22382, 2014, doi: 10.1021/jp507400n.

[223] P. B. Khoza *et al.*, "The effect of solvents, acetone, water, and ethanol, on the morphological and optical properties of ZnO nanoparticles prepared by microwave," *J Nanotechnol*, vol. 2012, 2012, doi: 10.1155/2012/195106.

[224] L. Qin *et al.*, "The template-free synthesis of square-shaped SnO2 nanowires: The temperature effect and acetone gas sensors," *Nanotechnology*, vol. 19, no. 18, 2008, doi: 10.1088/0957-4484/19/18/185705.

[225] A. Kar *et al.*, "Surface defect-related luminescence properties of SnO_2 nanorods and nanoparticles," *Journal of Physical Chemistry C*, vol. 115, no. 1, pp. 118–124, 2011, doi: 10.1021/jp110313b.

[226] B. Babu *et al.*, "One pot synthesis of Ag-SnO_2 quantum dots for highly enhanced sunlight-driven photocatalytic activity," *J Alloys Compd*, vol. 731, pp. 162–171, 2018, doi: 10.1016/j.jallcom.2017.10.011.

[227] A. Kar *et al.*, "Influence of size and shape on the photocatalytic properties of SnO_2 nanocrystals," *ChemPhysChem*, vol. 16, no. 5, pp. 1017–1025, 2015, doi: 10.1002/cphc.201402864.

[228] S. P. S. Porto *et al.*, "Raman spectra of TiO_2, MgF_2, ZnF_2, FeF_2, and MnF_2," *Physical Review*, vol. 154, no. 2, pp. 522–526, 1967, doi: 10.1103/PhysRev.154.522.

[229] S. H. Sun *et al.*, "Raman scattering study of rutile SnO_2 nanobelts synthesized by thermal evaporation of Sn powders," *Chem Phys Lett*, vol. 376, no. 1–2, pp. 103–107, 2003, doi: 10.1016/S0009-2614(03)00965-5.

[230] G. Xi *et al.*, "Ultrathin SnO_2 nanorods: Template- and surfactant-free solution phase synthesis, growth mechanism, optical, gas-Sensing, and surface adsorption properties," *Inorg Chem*, vol. 49, no. 5, pp. 2302–2309, 2010, doi: 10.1021/ic902131a.

[231] A. M. Al-Hamdi *et al.*, "Tin dioxide as a photocatalyst for water treatment: A review," *Process Safety and Environmental Protection*, vol. 107, pp. 190–205, 2017, doi: 10.1016/j.psep.2017.01.022.

[232] P. A. Luque *et al.*, "Efficient sunlight and UV photocatalytic degradation of Methyl Orange, Methylene Blue and Rhodamine B, using Citrus×paradisi synthesized SnO_2 semiconductor nanoparticles," *Ceram Int*, vol. 47, no. 17, pp. 23861–23874, 2021, doi: 10.1016/j.ceramint.2021.05.094.

[233] C. Deraedt *et al.*, "Sodium borohydride stabilizes very active gold nanoparticle catalysts," *Chemical Communications*, vol. 50, no. 91, pp. 14194–14196, 2014, doi: 10.1039/c4cc05946h.

[234] W. Zhang *et al.*, "A sensitive, point-of-care detection of small molecules based on a portable barometer: Aflatoxins in agricultural products," *Toxins (Basel)*, vol. 12, no. 3, 2020, doi: 10.3390/toxins12030158.

[235] A. Mamakhel *et al.*, "Continuous flow hydrothermal synthesis of rutile SnO_2 nanoparticles: Exploration of pH and temperature effects," *Journal of Supercritical Fluids*, vol. 166, pp. 1–8, 2020, doi: 10.1016/j.supflu.2020.105029.

[236] S. Das *et al.*, "Ag@SnO_2@ZnO core-shell nanocomposites assisted solar-photocatalysis downregulates multidrug resistance in Bacillus sp.: A catalytic approach to impede antibiotic resistance," *Appl Catal B*, vol. 259, no. May, p. 118065, 2019, doi: 10.1016/j.apcatb.2019.118065.

[237] J. Liu *et al.*, "Metal-free efficient photocatalyst for stable visible water splitting via a two-electron pathway," *Science (1979)*, vol. 347, no. 6225, pp. 970–974, 2015, doi: 10.1126/science.aaa3145.

[238] W. Wu *et al.*, "Non-centrosymmetric Au-SnO_2 hybrid nanostructures with strong localization of plasmonic for enhanced photocatalysis application," *Nanoscale*, vol. 5, no. 12, pp. 5628–5636, 2013, doi: 10.1039/c3nr00985h.

[239] X. Liu *et al.*, "Visible light photocatalytic degradation of methylene blue by SnO_2 quantum dots prepared via microwave-assisted method," *Catal Sci Technol*, vol. 3, no. 7, pp. 1805–1809, 2013, doi: 10.1039/c3cy00013c.

[240] Z. He *et al.*, "Photocatalytic degradation of rhodamine B by Bi_2WO_6 with electron accepting agent under microwave irradiation: Mechanism and pathway," *J Hazard Mater*, vol. 162, no. 2–3, pp. 1477–1486, 2009, doi: 10.1016/j.jhazmat.2008.06.047.

[241] M. H. Huang *et al.*, "Facet-Dependent Electrical, Photocatalytic, and Optical Properties of Semiconductor Crystals and Their Implications for Applications," *ACS Appl Mater Interfaces*, vol. 10, no. 1, pp. 4–15, 2018, doi: 10.1021/acsami.7b15828.

[242] S. J. Yang *et al.*, "Crystal Facet Dependent Energy Band Structures of Polyhedral Cu_2O Nanocrystals and Their Application in Solar Fuel Production," *Journal of Physical Chemistry Letters*, vol. 13, no. 27, pp. 6298–6305, 2022, doi: 10.1021/acs.jpclett.2c01632.

[243] J. Y. Ho *et al.*, "Synthesis of submicrometer-sized Cu_2O crystals with morphological evolution from cubic to hexapod structures and their comparative photocatalytic activity," *Journal of Physical Chemistry C*, vol. 113, no. 32, pp. 14159–14164, 2009, doi: 10.1021/jp903928p.

[244] J. Y. Huang *et al.*, "Modified Semiconductor Band Diagrams Constructed from Optical Characterization of Size-Tunable Cu_2O Cubes, Octahedra, and Rhombic Dodecahedra," *Journal of Physical Chemistry C*, vol. 122, no. 24, pp. 13027–13033, 2018, doi: 10.1021/acs.jpcc.8b02169.

[245] Y. H. Tsai *et al.*, "Direct formation of small Cu_2O nanocubes, octahedra, and octapods for efficient synthesis of triazoles," *Nanoscale*, vol. 6, no. 15, pp. 8704–8709, 2014, doi: 10.1039/c4nr02076f.

[246] C. Sun *et al.*, "Droplet-based millifluidic synthesis of a proton-conducting sulfonate metal–organic framework," *Chemical Engineering Journal*, vol. 474, no. September, 2023, doi: 10.1016/j.cej.2023.145892.

[247] J. Feng *et al.*, "Translational formulation of nanoparticle therapeutics from laboratory discovery to clinical scale," *J Transl Med*, vol. 17, no. 1, pp. 1–9, 2019, doi: 10.1186/s12967-019-1945-9.

[248] L. Falk *et al.*, "Performance comparison of micromixers," *Chem Eng Sci*, vol. 65, no. 1, pp. 405–411, 2010, doi: 10.1016/j.ces.2009.05.045.

[249] N. Hondow *et al.*, "Quantitative characterization of nanoparticle agglomeration within biological media," *Journal of Nanoparticle Research*, vol. 14, no. 7, 2012, doi: 10.1007/s11051-012-0977-3.

[250] S. M. Pawar *et al.*, "Multi-functional reactively-sputtered copper oxide electrodes for supercapacitor and electro-catalyst in direct methanol fuel cell applications," *Sci Rep*, vol. 6, no. October 2015, pp. 1–9, 2016, doi: 10.1038/srep21310.

[251] K. Chanda *et al.*, "Facet-dependent catalytic activity of Cu_2O nanocrystals in the one-pot synthesis of 1,2,3-triazoles by multicomponent click reactions," *Chemistry - A European Journal*, vol. 19, no. 47, pp. 16036–16043, 2013, doi: 10.1002/chem.201302065.

[252] M. Leng *et al.*, "Polyhedral Cu_2O particles: Shape evolution and catalytic activity on cross-coupling reaction of iodobenzene and phenol," *CrystEngComm*, vol. 14, no. 24, pp. 8454–8461, 2012, doi: 10.1039/c2ce26295a.

[253] L. Gou *et al.*, "Controlling the size of Cu_2O nanocubes from 200 to 25 nm," *J Mater Chem*, pp. 735–738, 2004, doi: 10.1039/b311625e.

[254] S. Sun *et al.*, "Template-free synthesis of weil-defined truncated edge polyhedral Cu_2O architectures," *Cryst Growth Des*, vol. 10, no. 2, pp. 541–547, 2010, doi: 10.1021/cg900756u.

[255] P. K. Sen *et al.*, "Effects of pre-micelles of anionic surfactant SDS on the electron transfer reaction between methylene blue and ascorbic acid," *J Mol Liq*, vol. 224, pp. 472–479, 2016, doi: 10.1016/j.molliq.2016.10.034.

[256] N. T. K. Thanh *et al.*, "Mechanisms of nucleation and growth of nanoparticles in solution," *Chem Rev*, vol. 114, no. 15, pp. 7610–7630, 2014, doi: 10.1021/cr400544s.

[257] S. Sun *et al.*, "Polyhedron-aggregated multi-facet Cu_2O homogeneous structures," *CrystEngComm*, vol. 13, no. 20, pp. 6040–6044, 2011, doi: 10.1039/c1ce05597f.

[258] S. Sun *et al.*, "High-index faceted metal oxide micro-/nanostructures: A review on their characterization, synthesis and applications," *Nanoscale*, vol. 11, no. 34, pp. 15739–15762, 2019, doi: 10.1039/c9nr05107d.

[259] D. F. Zhang *et al.*, "Delicate control of crystallographic facet-oriented Cu_2O nanocrystals and the correlated adsorption ability," *J Mater Chem*, vol. 19, no. 29, pp. 5220–5225, 2009, doi: 10.1039/b816349a.

[260] S. Sun *et al.*, "Recent advances in tuning crystal facets of polyhedral cuprous oxide architectures," *RSC Adv*, vol. 4, no. 8, pp. 3804–3822, 2014, doi: 10.1039/c3ra45445b.

[261] G. Kumar *et al.*, "Morphological evolution of cadmium oxide crystals showing color changes and facet-dependent conductivity behavior," *J Mater Chem C Mater*, vol. 10, no. 33, pp. 12125–12131, 2022, doi: 10.1039/d2tc02318k.

[262] Y. W. Peng *et al.*, "Formation of $CsPbCl_3$ Cubes and Edge-Truncated Cuboids at Room Temperature," *ACS Sustain Chem Eng*, vol. 10, no. 4, pp. 1578–1584, 2022, doi: 10.1021/acssuschemeng.1c07218.

[263] S. Thoka *et al.*, "Scalable Synthesis of Size-Tunable Small Cu_2O Nanocubes and Octahedra for Facet-Dependent Optical Characterization and Pseudomorphic Conversion to Cu Nanocrystals," *ACS Sustain Chem Eng*, vol. 7, no. 12, pp. 10467–10476, 2019, doi: 10.1021/acssuschemeng.9b00844.

[264] S. Sun *et al.*, "Highly symmetric polyhedral Cu_2O crystals with controllable-index planes," *CrystEngComm*, vol. 13, no. 7, pp. 2217–2221, 2011, doi: 10.1039/c0ce00679c.

[265] J. Friedli *et al.*, "Phase-field modeling of the dendrite orientation transition in Al-Zn alloys," *IOP Conf Ser Mater Sci Eng*, vol. 33, no. 1, 2012, doi: 10.1088/1757-899X/33/1/012111.

[266] R. Li *et al.*, "Gibbs-Curie-Wulff Theorem in Organic Materials: A Case Study on the Relationship between Surface Energy and Crystal Growth," *Advanced Materials*, vol. 28, no. 8, pp. 1697–1702, 2016, doi: 10.1002/adma.201504370.

[267] A. S. Barnard, "Direct comparison of kinetic and thermodynamic influences on gold nanomorphology," *Acc Chem Res*, vol. 45, no. 10, pp. 1688–1697, 2012, doi: 10.1021/ar3000184.

[268] S. Sun *et al.*, "Recent advances in tuning crystal facets of polyhedral cuprous oxide architectures," *RSC Adv*, vol. 4, no. 8, pp. 3804–3822, 2014, doi: 10.1039/c3ra45445b.

[269] U. Banin *et al.*, "Hybrid semiconductor-metal nanoparticles: From architecture to function," *Chemistry of Materials*, vol. 26, no. 1, pp. 97–110, 2014, doi: 10.1021/cm402131n.

[270] A. N. Tuama *et al.*, "An overview on characterization of silver/cuprous oxide nanometallic (Ag/Cu_2O) as visible light photocatalytic," *International Journal of Advanced Science and Technology*, vol. 29, no. 3, pp. 5008–5018, 2020.

[271] S. C. Hsu *et al.*, "Facet-dependent surface plasmon resonance properties of Au-Cu_2O core-shell nanocubes, octahedra, and rhombic dodecahedra," *Small*, vol. 11, no. 2, pp. 195–201, 2015, doi: 10.1002/smll.201401916.

[272] C. F. Hsia *et al.*, "Aqueous Phase Synthesis of Au-Cu Core-Shell Nanocubes and Octahedra with Tunable Sizes and Noncentrally Located Cores," *Chemistry of Materials*, vol. 28, no. 9, pp. 3073–3079, 2016, doi: 10.1021/acs.chemmater.6b00377.

[273] W. C. Wang *et al.*, "Investigation of the effects of polyhedral gold nanocrystal morphology and facets on the formation of Au-Cu_2O core-shell heterostructures," *Chemistry of Materials*, vol. 23, no. 10, pp. 2677–2684, 2011, doi: 10.1021/cm200708q.

[274] J. Li, Z. Sun *et al.*, “Simple synthesis of Ag nanoparticles /Cu_2O cube photocatalyst at room temperature: Efficient electron transfer improves photocatalytic performance,” *Inorg Chem Commun*, vol. 138, no. January, p. 109200, 2022, doi: 10.1016/j.inoche.2022.109200.